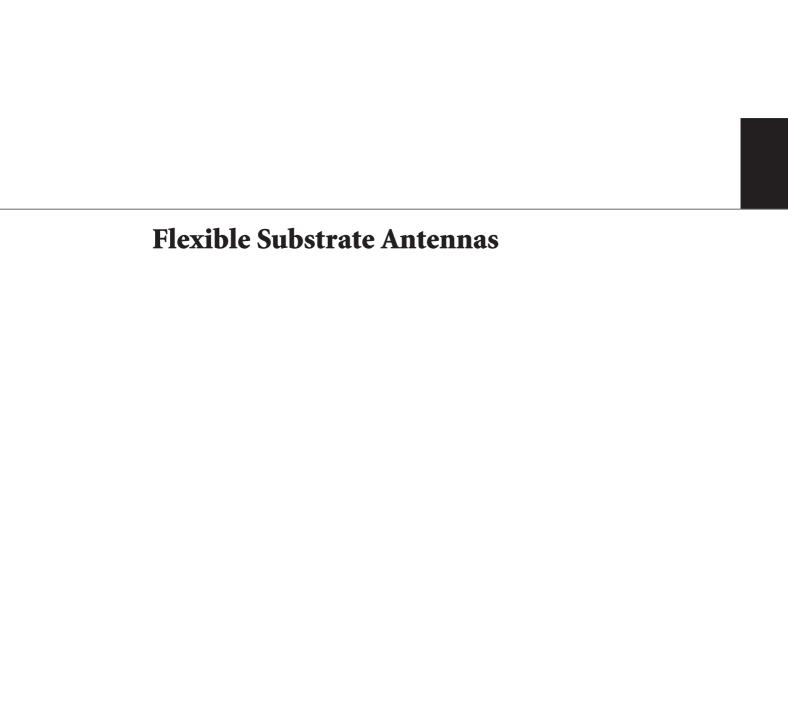
## Flexible Substrate Antennas

Guest Editors: Carles Fernández-Prades, Hendrik Rogier, Ana Collado, and Manos M. Tentzeris





## **Flexible Substrate Antennas**

Guest Editors: Carles Fernández-Prades, Hendrik Rogier, Ana Collado, and Manos M. Tentzeris



## **Editorial Board**

M. Ali, USA Charles Bunting, USA Felipe Cátedra, Spain Dau-Chyrh Chang, Taiwan Deb Chatterjee, USA Z. N. Chen, Singapore Michael Yan Wah Chia, Singapore Christos Christodoulou, USA Shyh-Jong Chung, Taiwan Lorenzo Crocco, Italy Tayeb A. Denidni, Canada Antonije R. Djordjevic, Serbia Karu P. Esselle, Australia Francisco Falcone, Spain Miguel Ferrando, Spain Vincenzo Galdi, Italy Wei Hong, China Hon Tat Hui, Singapore Tamer S. Ibrahim, USA Shyh-Kang Jeng, Taiwan

Mandeep Jit Singh, Malaysia Nemai Karmakar, Australia Se-Yun Kim, Republic of Korea Ahmed A. Kishk, Canada Tribikram Kundu, USA Byungje Lee, Republic of Korea Ju-Hong Lee, Taiwan L. Li, Singapore Yilong Lu, Singapore Atsushi Mase, Japan Andrea Massa, Italy Giuseppe Mazzarella, Italy Derek McNamara, Canada C. F. Mecklenbräuker, Austria Michele Midrio, Italy Mark Mirotznik, USA Ananda S. Mohan, Australia P. Mohanan, India Pavel Nikitin, USA A. D. Panagopoulos, Greece

Matteo Pastorino, Italy Sadasiva M. Rao, USA Sembiam R. Rengarajan, USA Ahmad Safaai-Jazi, USA Safieddin Safavi Naeini, Canada Magdalena Salazar-Palma, Spain Stefano Selleri, Italy Krishnasamy T. Selvan, India Zhongxiang Q. Shen, Singapore John J. Shynk, USA Seong-Youp Suh, USA Parveen Wahid, USA Yuanxun Ethan Wang, USA Daniel S. Weile, USA Quan Xue, Hong Kong Tat Soon Yeo, Singapore Jong Won Yu, Republic of Korea Wenhua Yu, USA Anping Zhao, China Lei Zhu, Singapore

#### **Contents**

Flexible Substrate Antennas, Carles Fernández-Prades, Hendrik Rogier, Ana Collado,

and Manos M. Tentzeris

Volume 2012, Article ID 746360, 2 pages

Novel Flexible Artificial Magnetic Conductor, M. E. de Cos and F. Las-Heras

Volume 2012, Article ID 353821, 7 pages

Flexible Sierpinski Carpet Fractal Antenna on a Hilbert Slot Patterned Ground, Vasa Radonić,

Keith Palmer, Goran Stojanović, and Vesna Crnojević-Bengin

Volume 2012, Article ID 980916, 7 pages

Performance of High-Permittivity Ceramic-Polymer Composite as a Substrate for UHF RFID Tag

**Antennas**, A. A. Babar, V. A. Bhagavati, L. Ukkonen, A. Z. Elsherbeni, P. Kallio, and L. Sydänheimo Volume 2012, Article ID 905409, 8 pages

Efficiency of a Compact Elliptical Planar Ultra-Wideband Antenna Based on Conductive Polymers,

Thomas Kaufmann, Akhilesh Verma, Van-Tan Truong, Bo Weng, Roderick Shepherd, and Christophe Fumeaux

Volume 2012, Article ID 972696, 11 pages

Development of Full-Scale Ultrathin Shell Reflector, Durmuş, Türkmen, Ömer Soykasap,

and Şükrü Karakaya

Volume 2012, Article ID 829780, 9 pages

High-Gain Textile Antenna Array System for Off-Body Communication, Maria Lucia Scarpello,

Luigi Vallozzi, Hendrik Rogier, and Dries Vande Ginste

Volume 2012, Article ID 573438, 12 pages

Textile UWB Antenna Bending and Wet Performances, Mai A. R. Osman, M. K. A. Rahim, N. A. Samsuri,

M. K. Elbasheer, and M. E. Ali

Volume 2012, Article ID 251682, 12 pages

New Flexible Medical Compact Antenna: Design and Analysis, Yann Mahe, Anne Chousseaud,

Marc Brunet, and Bruno Froppier

Volume 2012, Article ID 837230, 6 pages

Investigation of Flexible Textile Antennas and AMC Reflectors, M. Mantash, A.-C. Tarot, S. Collardey,

and K. Mahdjoubi

Volume 2012, Article ID 236505, 10 pages

Cylindrical Bending of Deformable Textile Rectangular Patch Antennas, Freek Boeykens, Luigi Vallozzi,

and Hendrik Rogier

Volume 2012, Article ID 170420, 11 pages

Flexible Hilbert-Curve Loop Antenna Having a Triple-Band and Omnidirectional Pattern for

WLAN/WiMAX Applications, Dang-Oh Kim, Che-Young Kim, and Dae-Geun Yang

Volume 2012, Article ID 687256, 9 pages

Inkjet Printed Planar Coil Antenna Analysis for NFC Technology Applications, I. Ortego, N. Sanchez,

J. Garcia, F. Casado, D. Valderas, and J. I. Sancho

Volume 2012, Article ID 486565, 6 pages

Low-Interference Dual Resonant Antenna Configurations for Multistandard Multifunction Handsets and Portable Computers, Mohamed Sanad and Noha Hassan Volume 2012, Article ID 407973, 8 pages

Hindawi Publishing Corporation International Journal of Antennas and Propagation Volume 2012, Article ID 746360, 2 pages doi:10.1155/2012/746360

## **Editorial**

#### Flexible Substrate Antennas

#### Carles Fernández-Prades, 1 Hendrik Rogier, 2 Ana Collado, 1 and Manos M. Tentzeris 3

- <sup>1</sup> Centre Tecnològic de Telecomunicacions de Catalunya, Communications Subsystems Area, 08860 Castelldefels, Spain
- <sup>2</sup> Department of Information Technology, Ghent University, 9000 Ghent, Belgium
- <sup>3</sup> School of Electrical and Computer Engineering, Georgia Institute of Technology, Atlanta, GA 30332, USA

Correspondence should be addressed to Carles Fernández-Prades, carles.fernandez@cttc.cat

Received 27 June 2012; Accepted 27 June 2012

Copyright © 2012 Carles Fernández-Prades et al. This is an open access article distributed under the Creative Commons Attribution License, which permits unrestricted use, distribution, and reproduction in any medium, provided the original work is properly cited.

Flexible electronics can currently be considered a wellestablished technology that has reached a certain degree of maturity in meeting the requirements of tightly assembled electronic packages, providing reliable electrical connections where the assembly is required to flex during its normal use or where board thickness, weight, or space constraints are driving factors.

In this context, flexible substrate antennas (FSAs) play a key role in the integration and packaging of wireless communication devices and sensor networks. Those antennas, which are designed such that the resonant peak frequency remains unaffected after bending, stretching, or twisting, are currently being embedded into materials such as textile fabrics, bandages, stickers, and bendable displays. FSAs are rapidly emerging as a popular choice for radio frequency identification (RFID) tags, multisystem wireless communication gadgets, wearable computer systems, and smart clothing and spurring new applications in wireless sensing such as monitoring of civil construction, health care supervision, or the integration in search and rescue satellite systems.

The introduction of new design concepts, new materials and new fabrication processes is adding momentum and interest to the development of flexible antennas for consumer electronics. Researchers are continuingly relying on flexible antenna technology to solve the problems of efficiency, reliability, cost, weight, shape, and reproducibility. There is also the need of using environmentally friendly and low-cost materials and production processes, in order to allow for the easy disposal of a massive number of those devices. This special issue aims at reflecting current research trends

and new approaches in FSAs, collecting 13 peer-reviewed articles (with an acceptance ratio of 52%) reporting original research coming from 46 authors of 19 institutions of 14 countries.

Authors of this special issue used a variety of materials such as silver nanoparticle ink printed on Kapton polyimide film, ceramic-polymer and carbon-epoxy composites, conductive polymers such as PEDOT or PPy, metamaterialbased artificial magnetic conductor structures, or a copperplated nylon fabric that acts as a conductive electrotextile material. They addressed a number of technologies located in different frequency bands, including near field communications (13,56 MHz), UHF RFID tag antennas (860 MHz), global navigation satellite systems (L2 band at 1.227 GHz and L1 band at 1.575 GHz), L-band DVB-H (1452-1492 MHz), GSM1800 (1710-1880 MHz), PCS1900 (1859-1990 MHz), UMTS (1900-2170 MHz), wireless local area networks such as WiFi and WiMAX (2.4-, 3.6-, and 5-GHz), Bluetooth (2.4 GHz), ultra-wideband (3.1 to 10.6 GHz), and even scientific applications at the Ku-band (12-18 GHz). This diversity reflects the lively momentum that research of FSAs is experiencing, as corroborated by the number of scientific publications on the topic shown in Figure 1.

#### **Acknowledgments**

We would like to thank many people whose efforts made this special issue possible. We thank the authors for their response to our initial call for papers, and we would like to acknowledge the significant contributions of the

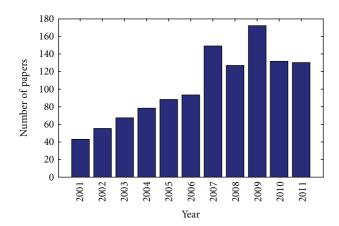


FIGURE 1: Number of papers that matches the search "flexible antennas" at the Thomson Reuters' Web of Science, using data from the Science Citation Index Expanded (SCI-EXPANDED) and Conference Proceedings Citation Index-Science (CPCI-S) databases.

reviewers who provided feedback on multiple versions of the papers.

Carles Fernández-Prades Hendrik Rogier Ana Collado Manos M. Tentzeris Hindawi Publishing Corporation International Journal of Antennas and Propagation Volume 2012, Article ID 353821, 7 pages doi:10.1155/2012/353821

## Research Article

## **Novel Flexible Artificial Magnetic Conductor**

#### M. E. de Cos and F. Las-Heras

Area de Teoría de la Señal y Comunicaciones, Departamento de Ingeniería Eléctrica, Universidad de Oviedo, Edificio Polivalente, Modulo 8, Campus Universitario de Gijón, Asturias, 33203 Gijón, Spain

Correspondence should be addressed to M. E. de Cos, medecos@tsc.uniovi.es

Received 15 February 2012; Revised 29 April 2012; Accepted 30 April 2012

Academic Editor: Carles Fernández-Prades

Copyright © 2012 M. E. de Cos and F. Las-Heras. This is an open access article distributed under the Creative Commons Attribution License, which permits unrestricted use, distribution, and reproduction in any medium, provided the original work is properly cited.

A novel flexible uniplanar AMC design is presented. An AMC prototype is manufactured using laser micromachining and it is characterized under flat and bent conditions by measuring its reflection coefficient phase in an anechoic chamber. The designed prototype shows broad AMC operation bandwidth (6.96% and higher) and polarization angle independency. Its angular stability margin, when operating under oblique incidence, is also tested obtaining  $\pm 8^{\circ}$  as limit for a 14.4 cm  $\times$  14.4 cm prototype.

#### 1. Introduction

Metamaterials have attracted a lot of attention in the recent years due to their unique properties in controlling the propagation of electromagnetic waves, which makes them able to solve some antennas and microwave circuits' problems. Between the metamaterial structures Artificial Magnetic Conductor (AMC) structures [1–10] are especially interesting in the design of highly efficient and low-profile antennas [11–17], due to their inherent in-phase reflection properties which in addition reduces the radiation to the body [18] in wearable applications [19–23].

Perfect Magnetic Conductors (PMCs) do not exist in nature. AMCs are synthesized PMCs and are dual to a Perfect Electric Conductor (PEC) from an electromagnetic point of view. AMCs exhibit a reflection coefficient with a magnitude value of 1 and a phase value of  $0^{\circ}$  in the ideal lossless case. It is considered [1–3] that AMCs behave as PMCs over a certain frequency band, the so-called bandwidth of AMC performance or AMC operation bandwidth, which is generally defined in the range from  $+90^{\circ}$  to  $-90^{\circ}$ , since in this range, the phase values would not cause destructive interference between direct and reflected waves.

AMCs are often implemented using two-dimensional periodic metallic lattices patterned on a conductor-backed dielectric surface. The research efforts recently focus on the

development of low-cost AMCs that can be easily integrated in microwave and millimeter wave circuits. This requires the use of geometries without via holes [2, 4–9] (in contrast to designs consisting in patches with via holes [1]) as well as the use of a unilayer periodic Frequency Selective Surface (FSS) over a metallic ground plane (in contrast to multilayered FSSs [10]). In the unilayer case, the main drawback is the very narrow AMC operation bandwidth. By optimizing the unit cell geometry design and using a low relative dielectric permittivity substrate, which in addition reduces the cost, this can be overcome to some extent.

The interest in flexible AMCs is growing since it would be desirable to have AMC being object-shape-adapted for many applications as Radio Frequency Identification (RFID) tags over metallic objects [24], wearable antennas [19–23], and RCS reduction [25]. This would require the AMC to be flexible (especially in the case of objects with curved surfaces) but without losing its functionality.

In this paper, a novel compact uniplanar AMC design without via holes is presented and manufactured using a bendable dielectric substrate, which adds the advantage of flexibility to the resulting AMC structure, preserving its remarked features. In addition, the novel AMC exhibits other advantages as broad AMC operation bandwidth and high angular stability.

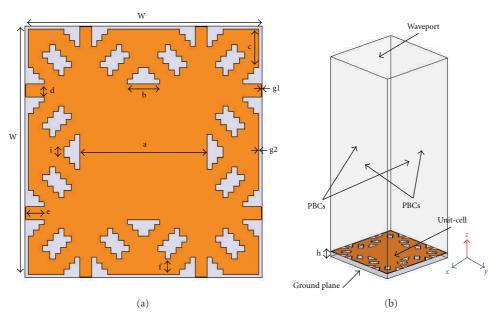


FIGURE 1: AMC unit-cell design: (a) unit-cell geometry top view and (b) simulation setup.

#### 2. AMC Desing

In an AMC structure each unit cell implements a distributed parallel LC network having one or more resonant frequencies. The resonance frequency is where the high impedance and AMC conditions occur and for a parallel LC circuit is equal to  $1/(2\pi\sqrt{LC})$ , while in-phase reflection bandwidth is proportional to  $\sqrt{L/C}$ . In order to achieve an AMC structure at a certain frequency and with the desired bandwidth a designer can modify the unit cell geometry together with substrate's relative dielectric permittivity and thickness. The thicker the dielectric substrate is, the wider the AMC bandwidth is. The higher the dielectric substrate relative permittivity, the lower the resonance frequency but also, the lower the AMC bandwidth [6]. Finally, by changing the unit cell geometry the equivalent LC resonant circuit is modified. In order to obtain a wider AMC operation bandwidth, it is necessary to increase L and reduce C. L can be increased using a thicker dielectric substrate and also including in the geometry narrow and long strips (lines). C can be reduced by reducing substrate's relative dielectric permittivity  $\varepsilon_r$  and increasing the gap between the metallization edge and the unit-cell edge (and so the gap between adjacent unit cells). In order to obtain both compact size and broad AMC operation bandwidth, a trade-off solution regarding  $\varepsilon_r$  and substrate thickness has to be adopted.

Taking all these considerations into account, a novel uniplanar AMC at 6 GHz has been designed using ROGER3003 substrate with a thickness h = 0.762 mm, relative dielectric permittivity  $\varepsilon_r = 3.0$ , and loss tangent  $tg_{\delta} = 0.0013$ .

Finite Element Method (FEM) together with the Bloch-Floquet theory is used in simulation to search for the frequency band in which the periodic structure behaves as an AMC. The AMC reflection coefficient for a uniform incident plane wave is simulated using HFSS of Ansoft, modeling a

single cell of the structure with periodic boundary conditions (PBC) on its sides and resembling the modeling of an infinite structure [1, 6, 7, 9]. The periodic structure is illuminated, launching normal plane waves using a waveport positioned a half-wavelength above it (see Figure 1(b)). The phase reference plane is taken on the periodic surface. The phase of the reflection coefficient of the AMC plane is compared to that of a PEC plane taken as reference and placed in identical position, in the same way as in [1].

The geometry of the AMC unit cell is shown in Figure 1(a). Its design has taken into account that the AMC will be subsequently bent. When defining "h," the thickness of the substrate is taken into account that it is desired to be as thin as possible considering the thickness commercially available and to be bendable. Also the thinner the dielectric substrate, the higher the AMC's angular stability under oblique incidence. Very narrow strips have been avoided since they may break when the AMC is bent, despite the long and narrow strips increasing the bandwidth of operation as AMC. Internal gaps in the geometry are used to modify the equivalent C and thus adjust the frequency and bandwidth, as desired (in addition to what has been explained earlier in this section). The final optimized dimensions for operation at 6 GHz are detailed in Table 1. From the simulated reflection coefficient phase of the designed AMC structure (see Figure 2), it can be concluded that the resonance frequency is 6 GHz with an AMC operation bandwidth of 500 MHz (8.33% with respect to the central frequency) which is a broad bandwidth for a low-profile AMC ( $\lambda_0/65.6$ at 6 GHz).

The AMC performance under different polarization of the electrical incident field (under normal incidence) and under oblique incidence is very important in some of the AMC intended applications as for example RFID tags, or wearable antennas. In the case of RFID tags when combining

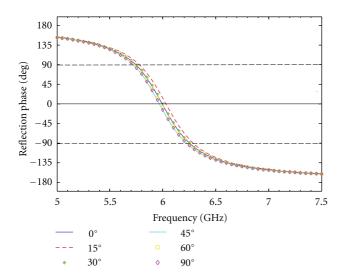


Figure 2: Simulated reflection phase of the AMC surface for different incident field ( $E_{inc}$ ) polarization angles =  $0^{\circ}$ ,  $15^{\circ}$ ,  $30^{\circ}$ ,  $45^{\circ}$ ,  $60^{\circ}$ , and  $90^{\circ}$ .

Table 1: Unit-cell dimensions.

Dimensions (mm)									
W	а	b	С	d	е	f	<i>g</i> 1	g2	i
12.0	6.456	1.646	1.827	0.609	0.945	0.730	0.032	0.154	0.522

the AMC with the antenna, the angular stability of the AMC will influence the antenna radiation performance, and this will have direct impact on the angular reading range of the final RFID tag depending on the position of the reader with respect to the tagged object. Following this, an AMC design with as higher angular stability as possible is desirable.

Aiming to study the angular stability margin [26] of the presented structure, the reflection coefficient phase versus frequency for different incident angles  $\theta_{\rm inc}$  between 0° and 60° has been simulated for transverse-electric- (TE-) polarized waves. The absolute and relative deviations of the resonant frequency which are, respectively, 50 MHz, 0.82% for  $\theta_{\rm inc}=40^\circ$  and 100 MHz, 1.6% for  $\theta_{\rm inc}=60^\circ$  can be obtained from Figure 3. The AMC operation bandwidth is slightly reduced from  $\theta_{\rm inc}=40^\circ$ . From these obtained results, it can be concluded that the presented AMC design is highly stable as its angular margin ranges from 0° to 60° preserving an AMC operation bandwidth of 260 MHz in which the operation frequency of 6 GHz is always included.

#### 3. Flexible AMC's Characterization

In order to validate the simulation results, a  $12 \times 12$  cells planar AMC prototype has been manufactured using laser micromachining to be measured.

There are many arbitrary ways of bending a flexible AMC. Two typical different bending patterns have been selected and tested (see Figure 4): a "creeping" pattern (henceforth referred to as creeping prototype) which can be caused in textile AMC integrated in the garment, for example

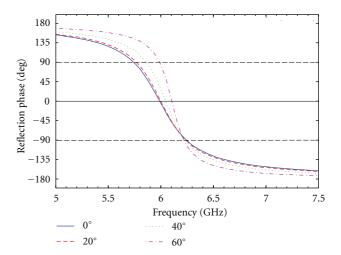


FIGURE 3: Simulated reflection phase of the AMC surface for TE polarizations for different incident angles  $\theta_{\rm inc}=0^{\circ}$ ,  $15^{\circ}$ ,  $30^{\circ}$ ,  $45^{\circ}$ , and  $60^{\circ}$ .

when the arm is bent at the elbow, and a "smooth" pattern (henceforth referred as smooth prototype) which can be caused in the torso or in the shoulder.

3.1. Measurement Setup in Anechoic Chamber. Two-horn antenna probes working in the band 5–7 GHz have been chosen as Tx and Rx (see Figure 5) in the measurement setup (similar to the one used in [7, 9]), being 3 m the separation between each probe and the object under test. The measured prototypes physical size is 14.4 cm  $\times$  14.4 cm (PEC and AMC have the same size). For the upper frequency (f=7 GHz), the far field distance (RFF =  $2D^2/\lambda$ ) is RFF,7GHz  $\sim$  0.97 m, whereas for the lower frequency (f=5 GHz) it decreases until RFF,5GHz  $\sim$  0.69 m. Thus, the prototypes have been measured in far field conditions.

3.2. Reflection Phase Measurement for AMC Band Determination. To calculate the reflection coefficient of the AMC structure the same methodology as for the full-wave simulation, based on the utilization of a reference measurement (metallic plate) [1, 7], is followed.

Firstly the flat AMC has been characterized and then the prototype has been bent and measured.

The measured reflection phase of the flat and bent manufactured prototypes for normal incidence conditions is shown in Figure 6. The flat prototype has the resonance at 6.178 GHz which means a 2.9% deviation with respect to the simulation (6.0 GHz), very probably due to under-etching in the laser micromachining.

From Table 2 and Figure 6, it can be observed that almost there is no frequency shift for the manufactured creeping bent prototype with respect to the flat prototype resonance, whereas the smooth bent prototype has its resonance at 6.208 GHz, which means just a 1.69% deviation with respect to the flat prototype. The flat prototype shows a 430 MHz (6.96%) AMC operation bandwidth in good agreement with the simulated value (8.33%) (see Figure 2), whereas the

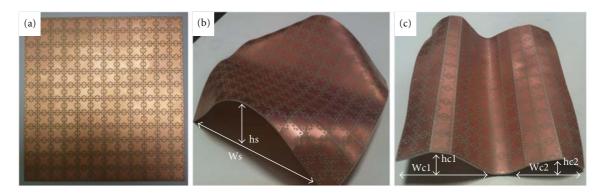


FIGURE 4: (a) Flat manufactured prototype and bending patters: (b) smooth prototype with Ws = 125 mm and hs = 30 mm; (c) creeping prototype with Wc1 = 60 mm, Wc2 = 52 mm, hc1 = 18 mm, and hc2 = 15 mm.

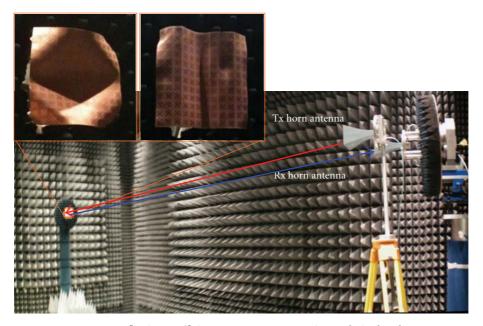


Figure 5: Reflection coefficient measurement setup in anechoic chamber.

Table 2: Prototypes comparison.

Prototype	Resonance frequency (GHz)	Frequency deviation with respect to flat (%)	Measured bandwidth (%)
Flat	6.178	0	6.96
Smooth	6.073	1.69	8.02
Creeping	6.208	0.48	10.07

creeping bent prototype exhibits 625 MHz (10.07%) and the smooth bent AMC shows 487 MHz (8.02%), even slightly wider than that of the flat prototype.

3.3. Reflection Phase Characterization for Different Field Polarization Angles. The reflection phase stability of the manufactured AMC prototypes with respect to the incident

field polarization angle  $(\varphi)$  has been also tested through measurements.

It has been proved that under normal incidence ( $\theta_{inc} = 0^{\circ}$ ) the flat prototype presents the same reflection phase for any polarization due to the unit cell symmetry (see Figure 7). In the case of the bent prototype, this invariance with respect to the polarization angle is also present.

3.4. Reflection Phase Characterization for Different Incidence Angles. The angular stability under oblique incidence has been analyzed for both the smooth and the creeping prototypes. The reflection coefficient phase versus frequency, for different incident angles  $\theta_{\rm inc}$ , has been measured. For the flat prototype, resonance conditions are met within an angular margin of  $\theta_{\rm inc} = \pm 10^\circ$  (see Figure 8), whereas for the smooth and creeping bent prototypes the obtained angular margin is  $\theta_{\rm inc} = \pm 8^\circ$  (see Figures 9 and 10). The differences between simulation and measurements can be

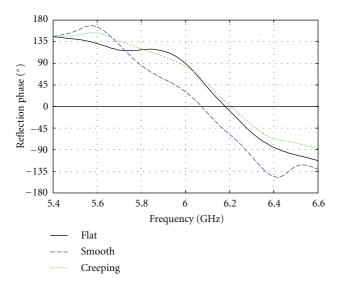


FIGURE 6: Measured reflection coefficient phase of the flat and bent prototypes versus frequency.

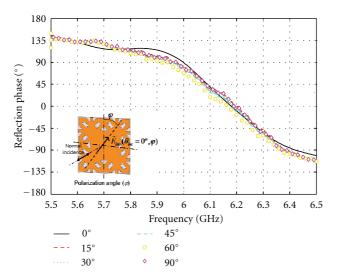
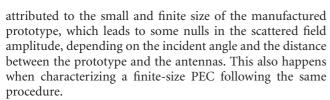


FIGURE 7: Reflection phase of the manufactured prototype for different incident field ( $\mathbf{E}_{\text{inc}}$ ) polarization angles ( $\varphi$ ).



The presented results show that it is possible to obtain a flexible AMC without reducing the bandwidth of AMC performance with respect to a rigid AMC that uses the same unit-cell design and preserving its angular stability under oblique incidence.

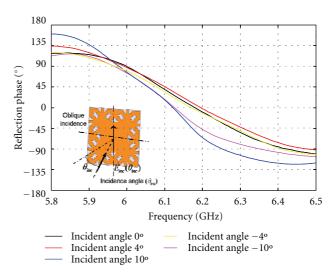


FIGURE 8: Reflection phase of the manufactured flat prototype for different incident angles ( $\theta_{\rm inc}$ ).

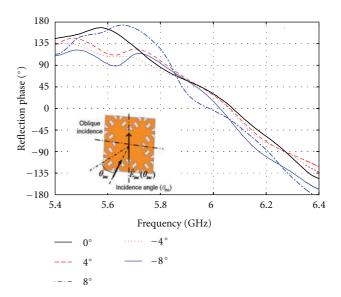


Figure 9: Reflection phase of the manufactured smooth prototype for different incident angles ( $\theta_{\rm inc}$ ).

#### 4. Conclusions

A novel flexible uniplanar AMC design based on FEM simulations has been presented. A prototype has been manufactured using a bendable dielectric substrate and it has been characterized by means of reflection coefficient phase measurements in anechoic chamber under flat and bent conditions. Broad AMC operation bandwidth, polarization angle independency under normal incidence, and high angular stability under oblique incidence have been found.

The presented uniplanar low-profile design without via holes, together with the flexible characteristic, low cost, simple fabrication, and integration, makes it very attractive

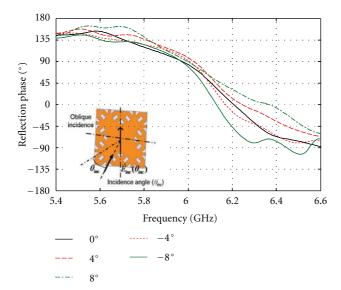


Figure 10: Reflection phase of the manufactured creeping prototype for different incident angles ( $\theta_{\rm inc}$ ).

for applications involving antennas in RFID tags, wearable systems, and RCS reduction. Also it could be used as part of Microwave Integrated Circuits (MICs).

#### Acknowledgments

This work has been supported by the Ministerio de Ciencia e Innovación of Spain/FEDER under Projects TEC2011-24492 (iScat) and CONSOLIDER-INGENIO CSD2008-00068 (TERASENSE), by the Gobierno del Principado de Asturias (PCTI)/FEDER-FSE under Projects EQUIP08-06, FC09-COF09-12, EQUIP10-31, and PC10-06 (FLEXANT).

#### References

- [1] D. Sievenpiper, L. Zhang, R. F. Jimenez Broas, N. G. Alexöpolous, and E. Yablonovitch, "High-impedance electromagnetic surfaces with a forbidden frequency band," *IEEE Transactions on Microwave Theory and Techniques*, vol. 47, no. 11, pp. 2059–2074, 1999.
- [2] F. R. Yang, K. P. Ma, M. Yongxi Qian, and T. Itoh, "A uniplanar compact photonic-bandgap (UC-PBG) structure and its applications for microwave circuits," *IEEE Transactions* on Microwave Theory and Techniques, vol. 47, no. 8, pp. 1509– 1514, 1999.
- [3] F. Yang and Y. Rahmat-Samii, *Electromagnetic Band-Gap Structures in Antenna Engineering*, The Cambridge RF and Microwave Engineering Series, Cambridge University, 2008.
- [4] J. McVay, N. Engheta, and A. Hoorfar, "High impedance metamaterials surfaces using Hilbert-curve inclusions," *IEEE Microwave and Wireless Components Letters*, vol. 14, no. 3, pp. 130–132, 2004.
- [5] Y. Kim, F. Yang, and A. Z. Elsherbeni, "Compact artificial magnetic conductor designs using planar square spiral geometries," *Progress in Electromagnetics Research*, vol. 77, pp. 43–54, 2007.

- [6] M. E. De Cos, F. L. Heras, and M. Franco, "Design of planar artificial magnetic conductor ground plane using frequencyselective surfaces for frequencies below 1 GHz," *IEEE Antennas* and Wireless Propagation Letters, vol. 8, pp. 951–954, 2009.
- [7] M. E. De Cos, Y. Álvarez, and F. Las-Heras, "Planar artificial magnetic conductor: design and characterization setup in the RFID SHF band," *Journal of Electromagnetic Waves and Applications*, vol. 23, no. 11-12, pp. 1467–1478, 2009.
- [8] D. J. Kern, D. H. Werner, A. Monorchio, L. Lanuzza, and M. J. Wilhelm, "The design synthesis of multiband artificial magnetic conductors using high impedance frequency selective surfaces," *IEEE Transactions on Antennas and Propagation*, vol. 53, no. 1 I, pp. 8–17, 2005.
- [9] M. E. De Cos, Y. Álvarez, R. C. Hadarig, and F. Las-Heras, "Novel SHF-band uniplanar artificial magnetic conductor," *IEEE Antennas and Wireless Propagation Letters*, vol. 9, pp. 44–47, 2010.
- [10] A. Monorchio, G. Manara, and L. Lanuzza, "Synthesis of artificial magnetic conductors by using multilayered frequency selective surfaces," *IEEE Antennas and Wireless Propagation Letters*, vol. 1, pp. 196–199, 2002.
- [11] F. Yang and Y. Rahmat-Samii, "Reflection phase characterizations of the EBG ground plane for low profile wire antenna applications," *IEEE Transactions on Antennas and Propagation*, vol. 51, no. 10 I, pp. 2691–2703, 2003.
- [12] J. McVay, A. Hoorfar, and N. Engheta, "Small dipole antenna near peano high-impedance surfaces," in *Proceedings of the IEEE Antennas and Propagation Society Symposium*, vol. 1, pp. 305–308, June 2004.
- [13] H. Mosallaei and K. Sarabandi, "Antenna miniaturization and bandwidth enhancement using a reactive impedance substrate," *IEEE Transactions on Antennas and Propagation*, vol. 52, no. 9, pp. 2403–2414, 2004.
- [14] L. Akhoondzadeh-Asl, D. J. Kern, P. S. Hall, and D. H. Werner, "Wideband dipoles on electromagnetic bandgap ground planes," *IEEE Transactions on Antennas and Propagation*, vol. 55, no. 9, pp. 2426–2434, 2007.
- [15] J. Liang and H. Y. D. Yang, "Radiation characteristics of a microstrip patch over an electromagnetic bandgap surface," *IEEE Transactions on Antennas and Propagation*, vol. 55, no. 6, pp. 1691–1697, 2007.
- [16] A. P. Feresidis, G. Goussetis, S. Wang, and J. C. Vardaxoglou, "Artificial magnetic conductor surfaces and their application to low-profile high-gain planar antennas," *IEEE Transactions* on Antennas and Propagation, vol. 53, no. 1 I, pp. 209–215, 2005
- [17] J. R. Sohn, K. Y. Kim, H. S. Tae, and J. H. Lee, "Comparative study on various artificial magnetic conductors for low-profile antenna," *Progress in Electromagnetics Research*, vol. 61, pp. 27– 37, 2006.
- [18] E. Rajo-Iglesias, L. Inclán-Sánchez, and Q. Quevedo-Teruel, "Back radiation reduction in patch antennas using planar soft surfaces," *Progress In Electromagnetics Research Letters*, vol. 6, pp. 123–130, 2009.
- [19] S. Zhu and R. Langley, "Dual-band wearable textile antenna on an EBG substrate," *IEEE Transactions on Antennas and Propagation*, vol. 57, no. 4, pp. 926–935, 2009.
- [20] M. Mantash, A-C. Tarot, S. Collardey, and K. Mabjoubi, "Dual-band antenna for W-LAN applications with EBG," in Proceedings of the 5th International Congress on Advanced Electromagnetic Materials in Microwave and Optics (Metamaterials '11), pp. 456–458, Barcelona, Spain, October 2011.
- [21] M. Mantash, A. C. Tarot, S. Collardey, and K. Mahdjoubi, "Dual-band CPW-fed G-antenna using an EBG structure," in

- Proceedings of the 6th Loughborough Antennas and Propagation Conference (LAPC '10), pp. 453–456, November 2010.
- [22] P. Salonen and Y. Rahmat-Samii, "Textile antennas: effects of antenna bending on input matching and impedance bandwidth," *IEEE Aerospace and Electronic Systems Magazine*, vol. 22, no. 3, pp. 10–14, 2007.
- [23] P. Salonen, F. Yang, Y. Rahmat-Samii, and M. Kivikoski, "WEBGA—Wearable electromagnetic band-gap antenna," in Proceedings of the IEEE Antennas and Propagation Society Symposium, vol. 1, pp. 451–454, Monterrey, Calif, USA, June 2004
- [24] R. C. Hadarig, M. E. De Cos Gomez, Y. Álvarez, and F. Las-Heras, "Novel bow-tie—AMC combination for 5.8-GHz RFID tags usable with metallic objects," *IEEE Antennas and Wireless Propagation Letters*, vol. 9, pp. 1217–1220, 2010.
- [25] M. E. de Cos, Y. Álvarez, and F. Las-Heras, "A novel approach for RCS reduction using a combination of artificial magnetic conductors," *Progress in Electromagnetics Research*, vol. 107, pp. 147–159, 2010.
- [26] C. R. Simovski, P. De Maagt, S. A. Tretyakov, M. Paquay, and A. A. Sochava, "Angular stabilisation of resonant frequency of artificial magnetic conductors for TE-incidence," *Electronics Letters*, vol. 40, no. 2, pp. 92–93, 2004.

Hindawi Publishing Corporation International Journal of Antennas and Propagation Volume 2012, Article ID 980916, 7 pages doi:10.1155/2012/980916

## Research Article

## Flexible Sierpinski Carpet Fractal Antenna on a Hilbert Slot Patterned Ground

#### Vasa Radonić, Keith Palmer, Goran Stojanović, and Vesna Crnojević-Bengin Vasa Radonić,

- <sup>1</sup> Faculty of Technical Sciences, University of Novi Sad, Trg Dositeja Obradovića 6, 21000 Novi Sad, Serbia
- <sup>2</sup> Department of Electrical and Electronic Engineering, Stellenbosch University, Private Bag X1, Matieland, Stellenbosch 7602, South Africa

Correspondence should be addressed to Vasa Radonić, vasarad@uns.ac.rs

Received 15 December 2011; Accepted 5 April 2012

Academic Editor: Carles Fernández-Prades

Copyright © 2012 Vasa Radonić et al. This is an open access article distributed under the Creative Commons Attribution License, which permits unrestricted use, distribution, and reproduction in any medium, provided the original work is properly cited.

This paper presents a novel design of fractal antenna on a flexible substrate that operates in UMTS band (universal mobile telecommunication system, 1.92–2.17 GHz). The antenna consists of a Sierpinski carpet fractal radiator, which reduces the overall size of the antenna, and it is realized on top of a Hilbert slot in the ground layer, to achieve required impedance matching. The antenna is compact with the overall dimensions equal to  $70 \,\mathrm{mm} \times 31 \,\mathrm{mm} \times 0.075 \,\mathrm{mm}$ . Influence that folding has on the initial planar topology is investigated in detail. The obtained results show that the proposed antenna is more tolerant to folding than the conventional patch and that it exhibits relatively stable radiation patterns even when folded in complex manners.

#### 1. Introduction

Designing a small antenna with good bandwidth performance presents a challenge for modern communication devices, such as Bluetooth or WLAN devices. To minimize the size of the antenna or to improve its characteristics, various solutions based on fractal geometry have recently been proposed [1–8]. Different fractal geometries, such as Peano, Hilbert, or Sierpinski curves, have been used to bring forth the benefits of small size [2, 4, 6–8], wide bandwidth [5], or multiband operation [3, 5, 6]. This paper presents a fractal topology that is tolerant to folding.

Fractal curves are unique for their self-similarity and space-filling properties. Due to the self-similarity, a fractal antenna being made up of many differently scaled copies of itself is likely to maintain similar radiation parameters in different bands proportional to the wavelengths. On the other hand, the space-filling property of fractals allows theoretically the design of infinite-length lines on finite substrate areas, thus leading to compact antennas.

Flexible electronics are becoming more viable with the recent technological developments opening up possibilities to integrate wireless functions into clothing, moving objects, or into animals to monitor various parameters of interest.

Although flexible technology offers components that can bend together with the host medium (e.g., textile) with practically no disturbance to the subject wearing it, bending can significantly deteriorate the performances of the wireless components, most notably the antenna. Significant research efforts are currently focused on study and analyzing the viability of these flexible substrate materials. Several experimental studies have been carried out recently to investigate the effects of antenna bending on its characteristics such as resonant frequency, return loss, impedance bandwidth, gain, and radiation patterns [8–13].

In this paper, we propose a novel flexible antenna based on the Sierpinski carpet fractal curve of the third order, realized on a Hilbert slotted ground. The proposed antenna was simulated using CST Microwave Studio and compared with the conventional patch antenna. Impact of folding on both antennas was analyzed in details. To validate the simulation results, the proposed antenna was fabricated and measured.

#### 2. Fractal Antenna

The proposed antenna consists of a Sierpinski carpet radiator realized on the top side of the flexible substrate with

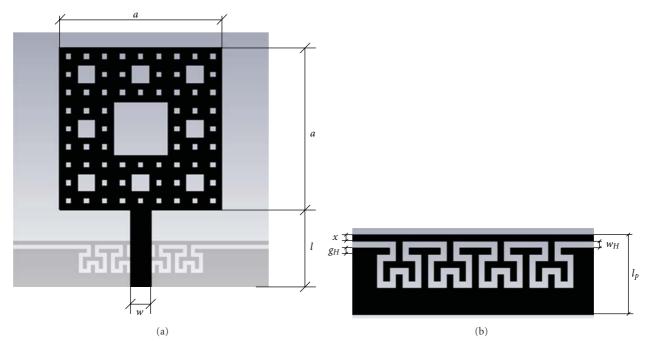


FIGURE 1: (a) Proposed fractal antenna on a Hilbert slot patterned ground (black: top metallic layer, dark gray: bottom metallic layer); (b) magnified detail of the patterned ground under the feed line (black: bottom metallic layer).

a Hilbert slot on the bottom side (Figure 1). The Sierpinski carpet antenna is in essence a square metallic patch divided into 9 congruent subsquares in a 3-by-3 grid, in which the metallization of the middle square section is removed. The same procedure is then applied recursively to the remaining 8 subsquares and again to the resulting elements. In that manner, the third-order fractal antenna is obtained with the dimensions of the radiator equal to  $20~\mathrm{mm} \times 20~\mathrm{mm}$ . The antenna is fed by a  $2.6~\mathrm{mm}$  wide and  $10~\mathrm{mm}$  long microstrip line.

In order to match the antenna to a 50  $\Omega$  SMA connector, four serially connected slots in the shape of the Hilbert fractal curve of the second order were printed in the ground plane (Figure 1(b)). The position and line width and spacing of the Hilbert slot are the most important parameters for the impedance matching as well as for obtaining a good radiation pattern and reflection coefficient of the antenna. The position x and the line width and spacing, denoted  $w_H$  and  $g_H$ , respectively, were optimized with the following values obtained: x = 0.6 mm,  $w_H = g_H = 0.5$  mm. The total length of the Hilbert slot is 6 mm. As can be seen from Figure 1(b), there is no ground plane under the radiator. The existing ground plane is split into two sections by the Hilbert slot, generating some electromagnetic coupling. As a consequence, apart from the reduction of the ground plane area, a decrease of the antenna resonant frequency is obtained, which additionally contributes to antenna miniaturization.

The antenna was designed using a 0.075 mm thick Kapton substrate with relative permittivity  $\varepsilon_r = 3.2$  and dissipation factor equal to 0.0019. All simulations were performed using CST Microwave Studio.

Various ways of bending the antenna were analyzed, shown in Figure 2. In Figure 2(a) the antenna is folded along one-third of its length in the y-direction, and two-thirds in Figure 1(b). In the cases shown in Figures 1(c) and 1(d) more demanding modifications are made: the antenna was folded twice, along the one and two third of its length, resulting in structures with a cross-section similar to letters C and C, respectively. In that way, the dimensions of the antenna were significantly changed: its length was decreased while its height was increased.

Figure 3 compares the simulated return loss of the initial planar fractal antenna with the return losses of its folded modifications. More detailed results are presented in Table 1, where the proposed fractal antenna is also compared to the conventional patch antenna realized on a partial ground plane and tuned to the same frequency, as well as to the patch's folded modifications obtained by bending the patch antenna in the same manner as shown in Figure 2. Final dimensions of the patch radiator are 24 mm  $\times$  24 mm, while the length of the partial ground is 2.1 mm. To facilitate the comparison, frequency shifts and variations in the bandwidth are also listed in Table 1, relative to the planar versions of the antenna in question.

As expected, it can be seen that any folding of the antenna directly impacts on its performances. However, this impact is significantly reduced in the case of the proposed fractal antenna: the frequency shift of the patch antenna due to bending ranges between 2.42 and 6.81%, while it is equal to 3.4% for the worst-case fractal antenna. Fractional bandwidth of the fractal antenna changes up to 25.14%, while conventional one exhibits 34.49%. The average frequency shift for the patch antenna is 4.09% while

TABLE 1: Detailed comparison between performances of the proposed fractal and the conventional patch antenna, for both the planar and	ł
the folded cases.	

Antenna type	Modification	$f_r$ [GHz]	$\Delta f_r$ [%]	FBW [%]	ΔFBW [%]	S <sub>11</sub> [dB]
	Planar	1.9850	_	5.37	_	-25.7
	1	2.0120	1.36	4.02	-25.14	-14.7
Fractal	2	2.0120	1.36	5.13	-4.47	-20.8
1140441	3	2.0525	3.40	n/a	n/a	-9.4
	4	2.0255	2.04	4.42	-17.69	-16.3
	Planar	1.9445	_	9.8	_	-34.4
	1	1.9985	2.78	8.1	-17.35	-18.4
Patch	2	1.9915	2.42	8.35	-14.80	-22.5
1 40011	3	2.0770	6.81	6.42	-34.49	-23.6
	4	2.0295	4.37	7.83	-20.10	-33.5

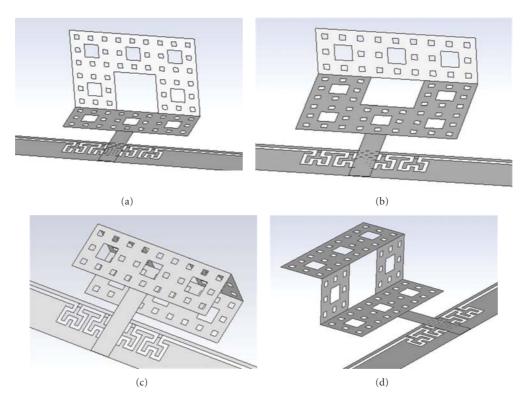


FIGURE 2: Different ways of folding the antenna: (a) modification 1, (b) modification 2, (c) modification 3, and (d) modification 4.

it is only 2.04% for the proposed fractal antenna. The same holds for the average variation of the fractional bandwidth: 21.7% for the conventional antenna versus only 15.3% for the fractal antenna. Inspecting the tabulated results, it can be concluded that the deterioration of performance observed for simple modifications of the patch antenna (modifications 1 and 2) is similar to the case of complex modifications of the fractal antenna (modifications 3 and 4). This illustrates the robustness to folding that the proposed fractal antenna exhibits over the conventional patch. In the same time, the fractal antenna occupies 30% smaller substrate area than the patch, and it is less sensitive to mechanical strain.

In Figures 4 and 5 radiation patterns in E-plane and H-plane for the planar fractal and patch antennas and their modifications relative to the flat antennas are shown. The patterns are omnidirectional in H-plane. The average gain

reduction in the case of conventional antenna is 46%, while the fractal antenna exhibits 41%. It can be seen that the change of the main lobe directivity is similar for both antennas and equal to 40%.

#### 3. Fabrication and Measurement

The proposed fractal antenna was fabricated using a Dimatix [14] material deposition printer DMP-3000, which is cartridge-based piezo inkjet printing system which enables direct deposition of fluids (functional materials). The resolution of the inkjet process is mainly governed by the nozzle diameter (approximately the droplet diameter) and the statistical variation of the droplet flight and spreading on the substrate. Resolution can be modified by adjusting

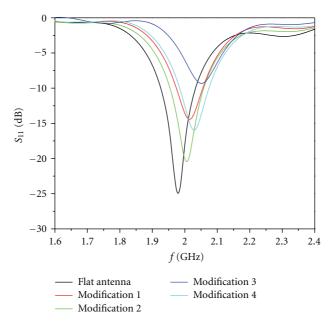


FIGURE 3: Simulated return loss for the proposed planar fractal antenna and its folded modifications.

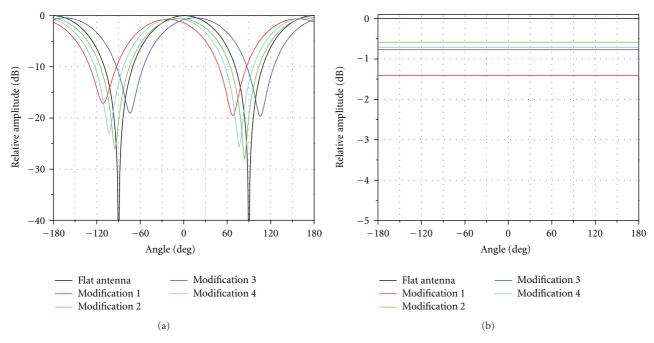


FIGURE 4: Radiations patterns for the proposed fractal antenna: (a) radiation pattern in E-plane, (b) radiation pattern in H-plane.

the angle of the printhead during printing. In the case of printing with silver nanoparticle ink (Suntronic Jet Silver U6503, [15]), the minimum droplet diameter was around 50  $\mu$ m and drop spacing was 25  $\mu$ m (center to center) which has obtained by changing the printhead angle. 16 nozzle printhead with the capacity of 1.5 mL was used. Spacing between each nozzle is 254 microns; nozzle diameter is around 25  $\mu$ m with average drop sizes of 10 pl. The voltage waveform amplitude used for piezoelement actuation was 27 V, with a firing frequency of 4 kHz. The proposed antenna was printed on 75  $\mu$ m thick Kapton film substrate with

dielectric constant of 3.2 and dissipation factor of 0.0019 [16]. After printing the pattern, silver nanoparticles were sintered on at 200°C for 45 minutes in order to get a uniform conductive structure of the fabricated antenna and the SMA connector was mounted using silver paste. Photographs of the fabricated fractal antennas are shown in Figure 6, while Figure 7 shows comparison of simulated and measured return loss for the planar fractal antenna and its measured gain.

Good agreement is observed, and the fundamental resonance occurs at 1.990 GHz as predicted, with reflection better

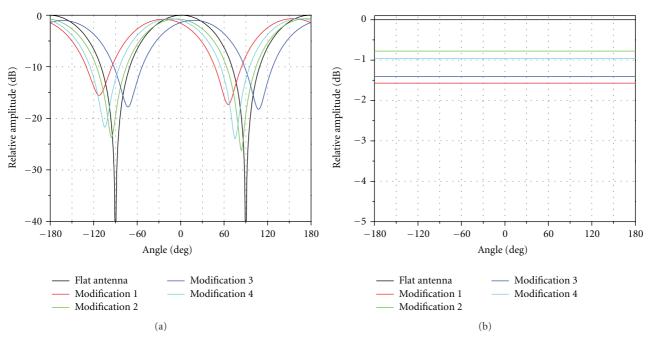


FIGURE 5: Radiations patterns for the conventional patch antenna: (a) radiation pattern in E-plane, (b) radiation pattern in H-plane.

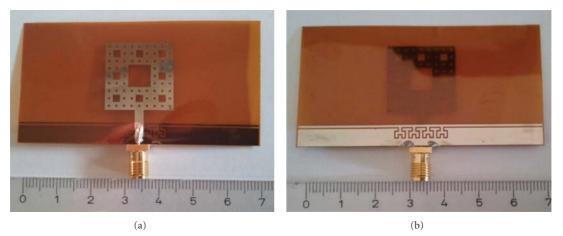


Figure 6: Photographs of the fabricated fractal antenna: (a) top layer, (b) bottom layer.

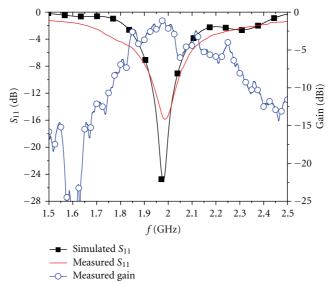


FIGURE 7: Comparison of simulated and measured return losses for the planar fractal antenna and the measured gain.

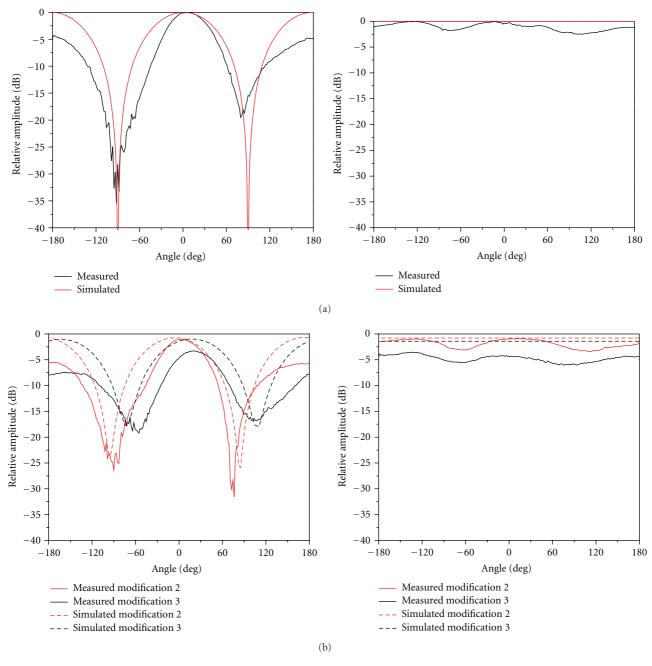


FIGURE 8: Comparison of simulated and measured radiations patterns in E-plane and H-plane for: (a) the planar fractal antenna and (b) modification 2 and modification 3 of the fractal antenna.

than -15 dB. The -10 dB bandwidth is contained between 1.93 GHz and 2.043 GHz, yielding 113 MHz bandwidth, that is, 5.7%.

Figure 8 shows the comparison of simulated and measured radiation patterns for the planar fractal antenna and its two modifications: modification 2 and modification 3. The pattern measurements were taken in an anechoic chamber using a vector network analyzer, and the measured patterns agree well with the simulated ones bar for some ripple that is ascribed to reflections in the chamber.

#### 4. Conclusion

A flexible Sierpinski carpet fractal antenna has been presented, more tolerant to folding than its conventional patch counterpart. The proposed antenna achieves improved performance such as the smaller influence of folding to the resonant frequency and the smaller variation of the gain, while the main lobe directivity changes similarly for both the fractal and the conventional antennas. The average frequency shift induced by folding of the patch antenna is 4.09% while it is only 2.04% for the proposed fractal antenna. The same

holds for the average variation of the fractional bandwidth: 21.7% for the conventional antenna versus only 15.3% for the fractal antenna. Moreover, the proposed fractal antenna occupies 30% smaller surface than the patch, and it is less sensitive to mechanical strain.

#### Acknowledgments

This work has been partially supported by the European Commission through FP7 Project MultiWaveS, Grant no. PIRSES-GA-2009-247532. The authors thank the Department of Broadband Infocommunications and Electromagnetic Theory, Budapest University of Technology and Economics, Budapest, Hungary, for the anechoic chamber measurements.

#### References

- [1] M. F. Pantoja, F. G. Ruiz, A. R. Bretones, and R. G. Martín, "GA design of wire pre-fractal antennas and comparison with other euclidean geometries," *IEEE Antennas and Wireless Propagation Letters*, vol. 2, pp. 238–241, 2003.
- [2] I. K. Kim, J. G. Yook, and H. K. Park, "Fractal-shape small size microstrip patch antenna," *Microwave and Optical Technology Letters*, vol. 34, no. 1, pp. 15–17, 2002.
- [3] C. Puente-Baliarda, J. Romeu, R. Pous, and A. Cardama, "On the behavior of the sierpinski multiband fractal antenna," *IEEE Transactions on Antennas and Propagation*, vol. 46, no. 4, pp. 517–524, 1998.
- [4] J. Anguera, C. Puente, C. Borja, and J. Soler, "Fractal-shaped antennas: a review," in *Wiley Encyclopedia of RF and Microwave Engineering*, K. Chang, Ed., vol. 2, pp. 1620–1635, Wiley, New York, NY, USA, 2005.
- [5] S. Wong and B. L. Ooi, "Analysus and bandwidth enchcement of Sierpinski carpet antenna," *Microwave and Optical Technology Letters*, vol. 31, no. 1, 2001.
- [6] R. Azaro, E. Zeni, T. Gazzini, R. Dallapiccola, and A. Massa, "Synthesis of a three-dimensional triband (*L1-L2* GPS and Wi-Fi) prefractal tree antenna," *Microwave and Optical Technology Letters*, vol. 49, no. 9, pp. 2114–2118, 2007.
- [7] J. P. Gianvittorio and Y. Rahmat-Samii, "Fractal antennas: a novel antenna miniaturization technique, and applications," *IEEE Antennas and Propagation Magazine*, vol. 44, no. 1, pp. 20–36, 2002.
- [8] S. R. Best, "On the resonant properties of the Koch fractal and other wire monopole antennas," *IEEE Antennas and Wireless Propagation Letters*, vol. 1, pp. 74–76, 2002.
- [9] E. C. Lee, P. J. Soh, N. B. M. Hashim et al., "Design and fabrication of a flexible Minkowski fractal antenna for VHF applications," in *Proceedings of the 5th European Conference on Antennas and Propagation (EUCAP '11)*, pp. 521–524, April 2011.
- [10] J. Jung, H. Lee, and Y. Lim, "Broadband flexible meander line antenna with vertical lines," *Microwave and Optical Technology Letters*, vol. 49, no. 8, pp. 1984–1987, 2007.
- [11] S. Subramaniam and B. Gupta, "Design and development of flexible fabric antenna for body-worn applications and its performance study under flat and bent positions," *Microwave and Optical Technology Letters*, vol. 53, no. 9, pp. 2004–2011, 2011.
- [12] T. F. Kennedy, P. W. Fink, A. W. Chu, N. J. Champagne, G. Y. Lin, and M. A. Khayat, "Body-worn E-textile antennas: the

- good, the low-mass, and the conformal," *IEEE Transactions on Antennas and Propagation*, vol. 57, no. 4, pp. 910–918, 2009.
- [13] C. Hertleer, H. Rogier, L. Vallozzi, and L. Van Langenhove, "A textile antenna for off-body communication integrated into protective clothing for firefighters," *IEEE Transactions on Antennas and Propagation*, vol. 57, no. 4, pp. 919–925, 2009.
- [14] http://www.dimatix.com/.
- [15] http://www.sunchemical.com/.
- [16] http://www.gts-flexible.co.uk.

Hindawi Publishing Corporation International Journal of Antennas and Propagation Volume 2012, Article ID 905409, 8 pages doi:10.1155/2012/905409

### Research Article

# Performance of High-Permittivity Ceramic-Polymer Composite as a Substrate for UHF RFID Tag Antennas

#### A. A. Babar, V. A. Bhagavati, L. Ukkonen, A. Z. Elsherbeni, P. Kallio, and L. Sydänheimo

- <sup>1</sup> Rauma Research Unit, Department of Electronics, Tampere University of Technology, 26100 Rauma, Finland
- <sup>2</sup> Micro and Nano Systems Research Group, Department of Automation Science and Engineering, Tampere University of Technology, 33720 Tampere, Finland

Correspondence should be addressed to A. A. Babar, abdul.babar@tut.fi

Received 12 December 2011; Accepted 4 April 2012

Academic Editor: Carles Fernández-Prades

Copyright © 2012 A. A. Babar et al. This is an open access article distributed under the Creative Commons Attribution License, which permits unrestricted use, distribution, and reproduction in any medium, provided the original work is properly cited.

A high-permittivity ceramic-polymer composite substrate is fabricated and proposed for its potential use in UHF RFID tags. The substrate is developed using high-permittivity Barium Titanate (BaTiO<sub>3</sub>) ceramic powder mixed with polydimethylsiloxane (PDMS) polymer. The resulting composite achieves a soft, hydrophobic, heat resistant, low loss, and flexible material with high dielectric constant. The percentage of the ceramic powder in the composite helps in achieving variable permittivity values. When this material is used as a substrate for a tag antenna, it will help the tag to be reduced in size, to conform to uneven or rough surface, and to be less vulnerable to breakage or other environmental damages. A small passive UHF RFID tag antenna is designed, fabricated, and attached to this type of composite substrate, to demonstrate the performance of this composite material.

#### 1. Introduction

There have been a growing demand and progress in the field of wireless communication and identification in recent years. The use of Radio frequency identification (RFID) technology as an effective and reliable way of tracking and sensing various objects is gaining much importance recently. An RFID system is composed of two main components, the reader and the tag. A commonly used passive RFID tag is composed of an IC chip and an antenna, which contains its own unique identification code (ID) [1]. The identification code is sent back to the reader when the tag is interrogated or energized through backscattered modulation of the incident continuous wave [2]. The input impedance of a passive UHF RFID tag antenna and reflectivity rely on the physical properties of the substrate or material it is attached to and on the antenna's geometry. The permittivity of the substrate has a great impact on the size of the tag antenna. Using higherpermittivity substrate can be useful in reducing the size of the tag antenna.

Substrates play a vital role in the development and use of electronic devices. Flexible substrates have gained much importance in recent years. Different techniques and types of materials have been used to develop flexible electronic substrates [3–6]. One of the most commonly used flexible plastic substrates is polyester, PEEK (polyaryletheretherketone) and polyimides [7, 8]. Several techniques are being studied and used to embed and integrate electronic components with these flexible substrate materials [9, 10]. There has been a growing interest in the development of flexible antennas using flexible substrates. This gives the advantage of having conformal antennas being placed and attached to uneven shaped structures and surfaces. It is more desirable to use flexible substrate materials that are less vulnerable to heat, water, and other damaging effects.

The size of the RFID tag antenna is also one of the major concerns for RFID applications. Reducing the size of the tag antenna comes at the cost of its performance, such as gain and efficiency of the antenna. Therefore, achieving a small RFID tag antenna, with improved efficiency is an important and challenging task for antenna designers. Using high-permittivity substrates is considered for reducing the overall size and for having compact antenna structures. Several commercially available substrates, with high permittivity values,

<sup>&</sup>lt;sup>3</sup> Electrical Engineering Department, The University of Mississippi, University, MS 38677, USA

have hard and rigid structures. They are more breakable, less conformal, and not suitable for uneven surfaces.

In this paper, new high-permittivity substrates have been developed and tested for RFID tag antenna designs. The substrates are soft and flexible in nature, resistant to water, heat, breaking, and other damaging effects. The substrates have been fabricated by mixing a ceramic powder known as barium titanate (BaTiO<sub>3</sub>) with polydimethylsiloxane (PDMS) polymer. Barium titanate is a ferroelectric material, with high dielectric constant values. The dielectric properties of the substrates depend on the fabrication process, the ratio and the type of ceramic powder used in the composite. The permittivity value of the substrates can be changed by changing the percentage of ceramic powder in PDMS. This provides the flexibility to achieve desired high permittivity values of the substrates.

To demonstrate the performance of the composite substrate for an RFID tag, a small passive UHF RFID tag antenna is designed and fabricated on a thin sheet of FR4. It is then attached to the ceramic-polymer substrate. This was useful to accurately fabricate the small tag antenna and analyze the performance of the substrate. The antenna is designed using miniaturization techniques to reduce the size of the tag antenna and make it more compact and suitable for various objects. The substrate of the antenna makes it possible to place and attach the tag on irregular surfaces and rough terrains. This type of high permittivity composite substrate allows the possibility of achieving small flexible thin tags for future applications which may include the design of fully flexible on-metal, thin, conformal, and embedded tags using inkjet printing.

The rest of the paper is organized as follows. In Section 2, properties of the ceramic and polymer will be discussed. This will be followed by the fabrication process of the composite substrate in Section 3. Section 4 will focus on the design and development of the tag antenna. Simulations and measurements results are discussed and shown in Section 5, followed by the conclusions in Section 6.

#### 2. Properties of Ceramic and Polymer

In this section, the properties and characteristics of both the ceramic powder and the polymer used in this experiment will be discussed. The ceramic powder used in the composite substrate is a ferroelectric material known as barium titanate (BaTiO<sub>3</sub>). Polydimethylsiloxane (PDMS) polymer is mixed with the ceramic powder and fabricated, to make it a soft and flexible solid composite substrate.

2.1. Characteristics of PDMS. PDMS is most widely used type of a silicon-based organic polymer, belonging to a group of siloxanes. It is available in fluid, elastomer, and resin form [11]. The chemical structure of PDMS is stated in [11].

PDMS materials have high thermal stability, low surface tension, characteristic pressure and bulk viscosity. They are transparent, hydrophobic in nature and durable at high temperatures. Other PDMS properties include lubricity, shear stability, high dielectric strength, antifriction, and good resistance to UV radiations [11, 12].

In the elastomer form, PDMS is suitable for flexible substrates. Elastomeric PDMS structures are typically fabricated using viscous liquid and a liquid cross-linking agent. Among other factors such as curing time and temperature, the bending stiffness depends on the amount of cross-linking agent used. Larger amounts of PDMS result in more rigid structures [12].

The most common applications of PDMS include rubber molds, surfactants, water repellents, adhesives, personal care and cosmetics, dielectric encapsulation, hydraulic fluids, lubricants, fuser oil, and protectants. It can also be used in various other applications such as contact lenses, medical and microfluidic devices, and applications [11–14].

2.2. Characteristics of BaTiO<sub>3</sub>. Barium titanate (BaTiO<sub>3</sub>) is a ferroelectric ceramic powder, with piezoelectric properties [15]. It is insoluble in water and alkalis, whereas soluble in some acids such as sulfuric, hydrofluoric, and hydrochloric acids. It usually has very high permittivity values. It can acquire four different shapes of crystals, cubic, tetragonal, orthorhombic, and rhombohedral. However, the permittivity depends on many factors, such as the grain size, shape and size of the crystals, impurities, and on processing techniques [16]. Ferroelectric ceramics can be used in several applications, such as capacitors, thermostatic devices, light switches, current controllers and to generate ultrasonic energy [15]. Similarly, barium titanate is used to manufacture many electronic components, such as multilayer capacitors [17], positive temperature coefficient (PTC) thermistors, transducers, and tunable phase shifters [18, 19].

Due to recent advances in electronics, much attention has been focused on small and miniaturized electronic devices. Growing interest is targeting the use of high permittivity material in electronics industry to decrease the size of electronic and wireless components and devices.

#### 3. Fabrication Technique Used for Ceramic-Polymer Composite Substrate Material

In this section, design and fabrication technique of the composite substrate is discussed. A stepwise approach is used to explain the fabrication process of PDMS-BaTiO<sub>3</sub> (barium titanate) composite substrate. A similar approach has also been used in [20]. The PDMS used is Sylgard-184, which is supplied as a two component Kit containing a "base prepolymer" (the viscous liquid) and a "curing agent" (the liquid cross-linking agent) manufactured by Dow Corning [21].

Following are the steps to make the ceramic-polymer composite substrate.

(1) First, the base prepolymer is mixed with the curing agent in a mass ratio of 10 (pre-polymer): 1 (curing agent). The mixture is then mixed vigorously for 5–10 minutes in a plastic container, which enables uniform cross-linking.



FIGURE 1: Degassing chambers used to degas the samples.

- (2) After mixing PDMS (the base pre-polymer with the curing agent), it is left for degassing in a degassing chamber for 15–20 minutes. This helps in extracting possible air bubbles formed during the process of mixing. The degassing chambers used for degassing of the samples are shown in Figure 1. In this step, the samples are placed in the bigger degassing chamber, to accommodate the plastic glass used for mixing.
- (3) The degassed mixture of PDMS is mixed with BaTiO<sub>3</sub> ceramic powder. The ceramic powder is provided from Sachtleben Pigments [22]. The percentage of ceramic powder mixed with PDMS is on a volume-based ratio, as defined in (1) [20]:

$$v\% = \frac{C_m/C_\rho}{C_m/C_\rho + P_m/P_\rho} \times 100\%.$$
 (1)

In the previous equation  $C_m$  and  $C_\rho$  refer to the mass and density of the ceramic (BaTiO<sub>3</sub>), respectively, whereas,  $P_m$  and  $P_\rho$  are the mass and density of the polymer (PDMS).

In this experiment, 15% and 25% of BaTiO<sub>3</sub> ceramic powder are mixed with PDMS. The BaTiO<sub>3</sub> ceramic powder provided by Sachtleben Pigments has a grain size equal to 80 nm. The density of BaTiO<sub>3</sub> is equal to 6.02 g/cm<sup>3</sup>, whereas the density of PDMS is equal to 1.05 gm/cm<sup>3</sup>.

- (4) After adding PDMS with the ceramic powder, vigorous stirring is done for about 15–20 min, as shown in Figure 2. The mixture is stirred until it transforms into a smooth paste. A smooth white paste without any lumps is a good indicator of a good mixture.
- (5) The mixture is then poured into a small Petri dish on a flat surface, to have an even distribution of the thick paste inside the container. This mixture can be poured into different types of molds, depending on the desired shape, as shown in Figure 3.
- (6) After pouring the mixture into the Petri dish, it is again left for degassing for a continuous time period of 5-6 hours, to remove excessive air bubbles. The first 5-6 hours are considered crucial, as they help in removing the maximum amount of air bubbles. It has been observed that, even after 5-6 hours of degassing,



FIGURE 2: Vigorous mixing of PDMS ceramic powder with PDMS mixture.



FIGURE 3: Pouring the well-mixed paste into a Petri dish.

few air bubbles are still popping out of the mixture. Therefore, to ensure that the mixture has no air bubbles left, it is kept under vacuum pressure for 30 hours, as shown in Figure 4. Usually a solid structure is achieved within 24 hours of curing. This process can be made faster, by heating the mixture after degassing. However, the heating of the composite can make the substrate structure more rigid, depending on the applied temperature.

(7) After curing, the composite substrate is carefully taken out of the Petri dish.

As shown in Figure 5, the final composite substrate is soft and flexible with a smooth surface. The substrate can be softer and more flexible by changing the thickness of the substrate.

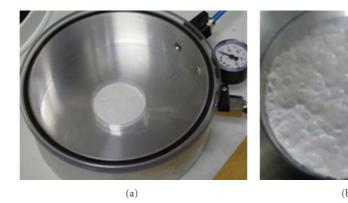


FIGURE 4: (a) Small degassing chamber, to degas the final composite mixture in room temperature. (b) Extraction of air bubbles from the surface of the composite mixture during degassing.

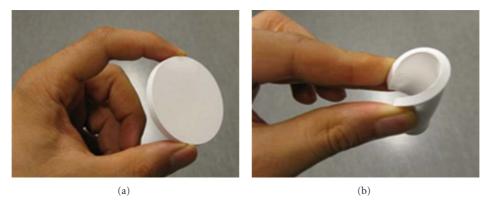


FIGURE 5: Final solid shape of the flexible composite substrate.

#### 4. Antenna Design Technique

In this section, UHF RFID tag antenna design techniques are discussed. The tag antenna is designed using Ansoft HFSS v.12 [23]. A multilayer substrate approach is used to design and fabricate the tag antenna. The tag antenna is first fabricated on a thin sheet of FR4 substrate layer of 0.16 mm thickness, using milling machine. Later the tag is attached to the ceramic-polymer composite substrate, as stated in Section 3.

Alien Higgs 3 IC with -18 dBm sensitivity is used in the tag antenna [24]. The IC provided by the manufacture comes with a strap attachment. In order to take the effect of the strap into account,  $0.2 \, \text{pF}$  of parasitic capacitance is added in parallel to the nominal IC impedance. The tag is matched at  $860 \, \text{MHz}$ .

Figure 6 shows the tag antenna in a form of a round symmetric dipole structure. The IC strap of the tag is attached between the two feeding pads with dimensions represented by *a* and *b*. Line *d* connects the two feeding pads with the two symmetric halves of the dipole structure along the *x*-axis, as shown in Figure 6. The two halves of the dipole structure are shorted or T-matched along the *x*-axis using line "*g*". The edge "*n*" of the two sides of the dipole structure is kept at a distance of 1 mm from each side. Table 1 lists the dimensions of the geometrical parameters of the tag, shown in Figure 6.

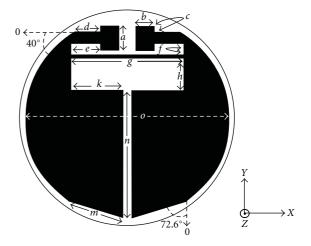


FIGURE 6: Geometrical parameters of the designed tag antenna.

Miniaturization techniques are used to reduce the overall size of the tag. T-matching technique is useful in reducing the overall size of the tag, by increasing the inductance of the antenna. T-matching works as an impedance transformer [25]. The length and width of the shorted line are of considerable importance in tuning the antenna. The tuning

Line	Length (mm)	Width (mm)
а	3.25	_
b	2.5	_
С	0.75	_
d	3.55	2
e	3.75	2
f	1	_
g	14.5	0.5
h	4.15	_
k	6.75	_
m	7.5	_
n	16.6	_
0	26.5	_

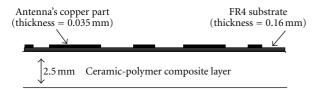


FIGURE 7: Side view of the tag antenna substrate.

and matching of the tag antenna to the desired frequency can also be done by changing the distance "f" of the shorted line "g" from the feeding pads.

A round-shaped tag with a feeding point aligned in the *x*-axis of the tag antenna provides a longer current path. This helps in reducing the overall size of the tag antenna and in achieving a compact shape of the tag. The tag antenna can be tuned further by increasing or decreasing the gap between the two "*n*" edges or by adjusting the separation distance between the two halves of the tag. Figure 7 shows the side view of the tag, demonstrating a multilayer structure of the tag's substrate.

Figure 7 illustrates two main layers of the substrate. First the tag is fabricated on a thin sheet of FR4, with 35  $\mu$ m copper cladding, using milling machine. This is attached to the custom made composite substrate layer of 2.5 mm thickness. The two layers were attached using commercially available adhesive glue. The effect of the glue is considered negligibly small to affect the tag antennas performance. The two layers are attached carefully, to avoid any air gap in between, as it can alter the effective permittivity of the substrate. The relative permittivity value of the ceramic-polymer composite layer in this experiment is approximately equal to 10.5 and 8 for 25% and 15% of BaTiO<sub>3</sub> mixtures, respectively. This is measured by agilent dielectric probe and verified by the experimental results presented in [26, 27].

#### 5. Simulation and Measurement Results

This section focuses on the simulation and measurement results of the tag, on a multilayer substrate. Section 5.1

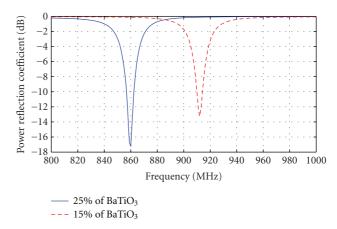


FIGURE 8: Simulated power reflection coefficient of the RFID tag antenna with 25% and 15% of BaTiO<sub>3</sub> concentration in the composite substrate material.

demonstrates the simulated power reflection coefficient and conjugate impedance matching of the designed tag antenna. In Section 5.2, measured results of the tag are discussed.

5.1. Simulation Results of the Tag Antenna. The transfer of power between the complex load (IC) impedance and the complex source (tag antenna) impedance is analyzed using (2). The power reflection coefficient can be analyzed by considering the ratio of the incident power on the tag antenna ( $P_{\text{tag}}$ ) and the power reflected back ( $P_{\text{rfl}}$ ), as defined in [28, 29] such that

$$\frac{P_{\rm rfl}}{P_{\rm tag}} = \left| \frac{Z_{\rm IC} - Z_a^*}{Z_{\rm IC} + Z_a} \right|^2. \tag{2}$$

In the previous equation  $Z_a = R_a + jX_a$  is the impedance of the tag antenna, whereas  $Z_{\rm IC} = R_{\rm IC} + jX_{\rm IC}$  is the impedance of the chip. The superscript (\*) denotes the complex conjugate. Lower value of the power reflection coefficient at the desired operating frequency indicates an optimal power transfer. An optimal power transfer enables the maximum achievable realized gain and read range of the tag.

The simulated power reflection coefficient of the tag is shown in Figure 8. The tag is matched to 860 MHz with a substrate having 25% of BaTiO<sub>3</sub> and to 915 MHz with 15% of BaTiO<sub>3</sub> composite substrate.

Figure 9 shows the input impedance of the tag antenna and the chip, on top of a 25% ceramic composite substrate, illustrating a good conjugate matching of the tag antenna with the chip, at 860 MHz. This is essential to minimize the reflection loss at this junction and improve the power transmission and maximize the read range.

5.2. Measurement Results of the Tag Antenna. The tag antenna is measured using Tagformance RFID measurements device in an anechoic chamber by Voyantic Ltd., [30]. The anechoic chamber is designed to measure the UHF RFID tag antennas. The chamber consists of a rotating table and a linearly polarized reader antenna. The linearly polarized

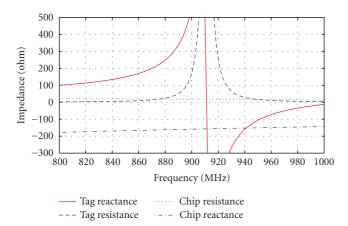


FIGURE 9: Simulated chip and antenna impedance of the UHF RFID tag on top of a 25% ceramic-polymer composite.

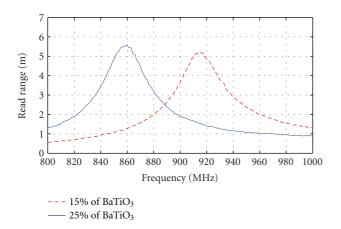


FIGURE 10: Calculated read range  $[d_{\text{tag}}]$  in +z direction of the tag antenna, with 15% and 25% of BaTiO<sub>3</sub> concentration in the composite substrates, based on measured results and (3).

reader antenna is connected to the Tagformance measurement equipment.

Read range of the tag is calculated using the measured results from the Tagformance, using [31].

$$d_{\text{tag}} = \frac{\lambda}{4\pi} \sqrt{\frac{1.64 \, P_{\text{ERP}}}{L_{\text{fwd}} P_{\text{th}}}}.$$
 (3)

In (3), " $d_{\text{tag}}$ " represents the read range of the tag antenna. " $L_{\text{fwd}}$ " is the measured path loss from the generator's output port to the input port of a hypothetic isotropic antenna placed at the tag's location. The forward path loss is achieved from the measured calibration data obtained from Tagformance measurement device. The European effective radiated power " $P_{\text{ERP}}$ " is considered to be equal to 2 W (33 dBm), as stated in [32]. " $P_{\text{th}}$ " represents the measured threshold power in the forward direction, from the transmitter to the tag antenna. The threshold power is the minimum continuous wave power from the transmitter, required to turn on the IC and enable the tag to send a response to EPC Gen 2 protocol's query command. The read range of the tag antenna with 15%

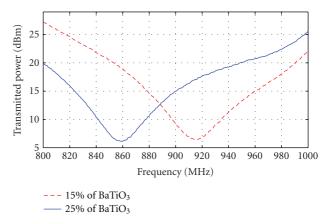


FIGURE 11: Measured threshold transmitted power in +z direction of the tag antenna, with 15% and 25% of BaTiO<sub>3</sub> concentration in the composite substrates.

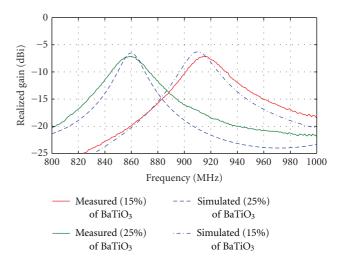


FIGURE 12: Simulated and measured realized gain in "+z" direction of the tag antenna with 15% and 25% of BaTiO<sub>3</sub> concentration in the composite substrates.

and 25% of  $BaTiO_3$  composite substrates, calculated using the measured results from (3), is shown in Figure 10.

According to Figure 10, the maximum read range achieved is between 5 and 6 meters at 860 MHz and 915 MHz. Figure 11 shows the threshold power of the tag required to turn on the IC, with 15% and 25% BaTiO<sub>3</sub> composite substrates.

The measured realized gain of the tag antenna is analyzed using the path loss measurement data from the Tagformance measuring equipment. This can be described as [31]

$$G_r = \frac{P_{\rm IC}}{L_{\rm fwd} \cdot P_{\rm th}}. (4)$$

In the previous equation " $P_{\rm IC}$ " refers to the sensitivity of the IC. " $L_{\rm fwd}$ " is the forward path loss from the transmitter to the tag antenna, and " $P_{\rm th}$ " represents the threshold power, as defined in (3). The maximum simulated and measured realized gain of the tag antenna with 15% and 25% BaTiO<sub>3</sub> composite substrate is shown in Figure 12.

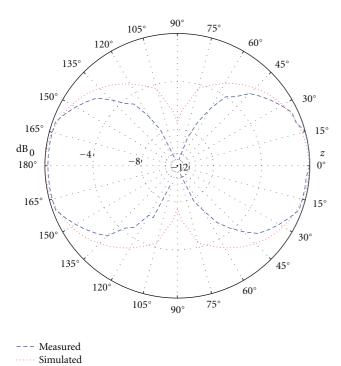


FIGURE 13: Measured and simulated *E*-plane (*yz*-plane) of the tags radiation pattern, using normalized gain (dB) values, at 860 MHz.

In Figure 12, the measured and simulated realized gains at 860 MHz and 915 MHz show a good agreement with each other. The maximum realized gain achieved at 860 MHz and 915 MHz frequency bands, shows a reasonable performance of such a small tag antenna. Figures 13 and 14 show the simulated and measured normalized gain radiation patterns of the tag at 860 MHz.

In Figures 13 and 14, *E* and *H* planes of the normalized gain radiation pattern are shown. The measured and simulated radiation patterns show dipole like omnidirectional radiation pattern.

#### 6. Conclusions

A ceramic-polymer composite substrate is fabricated and studied for use in UHF RFID tag antennas application. To achieve such a high dielectric substrate, ceramic (BaTiO<sub>3</sub>) powder is fabricated with a polymer known as polydimethylsiloxane. The composite achieves a high permittivity and low loss substrate material. The low-loss nature of the substrate enhances the realized gain and read range of the tag antenna. Various permittivity values can be achieved by changing the percentage of the ceramic in the substrate. To demonstrate this phenomenon, two substrates with 15% and 25% of BaTiO<sub>3</sub> ceramic were fabricated with the polymer. The composite substrate materials are flexible, low loss, hydrophobic in nature, and heat resistant. This gives the advantage to the tag to conform to several uneven surfaces, without bearing the risk of breaking and possible environmental damages. To demonstrate the performance of the two substrates, a small UHF RFID tag antenna is designed and fabricated

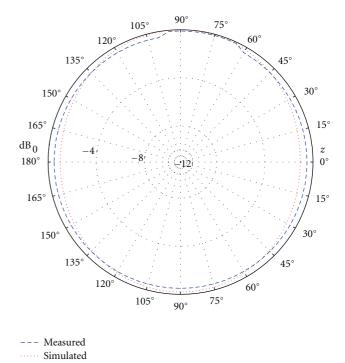


FIGURE 14: Measured and simulated *H*-plane (*xz*-plane) of the tags radiation pattern, using normalized gain (dB) values, at 860 MHz.

on top of a thin FR4 sheet and then glued to the custom made substrate. The measured and simulated results show that the tag antenna has a good performance with respect to its size. This type of small tag antennas can be useful in several applications, due to its small size with respect to its read range and omnidirectional radiation pattern properties. Possible future work may include fabricating thin high permittivity flexible substrates for embedded and on metal tags. To make the thin low-loss substrates fully flexible in nature, the tag antennas can also be printed directly on top of the composite substrate using inkjet printer.

#### Acknowledgments

The authors would like to thank Jani Kallioinen and Sachtleben Ltd. for providing BaTiO<sub>3</sub> powder samples. The authors would also like to thank Samu Hemmila from Tampere University of Technology for suggestions using PDMS.

#### References

- [1] D. M. Dobkin, *The RF in RFID: passive UHF RFID in Practice*, Elsevier, Amsterdam, The Netherlands, 2007.
- [2] G. Marrocco and F. Amato, "Self-sensing passive RFID: from theory to tag design and experimentation," in *Proceedings of* the 39th European Microwave Conference: Science, Progress and Quality at Radiofrequencies (EuMC '09), pp. 1–4, Rome, Italy, October 2009.
- [3] A. Sazonov, D. Striakhilev, C. H. O. Lee, and A. Nathan, "Low-temperature materials and thin film transistors for flexible

- electronics," *Proceedings of the IEEE*, vol. 93, no. 8, pp. 1420–1428, 2005.
- [4] T. H. Sterns, Flexible Printed Circuitry, McGraw-Hill, New York, NY, USA, 1996.
- [5] G. P. Crawford, Flexible Flat Panel Displays, John Wiley & Sons, Chichester, UK, 2005.
- [6] K. J. Allen, "Reel to real: prospects for flexible displays," *Proceedings of the IEEE*, vol. 93, no. 8, pp. 1394–1399, 2005.
- [7] S. R. Forrest, "The path to ubiquitous and low-cost organic electronic appliances on plastic," *Nature*, vol. 428, no. 6986, pp. 911–918, 2004.
- [8] K. Jain, M. Klosner, M. Zemel, and S. Raghunandan, "Flexible electronics and displays: high-resolution, roll-to-roll, projection lithography and photoablation processing technologies for high-throughput production," *Proceedings of the IEEE*, vol. 93, no. 8, pp. 1500–1510, 2005.
- [9] K. W. Paik, S. Cho, and J. G. Hyun, "Novel epoxy/BaTiO<sub>3</sub> composite embedded capacitor films embedded in organic substrates," in *Proceedings of the International IEEE Conference on Asian Green Electronics (AGEC '04)*, pp. 68–73, January 2004.
- [10] C. H. Wang and G. B. Lee, "Automatic bio-sampling chips integrated with micro-pumps and micro-valves for disease detection," *Biosensors and Bioelectronics*, vol. 21, no. 3, pp. 419– 425, 2005.
- [11] J. E. Mark, Polymer Data Handbook, Oxford University Press, New York, NY, USA, 1999.
- [12] J. Kuncová-Kallio and P. J. Kallio, "PDMS and its suitability for analytical microfluidic devices," in *Proceedings of the 28th Annual International Conference of the IEEE Engineering in Medicine and Biology Society (EMBS '06)*, pp. 2486–2489, September 2006.
- [13] H. S. El-Zaim and J. P. Heggers, "Silicones for pharmaceutical and biomedical applications," in *Polymeric Biomaterials*, *Revised and Expanded*, pp. 79–88, Marcel Dekker, New York, NY, USA, 2001.
- [14] A. Mata, A. J. Fleischman, and S. Roy, "Characterization of polydimethylsiloxane (PDMS) properties for biomedical micro/nanosystems.," *Biomedical Microdevices*, vol. 7, no. 4, pp. 281–293, 2005.
- [15] A. J. Moulson and J. M. Herbert, *Electroceramics: Materials, Properties, Applications*, John Wiley & Sons, 2003.
- [16] L. Guo, H. Luo, J. Gao, L. Guo, and J. Yang, "Microwave hydrothermal synthesis of barium titanate powders," *Materials Letters*, vol. 60, no. 24, pp. 3011–3014, 2006.
- [17] H. Saito, H. Chazono, H. Kishi, and N. Yamaoka, "X7R multilayer ceramic capacitors with nickel electrodes," *Japanese Journal of Applied Physics*, vol. 30, no. 9, pp. 2307–2310, 1991.
- [18] S. Chatterjee and H. S. Maiti, "Novel method of doping PTC thermistor sensor elements during sintering through diffusion by vapour phase," *Materials Chemistry and Physics*, vol. 67, no. 1–3, pp. 294–297, 2001.
- [19] B. Huybrechts, K. Ishizaki, and M. Takata, "The positive temperature coefficient of resistivity in barium titanate," *Journal of Materials Science*, vol. 30, no. 10, pp. 2463–2474, 1995.
- [20] S. Koulouridis, G. Kiziltas, Y. Zhou, D. J. Hansford, and J. L. Volakis, "Polymer-ceramic composites for microwave applications: fabrication and performance assessment," *IEEE Transactions on Microwave Theory and Techniques*, vol. 54, no. 12, pp. 4202–4208, 2006.
- [21] Dow Corning Corporation, "Sylgard 184, material properties," http://www.dowcorning.com/.
- [22] Sachtleben Pigments, Pori, Finland, http://www.sachtleben.com/.
- [23] Ansoft HFSS, http://www.ansoft.com/products/hf/hfss/.

- [24] Alien Technology. Higgs 2 product overview, http://www.alientechnology.com/docs/products/DS\_H2.pdf.
- [25] G. Marrocco, "The art of UHF RFID antenna design: impedance-matching and size-reduction techniques," *IEEE Antennas and Propagation Magazine*, vol. 50, no. 1, pp. 66–79, 2008.
- [26] Agilent Technologies, "85070E Dielectric Probe Kit," http:// www.agilent.com/.
- [27] S. Sankaralingam and B. Gupta, "Determination of dielectric constant of fabric materials and their use as substrates for design and development of antennas for wearable applications," *IEEE Transactions on Instrumentation and Measure*ment, vol. 59, no. 12, pp. 3122–3130, 2010.
- [28] K. Kurokawa, "Power waves and the scattering matrix," *IEEE Transactions on Microwave Theory and Techniques*, vol. 13, no. 2, pp. 194–202, 1965.
- [29] P. V. Nikitin, K. V. S. Rao, S. F. Lam, V. Pillai, R. Martinez, and H. Heinrich, "Power reflection coefficient analysis for complex impedances in RFID tag design," *IEEE Transactions on Micro*wave Theory and Techniques, vol. 53, no. 9, pp. 2721–2725, 2005.
- [30] Voyantic, "RFID measurements solutions," http://www.voyantic.com/.
- [31] J. Virtanen, T. Björninen, L. Ukkonen, and L. Sydänheimo, "Passive UHF inkjet-printed narrow-line RFID tags," *IEEE Antennas and Wireless Propagation Letters*, vol. 9, pp. 440–443, 2010.
- [32] EPC frequency regulations UHF.

Hindawi Publishing Corporation International Journal of Antennas and Propagation Volume 2012, Article ID 972696, 11 pages doi:10.1155/2012/972696

### Research Article

# **Efficiency of a Compact Elliptical Planar Ultra-Wideband Antenna Based on Conductive Polymers**

## Thomas Kaufmann,<sup>1</sup> Akhilesh Verma,<sup>1</sup> Van-Tan Truong,<sup>2</sup> Bo Weng,<sup>3</sup> Roderick Shepherd,<sup>4</sup> and Christophe Fumeaux<sup>1</sup>

- <sup>1</sup> The University of Adelaide, Adelaide, SA 5005, Australia
- <sup>2</sup> Defence Science and Technology Organisation (DSTO) Melbourne, Fischermans Bend, VIC 3207, Australia
- <sup>3</sup> University of Wollongong, Wollongong, NSW 2522, Australia

Correspondence should be addressed to Thomas Kaufmann, thomaska@eleceng.adelaide.edu.au

Received 14 December 2011; Revised 5 April 2012; Accepted 5 April 2012

Academic Editor: Carles Fernández-Prades

Copyright © 2012 Thomas Kaufmann et al. This is an open access article distributed under the Creative Commons Attribution License, which permits unrestricted use, distribution, and reproduction in any medium, provided the original work is properly cited.

A planar antenna for ultra-wideband (UWB) applications covering the 3.1–10.6 GHz range has been designed as a test bed for efficiency measurements of antennas manufactured using polymer conductors. Two types of conductive polymers, PEDOT and PPy (polypyrrole), with very different thicknesses and conductivities have been selected as conductors for the radiating elements. A comparison between measured radiation patterns of the conductive polymers and a copper reference antenna allows to estimate the conductor losses of the two types of conductive polymers. For a 158  $\mu$ m thick PPy polymer, an efficiency of almost 80% can be observed over the whole UWB spectrum. For a 7  $\mu$ m thick PEDOT layer, an average efficiency of 26.6% demonstrates, considering the room for improvement, the potential of this type of versatile materials as flexible printable alternative to conductive metallic paints. The paper demonstrates that, even though the PEDOT conductivity is an order of magnitude larger than that of PPy, the thicker PPy layer leads to much higher efficiency over the whole UWB frequency range. This result highlights that high efficiency can be achieved not only through high conductivity, but also through a sufficiently thick layer of conductive polymers.

#### 1. Introduction

Recent advances in material research have enabled the synthesis of a wide range of conductive polymers with characteristics that make them interesting for electromagnetic applications. Increasingly high electrical conductivity and mechanical elasticity, combined with the potential of low-cost mass production, make these types of materials highly interesting for the manufacture of antennas as integrated components for emerging all-polymer electronic devices. Additionally, some electroactive conductive polymers have the ability to change their properties through the application of a bias voltage, suggesting applicability for future designs of reconfigurable antennas. In this perspective, conductive polymers appear as an increasingly relevant type of materials with the potential to allow the creation of mechanically

flexible, electrically reconfigurable antennas at a low cost. Conductive polymer films can be manufactured and patterned with conventional inkjet printing or screening technology. It is expected that through the progress in composite polymers, a further increase in the present conductivities at room temperature will be achieved.

Previous work on conductive polymers includes numerous implementations from UHF to mm-waves. Often these antennas have been designed as proof of concept, whereas quantitative studies on the efficiency are less common. The following selection of publications on antennas constructed with less conductive materials illustrates the status of research, with some of the contributions providing efficiency estimations. Regarding the electromagnetic properties of conductive polymer for use in antenna design, previously published work at microwave frequencies has considered

<sup>&</sup>lt;sup>4</sup> The University of Sydney, Sydney, NSW 2006, Australia

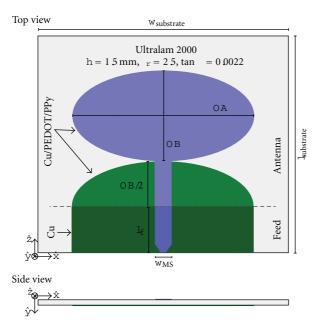


FIGURE 1: Schematic of the antenna. In all manufactured antennas, the feeding section was produced in copper, and the radiating elements have been manufactured alternatively in copper, PEDOT, or PPy.

narrowband microstrip patch antennas in [1-3]. In particular, the latter two references estimated the efficiency degradation due to the use of a top patch manufactured from different conductive polymers. Using a very promising type of conductive polymers, a carbon-nanotube- (CNT-) based textile microstrip patch antenna has been presented in [4], where the efficiency has been estimated at  $-2 \, dB$ compared to an ideal patch antenna. The application of a CNT ground plane for microstrip antennas, rather than for the resonant element, has been investigated in [5]. Another implementation of conducting textiles as a building block of antennas has been presented in [6] at the high VHF/low UHF range with conductive polymer-coated fibres. In a real-word application, the performance of a MIMO ad hoc network with transparent conductive polymer antennas [7] has been estimated at 2.5 GHz with promising results. At a lower frequency range, conductive polymer-based RFID antennas have been introduced in [8, 9] with evaluation of radiation performance. For these lower frequencies, the conductivity and thickness of the materials is often still quite low, leading to rather small efficiencies. In the realm of flexible, printed antennas, an inkjet-printed ultra-wideband (UWB) antenna based on conductive (metallic) ink with a paper substrate has been introduced in [10]. Also, a new printing process for metallic conductors has been introduced in [11] for 2.4 GHz applications, implemented on printed microstrip patch antenna with a plastic substrate. In the millimeter range, an extensive range of studies on the efficiency of CNT monopole antennas have been performed [12].

The characterization of conductive polymer antennas for high-frequency applications is in its infancy, and this paper explores the impact of losses in a practical antenna setup,

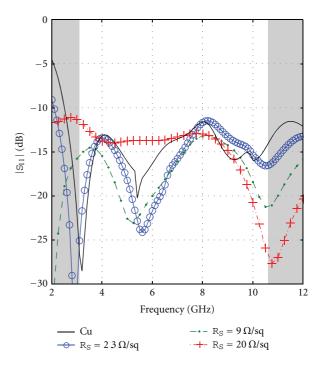


FIGURE 2: Simulated input reflections for different values of the sheet resistance of the conductive polymer antenna section. For PPy, the estimated sheet resistance is  $R_S = 2.3 \Omega/\text{sq}$ , and, for PEDOT, it is calculated as  $R_S = 9 \Omega/\text{sq}$ .

due to the use of nonideal conductors with thickness below requirement. Especially the relevant comparison between a conductor with low conductivity/large thickness (PPy) and high conductivity/small thickness (PEDOT) will shed some light of the efficiency of these conductors in relation to the skin depth in the UWB spectrum.

Two types of these conductors, PEDOT and polypyrrole (PPy), have been selected for the manufacture of the antennas presented in this paper. The PEDOT exhibits the highest conductivity and has the ability to directly be inkjet-printed on a carrier substrate, however with a feasible thickness presently limited to a few micrometers. PPy on the other side has lower electrical conductivity but can be produced in significantly thicker films. In the present form, PPy requires manual manufacture for small-scale prototype production.

The goal of this paper is to estimate the efficiency of antennas based on conductive polymers over a large frequency range. Therefore, a planar UWB antenna has been designed for operation from 3.1 to 10.6 GHz. This design acts as a test bed for the two different conductive polymers. By comparison with the same design built in copper for reference, the efficiency of the polymer conductors at various frequencies can be experimentally evaluated. The results show different performance for the two conductive polymer approaches explored here. With the knowledge of the present limitations in terms of conductivity and layer thickness, more elaborate antennas based on conductive polymers can be designed in the future.

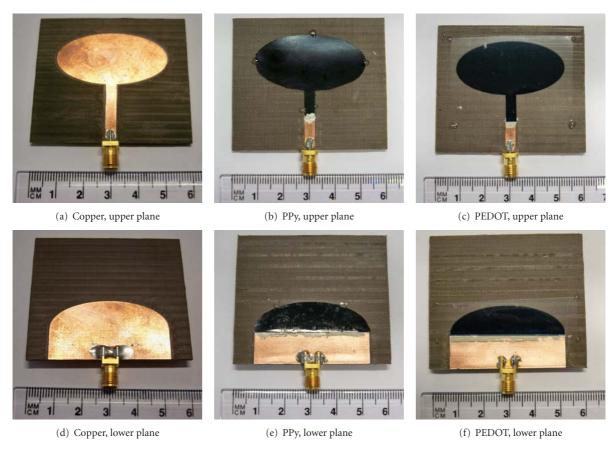


FIGURE 3: Upper and lower planes of the three antennas.

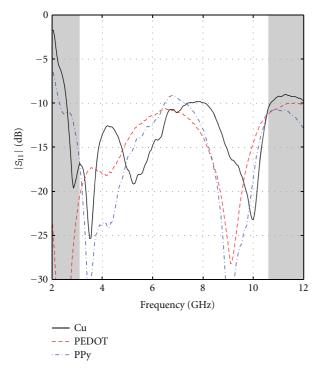


FIGURE 4: Input reflections for the antennas. The nonshaded area designates the operation UWB spectrum from 3.1 to 10.6 GHz.

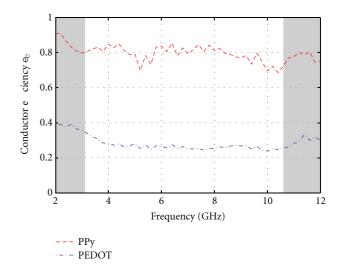


FIGURE 5: Efficiency for averaged gains in the *xz*-plane for the PPy and PEDOT antennas. The nonshaded area designates the UWB spectrum.

#### 2. Conductive Polymers

Polymers are large organic molecules that are omnipresent in nature, for example, in DNA and proteins. They are also

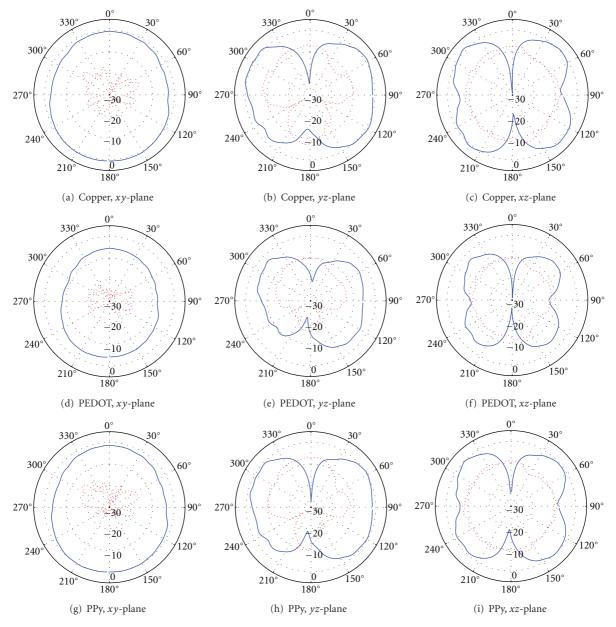


FIGURE 6: Radiation patterns for the antennas with the three different conductors at a frequency of 3.1 GHz. The solid line represents the copolarization and the dotted line the cross-polarization.

very important synthetic materials, including the class of plastic materials. Polymers are composed of large chains of carbon-based molecules linked by covalent bonds. Since the original demonstration of electrical conductivity in synthesized polymer materials [13], research efforts have resulted in a steady increase of the dc-conductivity of conductive polymers through improvement in their intrinsic properties or through the use of composite and doped polymers [14]. Long-term predictions arguably state that doped polymers or composites could approach metals in terms of dc-conductivity at room temperature. But beyond the promise in terms of electrical conductivity, conductive polymers such as PEDOT or PPy are very attractive materials

because of the possibility to pattern them as thin films through low-cost printing (screen or inkjet) and because of their flexibility.

The rapid developments in conductive polymer science provide a strong motivation for using these materials as alternatives to classical metallic conductors in the design and fabrication of electromagnetic devices as components in flexible electronics. Despite the fact that the conductivity of these polymers remains below that of metals, it has been proven to be high enough to build antennas [11, 15]. Clearly, antenna technology can strongly benefit from the exploitation of low-cost, flexible, light-weight plastic-like electrical conductors with suitable processing and patterning

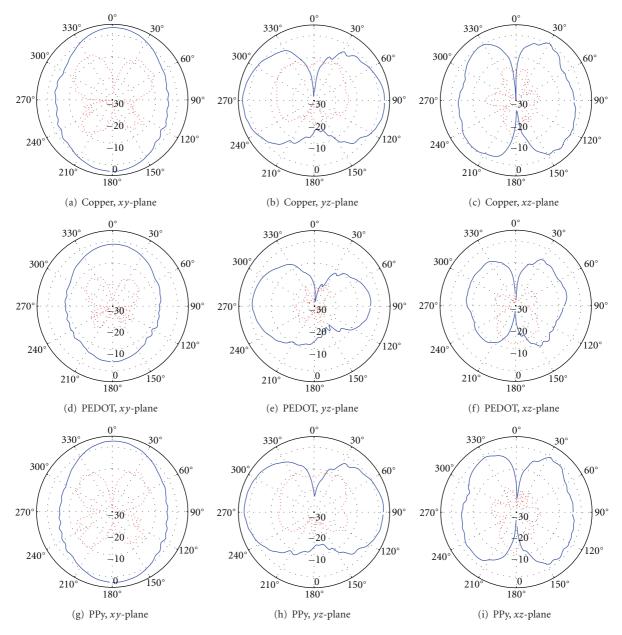


FIGURE 7: Radiation patterns for the antennas with the three different conductors at a frequency of 5 GHz. The solid line represents the copolarization and the dotted line the cross-polarization.

technology. But beyond these particular properties, there are also the promises of three other unique characteristics that are potentially realizable with conductive polymer materials. The first one is the optical transparency, which could allow the integration of antennas onto windshields, solar panels or displays. The second one is the biocompatibility and biodegradability, which, when combined to the flexibility, opens the door to wearable and biodegradable implantable devices [16]. The third one is the possibility of dynamically controlling the electrical properties of polymers in electroactive cells, which suggests the possibility of low-cost flexible reconfigurability in antenna applications. Such devices would be able to adapt to multiple functional requirements,

that is, work at multiple frequencies and/or dynamically adapt to their environment through polarization or space diversity.

The two different polymer materials employed in the present investigation are described in the following. They are representative of very different approaches, with different strengths and challenges.

2.1. PEDOT. PEDOT:PSS is a stable conductive polymer available as an aqueous dispersion for a variety of coating and printing methods including inkjet, flexographic, gravure, slot die, and screen. DC conductivities as high as 100,000 S/m

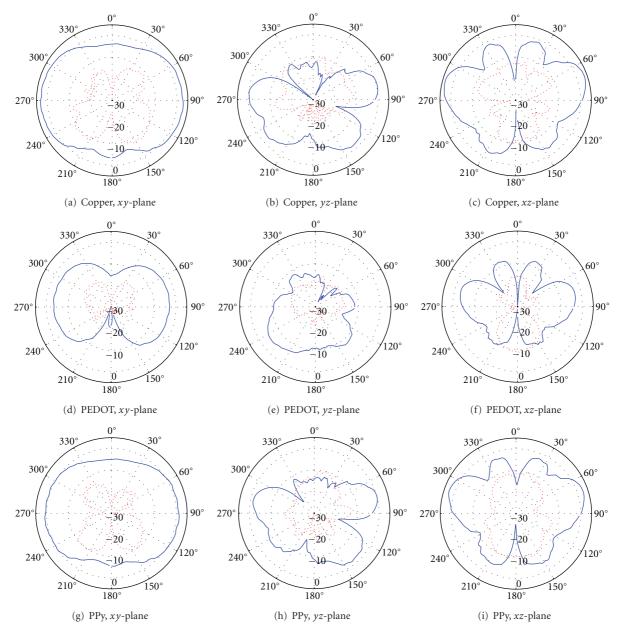


FIGURE 8: Radiation patterns for the antennas with the three different conductors at a frequency of 7 GHz. The solid line represents the copolarization and the dotted line the cross-polarization.

are achievable from commercial formulations, and, after low-temperature annealing, very stable films are produced. Film thicknesses are very much dependent on the processing method and typically range from 50 nm to  $100 \, \mu \text{m}$ . In this work, we employ inkjet printing as this method provides greatest design flexibility when optimizing device geometry and allows for printing complex patterns.

A Dimatix DMP2800 inkjet printer was used to process a commercial PEDOT ink Clevios P Jet HCv2 [17] and pattern a film of  $7\,\mu m$  thickness on a  $100\,\mu m$  polyethylene terephthalate (PET) substrate. The printed PEDOT film has a dc-conductivity of 16, 000 S/m. The inkjet system employed

is capable of printing very thin films (50 nm) of PEDOT. However, for antenna applications, film thicknesses of the order of micrometers are required, and therefore multiple layers were printed consecutively on top of each other. After heat annealing, the thickness of the final multilayer printed film was measured using a Dektak contact profiler. The inkjet system employed uses printheads with only 16 jets (0.6–0.8 mm print swathe width), and, as a result, the fabrication process is currently quite time consuming. Using wider format printheads with increased print swathe width would significantly reduce fabrication time even with multilayer patterning. Also, as PEDOT:PSS is available for a wide

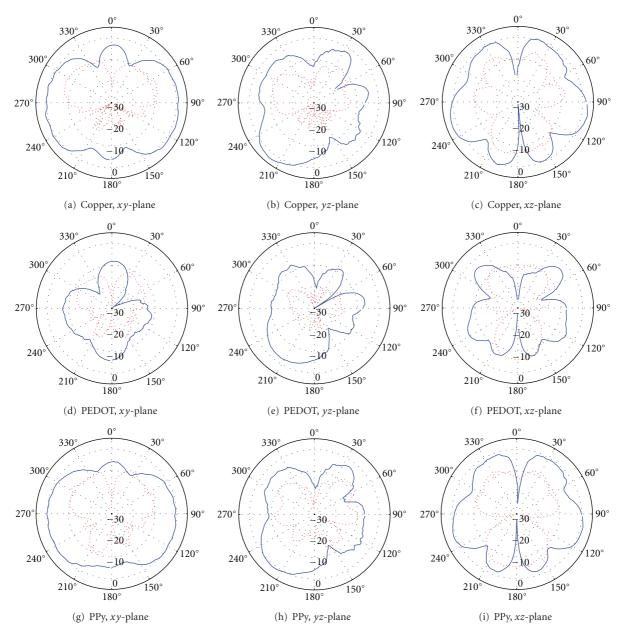


FIGURE 9: Radiation patterns for the antennas with the three different conductors at a frequency of 9 GHz. The solid line represents the copolarization and the dotted line the cross-polarization.

range of processing methods, once final antenna designs are chosen, other approaches can be employed to scale the fabrication process for industrial applications.

2.2. Polypyrrole (PPy) Conducting Polymers. PPy is one of the most popular conducting polymers used in applications owing to its thermal/environmental stability. Depending on the method of polymerization, PPy can be synthesized as free-standing films or powder. In the current form, free-standing film samples are used and must be patterned manually. In this case, the simple shapes have been carved out using a scalpel.

The PPy samples are obtained from the Defence Science and Technology Organization (DSTO) in Melbourne, Australia. The polymer was prepared in accordance with the procedure indicated by Truong and Ternan [18]; that is, through electrochemical polymerization in an aqueous solution. Sodium p-toluene sulphonate (p-TS) was used as the dopant. Electrodes of stainless steel were used for growing the film in a nitrogen environment. The films obtained by the above procedure are between 57 and 158  $\mu$ m thick and have been washed in acetonitrile/water (1:1 solution) to remove excess dopant. The films were then allowed to dry. In the present investigation, a free-standing sample with a

Table 1: DC conductivity and skin depths of the applied conducting materials at the lower and upper margins of the UWB spectrum.

	Copper	PEDOT	PPy
σ	$5.8 \cdot 10^7  \text{S/m}$	16,000 S/m	2,720 S/m
$\delta$ (3.1GHz)	$1.2\mu\mathrm{m}$	$71.5  \mu \mathrm{m}$	$173.3  \mu { m m}$
$\delta$ (10.6 GHz)	$0.6\mu\mathrm{m}$	38.6 µm	93.7 μm

thickness of  $158\,\mu\mathrm{m}$  is used. Using the four-probe technique, the dc-conductivity of the film sample could be measured as 2,720 S/m, that is, roughly one order of magnitude below the conductivity of the PEDOT sample. The thickness of the PPy film was accurately measured using a Scanning Electron Microscope (SEM) Philips XL 30.

## 3. UWB Antenna

The antenna design presented in this paper is an adaptation of a circular UWB dipole antenna [19]. The most important criteria for this layout is established by the availability of conductive polymer samples: due to the limited areas of free-standing PPy samples and the long printing times for patterned PEDOT films, the conductive area of the designed antenna has been minimized. Additionally, simple shapes were favoured to facilitate the manual cutting of PPy films. As low-loss substrate, Rogers Ultralam 2000 with a thickness of 1.5 mm (60 mil) has been selected as it exhibits accurately specified permittivity ( $\varepsilon_r = 2.5 \pm 0.1$ ) and allows for milling of the copper reference antenna as well as the contacting structure of the polymer antennas. A short feeding microstrip line section built in copper has been included in the present design to allow soldering of an SMA connector. The antenna starts after this launching section and is then manufactured using the two mentioned conductive polymers.

All numerical simulations for optimization of the present design have been performed using the finite-element frequency-domain solver of HFSS. The copper layers can be simulated using the traditional model with finite conductivities. The polymer conductors however are in the range of or much thinner than a skin depth (as shown in Table 1) in the chosen frequency range; therefore, the finite conductivity model is not applicable. Instead, the conductive polymers have been modeled as a thin layer of finite impedance with the sheet resistance  $R_S$  estimated through the dc-conductivity  $\sigma$  as [20]

$$R_S = \frac{1}{\sigma d},\tag{1}$$

where d designates the thickness of the conductor film. For the printed PEDOT conductor, a thickness of  $d=7 \,\mu \text{m}$  and conductivity of  $\sigma=16 \,\text{kS/m}$  lead to a sheet resistance of  $R_S=9 \,\Omega/\text{sq}$ . For the PPy sample, the sheet resistance could be estimated as  $R_S=2.3 \,\Omega/\text{sq}$  ( $d=158 \,\mu \text{m}$ ,  $\sigma=2,720 \,\text{S/m}$ ).

3.1. Design. After consideration of several design options, a microstrip line fed structure on two planes has been selected as shown in Figure 1 with a shape adapted from [21, 22]. This

arrangement minimizes the impact of production tolerances, in comparison to a coplanar waveguide feed.

On the upper plane, the microstrip line is connected to an elliptically shaped conductor. On the lower plane, the ground plane evolves into a half-ellipse (Figure 1). The width of the ground plane has also been minimized to reduce the amount of conducting material required. The opening slot between the ellipsoidal shapes on the two planes acts as a broadband radiating structure with a predominantly vertical linear polarization. The microstrip line is fed through a coaxial SMA connector, which is soldered onto a copper feeding structure.

The dimensions of the antenna have been optimized to give acceptable input reflections ( $|S_{11}| < -10 \,\mathrm{dB}$ ) for all different conductivities of the radiating elements while retaining a minimal size. For the antenna as shown in Figure 1, the ellipse with an axial ratio of AR = 0.5 has a major axis of OA = 44 mm and a minor axis of OB = 22 mm. The feeding structure has a length of  $l_f = 11 \,\mathrm{mm}$  to allow the feeding microstrip mode to establish after the transition from the coaxial SMA connector. For a 50  $\Omega$  impedance, the width of the microstrip line has been kept constant as  $w_{\rm MS} =$ 4 mm to facilitate the manufacturing process. A short taper (2 mm) at the transition between the coaxial connector and the microstrip line avoids coupling effects from the metallic connector case. The size of the substrate has been chosen sufficiently large to accommodate the antenna with a width of  $w_{\text{substrate}} = 60 \text{ mm}$  and a length of  $l_{\text{substrate}} = 52 \text{ mm}$ .

The simulated input reflections for a variation of sheet resistances  $R_S = [2.3, 9, 20] \Omega/\text{sq}$  and the metallic copper conductor are shown in Figure 2. The following observations can be made for increasing conductor losses. At first, the input reflections decrease with increasing sheet resistance. This happens up to a point where the mismatch between the copper and polymer microstrip line becomes too large (i.e., towards  $R_S = 20 \Omega/\text{sq}$ ), which manifests in generally larger reflections. Additionally, a shift of the first resonance to lower frequencies can be observed.

3.2. Manufacture. Three separate antennas have been manufactured. First, an all-copper antenna has been built for verification of the design and to provide a reference for efficiency estimations. Using classical milling technology, the shapes were cut from an all-copper layer on the Ultralam substrate.

For the second antenna, the antenna part in Figure 1 has been realized with a printed PEDOT layer. The initial transition from the coaxial SMA connector to the feed section remains in copper. Conductive epoxy has been used to establish a permanent galvanic connection between the feeding line/ground plane and the radiating elements. The thin PET substrate is facing away from the substrate so that the conductor can be directly connected to the feeding line. Due to the low dielectric constant ( $\varepsilon_r < 3$ ), low losses, and thin dimension, the effect of the PET layer can be neglected.

For the third antenna, the radiating part of the antenna has been manufactured in PPy. Using a prefabricated template, the shapes have been cut with a scalpel from the flexible free-standing PPy sample. The conductive polymer has then been fixed onto the substrate with a few dots of regular epoxy, and an electrical connection to the copper microstrip feeding line has been established through a small area of conductive epoxy at the feed/antenna transition. Due to the manual production process, deviation from the original design must be expected. Also, slight discrepancies in the alignment could not be avoided. Figure 3 shows the manufactured antennas.

#### 4. Measurements

To characterize the antennas, the input reflections ( $S_{11}$  parameter) and radiation patterns of all three antennas have been measured. The absolute gain patterns provides the basis for the estimation of the polymer antennas' efficiency by comparing their radiation performance with that of the reference copper device.

4.1. Input Reflections. The maximum acceptable input reflections correspond to  $|S_{11}| = -10$  dB. As shown in Figure 4, this has been nearly fulfilled for all antennas. The copper antenna shows a good correspondence with the simulated results. For the polymer antennas, the results somewhat deviate from the simulated values. This is attributed to tolerances in the manufacture, misalignment of the conductors and a nonideal transition using conductive glue from the microstrip feeding line to the polymer layers. Nevertheless, a shift of the resonances towards lower frequencies can be observed demonstrating consistency with the simulated results.

4.2. Patterns. The radiation patterns are shown in Figures 6, 7, 8, and 9 at the end of this paper for the frequencies f = [3.1, 5, 7, 9] GHz in form of the total realized gain.

A dipole-like behavior is expected, which should translate as an omnidirectional pattern in the xy-plane (subfigures (a), (d), and (g)). This is indeed observed at lower frequencies, while the omnidirectional characteristics slightly deteriorates towards the upper end of the UWB spectrum. As anticipated, the patterns in the xz- and yz-plane exhibit a zero along the dipole axis, that is, towards  $0^{\circ}$  and  $180^{\circ}$ . Again, the patterns deteriorate towards higher frequencies, where deviations in manufacturing quality have a larger impact.

It can generally be observed that all patterns exhibit similar characteristics. The *xz*-plane patterns offer the best similarity between the different conductors, and the patterns in the *yz*-plane show largest discrepancies between all antennas at all frequencies.

4.3. Efficiency. The efficiency  $e_{cd}$  of an antenna is included in the definition of the gain G in terms of its directivity D as

$$G = e_{cd}D, \qquad e_{cd} = e_c e_d, \tag{2}$$

where the efficiency  $e_c$  is related to conductor losses and  $e_d$  to dielectric losses. In this paper, the goal is to estimate the losses that occur because of the relatively low conductivity of the conductive polymer, that is, to characterize the efficiency

 $e_c$  at microwave frequencies. A straightforward method is to directly compare the radiation performance of the copper and polymer antennas. The dielectric substrate materials are identical and therefore show identical dielectric losses and associated dielectric efficiencies  $e_d$ . The losses of the copper can be assumed negligible, that is,  $e_c \approx 1$ . Therefore, the difference of the gains between the copper and the two polymer antennas is an indicator of the losses in the respective conductive polymer.

The efficiency is estimated here based on the performance in the *xz*-plane pattern where the patterns have the same shape, that is, the same directivity. The averaged total received power over all azimuthal angles is used as a measure of the average gain, and the efficiency can then be approximated as

$$e_c \approx \frac{\sum_{\phi} G_{\text{Polymer}}(\theta = 90^{\circ}, \phi) \Delta \phi}{\sum_{\phi} G_{\text{Cu}}(\theta = 90^{\circ}, \phi) \Delta \phi}.$$
 (3)

This simplified approach avoids performing measurements with a Wheeler Cap notoriously difficult through the UWB range or carrying out involved measurements of the whole three-dimensional pattern for a gain/directivity comparison [23, 24].

Figure 5 shows the resulting conductor efficiencies as a function of the frequency for the antennas based on PEDOT and PPy. The average efficiency over the whole UWB frequency band is  $e_c = 26.6\%$  for the PEDOT and  $e_c = 79.2\%$  for the PPy antenna. This is in good agreement with the results based on a microstrip patch antenna for the same two materials at 6 GHz in [3].

The same observation can be done with the patterns in the xy- and yz-plane, but, due to a divergence of the patterns towards higher frequencies (especially for the yz-plane), the curves are more noisy and the results are less reliable above 7 GHz. Nevertheless, these results are highly encouraging in a demonstration of the general feasibility of using these types of materials as conductor in microwave antenna structures.

#### 5. Conclusion

Conductive polymers are promising materials for the manufacture of low-cost and mechanically flexible antennas with potentially complex geometries. In this paper a planar antenna design realized with conducting polymer for ultrawideband applications has been presented. The design has been simplified to minimize the area of polymer samples required and allow for manual manufacture. A tapered elliptical aperture acts as radiating element between the two conductors.

Three antennas have been manufactured with a short feeding structure made out of copper for easy connection. The body of the radiating structure is built, respectively, in copper, PEDOT, or PPy conductive polymers. A reasonably omnidirectional dipole-like radiation pattern over a large frequency bandwidth with low-input reflections has been observed for all three antennas. The similarity of the patterns allowed to estimate the conductor losses by comparing the gain patterns.

For the PPy antenna, a very satisfying efficiency of  $e_c = 79.2\%$  averaged over the whole UWB spectrum could be measured. This good performance is due to the large thickness of the free-standing conductive polymer film. The disadvantage of this arrangement is however the (currently) manual manufacture of the geometry. The PEDOT technology allows for the direct printing of complex geometries onto a carrier substrate. However, the process is still presently limited in terms of achievable thicknesses, and, therefore, despite a higher conductivity compared to the PPy, less satisfactory performances were achieved. For this antenna, an efficiency of  $e_c = 26.6\%$  has been measured, which nevertheless encourages further investigation in this type of material given its potential.

It has been demonstrated in the present study that even though the PPy conductor exhibits a conductivity lower by an order of magnitude compared to PEDOT, this drawback can be compensated by increasing substantially the film conductor thickness to reach values close to the skin depth. This approach has resulted in an efficiency loss of only around 1 dB for the PPy antenna compared to a copper antenna. As for the PEDOT antenna, the currently achieved thickness of  $7\,\mu{\rm m}$  in inkjet printing needs to be increased as it is well below skin depth.

The research on the material side currently mainly focus on increasing conductivity, for example, in composite form with carbon nanotubes or graphene. The present results demonstrate the need for further research on improving the processability for achieving thicker layer thicknesses, as complementary path.

The degradation of efficiency coming about through the use of conducting polymers in the fabrication of antennas has to be put into the perspective of the attractive properties of the materials, such as plastic-like mechanical flexibility, processability, and potential for low-cost patterning. Potential designs will also benefit from the biocompatibility and biodegradability for medical applications and from the electroactivity for reconfigurable designs. Finally, polymer antennas could be seamlessly integrated in low-cost all-polymer electronic devices.

## Acknowledgments

The authors are grateful to Hansruedi Benedikter who performed the measurement at the Laboratory for Microwave Electronics and Electromagnetic Fields (IFH) at ETH Zurich, Switzerland. The authors acknowledge the support of the Australian Research Council (ARC) under Discovery Project DP120100661.

## References

- [1] H. Rmili, J.-L. Miane, H. Zangar, and T. Olinga, "Design of microstrip-fed proximity-coupled conducting-polymer patch antenna," *Microwave and Optical Technology Letters*, vol. 48, no. 4, pp. 655–660, 2006.
- [2] A. Verma, B. Weng, R. Shepherd et al., "6 GHz microstrip patch antennas with PEDOT and polypyrrole conducting polymers," in *Proceedings of the 12th International Conference on*

- Electromagnetics in Advanced Applications (ICEAA '10), pp. 329–332, September 2010.
- [3] A. Verma, C. Fumeaux, V. T. Truong, and B. D. Bates, "Effect of film thickness on the radiation efficiency of a 4.5 GHz polypyrrole conducting polymer patch antenna," in *Proceedings of the Asia-Pacific Microwave Conference (APMC '10)*, pp. 95–98, December 2010.
- [4] Y. Bayram, Y. Zhou, B. S. Shim et al., "E-textile conductors and polymer composites for conformal lightweight antennas," *IEEE Transactions on Antennas and Propagation*, vol. 58, no. 8, pp. 2732–2736, 2010.
- [5] A. Mehdipour, A. R. Sebak, C. W. Trueman, I. D. Rosca, and S. V. Hoa, "Performance of microstrip patch antenna on a reinforced carbon fiber composite ground plane," *Microwave* and Optical Technology Letters, vol. 53, no. 6, pp. 1328–1331, 2011.
- [6] P. Pillai, E. Paster, L. Montemayor, C. Benson, and I. W. Hunter, "Development of soldier conformable antennae using conducting polymers," Tech. Rep., Massachusetts Institute of Technology, 2010.
- [7] N. J. Kirsch, N. A. Vacirca, T. P. Kurzweg, A. K. Fontecchio, and K. R. Dandekar, "Performance of transparent conductive polymer antennas in a MIMO ad-hoc network," in *Proceedings of the 6th Annual IEEE International Conference on Wireless and Mobile Computing, Networking and Communications (WiMob* '10), pp. 9–14, October 2010.
- [8] N. J. Kirsch, N. A. Vacirca, E. E. Plowman, T. P. Kurzweg, A. K. Fontecchio, and K. R. Dandekar, "Optically transparent conductive polymer RFID meandering dipole antenna," in *Proceedings of the IEEE International Conference on RFID* (RFID '09), pp. 278–282, April 2009.
- [9] S. Cichos, J. Haberland, and H. Reichl, "Performance analysis of polymer based antenna-coils for RFID," in *Proceedings of the* 2nd International IEEE Conference on Polymers and Adhesives in Microelectronics and Photonics (POLYTRONIC '02), pp. 120–124, 2002.
- [10] G. Shaker, S. Safavi-Naeini, N. Sangary, and M. M. Tentzeris, "Inkjet printing of ultrawideband (UWB) antennas on paperbased substrates," *IEEE Antennas and Wireless Propagation Letters*, vol. 10, pp. 111–114, 2011.
- [11] M. Mäntysalo and P. Mansikkamäki, "An inkjet-deposited antenna for 2.4 ghz applications," *International Journal of Electronics and Communications*, vol. 63, no. 1, pp. 31–35, 2009.
- [12] A. Mehdipour, I. D. Rosca, and A. R. Sebak, "Carbon nanotube composites for wideband millimeter-wave antenna applications," *IEEE Transactions on Antennas and Propagation*, vol. 59, no. 10, pp. 3572–3578, 2011.
- [13] C. K. Chiang, C. R. Fincher, Y. W. Park et al., "Electrical conductivity in doped polyacetylene," *Physical Review Letters*, vol. 39, no. 17, pp. 1098–1101, 1977.
- [14] A. Epstein, "Insulator-metal transition and metallic state in conducting polymers," in *Handbook of Conducting Polymers*, pp. 15.1–15.75, 2007.
- [15] E. Yilmaz, D. P. Kasilingam, and B. M. Notaros, "Performance analysis of wearable microstrip antennas with low-conductivity materials," in *Proceedings of the IEEE International Symposium on Antennas and Propagation (AP-S 08)*, July 2008.
- [16] F. Migneco, Y. C. Huang, R. K. Birla, and S. J. Hollister, "Poly(glycerol-dodecanoate), a biodegradable polyester for medical devices and tissue engineering scaffolds," *Biomaterials*, vol. 30, no. 33, pp. 6479–6484, 2009.

- [17] Clevios, Heraeus Conductive Polymers Division, 2011, http://www.clevios.com/.
- [18] V.-T. Truong and J. G. Ternan, "Complex conductivity of a conducting polymer composite at microwave frequencies," *Polymer*, vol. 36, no. 5, pp. 905–909, 1995.
- [19] H. G. Schantz, "Planar elliptical dipoles," in Proceedings of the IEEE Antennas and Propagation Society International Symposium, 2002.
- [20] B. V. V. Zeghbroeck, *Principles of Semiconductor Devices*, Prentice Hall, 2009.
- [21] K. C. L. Chan, Y. Huang, and X. Zhu, "A planar elliptical monopole antenna for UWB applications," in *Proceedings of* the IEEE/ACES International Conference on Wireless Communications and Applied Computational Electromagnetics, pp. 182– 185, April 2005.
- [22] J. Liang, C. C. Chiau, X. Chen, and C. G. Parini, "Study of a printed circular disc monopole antenna for UWB systems," *IEEE Transactions on Antennas and Propagation*, vol. 53, no. 11, pp. 3500–3504, 2005.
- [23] H. Choo, R. Rogers, and H. Ling, "On the wheeler cap measurement of the efficiency of microstrip antennas," *IEEE Transactions on Antennas and Propagation*, vol. 53, no. 7, pp. 2328–2332, 2005.
- [24] H. Schantz, *The Art and Science of Ultrawideband Antennas*, Artech House, 2005.

Hindawi Publishing Corporation International Journal of Antennas and Propagation Volume 2012, Article ID 829780, 9 pages doi:10.1155/2012/829780

## Research Article

# **Development of Full-Scale Ultrathin Shell Reflector**

## Durmuş Türkmen,<sup>1</sup> Ömer Soykasap,<sup>2</sup> and Şükrü Karakaya<sup>3</sup>

- <sup>1</sup> Department of Mechanical Engineering, Pamukkale University, 20070 Denizli, Turkey
- <sup>2</sup> Department of Material Science and Engineering, Afyon Kocatepe University, 03200 Afyonkarahisar, Turkey
- <sup>3</sup> Department of Mechanical Education, Afyon Kocatepe University, 03200 Afyonkarahisar, Turkey

Correspondence should be addressed to Ömer Soykasap, soykasap@aku.edu.tr

Received 16 December 2011; Accepted 21 March 2012

Academic Editor: Carles Fernández-Prades

Copyright © 2012 Durmuş Türkmen et al. This is an open access article distributed under the Creative Commons Attribution License, which permits unrestricted use, distribution, and reproduction in any medium, provided the original work is properly cited

It is aimed that a new ultrathin shell composite reflector is developed considering different design options to optimize the stiffness/mass ratio, cost, and manufacturing. The reflector is an offset parabolic reflector with a diameter of 6 m, a focal length of 4.8 m, and an offset of 0.3 m and has the ability of folding and self-deploying. For Ku-band missions a full-scale offset parabolic reflector antenna is designed by considering different concepts of stiffening: (i) reflective surface and skirt, (ii) reflective surface and radial ribs, and (iii) reflective surface, skirt, and radial ribs. In a preliminary study, the options are modeled using ABAQUS finite element program and compared with respect to their mass, fundamental frequency, and thermal surface errors. It is found that the option of reflective surface and skirt is more advantageous. The option is further analyzed to optimize the stiffness/mass ratio considering the design parameters of material thickness, width of the skirt, and ply angles. Using the TOPSIS method is determined the best reflector concept among thirty different designs. Accordingly, new design can be said to have some advantages in terms of mass, natural frequency, number of parts, production, and assembly than both SSBR and AstroMesh reflectors.

## 1. Introduction

There have been extensive studies on spaceborne reflectors to increase the performance with a reduced cost. There are a number of reflector concepts; selection of the best concept depends on application and size of the reflectors. The main requirement for large reflectors is that they must be packaged in the limited volume of the launch vehicle, and they must be deployed to required shape in orbit. In order to compactly package a large reflector, the structure is to be folded or bent; the smaller packaged volume is required to lower the launch cost [1, 2]. Folding and self-deploying shell reflector has a thin reflective surface and some reinforcements to stiffen the structure, which are designed to allow folding [3]. Tan et al. studied the stiffened spring-back reflector (SSBR), showing the feasibility, folding, and self-deploying capability of a 0.8 scaled demonstrator. The full-size high-accuracy offset reflector of 6 m diameter met the requirements for Kuband application [4]. Datashvili et al. studied the technical assessment of the high-accuracy large-spaceborne reflector antenna concepts for Ku-band. Thin shell reflector antenna (SSBR) was selected as one of the best options. The SSBR concept has several advantages over the current state-of-theart AstroMesh reflector, namely, simplicity, relatively lower manufacturing costs, a lower surface error, and a simpler folding. On the other hand, the main advantages of Astro-Mesh are its lower mass and its small packaged volume [1, 5].

In this study, it is aimed that a new ultrathin shell composite reflector is developed considering different design options to optimize the stiffness/mass ratio, cost, and manufacturing. SSBR is taken as reference reflector with a diameter of D=6 m, a focal length of F=4.8 m, and an offset distance of 0.3 m. The concepts of stiffening the reflector structure include (i) reflective surface and skirt, (ii) reflective surface and radial ribs, and (iii) reflective surface, skirt, and radial ribs. In a preliminary study, the options are modeled using the ABAQUS finite element program [6] and compared in terms of their mass and fundamental frequencies. It is found the concept of reflective surface and skirt is more advantageous over the other options. The concept is further analyzed to optimize the stiffness/mass ratio considering the design parameters of thickness of the skirt, width of the skirt, and

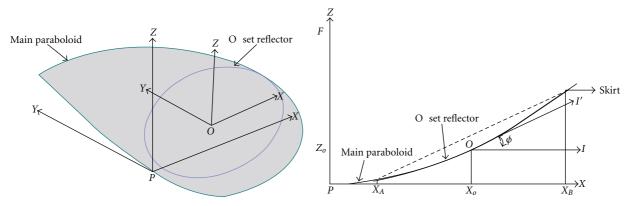


FIGURE 1: Offset reflector.

ply angles. Using the TOPSIS method will be determined the best reflector design among thirty different designs. Then, new design will be compared with SSBR and AstroMesh reflectors.

## 2. Preliminary Design

The full-scale reflector is an offset parabolic reflector with a diameter of D = 6 m, a focal length of F = 4.8 m, and an offset of  $X_A = 0.3$  m. The reflector is modeled in the ABAQUS finite element software; first, the main paraboloid is created; next the offset reflector surface is obtained by a cut using a cylinder with its axis z being parallel to the axis Z of the paraboloid. Figure 1 shows the details of the modeling, where offset distance  $X_A = 0.3$  m and diameter of the reflector D = $X_B - X_A = 6$  m. There is also flat skirt with a width of 0.15 m around the rim of the reflector. The SSBR used a triaxial carbon fiber/epoxy for the reflector, but there are thermal distortion problems in the triaxial material; hence, a plain weave carbon/epoxy is chosen instead for the new reflector. The reflector is assumed to be made of plain weave carbon T300B/L160 epoxy, with an areal density of dry cloth of 94 g/m<sup>2</sup> and a ply thickness of 0.11 mm. Material properties of a single ply are obtained for a fiber volume fraction of  $V_f = 0.485$  as  $E_1 = E_2 = 60.2$  GPa,  $G_{12} = 2.94$  GPa,  $v_{12} = 0.485$ 0.031, and  $\rho = 1.440 \text{ kg/m}^3$ , which is based on the analytical approach developed for plain-woven composite materials [7]

The three concepts of stiffening the reflector structure include (i) reflective surface and skirt, (ii) reflective surface and radial ribs, and (iii) reflective surface, skirt, and radial ribs. The reflector surface is modeled as a laminated composite shell, using *S4R* quadratic elements, with a total number of elements of 14250. The concepts are compared in terms of mass and fundamental frequency.

2.1. The Concept of Reflective Surface and Skirt. It is envisaged that a reflector with much simpler design and significantly lower mass and lower cost is possible by considering some design changes on SSBR. First, several stiffening elements including radial, spiral, central, and rim reinforcements and a skirt were used in the original SSBR. All reinforcing

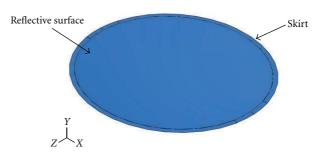


FIGURE 2: Reflective surface with flat skirt, case E.

elements except the skirt are removed in the new reflector in order to simplify the structure and to reduce its mass. Second, there were circumferential slits on the skirt near the rim that was introduced to reduce the stress and/or strain in the structure during folding. All slits are removed in the new concept. Hence, we consider only reflective surface with a flat skirt to investigate full advantage of stiffening.

The concept is modeled in ABAQUS as seen in Figure 2. It consists of two parts: reflective surface and skirt that are connected to each other by tie constraints. The skirt is made of three plies (0/45/0) and a width of  $0.15 \, \text{m}$ , whereas the reflective surface is made of either three plies (0/45/0) or two plies (0/45). The case of reflective surface and skirt is denoted as case E.

2.2. The Concept of Reflective Surface and Rib. Composite tape springs are commonly used for deployable structures for stiffening the structure. The tape springs exhibit high initial stiffness in deployed configuration and folds and deploys elastically (can be seen in Figure 7).

Therefore, it can be a good choice to stiffen the reflective surface as a rib. Figures 3 and 4 show the modeled reflector with initially curved large tape springs. Two options are considered: (i) the tape springs are attached to the back of the reflective surface and subject to opposite sense bending during folding of the reflector denoted as case T and (ii) the tape springs are attached to the back of the reflective surface and subject to equal sense bending during folding of

Designs		Frequency, (Hz)						mass (kg)	
Designs	Mode 1	Mode 2	Mode 3	Mode 4	Mode 5	Mode 6	Mode 7	Mode 8	mass (kg)
case E <sup>a</sup>	1.025	1.124	3.362	3.385	6.735	6.775	9.282	9.734	15.91
case E <sup>b</sup>	1.110	1.212	3.632	3.654	6.920	6.942	7.712	7.725	11.08
case Ta	0.254	0.274	0.328	0.395	0.407	1.018	1.092	1.097	17.69
case T <sup>b</sup>	0.232	0.277	0.295	0.351	0.356	0.796	0.905	1.065	12.86
case Da	1.515	1.536	2.262	2.475	2.605	3.251	3.612	3.674	17.69
$\boldsymbol{case}\ \mathbf{D}^{b}$	1.448	1.461	2.078	2.290	2.328	2.681	2.865	2.914	12.86
case ETa	1.102	1.190	3.516	3.531	6.789	7.145	9.680	9.796	19.15
case ET <sup>b</sup>	1.178	1.260	3.712	3.722	6.925	7.353	8.288	8.479	14.32
case ED <sup>a</sup>	2.254	2.314	5.077	5.089	8.306	8.476	9.990	10.18	19.15
case ED <sup>b</sup>	2.293	2.342	5.160	5.182	7.972	8.136	8.426	8.635	14.32

Table 1: Comparison of different design cases.

<sup>&</sup>lt;sup>a</sup>: reflective surface with three plies, <sup>b</sup>: reflective surface with two plies.

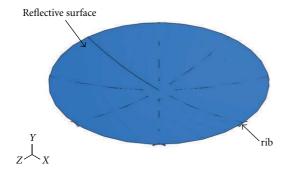


FIGURE 3: Reflective surface with tape springs, case T.

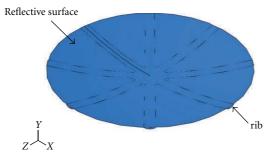


FIGURE 4: Reflective surface with tape spring, case D.

the reflector denoted as case D. For case T, the tape springs have the same longitudinal curvature as the reflective surface and are connected to the reflective surface tangentially. For case D, the tape springs have the same longitudinal curvature as the reflective surface, but are connected to the reflective surface through their edges. For both cases, eight tape springs are considered and connected to reflective surface by tie constraints. The tape springs have a subtended angle of 60 deg and transverse radius of 0.3 m and are made of three ply (0/45/0) composites of the same material. Again the reflective surface is assumed to be made of either three plies (0/45/0) or two plies (0/45).

- 2.3. Concept of Reflective Surface with Skirt and Ribs. In this concept the reflective surface is stiffened by both skirt and ribs. Flat skirt is added to the models shown in Figures 3 and 4 by tie constraints. The skirt and ribs are assumed to have three plies (0/45/0). The cases of reflective surface with skirt and ribs are denoted as case ED and case ET.
- 2.4. Results of Preliminary Analysis. The modal analysis is carried out for each reflector under free boundary conditions; the natural frequencies, mass, and the mode shapes are obtained. The results are given in Table 1. The cases of E, D, and ED with reflective surface of two plies are better when high fundamental frequency with low mass is considered. The reflective surface with two plies is advantageous due to less thickness and material cost.

The reflective surface with skirt, case E, has the lowest mass, and it also satisfies the requirement of a minimum fundamental frequency of 1 Hz. It can be manufactured as a single piece. It allows folding and self-deploying. Hence, it is the best option compared to the other cases.

The reflective surface with rib, case D, has a slightly higher mass and a higher fundamental frequency. However, the other modes except mode two have less natural frequencies than that of case E. The reflective surface and the ribs must be manufactured separately. Attachment of the ribs to the reflective surface is another issue that must be further studied. 3D folding behavior of the ribs or the reflective surface with ribs should be investigated.

The reflective surface with skirt and ribs, case ED, has the highest fundamental frequency but with a higher mass. This makes manufacturing even more difficult, and it has still the same drawbacks of case D.

The mode shapes of the options are given in Figure 5. In all cases mode shapes have circumferential sine waves along the rim of the reflector. Two consecutive natural frequencies are close to each other; corresponding modes are similar but with a phase angle.

2.5. Thermal Analysis. Structural parts that work in space environment are subject to great temperature variance. So, the structural parts need to be made of materials with low

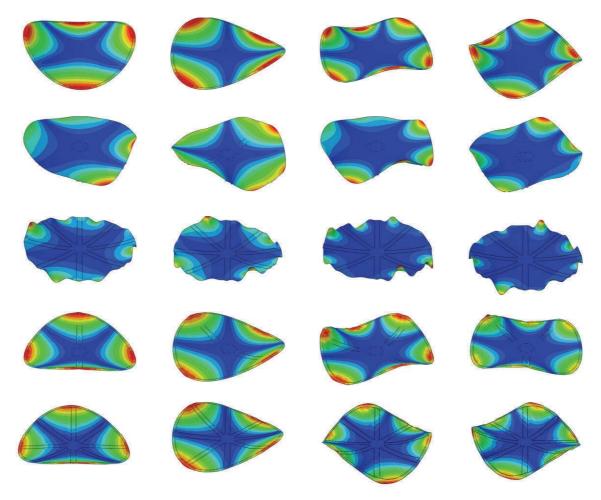


FIGURE 5: First four modes of the cases E, T, D, ET, and ED with three-ply reflective surface, from top to down.

coefficient of thermal expansion (CTE). Thermal changes that occur in orbit cause surface errors and reductions in performance. Thermal analysis is carried out under thermal loads for the best three designs of case  $E^b$ , case  $D^b$ , and case  $ED^b$ , and then the surface error is estimated, which can be used to estimate the electrical performance. In order to measure the surface accuracy, root mean square error (RMS) is considered. The surface accuracy of reflective surface can be obtained by considering the ideal design surface and the best-fit paraboloid surface. The best-fit paraboloid is defined in XYZ coordinate system as  $Z = (X^2 + Y^2)/(4F)$ , and it is obtained by minimizing the RMS error using parameters of Euler rotation angles  $(\theta, \phi, \varphi)$  and the parameters of translations  $(x_0, y_0, z_0)$  from the xyz coordinate system as follows:

$$\begin{bmatrix} X \\ Y \\ Z \end{bmatrix} = BCD \begin{bmatrix} x \\ y \\ z \end{bmatrix} + \begin{bmatrix} x_0 \\ y_0 \\ z_0 \end{bmatrix},$$

$$B = \begin{bmatrix} \cos(\psi) & \sin(\psi) & 0 \\ -\sin(\psi) & \cos(\psi) & 0 \\ 0 & 0 & 1 \end{bmatrix},$$

$$C = \begin{bmatrix} 1 & 0 & 0 \\ 0 & \cos(\theta) & \sin(\theta) \\ 0 & -\sin(\theta) & \cos(\theta) \end{bmatrix},$$

$$D = \begin{bmatrix} \cos(\phi) & \sin(\phi) & 0 \\ -\sin(\phi) & \cos(\phi) & 0 \\ 0 & 0 & 1 \end{bmatrix}.$$
(1)

RMS error in Z direction is calculated for all the nodes as follows:

$$\delta_{\rm rms} = \sqrt{\frac{\sum \left(\hat{Z}_i - Z_i\right)^2}{n}},\tag{2}$$

where  $\hat{Z}_i$  is the coordinate of a point of distorted surface and  $Z_i$  is the corresponding coordinate of the best-fit paraboloid.

The woven carbon/epoxy composite, which is used for the reflective surface and the ribs, has a CTE of between  $2 \times 10^{-6}$ /°C and  $6 \times 10^{-6}$ /°C. However, a lower CTE is obtained when special resin for the space applications is used; hence a CTE of  $0.5 \times 10^{-6}$ /°C is taken for the analysis. Thermal

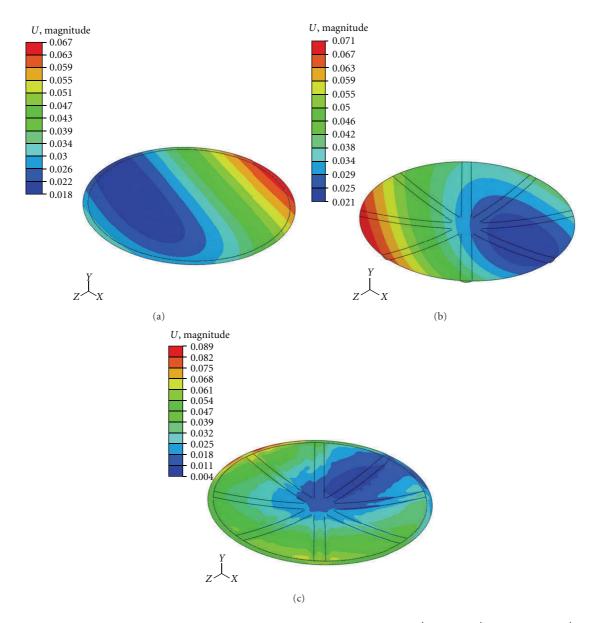


FIGURE 6: Displacement magnitudes due to LC3 thermal loading (units in mm), case E<sup>b</sup> (a), case D<sup>b</sup>, (b), and case ED<sup>b</sup> (c).

Table 2: RMS errors for thermal loads.

Thermal loads	$E_p$	$E^b$		$\mathrm{D}^{\mathrm{b}}$		$\mathrm{ED^b}$	
Thermal loads	RMS (mm)	F (mm)	RMS (mm)	F (mm)	RMS (mm)	F (mm)	
LC1	0.003	4800.25	0.06	4800.36	0.045	4800.16	
LC2	0.050	4802.52	0.08	4800.75	0.055	4800.90	
LC3	0.035	4800.40	0.04	4800.20	0.032	4800.25	

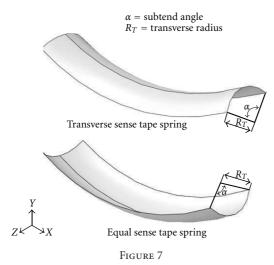
loading conditions are as follows [1, 8]:

LC1: a gradient along the *x*-direction of 100°C over the total length of the reflector,

LC2: uniform absolute temperature  $-150^{\circ}$ C,

LC3: uniform absolute temperature 170°C.

The thermal loads are applied to the finite element model of three concepts using initial temperature of 20°C. The displacement contours are shown in Figure 6 for each concept. The focal length and RMS error for each concept are given in Table 2. The worst loading is LC2 for both RMS and the focal length. All concepts yield similar results of



a low RMS error and small variation in the design focal length; hence they all are acceptable.

## 3. Optimization of the Reflector with Skirt

The preliminary study showed that the option of reflective surface with skirt suits better for low cost, low mass, and sufficient stiffness. Therefore, it is chosen as the best concept for the new thin shell reflector. In order to increase stiffness while keeping low mass the structure is optimized considering design changes. During the optimization the following is considered for the design. First the reflective surface is to have a continuous surface; no discontinuity is allowed. Next the reflector mass should be less than 14 kg. Then the reflector has the minimum number of parts with manufacturing ease and low cost. Last but not least the reflector must be foldable.

The design parameters are the thickness of the skirt,  $t_2$ , width of the skirt, w, and composite ply angles of the skirt. Three different widths, 150 mm, 200 mm, and 250 mm, for the skirt and a maximum of six plies for the skirt are considered. The reflective surface has the plies 0/45 with a thickness of 0.22 mm, which are taken to be constant. The mass and fundamental frequencies are given in Table 3.

Adding 45 deg plies to the skirt increases the frequency. Increasing the width of the skirt increases both the mass and the frequency of the structure. The design with a skirt of 0/45/45/0 and a width of 250 mm has the highest frequency/mass ratio. However, the frequency is not critical; the design with a skirt of 0/45/0 and a width of 250 mm has the second highest frequency/mass ratio but has a lower mass and frequency.

3.1. Determination of the Best Offset Reflector Model Using TOPSIS Method. The TOPSIS method developed by Hwang and Yoon is one of the multicriteria decision-making techniques. The basis of the method is the decision points based on the proximity of the ideal solution. With this method, the maximum and minimum values can be compared to

Table 3: Comparison of different designs of reflective surface with skirt.

skirt.						
Design no.		Skirt wi	th plies $0_n$ , $w =$	150 mm		
	n	t <sub>2</sub> (mm)	mass (kg)	Freq. (Hz)		
1	2	0.22	10.600	0.768		
2	3	0.33	11.085	0.850		
3	4	0.44	11.550	0.912		
4	5	0.55	12.020	0.954		
5	6	0.66	12.500	0.988		
		Skirt wi	th plies $0_n$ , $w = 1$	200 mm		
	n	<i>t</i> <sub>2</sub> (mm)	mass (kg)	Freq. (Hz)		
6	2	0.22	10.930	1.025		
7	3	0.33	11.560	1.127		
8	4	0.44	12.200	1.199		
9	5	0.55	12.840	1.245		
10	6	0.66	13.475	1.278		
		Skirt wi	th plies $0_n$ , $w = 1$	250 mm		
	n	<i>t</i> <sub>2</sub> (mm)	mass (kg)	Freq. (Hz)		
11	2	0.22	11.260	1.330		
12	3	0.33	12.060	1.469		
13	4	0.44	12.860	1.533		
14	5	0.55	13.660	1.569		
15	6	0.66	14.460	1.585		
		Skirt with plies $0/45_n/0$ , $w = 150 \text{ mm}$				
	n	t <sub>2</sub> (mm)	mass (kg)	Freq. (Hz)		
16	0	0.22	10.600	1.070		
17	1	0.33	11.085	1.195		
18	2	0.44	11.550	1.350		
19	3	0.55	12.020	1.388		
20	4	0.66	12.500	1.399		
		Skirt with	plies $0/45_n/0$ , w	= 200 mm		
	n	t <sub>2</sub> (mm)	mass (kg)	Freq. (Hz)		
21	0	0.22	10.930	1.470		
22	1	0.33	11.560	1.620		
23	2	0.44	12.200	1.829		
24	3	0.55	12.840	1.851		
25	4	0.66	13.475	1.852		
			plies $0/45_n/0$ , w			
	n	t <sub>2</sub> (mm)	mass (kg)	Freq. (Hz)		
26	0	0.22	11.260	1.702		
27	1	0.33	12.060	1.990		
28	2	0.44	12.860	2.145		
29	3	0.55	13.660	2.135		
30	4	0.66	14.460	2.105		

the ideal state [9–13]. The TOPSIS method consists of six steps. The TOPSIS method steps are described below.

Table 4: Reflector designs.

Weight coefficients	$w_1$	$w_2$	$w_3$	$w_4$	Value of proximity to decision $C_i^*$
Designs	Mass, (kg)	Fundamental frequency (Hz)	Manufacturing cost	Packing volume	varies of proximity to decision of
1	10.60	0.768	1	5	0.405
2	11.08	0.850	2	4	0.355
3	11.55	0.912	3	3	0.286
4	12.02	0.954	4	2	0.223
5	12.50	0.988	5	1	0.214
6	10.93	1.025	1	5	0.458
7	11.56	1.127	2	4	0.430
8	12.20	1.199	3	3	0.388
9	12.84	1.245	4	2	0.351
10	13.47	1.278	5	1	0.340
11	11.26	1.330	1	5	0.549
12	12.06	1.469	2	4	0.564
13	12.86	1.533	3	3	0.539
14	13.66	1.569	4	2	0.498
15	14.46	1.585	5	1	0.464
16	10.60	1.070	1	5	0.465
17	11.08	1.195	2	4	0.444
18	11.55	1.350	3	3	0.435
19	12.02	1.388	4	2	0.391
20	12.50	1.399	5	1	0.361
21	10.93	1.470	1	5	0.587
22	11.56	1.620	2	4	0.612
23	12.20	1.829	3	3	0.636
24	12.84	1.851	4	2	0.578
25	13.47	1.852	5	1	0.525
26	11.26	1.702	1	5	0.672
27	12.06	1.990	2	4	0.750
28	12.86	2.145	3	3	0.725
29	13.66	2.135	4	2	0.654
30	14.46	2.105	5	1	0.588

Step 1 (creating the decision matrix). The decision matrix consists of rows of decision point located in the lines. Factors in the evaluation takes place in the columns. The decision matrix is shown as follows:

$$A_{ij} = \begin{bmatrix} a_{11} & a_{12} & \cdots & a_{1n} \\ a_{21} & a_{22} & \cdots & a_{2n} \\ \vdots & & & \vdots \\ a_{m1} & a_{m2} & \cdots & a_{mn} \end{bmatrix}, \tag{3}$$

 $A_{ij}$  is the matrix, m the number of decision point, and n the number of assessment factor.

*Step 2* (creating standard decision matrix (*R*)). Standard decision matrix is calculated using the following formula:

$$r_{ij} = \frac{a_{ij}}{\sqrt{\sum_{k=1}^{m} a_{kj}^2}}. (4)$$

Thus, the *R* matrix is obtained as follows:

$$R_{ij} = \begin{bmatrix} r_{11} & r_{12} & \dots & r_{1n} \\ r_{21} & r_{22} & \dots & r_{2n} \\ \vdots & & & \vdots \\ r_{m1} & r_{m2} & \dots & r_{mn} \end{bmatrix}.$$
 (5)

Step 3 (constructing the weighted normalized decision matrix (V)). Weight values are determined according to

	New Design	SSBR [1–4]	AstroMesh [15]
Aperture Diameter, m	6	6	6
F/D	0.8	0.8	0.64
Offset, m	0.3	0.3	0.75
Mass, kg	12.06	23.6	14.50
Fundamental frequency, Hz	1.99	1.87	2.00
Number of parts	Monolithic	Monolithic	Many (nets, meshes, ring truss, etc.)
Manufacturing and assembly	Easier	Easy	Difficult

TABLE 5: Comparison of new design, SSBR, and AstroMesh.

purpose ( $\omega ij: i: 1,2,...N$ ). Then each column of the *R* matrix elements multiplying with  $\omega ij$  value and *V* matrix is created:

$$V_{ij} = \begin{bmatrix} w_1 r_{11} & w_2 r_{12} & \dots & w_n r_{1n} \\ w_1 r_{21} & w_2 r_{22} & \dots & w_n r_{2n} \\ \vdots & & & \vdots \\ w_1 r_{m1} & w_2 r_{m2} & \dots & w_n r_{mn} \end{bmatrix}.$$
(6)

Step 4 (ideal  $(A^*)$  and negative ideal  $(A^-)$  creating solutions). For creating the ideal solution set, the elders of column values of V matrix are selected. Finding the ideal solution set is shown in the following formula:

$$A^* = \left\{ \left( \max_{i} v_{ij} \mid j \in J \right), \left( \min_{i} v_{ij} \mid j \in J' \right) \right\}.$$
 (7)

Here,  $A^* = \{v_1^*, v_2^*, \dots, v_n^*\}$  and J is maximization and J' minimization of the value negative ideal.

For creating the negative ideal solution set, the smaller of column values of V matrix are selected. Finding the negative ideal solution set is shown in the following formula:

$$A^{-} = \left\{ \left( \min_{i} \nu_{ij} \mid j \in J \right), \left( \max_{i} \nu_{ij} \mid j \in J' \right) \right\}. \tag{8}$$

Here,  $A^- = \{v_1^-, v_2^-, \dots, v_n^-\}$  is shown.

Step 5 (calculating the separation measure). For finding the deviations of solution set the Euclidian distance approach is utilized. Here, the obtained deviation values are called ideal  $(S_i^*)$  and negative ideal separation  $(S_i^-)$  measures. Ideal and negative ideal separation are calculated using the following formula:

$$S_{i}^{*} = \sqrt{\sum_{j=1}^{n} (v_{ij} - v_{j}^{*})^{2}},$$

$$S_{i}^{-} = \sqrt{\sum_{j=1}^{n} (v_{ij} - v_{j}^{-})^{2}}.$$
(9)

Step 6 (calculating the relative closeness for the ideal solution). To calculate the ideal solution proximity  $(C_i^*)$ ,

the ideal and negative ideal separation measure is used. Calculation of the relative proximity to the ideal solution is shown in the following formula:

$$C_i^* = \frac{S_i^-}{S_i^- + S_i^*}. (10)$$

Here,  $C_i^*$  value gets the range of  $0 \le C_i^* \le 1$  [14].

3.2. Determining the Best Reflector Design. The natural frequency and mass constitute the first two-column decision matrix of values in Table 4. The other two columns are manufacturing costs and packaging volume. While skirt thickness and skirt width increase, the manufacturing cost increases. The same situation is valid for packing volume. The package volume increases with the skirt thickness. This is due to the fact that the minimum bend radius increases with the thickness of material. For these reasons, these criteria are taken into account using scores from 1 to 5. Weight coefficients of decision matrix are determined as  $w_1 = 0.4$ ,  $w_2 = 0.35$ ,  $w_3 = 0.05$ , and  $w_4 = 0.20$ .

The decision-making process is evaluated with the TOPSIS method by taking into account four different criteria and thirty different designs. Value of proximity to decision is seen in Table 4. The ideal design is obtained when value of proximity to decision is the highest. According to this, the best design is the twenty-seventh design. The optimized results are compared with SSBR and Astromesh reflector as given in Table 5. The new design has some advantages in terms of lower mass, number of parts, ease of manufacturing and assembly. The 1/3 scale predesign reflector is accomplished and a part of ground tests such as folding, modal, and deploying have been completed. Predesign reflector made of three-ply (0/45/0) plain weave carbon/epoxy can be seen in Figure 8.

## 4. Conclusions

A new ultrathin shell composite reflector is developed considering different design options to optimize the stiffness/mass ratio, cost, and manufacturing. The stiffened spring-back reflector is taken as reference reflector. Preliminary design study shows that the reflective surface with only a skirt has simpler design with high stiffness/mass ratio. This option is further analyzed to optimize the stiffness/mass ratio



Folded reflector from one point



FIGURE 8

considering the design parameters of material thickness, width of the skirt, and ply angles. The optimized reflector has a mass of 12.06 kg and a fundamental frequency of 1.99 Hz. The new design has some advantages compared with previous design of both the stiffened spring-back reflector and AstroMesh reflector.

## Acknowledgments

This research work is supported by the Scientific and Technological Research Council of Turkey under Grant 109M421 and the Pamukkale University Scientific Research Center.

## References

- [1] Ö. Soykasap and L. T. Tan, "High-precision offset stiffened springback composite reflectors," *AIAA Journal*, vol. 49, no. 10, p. 2144, 2011.
- [2] Ö. Soykasap, A. Watt, S. Pellegrino, and P. Howard, "Novel concept for all-composite deployable SAR reflectors," in *Proceedings of the European Conference on Spacecraft Structures, Materials & Mechanical Testing (ESA/ESTEC '05)*, Noordwijk, The Netherlands, 2005.
- [3] Ö. Soykasap and S. Karakaya, "Design of folding and self-deploying thin shell reflector," in *Proceedings of the International Scientific Conference on Advanced Lightweight Structures and Reflector Antennas*, Tbilisi, Ga, USA, October 2009.
- [4] L. T. Tan, Ö. Soykasap, and S. Pellegrino, "Design & manufacture of stiffened spring-back reflector demonstrator," in Proceedings of the 46th AIAA/ASME/ASCE/AHS/ASC Structures, Structural Dynamics and Materials Conference, AIAA Paper 2005–2048, pp. 3078–3088, Austin, Tex, USA, April 2005.
- [5] L. Datashvili, M. Lang, C. Zauner et al., "Technical assessment of high accuracy large space borne reflector antenna (TAHARA)," Tech. Rep. number TR LLB-R-12/07/04-02D-02, Technical University of Munich, Munich, Germany, 2004.
- [6] "ABAQUS/Standard User's Manual," Ver. 6.10, Dassault Systèmes Simulia Corp., Pawtucket, RI, USA, 2010.
- [7] Ö. Soykasap, "Analysis of plain-weave composites," *Mechanics of Composite Materials*, vol. 47, no. 2, pp. 161–176, 2011.

- [8] Y. Gowayed, W. Zou, and S. Gross, "Analytical approach to evaluate the coefficients of thermal expansion of textile composite materials," *Polymer Composites*, vol. 21, no. 5, pp. 814– 820, 2000.
- [9] P. Liu, "An extended TOPSIS method for multiple attribute group decision making based on generalized interval-valued trapezoidal fuzzy numbers," *Informatica*, vol. 35, no. 2, pp. 185–196, 2011.
- [10] G. R. Jahanshahloo, F. H. Lotfi, and M. Izadikhah, "Extension of the TOPSIS method for decision-making problems with fuzzy data," *Applied Mathematics and Computation*, vol. 181, no. 2, pp. 1544–1551, 2006.
- [11] F. Ecer, "Bulanık Ortamlarda Grup Kararı Vermeye Yardımcı Bir Yöntem Fuzzy TOPSIS Ve Bir Uygulama," *Dokuz Eylül* Üniversitesi, İşletme Fakültesi Dergisi, vol. 7, no. 2, pp. 77–96, 2006.
- [12] J. Dodangeh, R. B. M. Yusuff, and J. Jassbi, "Using topsis method with goal programming for best selection of strategic plans in BSC model," *Journal of American Science*, vol. 6, no. 3, 2010
- [13] O. Jadidi, F Firouzi, and E. Bagliery, "TOPSIS method for supplier selection problem," World Academy of Science, Engineering and Technology, vol. 71, 2010.
- [14] http://www.deu.edu.tr/userweb/k.yaralioglu/dosyalar/ TOPSIS\_Yontemi.doc.
- [15] "AstroMesh Reflector," Document No. DS-409, Astro Aerospace, Redondo Beach, Calif, USA, 2004.

Hindawi Publishing Corporation International Journal of Antennas and Propagation Volume 2012, Article ID 573438, 12 pages doi:10.1155/2012/573438

## Research Article

# **High-Gain Textile Antenna Array System for Off-Body Communication**

## Maria Lucia Scarpello, Luigi Vallozzi, Hendrik Rogier, and Dries Vande Ginste

Electromagnetics Group, Department of Information Technology (INTEC), Ghent University, Sint-Pietersnieuwstraat 41, 9000 Gent, Belgium

Correspondence should be addressed to Maria Lucia Scarpello, marialucia.scarpello@ugent.be

Received 20 September 2011; Revised 8 March 2012; Accepted 8 March 2012

Academic Editor: Carles Fernández-Prades

Copyright © 2012 Maria Lucia Scarpello et al. This is an open access article distributed under the Creative Commons Attribution License, which permits unrestricted use, distribution, and reproduction in any medium, provided the original work is properly cited.

A novel high-gain textile antenna array system, fully integrated into a rescue-worker's vest and operating in the Industrial, Scientific, and Medical wireless band (2.4–2.4835 GHz), is presented. The system comprises an array consisting of four tip-truncated equilateral triangular microstrip patch antennas (ETMPAs), a power divider, line stretchers, and coaxial cables. The array is vertically positioned on the human torso to produce a narrow beam in elevation, as such reducing fading and allowing to steer the maximum gain in a small angular sector centered around the broadside direction. To allow simple low-cost beam steering, we specifically minimize mutual coupling by using a relative large distance between the patches and by selecting the ETMPA element as the most suited topology from three potential patch geometries. Moreover, we investigate the stability of return loss and mutual coupling characteristics under different relative humidity conditions, when bending the array, when placing the system on-body, and when covering it by different textile layers. Reflection coefficient and gain patterns are simulated and measured for the antenna system in free space and placed on the human body.

## 1. Introduction

Garments present a large platform for deploying smart textile systems combining textiles, electronics, and antennas. Being flexible, light weight, and conformable to the wearer, a communication system based on textile antennas can be fully integrated into clothing [1-5]. For example, one type of application for wearable antenna systems involves monitoring the activity and life signs of rescue workers active in the field, with the electronics being integrated into protective garments, setting up the off-body wireless communication link between the wearer and the closest base station [6]. In the literature, much research has been published about textile antennas based on a single radiating element, operating in the 2.45 GHz Industrial, Scientific, and Medical (ISM) band (2.4-2.4835 GHz) [7-10], achieving good performance in terms of reflection coefficients and gain. The state of the art of research in wearable antenna arrays shows that a 3 × 3 fabric Electromagnetic Band Gap (EBG) antenna array with an overall thickness of 4.48 mm and size of

 $120\times120\,\mathrm{mm^2}$  can cover the 2.45 GHz ISM band, with a maximum measured gain of 6.4 dBi at 2.45 GHz in free space [11]. In [12] a four-element microstrip array on a 3D woven composite, operating at 1.54 GHz, is presented, but its gain is really low, and even not indicated. In [13], a two-element microstrip parallel array on a 3D orthogonal woven composite is studied, operating at 1.5 GHz with a gain equal to 6.4 dBi.

In [11–13], the mutual coupling between the adjacent elements of the array is not studied, whereas in this paper, we present the design and characterization of a 4-port textile antenna array system, able to operate in a wireless body and personal area network, in the 2.45 GHz ISM band. For the first time in the literature, a complete study of the mutual coupling between the adjacent elements of the wearable array is performed when the array is in planar and bent state. The presented textile array is able to provide more reliable wireless off-body links, thanks to its array gain and its steerable narrow main beam. This is realized by deploying the array vertically on the human torso, allowing to steer

the main beam in elevation within a narrow angular sector around the broadside direction, that is, away from the rescue worker and with the main beam pointing towards the closest base station, as requested by its intended application. The large aperture of the array leads to beam confinement, which in turn results in a smaller number of propagation paths and thereby less fading.

To achieve simple low-cost beam steering, we adopt a Uniform Linear Array (ULA) topology, composed of fourpatch antennas. Three different patch topologies are investigated in order to choose the one yielding the lowest mutual coupling between two adjacent elements. The simulated topologies are tip-truncated Equilateral Triangular Microstrip Patch Antenna (ETMPA), square ring patch antenna, and rhomboidal ring patch antenna. First, the distance between patches is chosen to be  $3/4 \lambda$ , where  $\lambda$  is the freespace wavelength, to minimize mutual coupling between two adjacent elements, while allowing beamsteering within an angle of 20° around broadside without grating lobes. Second, it is decided to adopt the ETMPA topology-for the first time in the literature chosen as radiating element for a textile antenna array system—since the ETMPA exhibits lower mutual coupling between adjacent elements than the other two patch topologies. Third, when deploying the system on-body, it is verified by real-life measurements that mutual coupling levels remain low under different adverse conditions: bending, varying relative humidity conditions, coverage by different textile layers, and proximity effects due to the body of the wearer.

Section 2 presents the design of the textile array. First, the choice of the array topology is explained, then a comparison between three different patch topologies is performed by means of full-wave simulations performed on the different array topologies. This comparison results in the optimal topology to be adopted as antenna element for the array in the remainder of the paper. Next, an accurate study of the textile array with the chosen patch topology is performed. In this section, it is also shown that the design choices lead to reliable off-body communication links, thanks to reduced fading. In Section 3, we show the simulations and measurements performed on the complete system, being a ULA connected by four coaxial cables to four line stretchersproviding the phase shifts necessary for beam steering—and a commercial four-way power divider. The influence of the relative humidity (rH) on the reflection coefficient of the antenna array is discussed based on reliable and reproducible measurements in a controlled environment. Reflection coefficients and gain of the array are simulated by means of CST Microwave Studio and measured in free space and on the human body. Additional measurements of gain are carried out when the array is operating in other reproducible, but potentially adverse, conditions, demonstrating the array's functionality while being placed inside a firefighter jacket. For the evaluation of performance and safety issues, the 10g averaged Specific Absorption Rate (SAR) is calculated and compared to the ICNIRP [14] and FCC guidelines [15]. A comprehensive study of the mutual coupling between each patch of the antenna and the other three elements is carried out when the antenna is in planar and bent state, and

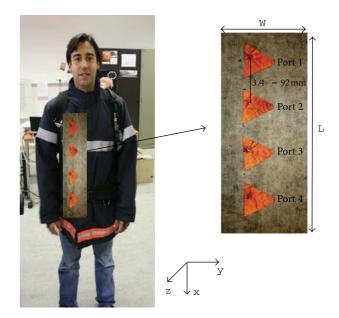


FIGURE 1: Top view of the textile antenna array and its position on the human body. (Note that in this figure, for illustrative purposes, the array is shown exposed on top of the garment. In reality, however, it is integrated into the garment.).

under different rH conditions. In Section 4, conclusions are summarized.

## 2. Design of the Textile Antenna Array

We now present a textile array providing a higher gain and offering more reliable communication links in a multipath environment than a single textile patch antenna. Therefore, we carefully chose the array and antenna element topology with the aim of maximizing the antenna aperture and minimizing the mutual coupling between two adjacent elements of the array.

2.1. Choice of Array Topology. We adopted a ULA topology, composed of four single patch antennas. The textile array is meant to be worn by a person, and it is vertically positioned on the human torso, as shown in Figure 1, in between two layers of garment, to avoid being directly in touch with the skin of the person. The array aperture was chosen in order to fully exploit the large platform presented by the garment. Deploying a vertical array allows to confine the energy within a narrow beam, centered around the azimuth plane. The vertical array offers limited steering capabilities of the beam maximum in a narrow angular sector, centered around the broadside direction. The total size of the array is 480  $\times$ 180 mm<sup>2</sup> and the distance between the four patches is  $3/4\lambda$ , where  $\lambda$  is the free-space wavelength, being approximately 122 mm, as shown in Figure 1. The choice of 92 mm between two consecutive feeding points is a convenient choice as the complete array should be fit vertically on the human torso. Also the rather large spacing between two elements is chosen to minimize mutual coupling, while still allowing limited steering, and to yield a low-cost array with a large aperture.

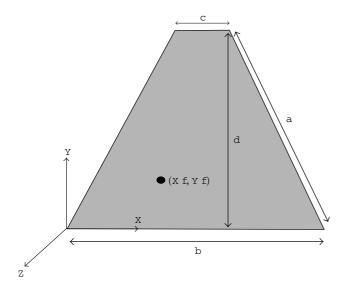


FIGURE 2: ETMPA.

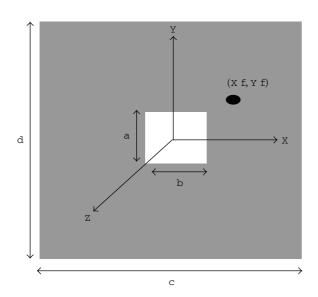


FIGURE 3: Square ring patch antenna.

2.2. Choice of Antenna Element Topology. In order to obtain the optimal performance from the chosen antenna array topology, we carefully investigated three antenna element topologies: tip-truncated ETMPA, square ring patch, and rhomboidal ring patch. Each single radiating element is shown in Figures 2, 3, and 4, and their dimensions are listed in Table 1. Four equal radiating elements are part of one ULA. Both the patch and ground plane of the array are made of Flectron, a breathable and highly conductive electrotextile material, being a copper-plated nylon fabric with a surface resistivity of less than  $0.10 \Omega/sq$ . The three ULAs are simulated on a polyurethane protective foam, called "Azzurri", manufactured by Brunet Lion [16], whose thickness is 3.55 mm and which is typically used in firefighters jackets. The dielectric characteristics of the substrate are  $\epsilon_r = 1.19$  and  $\tan \delta = 0.003$ .

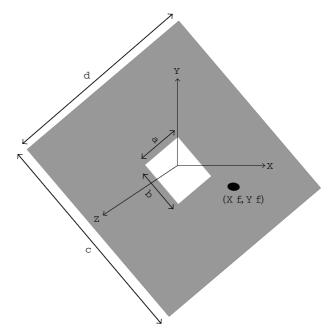


FIGURE 4: Rhomboidal ring patch antenna.

TABLE 1: Patch dimensions of the three antenna element topologies on Azzurri foam, used in the simulation study.

	ETMPA (mm)	Square (mm)	Rhombus (mm)
а	60.1	8.4	8.4
b	69	9.5	9.5
С	8	51.52	51.93
d	52.8	48.44	48.85
Xf	27.5	8.29	10.03
Yf	10	5.56	-2.24

The substrate and patch dimensions were chosen to satisfy the following design criteria within the entire 2.45 GHz ISM band:

$$\left|S_{ij}\right| < -10 \text{ dB} \quad \text{for } i = j,$$
 (1)  
 $\left|S_{ij}\right| < -25 \text{ dB} \quad \text{for } i \neq j,$  (2)

$$\left|S_{ij}\right| < -25 \text{ dB} \quad \text{for } i \neq j,$$
 (2)

$$i, j = 1, 2, 3, 4,$$
 (3)

where *i* and *j* indicate the port numbers of the antenna array (Figure 1) and the  $S_{ij}$  denote the pertinent S-parameters. In Figure 5, the simulated return loss of one patch of each one of the three ULAs is indicated and, in correspondence to (1), the ISM band is completely covered for the three topologies. Figure 6 shows the mutual coupling level between the first and the second antenna element obtained for each of the three arrays and it is seen that (2) is satisfied. The lowest mutual coupling value, however, is obtained for the ULA with the tip-truncated ETMPA elements. Using this topology,  $|S_{12}|$  remains below -30 dB within the entire ISM band. This margin of 5 dB with respect to constraint (2) is necessary as Figure 6 is the result of a simulation, and it can be expected

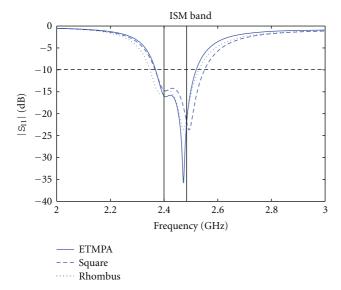


FIGURE 5: Simulated reflection coefficients of one port of the ULA array: tip-truncated ETMPA (full line), square ring patch (dashed line), and rhomboidal ring patch (dotted and dashed line).

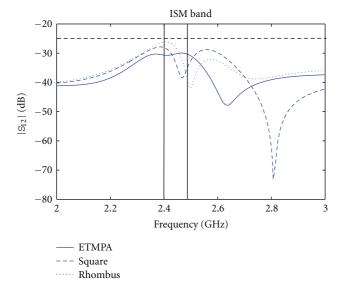


FIGURE 6: Simulated mutual coupling between the first and second port of the ULA array: tip-truncated ETMPA (full line), square ring patch (dashed line), and rhomboidal ring patch (dotted and dashed line).

that actual measured mutual coupling values of the manufactured array will be higher (see Section 3.4). Therefore, we proceed our study with ULAs consisting of tip-truncated ETMPA elements. The triangular patch, used as antenna element, not only guarantees low mutual coupling between adjacent elements, it also provides radiation characteristics similar to a rectangular microstrip antenna while occupying a smaller area. It is frequently used as a microstrip element, microstrip radiator or for array design on rigid substrates [17], but never before on a textile substrate. By cutting off

TABLE 2: Patch dimensions of the tip-truncated ETMPA on the Azzurri and cotton substrates, used as antenna elements in the array prototypes.

	Azzurri (mm)	Cotton (mm)
а	60.1	51.3
b	69	53
С	8	6.6
d	52.8	45.8
Xf	27.5	20.8
Yf	10	7.7

a triangle from one of the tips of the patch [18, 19], the size of the ETMPA was further reduced.

2.3. Antenna Array Design and Prototyping. The complete array was hand cut and glued. The four tip-truncated ETMPAs are fed by means of 50  $\Omega$  coaxial SMA connectors, which are manually soldered. To be able to study the stability of the array characteristics in different relative humidity conditions (Section 3), the optimal array topology is implemented on two different nonconductive textile substrates, having very different Moisture Regains (MR), that is, the above introduced polyurethane protective foam, "Azzurri," and a cotton fabric. The characteristics of the Azzurri foam are of course the ones presented in Section 2.2. The cotton substrate, composed of four thin layers of cotton fabric to provide a large enough bandwidth, has a total thickness of 2.27 mm and its dielectric characteristics are  $\epsilon_r = 1.94$  and  $\tan \delta = 0.02$ . Geometrical parameters of the patches are listed in Table 2 and indicated in Figure 2. Obviously, also for the implementation on cotton, the patch dimensions and choice of substrate material and thickness are chosen to satisfy (1) and (2). When deployed, both textile array implementations—on cotton and on Azzurri—result to be light weight, conformal to the body, and easy to bend.

2.4. Benefit of the Array in a Multipath Environment. It is now demonstrated that the above design choices indeed lead to more reliable off-body communication links. In a line-of-sight scenario in absence of multipath, the use of a vertical array is expected to provide 6 dB of array gain compared to a single textile patch, thanks to the confinement of the beam in elevation. In the receive case, an extra 6 dB of gain is obtained as the signal is received by the four antenna elements of the array. When deploying the array in a multipath environment, the beam confinement along the elevation direction will reduce the number of paths contributing to fading, and it is expected that fluctuations due to fading will be smaller compared to the single textile antenna case. This statement was validated by means of the ray tracer Winprop V7.40 of AWE Communications. We considered a wireless link in an office building of Ghent University, of which the floor plan is shown in Figure 7. A 2.45 GHz ISM band access point is located at one end of the corridor, being position C in Figure 7. A firefighter equipped with a textile antenna system as shown in Figure 1 walks

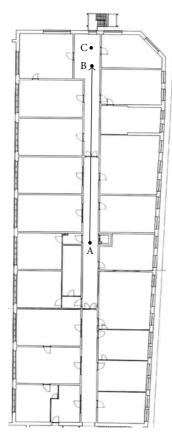
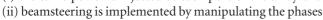


FIGURE 7: Plan of the indoor environment: the person wearing the firefighter jacket walks for 21 m from the position A to B, while the transmitting access point antenna is positioned in location C.

towards the access point from position A to position B, for a total distance of 21 m. Figure 8 displays the amplitudes of the signal received by a single textile patch and by the vertical textile array after beamforming, taking into account the antenna's gain patterns shown in Figures 12 and 13. This clearly demonstrates the benefits of beam confinement in elevation by the textile array. First, for the receive case, we clearly observe an array gain thanks to beamforming (Note that, for the transmit case, the full line will decrease by 6 dB, since the available power must be equally distributed over the four antenna elements). Second, the large fading dips seen in the dotted curve for the single textile antenna are clearly reduced by the narrow beam generated by the vertical array (full curve). Hence, both in outdoor and indoor scenarios, the proposed system will provide more reliable links than a single textile patch.

#### 3. Simulation and Measurements

To feed the array in the system, a commercially available conventional four-way power divider is used, attached to the array by means of four thin flexible coaxial cables containing four line stretchers, as shown in Figure 9, to guarantee that (i) the same power is injected at each port of the array and



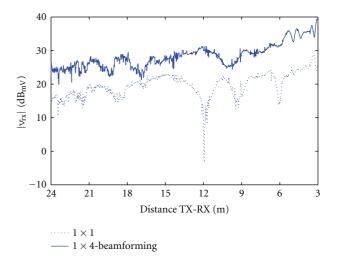


FIGURE 8: Amplitude of the signal received by the array after beamforming (full line) versus the amplitude of the signal received by a single patch antenna (dotted line), as a function of distance to the transmit antenna.

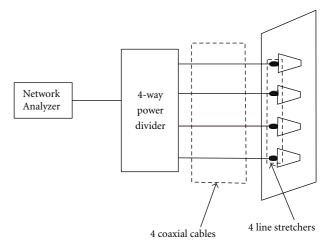


FIGURE 9: Entire antenna system, consisting of a four-way power divider, four cables, four line stretchers, and the textile antenna array.

of the line stretchers. We now evaluate the performance of the complete textile array system by means of simulations and measurements. The simulations are all performed using the 3D simulator CST Microwave Studio. First, the reflection coefficient of the array system is measured for varying rH conditions created in a controlled environment. Second, the array is placed in the anechoic chamber for the measurement of gain in free space and when being deployed on the human torso. Third, a comprehensive mutual coupling study is carried out when the antenna is in planar and bent state and while varying the rH conditions.

3.1. Reflection Coefficient Measurement under Varying Relative Humidity Conditions. Environmental changes, such as humidity, can influence the performance of textile antennas.

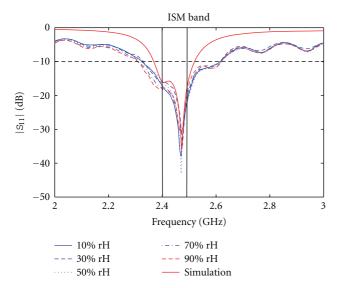


FIGURE 10: Array on Azzurri: reflection coefficients, simulation (full line) versus measurements (dashed line).

For example, as fire fighters are subjected to heat and heavy physical exertion, there is an increase of thermal sweating, substantially changing the rH. Therefore, in this paper, the influence of rH on the performance of the array system is studied. The choice of Azzurri foam and cotton fabric, as nonconductive antenna substrates, is made as these are textile materials characterized by a small and a large moisture regain (MR), respectively: MR of Azzurri is 1.7%, whereas the MR of cotton is 6.9%. To obtain reproducible and reliable measurements, the two implementations of the array were conditioned for 24 hours in a climate test cabinet (WK 350 from Weiss Technik) at a temperature of 23°C and the rH was varied each day. At the end of each day, they were taken out of the test cabinet, one by one, and immediately measured with an Agilent RF Network Analyzer placed in the nonanechoic lab environment where the climate test cabinet is located to prevent any possible change in the conditions of the antenna. Note that, to cover the complete ISM band, the required -10 dB impedance bandwidth of the antenna is 83.5 MHz in the [2.4–2.4835] GHz ISM band. The reflection coefficient of the entire antenna system, consisting of the four-way power divider, the four line stretchers, and the four coaxial cables (Figure 9), attached to the array implemented on either of the two substrates, were measured for an rH equal to 10%, 30%, 50%, 70%, and 90%. Figures 10 and 11 show the measured reflection coefficient of the array on Azzurri and on cotton, respectively, in comparison with the simulated reflection coefficient. The difference between simulated and measured results in Figures 10 and 11 stems from the losses that are present in the complete system. The insertion loss (IL) of the power divider is approximately 6 dB, the IL of each cable is 0.76 dB and the IL of each line stretcher is 0.2 dB. In the simulations, the IL of the cables and line stretchers were not considered. On the one hand, the antenna on Azzurri exhibits a very stable performance, fully covering the ISM band. On the other hand, for the

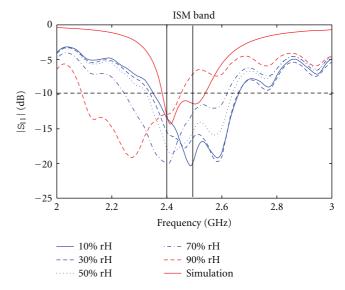


FIGURE 11: Array on cotton: reflection coefficients, simulation (full line) versus measurements (dashed line).

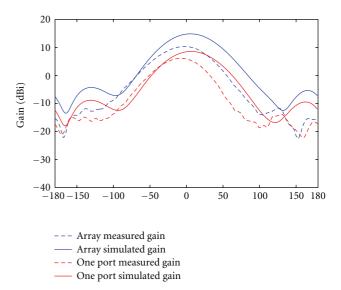


FIGURE 12: Array on Azzurri: gain pattern at 2.45 GHz, in the azimuth plane (yz-plane), simulation versus measurement of the entire array and of one single patch.

antenna on cotton, the resonance frequency decreases with increasing rH, and the ISM band is no longer covered when the rH is 90%. This is related to the MR value of the two nonconductive substrates: in fact, when choosing a textile material as a substrate for a textile antenna suitable for integration into garment, the MR value of the textile must be taken into account, as indicated in [20]. When varying the rH, the antenna efficiency of the array fabricated on Azzurri substrate remains nearly constant, whereas for the antenna elements of the array produced on the cotton substrate, the radiation efficiency decreases with increasing rH [21]. Predicting the change of the dielectric constant of substrates, due to changes in rH, and predicting the

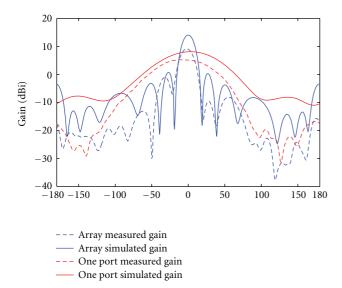


FIGURE 13: Array on Azzurri: gain pattern at 2.45 GHz, in the elevation plane (*xz*-plane), simulation versus measurement of the entire array and of one single patch.

variation of the thickness of the substrates, due to swelling of, for example, the cotton fibers, would be possible by using techniques described in [22]. However, in this paper, we opted to skip this step and to immediately implement two designs, validating directly the end results by means of reliable measurements in a controlled environment. Given the lack of stability in the reflection coefficient of the array on the cotton substrate under varying humidity conditions, we decided to continue the study for the textile array implemented on Azzurri foam only.

3.2. Free-Space Measurements. To check if the present array on Azzurri is a better solution in terms of gain with respect to the single patch antenna, we performed measurements and simulations comparing the configuration where the four ports are equally fed by the four-way power divider to the one where only one of the four patches is excited, while the other three patches are connected to a 50  $\Omega$  load. Figure 12 shows the gain pattern of the array at 2.45 GHz, in the azimuth plane (yz-plane). The array's simulated gain is 6 dB larger than the simulated gain of the single patch antenna. This is a predictable result because the array is a four-port array, gaining 6 dB with respect to the single patch. In reality, this value cannot be achieved. The entire system, as illustrated in Figure 9, encompasses different elements, such as line stretchers, cables, and a power divider, which generate losses that are hard to avoid. Consequently, the measured gain is 4 dB larger than the gain of a single patch antenna. The simulated gain pattern has the beam steered along  $\phi_m = 0^{\circ}$ , with  $\phi_m$  indicating the angle  $\phi$  in the yz-plane where the gain is maximum. The measured gain pattern exhibits a beam steered along  $\phi_m = -4^\circ$ . This deviation is due to the difficulty to position the entire antenna system (Figure 9) in the anechoic chamber for measurements. Nonetheless, this small positioning error does not result in major degradation of the

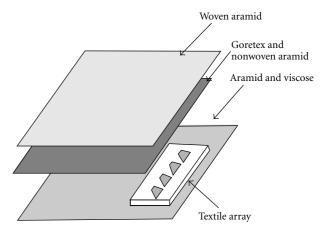


FIGURE 14: Antenna between textile layers composing the firefighter suit.

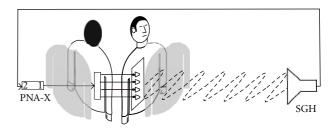


FIGURE 15: Entire antenna system placed on the human body: port 2 of the Agilent N5242A PNA-X Network Analyzer is connected to the Standard Gain Horn (SGH) and port 1 is connected to the 4-port power divider.

array performance, given the sufficiently large beamwidth of the array. Figure 13 shows the gain pattern of the array at 2.45 GHz in the elevation plane (*xz*-plane). The array's measured 3 dB beam width is equal to 18° and similar conclusions concerning the difference between measured and simulated gain, as for Figure 12, can be drawn.

3.3. On-Body Measurements. In real-life applications, the antenna is positioned vertically on the torso of the human body, to steer the beam poviding the maximum gain in a narrow angular sector in the broadside direction, where the base station is located. The array may be deployed in a firefighter jacket, whose composing textile layers are shown in Figure 14. The first layer on top of the array is a combined moisture and thermal barrier, made of Goretex and nonwoven aramid, and above it there is an outer shell fabric layer made out of woven aramid. Below the ground plane there is a third layer, composing the jacket liner, made out of aramid and viscose. The resulting effect on the gain was investigated by means of simulations, with the 3D simulator CST Microwave Studio, and by measurements.

During measurements, the layout shown in Figure 15 is adopted to place the entire antenna system on the human body: the array is integrated into the firefighter jacket, in front of the human torso, between the textile layers combined the suit. Four line stretchers are placed between the four SMA

	Antenna	
$\triangle$ Air gap d = 2 mm		
Skin 1 mm	$_{r} = 38$	= 1.46  S/m
Fat 3 mm	$_{\rm r} = 5.28$	$= 0.1 \mathrm{S/m}$
Muscle 18 mm	r = 52 72	= 1 73 S/m

FIGURE 16: The textile array is placed on top of the model of a human body used for the simulations [23]. The dielectric values of three different human tissues, at 2.45 GHz, are those reported in [24–26].

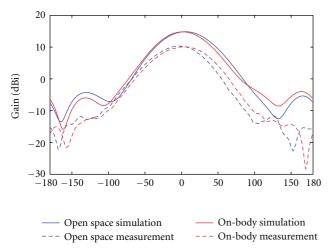


FIGURE 17: Gain pattern in the azimuth plane (*yz*-plane) at 2.45 GHz in open space and when the antenna is placed on-body in a firefighter jacket: simulations (full line) versus measurements (dashed line).

connectors and the four coaxial cables that are routed along the side of the chest to reach the back of the shoulder where the four-way power divider is located.

As for simulations, we rely on the model [23] depicted in Figure 16 to simulate the on-body situation: we use a thickness of 1 mm for the skin layer, 3 mm for the fat layer, and 18 mm for the muscle layer, together with the dielectric values of the three human tissues specified in Figure 16.

Figure 17 shows the simulated and measured gain patterns of the array in the azimuth plane (yz-plane) when located in free space and when deployed on the human body. The two situations present similar gain patterns, indicating that the presence of the body does not degrade the performance of the array. For the on-body case, we obtain a maximum simulated gain of 14.7 dBi versus 10.2 dBi of maximum measured gain. This should be compared to 14.8 dBi of simulated gain versus 10.3 dBi of measured gain

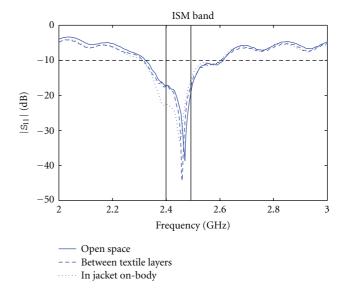


FIGURE 18: Measured reflection coefficients in three different situations: array in open space (full line), array placed between textile layers (dashed line), and array placed on-body in a firefighter jacket (dotted line).

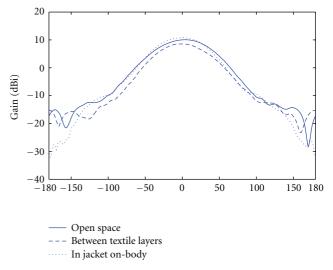


FIGURE 19: Measured gain pattern in the azimuth plane (*yz*-plane) at 2.45 GHz in three different situations: array in open space (full line), array placed between textile layers (dashed line), and array placed on-body in a firefighter jacket (dotted line).

in the free-space case. Note that, although here the pattern is steered along broadside, in the actual application, the steering capabilities of the array allow to adjust the direction of the main lobe.

Due to mechanical limitations of the measurement system in the anechoic chamber, on-body gain patterns in the elevation plane cannot be measured. Figures 18 and 19 show the measured reflection coefficient and the gain pattern in the azimuth plane (*yz*-plane), respectively, of the textile array in three situations: open space, placed between the textile layers shown in Figure 14, and integrated into the firefighter jacket

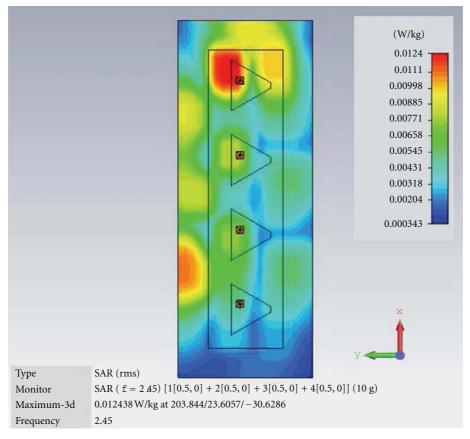


FIGURE 20: SAR distribution.

worn by a person. In all the three cases, the ISM band is fully covered and the gain patterns exhibit the same trend.

The human body has a very complex structure in terms of electrical parameters of each tissue, thus the energy of high frequency electromagnetic waves is absorbed by the human body with various intensity, depending on the part of the body and on the wave frequency. To analyze this problem and to guarantee that the antenna in this paper does not harm the person wearing it, the Specific Absorption Rate (SAR) is calculated, using the 3D simulator CST Microwave Studio, which computes the amount of energy absorbed by the human body. The human body model used for the simulations is shown in Figure 16. Figure 20 presents the SAR distribution in the xy-plane of the array at z=0 when the input power at each port is 0.5 W. The 10-g averaged SAR peak value is 0.0124 W/Kg. This value fulfills the ICNIRP [14] and FCC [15] guidelines for general public exposure.

3.4. Mutual Coupling Measurements . To assess the sensitivity of the mutual coupling in the array w.r.t. environmental conditions, more specifically, w.r.t. to changes in the relative humidity, two types of measurements are performed in a real nonanechoic lab environment after 24 h of conditioning in the climate test cabinet and the results are verified against the conditions (1) and (2): first, the reflection coefficient of each individual array element is measured, while terminating the other three elements with a 50  $\Omega$  load; second, the mutual

coupling between each pair of antenna elements is measured, while terminating the other two elements with a 50  $\Omega$  load. Figure 21(a) shows the measured reflection coefficient at port 1 of the array, and Figures 21(b), 21(c), and 21(d) show the mutual coupling between port 1 of the antenna array and the other three ports, setting rH to be 20%, 40%, 60%, and 80%. It is observed that the array is rather insensitive w.r.t. to environmental conditions, always satisfying (1). For the other antenna elements (ports 2–4) a similar behavior is observed. Thanks to the careful design, the mutual coupling between the individual radiators remains low enough and (2) is always satisfied. Similar characteristics are obtained for the other combinations of port pairs, being 2 and 3; 2 and 4; 3 and 4.

Next, the mutual coupling between each pair of ports of the array was measured when the array—in flat condition—is positioned in our anechoic chamber in three conditions, being in open space, between the textile layers composing the firefighter suit shown in Figure 14, and when it is fully integrated inside the firefighter jacket. Results are shown in Figures 22(a), 22(c), and 22(e). We note that, given the fact that the measurements are now performed in anechoic conditions, the mutual coupling levels are lower than the ones found in Figures 21(b), 21(c), 21(d) and that they vary little for the different setups. To verify the effects of bending on the mutual coupling between each pair of antenna elements, the array is bent around a plastic cylinder

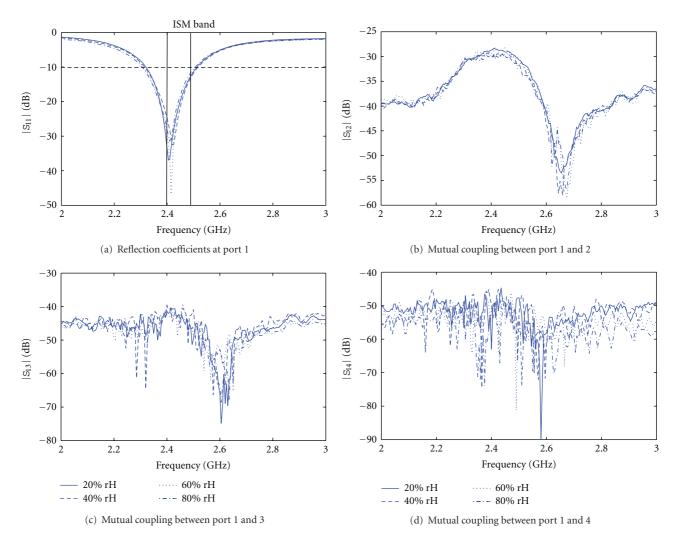


FIGURE 21: S-parameter measurements after acclimatization of the array, measured in a nonanechoic environment: reflection coefficients at port 1 of the array and mutual coupling between port 1 of the array and the other three ports.

with a diameter of 15 cm, oriented vertically, that is, along the *y*-axis, representing an extreme case where the array is bent around an arm. The mutual coupling was measured when the array is in open space and between the textile layers, composing the firefighter suit, shown in Figure 14. It is found that mutual coupling is not significantly affected by bending the textile array. Finally, we observe that both in planar and bent state, (2) is always satisfied. Similar characteristics are obtained for the other combinations of port pairs, that is, 2 and 3; 2 and 4; 3 and 4.

## 4. Conclusion

The design, manufacturing, and measurements were discussed of a wearable system composed of a four-way power divider and line stretchers interconnecting a four-element ULA textile array consisting of tip-truncated ETMPAs implemented on two different nonconductive textile substrates, that is, cotton fabric and Azzurri foam, operating in the 2.45 GHz ISM band. Thanks to the exclusive use of isolating

and conductive textiles, the array is breathable, flexible and may be fully integrated into garments, worn by rescue workers or fire fighters, active in a disaster area. The array should be placed vertically on the human torso, to steer the beam providing the maximum gain in elevation angle within a narrow angular sector around the broadside direction, ensuring that the main beam points towards the base station. Thereto, a four-patch ULA was chosen with a relatively large spacing between the individual elements. This leads to a lowcost design with a large antenna aperture and low mutual coupling between the patches, allowing easy steering. The narrow antenna beam also results in less fading and, hence, reliable communication. Under reproducible rH conditions, realized in the climate test cabinet, measurements of the reflection coefficient of the array system were performed: the implementation of the array on Azzurri foam exhibits perfectly stable characteristics. For the implementation on cotton, however, the resonance frequency decreases with increasing rH, and the ISM band is no longer covered when the rH is 90%. Hence, when choosing a textile material as

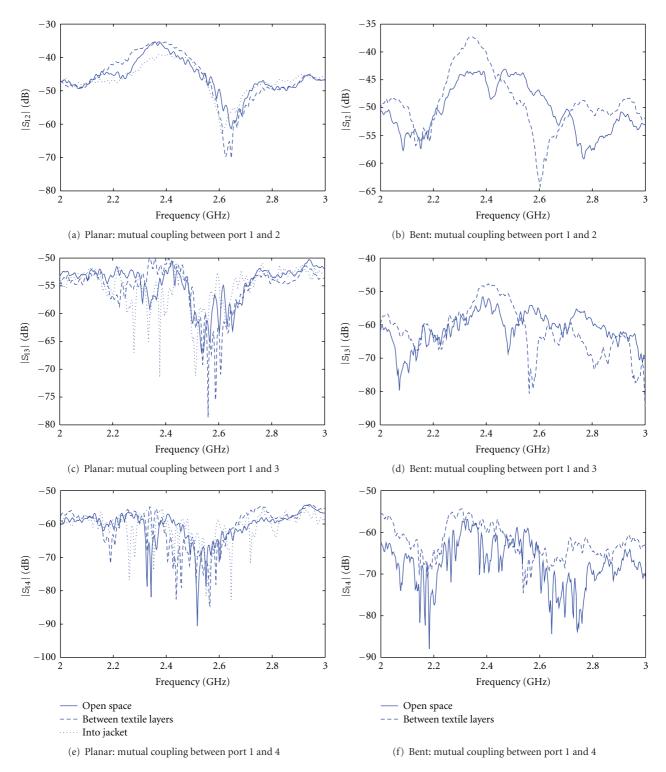


FIGURE 22: Mutual coupling between port 1 of the array and the other three ports, when the array is in planar and bent state.

a substrate for a textile antenna array to integrate into a garment, the MR value of the textile material must be taken into account. Consequently, a comprehensive study of the performance of the array system was carried out for the textile implementation on the Azzurri foam substrate only. Measurements of the reflection coefficient in the 2.45 GHz

ISM band demonstrate a large bandwidth, providing full coverage of the ISM band, both when the array system is operating in free space and when it is deployed on a human body. Simulations and measurements of the gain patterns in free space and on-body show very good correspondence, demonstrating that the human body does not degrade the

performance of the textile antenna system. Injecting an input power of 0.5 W at each port of the array, the calculated SAR values averaged in 10-g tissue show that the textile antenna array respects the ICNIRP and FCC guidelines for general public exposure. Next, the mutual coupling between the four ports of the array was measured for varying rH levels, to check the sensitivity of the array to environmental changes. Moreover, a careful study of the mutual coupling between the four ports of the array was carried out with the array in planar and bent state, for different setups: in open space, between textile layers composing the firefighter suit, and inside the firefighter jacket. Thanks to the ETMPA topology of the individual patches and the rather large spacing of  $3/4\lambda$  between them, the mutual coupling is always low.

In summary, thanks to a careful design and a thorough study of mutual coupling effects, we managed to present a low-cost textile antenna array system functioning in the 2.45 GHz ISM band, with low-cost steering capabilities, significantly higher gain than a single patch antenna, tolerant to being placed on the body and resistant to environmental changes, and resulting in reliable off-body communication links thanks to reduced fading.

#### References

- [1] M. Klemm, I. Locher, and G. Tröster, "A novel circularly polarized textile antenna for wearable applications," in *Proceedings of the 7th European Microwave Week*, pp. 137–140, October 2004.
- [2] P. Salonen and H. Hurme, "A novel fabric WLAN antenna for wearable applications," in *Proceedings of the IEEE Antennas and Propagation Society International Symposium*, pp. 700–703, June 2003.
- [3] E. K. Kaivanto, M. Berg, E. Salonen, and P. de Maagt, "Wearable circularly polarized antenna for personal satellite communication and navigation," *IEEE Transactions on Antennas and Propagation*, vol. 59, no. 12, pp. 4490–4496, 2011.
- [4] G.-Y. Lee, D. Psychoudakis, C.-C. Chen, and J. L. Volakis, "Omnidirectional vest-mounted body-worn antenna system for UHF operation," *IEEE Antennas and Wireless Propagation Letters*, vol. 10, pp. 581–583, 2011.
- [5] C. Hertleer, A. Tronquo, H. Rogier, and L. Van Langenhove, "The use of textile materials to design wearable microstrip patch antennas," *Textile Research Journal*, vol. 78, no. 8, pp. 651–658, 2008.
- [6] C. Hertleer, H. Rogier, L. Vallozzi, and L. Van Langenhove, "A textile antenna for off-body communication integrated into protective clothing for firefighters," *IEEE Transactions on Antennas and Propagation*, vol. 57, no. 4, pp. 919–925, 2009.
- [7] J. Vicente and A. A. Moreira, "Electro-textile printed slot antenna over finite EBG structure," in *International Workshop on Antenna Technology (iWAT '10)*, pp. 1–4, March 2010.
- [8] Q. Bai and R. Langley, "Wearable EBG antenna bending and crumpling," in *Proceedings of the Loughborough Antennas and Propagation Conference (LAPC '09)*, pp. 201–204, Loughborough, UK, November 2009.
- [9] L. Vallozzi, P. Van Torre, C. Hertleer, H. Rogier, M. Moeneclaey, and J. Verhaevert, "Wireless communication for firefighters using dual-polarized textile antennas integrated in their garment," *IEEE Transactions on Antennas and Propagation*, vol. 58, no. 4, pp. 1357–1368, 2010.

- [10] L. Vallozzi and H. Rogier, "Radiation characteristics of a textile antenna designed for apparel application," in *Proceedings of the IEEE Symposium for Space Applications of Wireless and RFID* (SWIRF '07), May 2007.
- [11] S. Zhu and R. Langley, "Dual-band wearable textile antenna on an EBG substrate," *IEEE Transactions on Antennas and Propagation*, vol. 57, no. 4, pp. 926–935, 2009.
- [12] C. Du, S. Zhong, L. Yao, and Y. Qiu, "Textile microstrip array antenna on three-dimensional orthogonal woven composite," in *Proceedings of the 4th European Conference on Antennas and Propagation (EuCAP '10)*, pp. 1–2, April 2010.
- [13] C. Du, S. Zhong, L. Yao, and Y. Qiu, "Textile microstrip twoelement array antenna on 3D orthogonal woven composite," in *Proceedings of the International Symposium on Signals, Sys*tems and Electronics (ISSSE '10), vol. 2, pp. 1–2, September 2010.
- [14] ICNIRP, "Guidelines for limiting exposure to time-varying electric, magnetic, and electromagnetic fields," *Health Physics*, vol. 74, no. 4, pp. 494–522, 1998.
- [15] FCC, "Evaluating Compliance with FCC Guidelines for Human Exposure to Radiofrequency Electromagnetic Fields," Supplement C to OET Bulletin 65, Washington, DC, USA, 2001.
- [16] http://www.lioninternational.fr/index.php.
- [17] Y. Siddiqui Jawad and G. Debatosh, "Applications of triangular microstrip patch: circuit elements to modern wireless antennas," *Mikrotalasna Revija*, vol. 13, no. 1, pp. 8–11, 2007.
- [18] S. Sadat Karimabadi, Y. Mohsenzadeh, A. Reza Attari, and S. Mahdi, "Bandwidth enhancement of single-feed circularly polarized equilateral triangular microstrip antenna," in *Proceedings of the Progress in Electromagnetic Research Symposium*, pp. 147–150, Hangzhou, China, March 2008.
- [19] C. Tang, J. Lu, and K. Wong, "Circularly polarised equilateraltriangular microstrip antenna with truncated tip," *Electronics Letters*, vol. 34, no. 13, pp. 1277–1278, 1998.
- [20] C. Hertleer, A. Van Laere, H. Rogier, and L. Van Langenhove, "Influence of relative humidity on textile antenna performance," *Textile Research Journal*, vol. 80, no. 2, pp. 177–183, 2010
- [21] F. Declercq, Characterization and design strategies for active textile antennas [Ph.D. thesis], Ghent University, 2011.
- [22] F. Declercq, I. Couckuyt, H. Rogier, and T. Dhaene, "Complex permittivity characterization of textile materials by means of surrogate modelling," in *Proceedings of the IEEE International* Symposium Antennas and Propagation and CNCUSNC/ URSI Radio Science Meeting, July 2010.
- [23] M. Klemm, I. Z. Kovcs, G. F. Pedersen, and G. Troster, "Novel small-size directional antenna for UWB WBAN/WPAN applications," *IEEE Transactions on Antennas and Propagation*, vol. 53, no. 12, pp. 3884–3896, 2005.
- [24] C. Gabriel, S. Gabriel, and E. Corthout, "The dielectric properties of biological tissues: I. Literature survey," *Physics in Medicine and Biology*, vol. 41, no. 11, pp. 2231–2249, 1996.
- [25] S. Gabriel, R. W. Lau, and C. Gabriel, "The dielectric properties of biological tissues: II. Measurements in the frequency range 10 Hz to 20 GHz," *Physics in Medicine and Biology*, vol. 41, no. 11, pp. 2251–2269, 1996.
- [26] C. Gabriel, S. Gabriel, and E. Corthout, "The dielectric properties of biological tissues: III. Parametric models for the dielectric spectrum of tissues," *Physics in Medicine and Biology*, vol. 41, no. 11, pp. 2271–2293, 1996.

Hindawi Publishing Corporation International Journal of Antennas and Propagation Volume 2012, Article ID 251682, 12 pages doi:10.1155/2012/251682

## Research Article

## **Textile UWB Antenna Bending and Wet Performances**

## Mai A. R. Osman, M. K. A. Rahim, N. A. Samsuri, M. K. Elbasheer, and M. E. Ali<sup>3</sup>

- <sup>1</sup>Radio Communication Engineering Department (RaCED), Faculty of Electrical Engineering, Universiti Teknologi Malaysia, 81310 Johor, Malaysia
- <sup>2</sup> Mechanical Engineering Department, Faculty of Engineering, Sudan University of Science and Technology, Khartoum 407-111, Sudan <sup>3</sup> Electronic and Electrical Engineering Department, School of Engineering and Built Environment, Edinburgh Napier University, Merchiston Campus, EH10 5DT Edinburgh, UK

Correspondence should be addressed to Mai A. R. Osman, mayoya78@gmail.com

Received 15 November 2011; Revised 11 February 2012; Accepted 7 March 2012

Academic Editor: Hendrik Rogier

Copyright © 2012 Mai A. R. Osman et al. This is an open access article distributed under the Creative Commons Attribution License, which permits unrestricted use, distribution, and reproduction in any medium, provided the original work is properly cited.

The vision and ideas of wearable computing systems describe future electronic systems as an integral part of our everyday clothing that provides the wearer with such intelligent personal assistants. Recently, there has been growing interest in the antenna community to merge between wearable systems technology, ultrawideband (UWB) technology and textile technology. This work aimed to make closer steps towards real wearability by investigating the possibilities of designing wearable UWB antenna where textile materials are used for the substrate as well as the conducting parts of the designed antenna. Two types of conducting materials have been used for conducting parts, while a nonconducting fabric has been used as antenna substrate material. A set of comparative results of the proposed design were presented and discussed. Moreover, effects on the return loss by means of measurements for each fabricated antenna prototype under bent and fully wet conditions were discussed in more details.

## 1. Introduction

Portable electronic devices have become part of everyday human life acting as mobile phones that are quite often carried throughout the day and allow not just telephone calls alone but also provide internet access, multimedia, and personal digital assistant. This form of "always on" and constantly connected status can be considered as a step towards the pervasive computing paradigm. According to that, extensive worldwide research has been carried out on new wearable devices where wearable computers will be capable to perform as ancestors to smart clothes. In that sense, smart clothes will ensure the ability of wearable devices to escape from the confines of the rigid box and hence merge with textile technology. This kind of incorporation of antennas into uniform will add the benefit of eliminating clumsy devices that can be entangled to some extent [1-3]. However, as technologies advances, new and a vast number

of potential applications emerged, such as: wireless transactions, general network connections, navigation support, location-based services, tourism, security, emergency, child protection, intelligent transportation system, military applications, smart suits, backpack radar, battlefield personnel care, medical monitoring, smart diagnosis, aging care, biosensors, space applications, and astronaut monitoring.

On the other hand, the key considerations for wearable electronics are to be lightweight, flexible, small size, inexpensive, able to withstand damage from obstacles (robust), and comfortable to wear [4–6]. Since the Federal Communications Commission (FCC) in 2002 approved the commercial use of frequency bands from 3.1 to 10.6 GHz for Ultrawideband(UWB) systems, UWB antennas received more and more attention with the advancement of communication technology [7–9]. The attractive features of UWB antennas, such as low profile, low cost, and radiation properties, do not need to transmit a high-power signal to the receiver, can

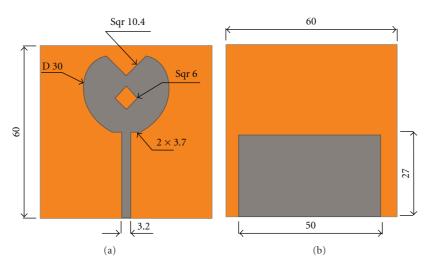


FIGURE 1: CST model along with the geometry and dimensions in millimetre of the current paper design; (a) front view and (b) back view of the proposed antenna design.

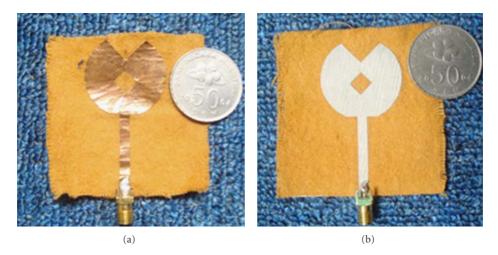


FIGURE 2: The fabricated wearable UWB antenna prototypes using flannel fabric with: (a) copper conducting sheet, (b) Shieldit conducting fabric.

have a longer battery life, and the compact size enhanced the possibilities of reducing the wearable devices size and therefore ease the fabrication process [9, 10].

Since 1997, wearable telecommunication systems have become popular topics in research institutions. Numerous papers have been published about the design, fabrication and applications of wearable antennas and systems. Some of these developments are highlighted below. Several researches have taken quantum leaps in utilizing textile materials as antenna substrate [10–12]. Wearable antennas have been developed in the form of flexible metal patches on textile substrates [13–15]. A dual-band wearable antenna was discussed in detail [16, 17]. Furthermore, another investigation of using electrotextile materials for designing microstrip patch antenna as well as UWB antenna were reported in [18, 19]. In addition, UWB sensors and their suitability for medical applications were also considered [20–22]. With all these mentioned findings, markets opened up to a wide range of potential

requirements and investigations for these novel materials considering UWB antenna designs and applications. Consistent with all these facts mentioned above, authors of the current paper aimed to make closer steps towards real wearability. Moreover, full success can be achieved only when the antenna and all related components are entirely converted into 100% textile materials where the use of embedded textile components guarantees washing of the electronic suit and accordingly reuse of it. In this work, a fully textile UWB antenna is presented with detailed discussion about the concept, simulation, as well as manufacturing process. Two types of conducting materials have been used for conducting parts, while a nonconducting fabric has been used as antenna substrate material. In the following sections, materials that have been used to accomplish the wearable antenna design, successive design steps, and a set of comparative results of the proposed design shall be presented. Moreover, effects on the return loss by means of

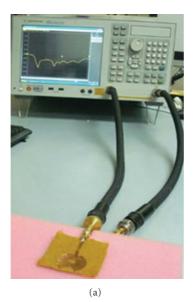




Figure 3: Snapshot of ( $|S_{11}|$ ) measurement environment of both antenna prototypes using (a) copper conducting tape and (b) Shieldit conducting fabric.

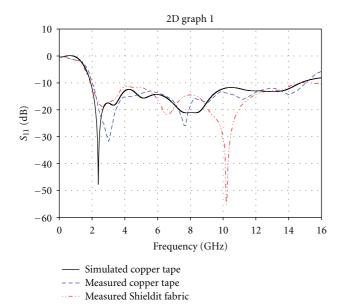


Figure 4: Comparison between simulated and measured ( $|S_{11}|$ ) results of the proposed wearable textile UWB antenna design.

measurements for each fabricated antenna prototype under bent and fully wet conditions will be discussed in more details.

## 2. Material Selection

The most important properties of textile materials that are mobilized in wearable applications are flexibility to conform to the body, comfort to touch, and softness. Applications also need to be cost-effective, widely available, allow easy interpretation, and provide consistent results. The terms textile

and fabric antenna are used interchangeably here. However, in most cases, textile antenna refers to an antenna, whereas the term fabric relates to the substrate material. In this paper, a fully textile UWB wearable antenna is designed and analyzed. The proposed antenna designs are made from flannel fabric substrate material along with two types of conducting materials that will be discussed in more details in the following sections.

2.1. Substrate Material. For flexible antennas, textile materials form interesting substrates because fabric antennas can be easily integrated into clothes. Textile materials generally have a very low dielectric constant which reduces surface wave losses and improves antenna's impedance bandwidth [19, 20]. In this work, our study focuses on using flannel fabric as substrate material. Flannel fabric is a kind of 100% cotton material with smooth, firm, and fluffy surface that made the fabric suitable for wearable applications. Moreover, fabric substrate material features might aid in maintaining the distance to remain constant between the radiating patch and the ground plane in order to control antenna's electrical characteristics. In fact, the smooth and firm surface of fabric substrate material is required to allow conductive sheets to be fastened evenly and stoutly on fabric surface. If the copper sheet detaches merely from one corner and the space between the metal layers varies, the resonant frequency of the proposed antenna changes. The thickness of this fabric is almost 1 mm, but in order to characterize the effect of textile materials accurately, it is important to know its relative permittivity. Thus, using the commercial dielectric probe (reflected method), the measured relative permittivity of flannel fabric covering the frequency range from 300 MHz up to 20 GHz is approximately 1.7 while the loss tangent is about 0.025.

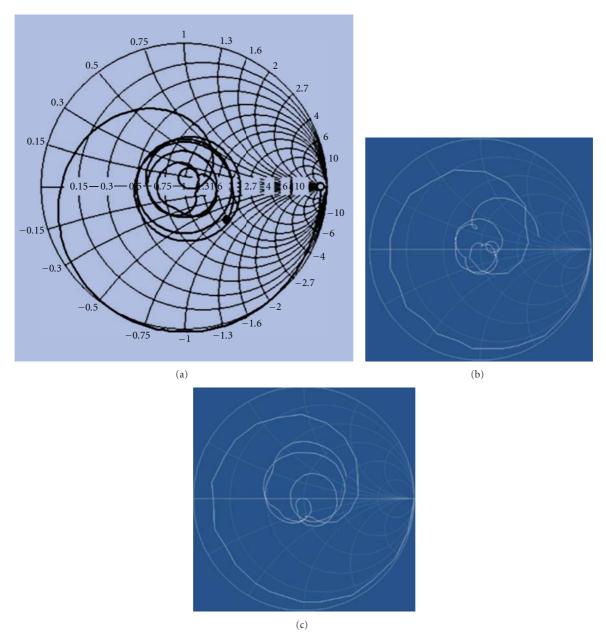


FIGURE 5: Comparison between simulated and measured results of the input impedance locus using smith chart. (a) Simulated antenna using copper conducting sheet, (b) measured results of copper conducting sheet, and (c) measured results of Shieldit conducting fabric.

2.2. Conducting Materials. A systematic study was demonstrated using two types of conducting materials. Firstly, copper conducting sheet with a thickness of 0.03 mm is used in UWB antenna design and numerical analyses for the sake of preliminary design investigation. After that, another type of conducting material (Shieldit conducting fabric) with a thickness of 0.17 mm is proposed for investigation. The proposed conducting material which is so called "electrotextile material" seems to be most suitable and convenient for textile wearable antenna applications when compared with the unfeasible features of copper conducting sheet (not possible to be washed, not attractive to the wearer, unable to withstand multiple deformation processes, etc.).

Shieldit conducting fabric is made from strong polyester substrate that is plated with nickel and copper, hence it can perform as high quality flame retardant fabric. The fabric is coated on one side with nonconductive hot melt adhesive which make the attachment process easier by ironing the conducting fabric on to the surface of flannel fabric substrate material. The proposed conducting fabric can be washed as well as its ability to resist temperature up to 200°C.

## 3. Design Consideration

In general, the design and construction of the UWB planer monopole antenna consist of a circular parch to be placed at

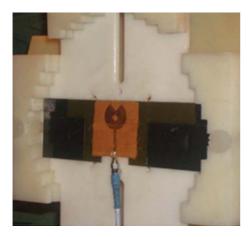


FIGURE 6: Snapshot of measured radiation pattern environment of the UWB textile antenna using copper conducting sheet.

the top of flannel fabric substrate material—a microstrip feed line and a partial ground plane beneath the fabric substrate material. At the starting point in designing UWB fabric antenna, the main patch is initially calculated using (1) below in order to create circular patch at the centre frequency of the UWB spectrum at 7.85 GHz. Where a is the radius of the circular patch antenna in millimetre,  $f_r$  is the resonance frequency in GHz, and  $\varepsilon_r$  is the relative permittivity of the textile substrate material:

$$a = \frac{87.94}{f_r \sqrt{\varepsilon_r}}. (1)$$

The transmission line feeding technique is introduced in order to connect the main radiating circular patch to the  $50 \Omega$  Sub Miniature Version (SMA) connector. Moreover, the partial ground plane was implemented for the proposed antenna design; hence such types of truncated ground plane play an important role in broadband and wideband characteristics of the designed antennas. In particular, the process of ground plane truncation acts as an impedance matching element that controls the impedance bandwidth of the circular patch. Thus, it creates a capacitive load that neutralizes the inductive nature of the patch to produce nearly pure resistive input impedance. According to that, ground plane truncation is achieved by slicing the top portion of the ground plane that covers the radiating patch element to less than half and covers the transmission line section only.

Using CST microwave office software simulation package, the UWB fabric antenna design with copper conducting sheet was initially proposed and numerically analyzed based on the characterization information of flannel fabric substrate material mentioned before. On the contrary, no numerical analysis has been performed for the UWB antenna using Shieldit fabric due to software limitation which allows the setting of copper conducting material only. For further optimizations, one slit at the top of the circular patch and two slits at the bottom of both sides of the main radiating patch are introduced. In addition, a rotated square hole (slot) at the centre of the circular patch is also needed to fine tune

the impedance bandwidth at certain frequencies. Thus, with the incorporation of these slits and even the centre slot, the impedance bandwidth throughout the spectrum of the UWB antenna frequencies is well-matched below the level of  $-10 \, \mathrm{dB}$ . A 50 ohm microstrip feed line was provided for the antenna feed; hence the position was determined according to [23, 24].

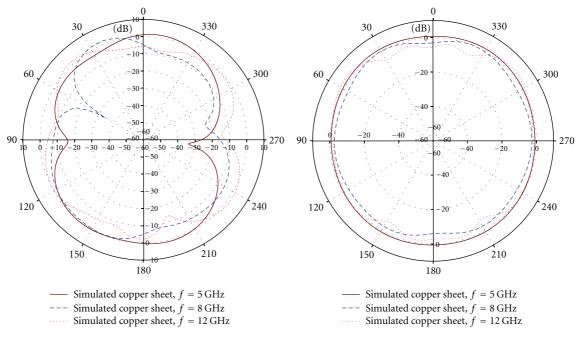
Pursuing the simulation process, both UWB antenna prototypes are fabricated utilizing copper conducting sheet for the first antenna prototype and Shieldit conducting fabric for the second antenna prototype. Figure 1 below demonstrates the CST model along with the geometry and dimensions in millimetre of the current paper design after optimization considering that the design of this antenna has been conducted in air space. The size of the substrate is set to  $60 \text{ mm} \times 60 \text{ mm}$  while the patch radius is set to 15 mm for both proposed and fabricated antenna prototypes and the ground plane size is set to  $50 \text{ mm} \times 27 \text{ mm}$ . Yet, all these dimensions are shown in Figure 1. Measured results of both fabricated prototypes are compared with the simulated results of copper conducting sheet antenna design.

## 4. Textile Antenna Fabrication

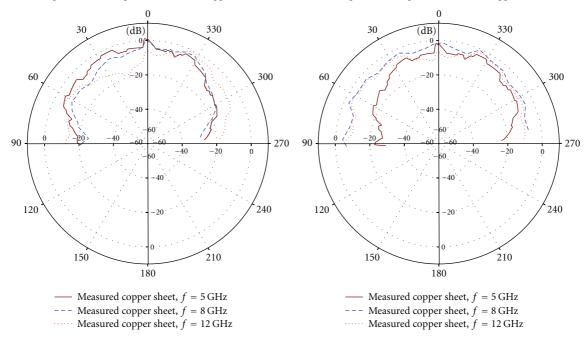
Fabrication process of the wearable textile UWB antenna has been achieved using flannel fabric as substrate material. The copper conducting sheet and Shieldit conducting fabric are used as the conducting materials for the radiating element (front side). However, the ground metal (back side) of both antenna prototypes is made from copper conducting sheet in order to study the effect of conducting materials in more comparable and accurate manner. Moreover, direct metal soldering is used to connect the feed line of the top radiating patch and the ground plane to the SMA coaxial connector in both fabricated antenna prototypes as illustrated in Figure 2. On the other hand, the process of cutting both types of conducting materials turns out to be very critical, hence only a simple cutting tool (scalpel) is used. Thus, the process of making conducting materials edges precise and accurate was essential. On the contrary, the attachment process of both types of conducting materials seemed to be easy, hence the copper conducting sheet which is backed by selfadhesive has been pressed easily and nicely over flannel fabric substrate material. Besides that, Shieldit conducting fabric that is coated on one side with a nonconductive hot melt adhesive has been attached to flannel fabric by ironing and pressing it firmly and easily. Thus, both types of conducting materials turned out to be good solutions as both have been evenly placed and fastened over flannel fabric substrate material. Figures 2(a) and 2(b) demonstrate the fabricated antenna prototypes using copper conducting sheet and Shieldit conducting fabric, respectively.

#### 5. Results and Discussions

In order to provide better investigation, this section shall firstly present the simulated and measured reflection coefficient  $(|S_{11}|)$  and bandwidth results of the UWB antenna



- (a) E-Co polar horizontal plane of simulated copper sheet results.
- (b) E-Co polar vertical plane of simulated copper sheet results.



- (c) E-Co polar horizontal plane of measured copper sheet results.
- (d) E-Co polar vertical plane of measured copper sheet results.

FIGURE 7: The behaviour of simulated and measured 2D radiation pattern results of the wearable textile UWB antenna design using copper conducting sheet considering three different selected frequency samples that represent the overall achieved bandwidth.

design and then briefly discuss and compare between measured results obtained by both antenna prototypes. After that, simulated and measured radiation patterns results will be considered and briefly discussed. Moreover, effects on the return loss by means of measurements on each fabricated antenna prototype under bent and fully wet conditions will be addressed at the end of this section. 5.1. Simulated and Measured Return Loss Results. The wearable textile UWB antenna simulated design produced good impedance matching with reflection coefficient being below –10 dB. The bandwidth expands from the lower frequency of 2 GHz till the upper frequency of 15 GHz and thus resulted in BW of 7.5% over the intended UWB frequency range. According to that, a network analyzer was used to

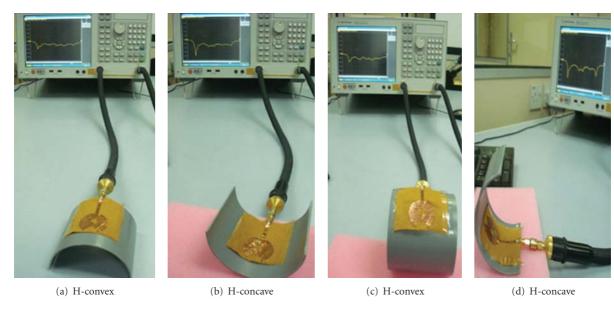


FIGURE 8: Snapshots of measurement environment of UWB antenna prototype using copper conducting sheet.

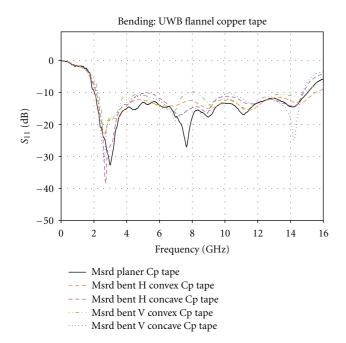


Figure 9: Measured ( $|S_{11}|$ ) bending results of UWB antenna prototype using copper conducting sheet.

measure the return loss of both antenna prototypes as a function of frequency. Figure 3 demonstrates snapshots of ( $|S_{11}|$ ) measurement environment of the current paper antenna prototypes, while Figure 4 made a clear verification and comparison between simulated ( $|S_{11}|$ ) results of copper conducting sheet antenna design and measured ( $|S_{11}|$ ) results of both antenna prototypes considering each type of conducting material.

The black solid line demonstrates the simulated ( $|S_{11}|$ ) and bandwidth results of the UWB antenna design using copper conducting sheet, while the blue long dashed line shows the measured ( $|S_{11}|$ ) and bandwidth results of the antenna prototype with copper conducting sheet as well. Moreover, the red dash-dotted line shows the measured return loss and bandwidth results of the UWB antenna prototype utilizing Shieldit conducting fabric.

Although the slight deviation between the presented results, Figure 4 exhibited that ( $|S_{11}|$ ) results were comparable; hence each of the proposed antenna design achieved more than 12 GHz BW within the UWB intended frequency range. Moreover, All UWB antenna prototypes maintained return loss results below the level of 10 dB with an acceptable and reasonable variation in resonance frequencies depths due to fabrication and measurement tolerances as well as the variation in conductivity related to each conducting material involved in the current investigation. Results indicated that the measured values of flannel fabric dielectric properties were valid enough to provide design information, since the targeted UWB range of frequency is reasonably well met and hence produced comparable measured results.

In addition, Figure 5 expresses the comparison between simulated and measured results of the input impedance locus using smith chart. Figure 5(a) represents the simulated results of the antenna prototype using copper conducting sheet where several loops can be observed on the smith chart within the VSWR = 2 circles. Conveniently, these loops correspond to locations on smith chart where the antenna's impedance locus crosses the real axis and hence indicated that resonance frequencies are those at which the input impedance is purely real. Similar performances have been achieved for the input impedance measured results for the fabricated antennas utilizing copper conducting sheet, and Shieldit conducting fabric as shown

in Figures 5(b) and 5(c), respectively. Although the slight deviations between simulated and measured results are visible to some extent, Figure 5 exhibited that all fabricated antennas input impedance results were comparable.

5.2. Simulated and Measured Radiation Pattern Results. Although the limitation of measurement equipments used, the behaviour of 2D simulated and measured radiation pattern components of UWB antenna using copper conducting sheet only is presented, measured and discussed. A snapshot of measured, radiation pattern environment is depicted in Figure 6 where the antenna is located in an anechoic chamber. Furthermore, Figure 7 clarifies the 2D simulated and measured copolar radiation pattern components in the horizontal and vertical planes with three different frequency samples at 5 GHz, 8 GHz, and 12 GHz achieved by copper conducting sheet UWB antenna design of the current paper, where measurement process has been conducted in air space. However, for the sake of better comparison, the measured radiation pattern results were plotted in the range between  $-90^{\circ}$  and  $+90^{\circ}$ . Moreover, the magnitude of the radiation pattern has been normalized to simplify the viewing of measured results.

Figures 7(a) and 7(b) represent the simulated horizontal and vertical planes copolar radiation pattern components respectively of UWB antenna design using copper conducting sheet. On the other hand, the measured copolar radiation pattern components of the fabricated antenna prototype using copper conducting sheet representing the horizontal and vertical planes respectively are demonstrated in Figures 7(c) and 7(d).

From Figures 7(a) and 7(b), it can be noticed that the antenna resembles omnidirectional radiation pattern components in the vertical plane whatever the frequency under analysis, while two nulls are visible along the horizontal plane for each frequency under analysis. Moreover, from Figures 7(c) and 7(d), one can observe the slight difference between simulated and measured radiation pattern results in the horizontal and vertical planes. This slight difference can be related to fabrication tolerance and misalignment during measurement setup. However, both results correlate well to each other hence the patterns are similar. Although the other antenna prototype using Shieldit conducting fabric was not measured due to limitations in measurement equipments, the expectation of producing omni directional radiation pattern are high. Thus, these results claimed that future antenna designers need to ensure that wearable telecommunication devices operate properly in the vicinity of human body. In particular, even though UWB antennas known by its lowpower operation and extremely low radiated power, special attention must be paid to the specific absorption rate (SAR) in order to avoid harm to human body.

5.3. Simulated Gain and Efficiency Results. The variations of frequencies versus the gain of the wearable textile UWB antenna design are all demonstrated in Table 1. The maximum gain achieved was about 4.8 dB at 10 GHz. In contrast, the highest percentage of efficiency reached 95% at 6 GHz

Table 1: Gain and efficiency simulated results of textile uwb antenna design.

Frequency (GHz)	Gain (dB)	Efficiency (%)
2	2.6	92
3	3.6	93
4	3.0	93
5	2.8	94
6	3.4	95
7	4.2	94
8	4.0	92
9	4.2	95
10	4.8	91
11	4.3	89
12	3.9	91
13	4.0	92
14	4.0	91
15	4.0	85

and 9 GHz. However, the lowest efficiency was about 85% at 15 GHz. Consequently, results showed that this present paper design has low power consumption due to the achievement of gain results that was less than 5 dB in most range of frequencies between 3 GHz and 15 GHz. In addition, the efficiency of the antenna could be considered vast compared to commercial antennas.

5.4. Effects of Antenna Bending on Measured Return Loss. In a realistic on-body application, the antenna is supposed to be integrated into a suit, and accordingly it will be subject to bending and wetness. Therefore, the effects of bending by means of measurements on both proposed UWB antenna prototypes are investigated. Both antenna prototypes are tested on polystyrene cylinder with a diameter of 80 mm that corresponds approximately to the typical size of human adult arm. Moreover, each antenna is studied in conventional planer form (as discussed previously) and at four bending positions: horizontal convex, horizontal concave, vertical convex, and vertical concave. Figure 8 demonstrates snapshots of measurement environment of UWB antenna prototype using copper conducting sheet, while Figure 9 illustrates measured (|S<sub>11</sub>|) bending results of copper sheet antenna prototype.

The impedance performances of UWB antenna with copper sheet considering all bent positions are nearly the same with slight fluctuations in return loss when compared with measured planer position. According to that, results indicated that UWB antenna with copper conducting sheet functions satisfactorily under most bending conditions. However, further investigations need to be performed in order to study the effect of severe bending angles as well as crumbling effect on antenna performances.

On the other hand, similar investigations have been performed on the UWB antenna prototype using Shieldit conducting fabric. Figure 10 demonstrates snapshots of

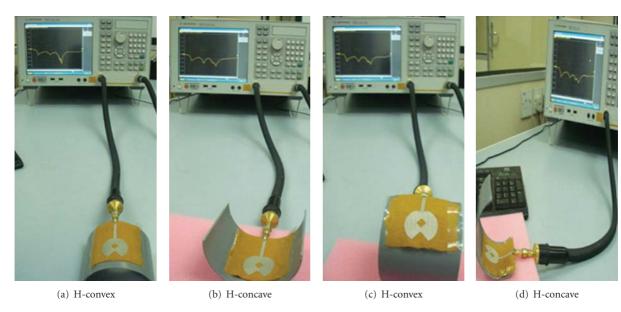


FIGURE 10: Snapshots of measurement environment of UWB antenna prototype using Shieldit conducting fabric.

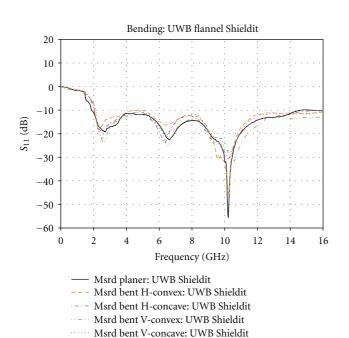


FIGURE 11: Measured ( $|S_{11}|$ ) bending results of UWB antenna prototype using Shieldit conducting fabric.

measurement environment of UWB antenna prototype using Shieldit conducting fabric, while Figure 11 illustrates the measured bending results of Shieldit conducting fabric antenna prototype. The impedance performances of UWB antenna with Shieldit conducting fabric considering all bent positions are almost identical with slight fluctuations in return loss when compared with the measured flat position. According to that, results indicated that UWB antenna with Shieldit conducting fabric functions satisfactorily under most bending conditions. However, further investigations

need to be performed in order to study the effect of severe bending angles as well as crumbling effect on the proposed antenna performances.

5.5. Antenna Performance on Wet Conditions. Water has got a very high dielectric constant as compared to any fabric substrate material. Thus, when an antenna absorbs water, the moisture might change the antenna performance parameters significantly. The higher dielectric constant of water dominates the antenna performance by changing the resonant frequency. According to that, wearable antennas need to be measured considering wetness aspects.

In the current paper, measured results of four different states considering wetness, dampness and even when fully dried again for the UWB antenna prototype using copper conducting sheet and Shieldit conducting fabric are depicted in Figures 12 and 13, respectively.

Moreover, Figures 14 and 15 illustrate, the measured  $(|S_{11}|)$  results of UWB antenna prototypes using copper conducting sheet and Shieldit conducting fabric, respectively. Firstly, the textile antenna prototype was kept under water for more than three hours and measured inside water. After that, antenna under test was taken out of the water and measured immediately. Then, the antenna has been dried up using dry towel and measured; hence this state is recalled as approximately dry condition. Finally, the performance of the integrated antenna was tested when fully dried again.

From Figures 14 and 15, the blue solid line demonstrates the planner antenna performance when it was dry (before putting the antenna inside water) and after completely dried, while the dotted line shows the antenna performance inside water (completely wet). On the other hand, the short dashed line represents the immediately wet antenna state; hence the antenna was measured when it has been taken immediately out of water. Moreover, the dash-dotted line illustrates the

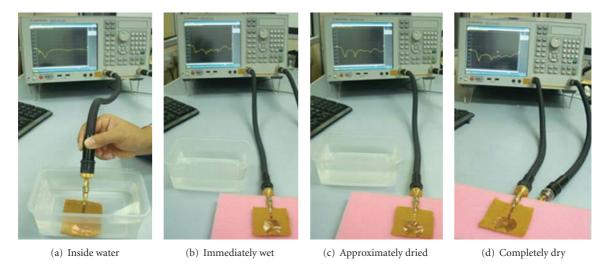


FIGURE 12: Snapshots of measured results of UWB antenna prototype using copper conducting sheet considering different states of wetness, dampness, and fully dried.

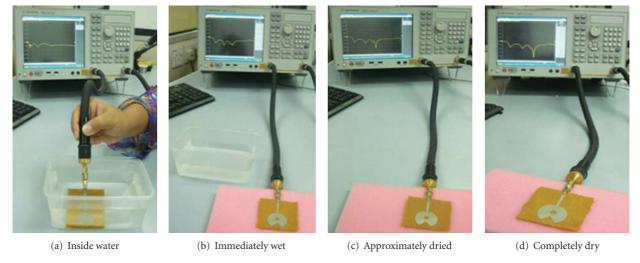


FIGURE 13: Snapshots of measured results of UWB antenna prototype using Shieldit conducting fabric considering different states of wetness, dampness, and fully dried.

performance of the antenna after it has been dried (using dry towel) and measured.

In the case of copper sheet antenna prototype, the inside water and immediately wet measurements indicated that the antenna was able to resonate with an expected degradation in resonance frequency while the frequency depth maintained to be below -8 dB in all UWB frequency range. After drying the antenna with dry towel, measured results (approximately dry) indicated that the antenna showed good impedance matching performances from 2 GHz up to 15 GHz with some negligible effect of water and moisture on antenna performance. Finally, results reported that the performance before and after wetness as the antenna has been fully dried remained unchanged.

However, Shieldit fabric antenna prototype is measured inside water and hence results indicated that the antenna is able to resonate with an expected degradation in resonance

frequency while the frequency depth maintained to be below –8 dB in all UWB frequency range. Although the slight deviation, measured results of immediately wet state, approximately dry state, and fully dried condition showed that the antenna performances remained unchanged when compared with measured results of planer state before wetness. Results indicated that the minor effect of water and moisture on antenna performance makes the proposed antenna suitable for humid conditions as well.

#### 6. Conclusion

Fully textile antennas and specially electrotextile materials themselves have strong potential to be used as antennas for transmission purposes in garments. In the current manuscript, UWB wearable antenna using fully textile materials are proposed and presented. The proposed antenna

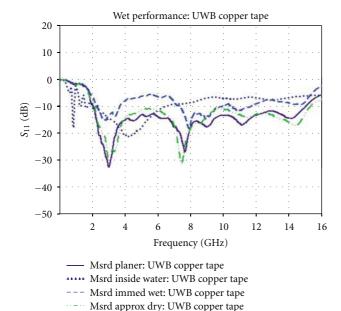


FIGURE 14: Measured ( $|S_{11}|$ ) results of UWB antenna prototype using copper conducting sheet considering several wet conditions.

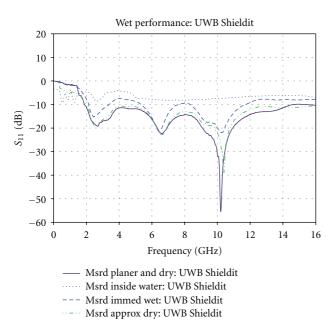


FIGURE 15: Measured ( $|S_{11}|$ ) results of UWB antenna prototype using Shieldit conducting fabric considering several wet conditions.

design provides more than 12 GHz bandwidth with such compact size and flexible materials and showed good measured return loss ( $|S_{11}|$ ) characteristics, omnidirectional patterns, as well as adequate gain and efficiency results. Moreover, effects of bending and wetness by means of measurements on both proposed UWB antenna performances are investigated. Results indicated that flannel fabric can act and perform as good candidate for textile wearable applications and possible to replace rigid board substrate materials. Besides that, the fabricated antennas using textile

conducting materials complied wearable antennas requirements by providing the wearer with compact antenna prototypes, flexible materials, ease of washing as well as ensuring the attractiveness of wearable devices. However, washable packaging of the electronics and durable interconnections remain major challenges to be tackled for all wearable electronics. Consequently, evaluation of long-term behaviour, durability and system performance after repeated wetness and laundering should invariably be considered in research tasks.

#### Acknowledgments

Authors wish to acknowledge the support of Ministry of Higher Education (MOHE), Research Management Centre (RMC), Radio Communication Engineering Department (RaCED), Faculty of Electrical Engineering, Universiti Teknologi Malaysia for supporting this research work under Grant no. 4L008 and 74578. The authors also wish to thank Sudan University of Science and Technology for supporting this research paper.

#### References

- [1] L. van Langenhove, *Smart Textiles for Medicine and Healthcare*, CRC Press, Cambridge, UK, 2007.
- [2] A. R. Chandran and W. G. Scanlon, "Dual-band low profile antennas for body-centric communications," in *Proceedings* of the International Workshop on Antenna Technology: Small Antennas, Innovative Structures and Materials (iWAT '10), pp. 1–4, Lisbon, Portugal, March 2010.
- [3] H. Rogier, C. Hertleer, L. Vallozzi, P. van Torre, F. Declercq, and M. Moeneclaey, "Indoor off-body communication based on a textile multi-antenna system integrated in clothing for rescue workers," in *Proceedings of the 2nd IET Seminar on Antennas and Propagation for Body-Centric Wireless Communications*, pp. 1–36, London, UK, April 2009.
- [4] B. Sanz-Izquierdo, J. C. Batchelor, and M. I. Sobhy, "Compact UWB wearable antenna," in *Proceedings of th 3rd Loughbor-ough Antennas and Propagation Conference (LAPC '07)*, pp. 121–124, Loughborough, UK, April 2007.
- [5] L. Januszkiewicz, S. Hausman, and T. Kacprzak, "Textile bodyworn exponentially tapered vee antenna," *Electronic Letters*, vol. 42, no. 3, 2007.
- [6] N. Chahat, M. Zhadobov, R. Sauleau, and K. Mahdjoubi, "Improvement of the on-body performance of a dual-band textile antenna using an EBG structure," in *Proceedings of* the 6th Loughborough Antennas and Propagation Conference (LAPC '10), pp. 465–468, Loughborough, UK, November 2010.
- [7] S. Barbarino and F. Consoli, "UWB circular slot antenna provided with an inverted-L notch filter for the 5 GHz WLAN band," *Progress in Electromagnetics Research*, vol. 104, pp. 1–13, 2010.
- [8] M. A. Matin, *Ultra Wideband Communications: Novel Trends in Antennas and Propagations*, InTech, Rijeka, Croatia, 2011.
- [9] I. Minin, Microwave and Millimeter Wave Technologies: Modern UWB Antennas and Equipment, InTech, Uttarakhand, India, 2010.
- [10] M. A. R. Osman, M. K. A. Rahim, M. Azfar, A. K. Kamardin, F. Zubir, and N. A. Samsuri, "Performance and evaluation of

- ultra-wideband wearable textile antenna," in *Proceedings of the IEEE European Conference on Antennas and Propagation (EuCAP '11)*, Rome, Italy, April 2011.
- [11] P. van Torre, L. Vallozzi, C. Hertleer, H. Rogier, M. Moeneclaey, and J. Verhaevert, "Indoor Off-Body wireless MIMO communication with dual polarized textile antennas," *IEEE Transactions on Antennas and Propagation*, vol. 59, no. 2, pp. 631–642, 2011.
- [12] S. Sankaralingam and B. Gupta, "Determination of dielectric constant of fabric materials and their use as substrates for design and development of antennas for wearable applications," *IEEE Transactions on Instrumentation and Measure*ment, vol. 59, no. 12, pp. 3122–3130, 2010.
- [13] P. J. Soh, G. A. E. Vandenbosch, V. Volski, and H. M. R. Nurul, "Characterization of a simple broadband textile planar inverted-F antenna (PIFA) for on body communications," in *Proceedings of the 20th International Conference on Applied Electromagnetics and Communications (ICECom '10)*, pp. 1–4, Dubrovnik, Croatia, September 2010.
- [14] S. Zhu and R. J. Langley, "Dual-band wearable antennas over EBG substrate," *IET Electronics Letters*, vol. 43, no. 3, pp. 141– 143, 2007.
- [15] M. Tanaka and J. H. Jang, "Wearable microstrip antenna," in Proceedings of the IEEE International Symposium on Antennas and Propagation and URSI North American Radio Science Meeting, Columbus, Ohio, USA, June 2003.
- [16] B. Sanz-Izquierdo, F. Huang, and J. C. Batchelor, "Covert dualband wearable button antenna," *Electronics Letters*, vol. 42, no. 12, pp. 668–670, 2006.
- [17] R. Langley and S. Zhu, "Dual band wearable antenna," in Proceedings of the Loughborough Antennas and Propagation Conference (LAPC '08), pp. 14–17, Loughborough, UK, March 2008.
- [18] M. A. R. Osman, M. K. A. Rahim, S. H. S. Ariffin, and S. K. S. Yuosf, "The investigation of flannel fabric layers," in *Proceedings of the International Symposium on Antennas and Propagations*, Macao, China, November 2010.
- [19] M. Klemm and G. Troester, "Textile UWB antennas for wireless body area networks," *IEEE Transactions on Antennas* and Propagation, vol. 54, no. 11, pp. 3192–3197, 2006.
- [20] A. Lazaro, D. Girbau, and R. Villarino, "Weflighted centroid method for breast tumor localization using an UWB radar," *Progress in Electromagnetics Research B*, no. 24, pp. 1–15, 2010.
- [21] S. Gao, S. Xiao, D. Jin, and B. Z. Wang, "WideBand antenna for ultra-wideband (UWB) body-centric wireless communications," in *Proceedings of the IEEE International Conference* on Ultra-Wideband (ICUWB '10), pp. 1–4, Nanjing, China, September 2010.
- [22] P. Sungmee and S. Jayaraman, "Wearable biomedical systems: research to reality," in *Proceedings of the IEEE International Conference on Portable Information Devices (PORTABLE '07)*, Orlando, Fla, USA, March 2007.
- [23] C. A. Balanis, Antenna Theory Analysis and Design, John Wiley & Sons, New York, NY, USA, 2005.
- [24] W. L. Stutzman and G. A. Thiele, Antenna Theory and Design, John Wiley & Sons, New York, NY, USA, 2nd edition, 1998.

Hindawi Publishing Corporation International Journal of Antennas and Propagation Volume 2012, Article ID 837230, 6 pages doi:10.1155/2012/837230

# **Application Article**

## New Flexible Medical Compact Antenna: Design and Analysis

#### Yann Mahe, Anne Chousseaud, Marc Brunet, and Bruno Froppier

Lunam Université de Nantes, UMR 6164 Institut d'Electronique et de Télécommunications de Rennes, Site de Nantes, Polytech Nantes, rue Christian PAUC, BP 50609, 44306 Nantes Cedex 3, France

Correspondence should be addressed to Yann Mahe, yann.mahe@univ-nantes.fr

Received 14 December 2011; Revised 16 February 2012; Accepted 19 February 2012

Academic Editor: Hendrik Rogier

Copyright © 2012 Yann Mahe et al. This is an open access article distributed under the Creative Commons Attribution License, which permits unrestricted use, distribution, and reproduction in any medium, provided the original work is properly cited.

Some results on embedded antennas for medical wireless communication systems are presented. Medical telemetry can advantageously assist medical diagnostics. For example, you can better locate a diseased area by monitoring temperature inside the human body. In order to establish efficient wireless links in such an environment, a special attention should be paid to the antenna design. It is required to be of a low profile, very small regardless of the working frequency—434 MHz in the ISM band, safe, and cost effective. Design of the as-considered antenna is proposed based on a simple model. The approach has been demonstrated for a compact flexible antenna with a factor of 10 with respect to the half-wave antenna, rolling up inside an ingestible pill. Measured and calculated impedance behaviour and radiation characteristics of the modified patch are determined. Excellent agreement was found between experiment and theory.

#### 1. Introduction

Medical applications benefited from recent research in the field of miniaturized wireless communication systems. Depending on the working frequencies, one of the main challenges is to design very small antennas; that would be to make these communication systems implantable or ingestible in the human body. Various types of compact antennas have been investigated [1–7]. Nevertheless, it is sometimes quite difficult to design the same kind of proposed antennas when the working frequency or the available space is different. Indeed, no design rules have been given to help the engineers.

In the case of digestive monitoring system, an ingestible capsule with a small size is required. Therefore, all monitoring systems must be implemented inside the desired pill.

For example, we can retain a classical used pill as shown in Figure 1. The space allowed is very limited. This is especially true when not only the antenna but also other active parts (batteries, sensors, etc.) of the communication system are embedded within a pill.

Moreover, these parts have to be shielded from a radiation that can interfere with the sensor and generate erroneous data.

The dimensions of the selected pill are 7 mm diameter and 17 mm height. So, we propose to investigate a microstrip

patch antenna for which a particular effort in terms of miniaturization must be done. Two main points support this decision. Firstly, this kind of antenna presents a ground plane on its bottom face which can advantageously be used for shielding the electronic part of the module from radiation. Secondly, if this antenna is manufactured on a flexible substrate, it can easily be rolled up inside the pill.

The retained frequency for this specific application is from the ISM bandwidth (433.05; 434.79 MHz) in which equivalent isotropic radiated power (EIRP) must be lower than 14 dBm. So the main challenge is to reduce the size of the antenna for about a factor of 90% compared with classical half-wavelength patch antenna and to ensure the conformability inside the pill.

Herewith, we will start by presenting the antenna geometry and the design rules to obtain an initial structure close to the optimal one. Our aim is to provide a very simple model in order to limit the optimization effort.

This approach proves its efficiency because the length of the proposed antenna for first estimation and final solution is slightly modified.

A first didactic example of low-cost antenna in free space on FR4 dielectric ( $\varepsilon_r = 4.4$  and height = 1.58 mm) is proposed.



FIGURE 1: Example of possible pill.

This structure has been optimised with CAD simulation tool like Ansoft HFSS. Scattering parameter  $(S_{11})$  shows a good agreement between simulation and measurement. The input impedance of the antenna can take any value between 0 and a maximum value fixed by the geometry. To illustrate this concept, an example of 25  $\Omega$  input impedance antenna is proposed. This input impedance can be easily changed by choosing an appropriate position of the feeding point along the structure. Finally, the dimensions of a medical folding antenna is proposed and investigated. All are within an environment whose properties are close to those of the human body with concluding results.

The preliminary design method will be described in detail below.

#### 2. Theoretical Considerations

2.1. Physical Analysis of Field Distributions. Patch antennas (Figure 2) are very common structures, but their size is one of the main drawbacks (half guided wavelength size). As long as the patch antenna works on its  $TM_{01}$  mode, it is possible to state that the electrical field has constant amplitude along its width (W) and varies in cosine along its length (L). A common technique to reduce the overall size of a microstrip patch antenna is to use only half part of this antenna placing some shorting points on the null electric field plane. The field distribution remains unchanged in both the cases. In this configuration (Figure 2(b)), the antenna length corresponds approximately to a quarter guided wavelength [8].

Introducing one or more impedance steps in the structure (Stepped Impedance Resonator, SIR Concept, Figure 3) will lead to either one of the following: a nonperiodic frequency behaviour with nonharmonic values resonant frequencies [9, 10] or smaller structures without changing their fundamental working frequency. One typical example for this is the H-antenna [11, 12] obtained from a half-wave structure. An example to reduce the overall size of such antenna would be to combine the two previous techniques as shown in Figure 4.

Finally, if the smallest line width is long enough in this last structure, it is possible to further reduce the length of the antenna by meandering it. The concept of using these three miniaturization techniques is very appealing in terms of compactness. However, it would be more interesting if one

can determine approximate dimension of such a structure in a simple way.

2.2. Design Method. It is well known that resonance conditions are achieved when the imaginary part of the equivalent input impedance of a resonator is null. In case of short-ended SIR antenna, by neglecting the discontinuity effects, it is possible to propose a simple model for this kind of structure. The SIR antenna is now reduced to two transmission lines with different characteristic impedances, ended with one part by a short circuit and the other part by an open circuit. This model is presented in Figure 5.

The impedance  $Z_{\text{input}}$  at a distance L from a given impedance load through a lossless transmission line with an homogeneous characteristic impedance  $Z_c$  and a wave number  $\beta$  is given below

$$Z_{\text{input}} = Z_c \cdot \frac{Z_{\text{load}} + j \cdot Z_c \cdot \tan(\beta \cdot L)}{Z_c + j \cdot Z_{\text{load}} \cdot \tan(\beta \cdot L)}.$$
 (1)

This equation can be applied to both sections of the proposed design. So, for the structure described in Figures 3 and 4, the equivalent impedance  $Z_{r1}$  presented at the end of the first line section  $(W_1, L_1)$  loaded by an open circuit is given as follows:

$$Z_{r1} = \frac{-j \cdot Z_{c1}}{\tan(\beta_1 \cdot L_1)}.$$
 (2)

Through the second line  $(W_2, L_2)$ , the equivalent impedance can be calculated by substituting  $Z_{r2}$  equal to zero on the short cut plane (short circuit) at the working frequency:

$$Z_{r2} = Z_{c2} \cdot \frac{Z_{r1} + j \cdot Z_{c2} \cdot \tan(\beta_2 \cdot L_2)}{Z_{c2} + j \cdot Z_{r1} \cdot \tan(\beta_2 \cdot L_2)} = 0.$$
 (3)

We can get the condition of resonance (4) by solving (2) and (3) which will lead us to a two-equation system given by (5).

$$Z_{c2} \cdot \frac{-j \cdot Z_{c1} + j \cdot Z_{c2} \cdot \tan(\beta_2 \cdot L_2) \cdot \tan(\beta_1 \cdot L_1)}{Z_{c2} \cdot \tan(\beta_1 \cdot L_1) + Z_{c1} \cdot \tan(\beta_2 \cdot L_2)} = 0,$$
(4)

$$-Z_{c1} + Z_{c2} \cdot \tan(\beta_2 \cdot L_2) \cdot \tan(\beta_1 \cdot L_1) = 0,$$
  

$$Z_{c2} \cdot \tan(\beta_1 \cdot L_1) + Z_{c1} \cdot \tan(\beta_2 \cdot L_2) \neq 0.$$
(5)

Here, we have to find the optimal value of the quadruplet  $(Z_{c1}, Z_{c2}, L_1, L_2)$  which satisfies the conditions given by (5). Equation (5) represents an overdefined system. This leads designers to choose which variable should be fixed first.

Since the problem is related to compactness, the width and the length of the first part have to be first chosen.

An important effort of miniaturization is made by meandering the high impedance line. To improve this effect, the second line width has to be compatible with meandering, and it also should be fixed.

By setting the values of  $W_1$ ,  $W_2$ , and  $L_1$ , it is possible to determine the length  $L_2$  for which the given operating frequency is achieved. For example, if we choose  $W_1 = 18$  mm,

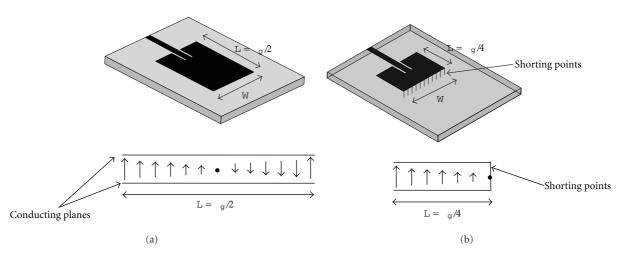


FIGURE 2: Example of elementary half (a) and quarter wave (with shorting points) (b) patch antennas. Electric field distributions along the antenna lengths.

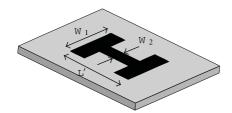


FIGURE 3: H antenna example.

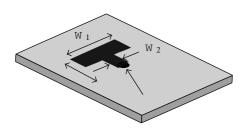


FIGURE 4: Short-circuited SIR antenna.

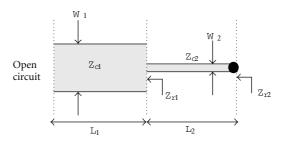


Figure 5: Description of the structure.

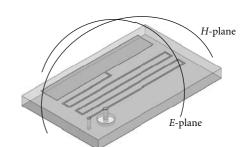


FIGURE 6: Final antenna.

 $L_1 = 3$  mm, and  $W_2 = 0.2$  mm, then  $L_2$  can be calculated as 67 mm for the resonant frequency of 434 MHz.

As the difference in width goes higher, more importance will be placed on compactness.

To further increase the compactness, the second line section can be meandered according to the width of the first section line (Figure 6). The gap between meandered lines has to be adjusted to have a capacitive coupling between arms as low as possible. Thus, the chosen gap will be five times greater than its width. The feeding point along the antenna is dependent on the input impedance chosen for the antenna. Indeed, the antenna can be matched directly on any real impedance under a maximum value determined by the geometry. An HFSS simulation is also required using  $L_2$  as the only optimization parameter.

#### 3. Results

3.1. First Realization on Rigid and Low-Cost Substrate. According to the design rules previously presented, a free space antenna built on FR4 substrate is fabricated. A gap between two meandered lines is chosen equal to 1 mm as mentioned before. This structure is simulated and optimized using Ansoft HFSS. Optimal dimensions are  $18 \text{ mm} \times 9 \text{ mm}$  with the first line section dimension of  $3 \times 18 \text{ mm}^2$  and for the second one  $0.2 \times 75 \text{ mm}^2$ . The  $L_2$  length is shifted 8 mm from formula compared with simulations and measurements results. This could be explained by discontinuities effects along the antenna which are not taken into account in the simple used model.

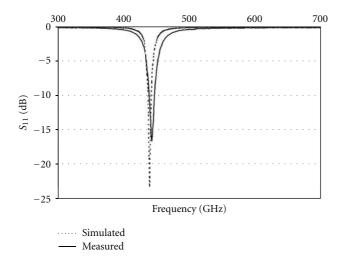


FIGURE 7:  $S_{11}$  coefficient (dotted lines: HFSS simulation, solid lines: measurement) for 25  $\Omega$  access.

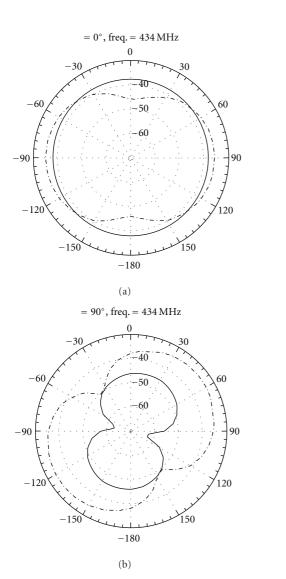


FIGURE 8: Radiation pattern  $G_{\varphi}$  (dot dash) and  $G_{\theta}$  (solid) at 434 MHz and 25  $\Omega$  access as simulated.

The design of the proposed antenna is given in Figure 6. The input impedance chosen for the antenna is, for example,  $25 \Omega$ , but it can vary from 0 up to  $6 k\Omega$  in this topology.

Measurements of scattering parameter  $S_{11}$  are in a good agreement with simulations as shown in Figure 7.

Radiation pattern is given in Figure 8 in two characteristic planes. Maximum radiation gain is around -33 dBi, with a radiation pattern quite omnidirectional in the  $\varphi=0$  plane. The gain can be improved by increasing the length of the  $L_1$  section but at the expense of compactness.

We have proposed an antenna design method with strong constraint in terms of compactness. This method is based on the prior knowledge of characteristic impedance and propagation constant values of the two line sections. This information could be evaluated by the formula given by [13]. The length of  $L_2$  is then evaluated using (5) to fix the resonant frequency. This method has been applied to design a conformal antenna for medical application in an environment whose properties are close to those of the human body. In this type of application, a flexible substrate is suitable to roll in the antenna inside a pill.

3.2. Realization on Flexible Substrate. To ensure compactness constraints of ingestible pills, the design has been carried out on a 50  $\mu$ m thickness flexible substrate (AP8525 from DuPont Pyralux) with a metal thickness of 18  $\mu$ m and a relative permittivity of 3.4.

Antenna dimensions are evaluated based on the previous design rules.

As stated before, the method is based on the prior knowledge of characteristic impedance and propagation constant values for each line sections. These values are thus computed by HFSS modelling each line cross-section. Fixing the width and the length of the first line section  $(18 \times 3 \text{ mm}^2)$  and the width of the second one (0.2 mm), the length  $L_2$  could be calculated according to (5). The computed length  $L_2$  is found equal to 22.5 mm. As in the case of the first studied antenna, a shift of 6.5 mm from formula compared with simulation and measurement results is observed. The second line section dimensions are therefore  $0.2 \times 16 \text{ mm}^2$ . Dimensions of the antenna built on flex are  $18 \times 5.4 \text{ mm}^2$  which is completely compatible with the dimensions of the selected pill.

A prototype of the antenna has been fabricated and investigated according to the measurement setup described in Figure 9. This consists of the antenna under test (1) immersed in a 20 cm diameter container (2) full of specific human tissue equivalent liquid material with a dielectric constant of 49.6 and a conductivity of 0.51 S/m. The receiver (3), 80 cm aside from the container, consists of a half-wave vertical polarized patch antenna (5 dBi gain) associated with low noise amplifier (LNA) to be as close as possible to the target application. The reflection and transmission coefficients were measured by a vector network analyzer (VNA) (4) operating over the range of 300 kHz–20 GHz with 50  $\Omega$  RF input impedance.

Measurement results show a good matching with simulation in terms of frequency setting and scattering parameters (Figure 10). The link budget (transmission coefficient) has

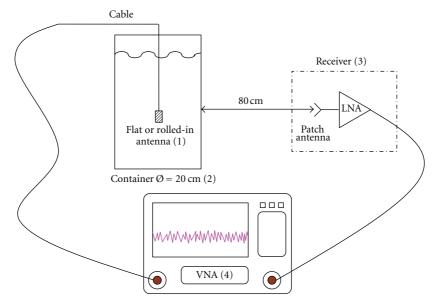


FIGURE 9: Structure of the system.

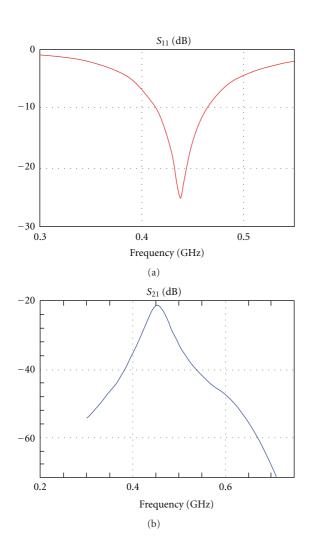


FIGURE 10: Measured scattering parameter of the antenna deep in tissue-equivalent liquid material.

been measured when the antenna is rolled in or not in the pill. No major change has been observed between the two configurations. Moreover, the radiation of the proposed antenna is quite omnidirectional. Different configurations have been tested, and the budget link is slightly modified (less than 3 dB over 360° range).

To improve the link budget, one can actually imagine a receiver placed on the human body interface. In this case, the received antenna should be designed properly taking into consideration the human body impact.

A first prototype of the final system is presented in Figure 11. The antenna is rolling up inside the capsule, and therefore the active part is shielded by the ground plane of the antenna.

#### 4. Conclusion

In this paper, we have demonstrated that a very compact antenna ( $\lambda_g/20$ ) can be obtained using several miniaturization techniques. The dimensions of the design have been calculated from a simple theoretical model. The difference between first estimation and final solution is minimal which proves the approach efficiency. To illustrate this concept, we have designed an antenna working around 434 MHz frequency. An antenna of size 18 mm × 9 mm is designed compared with classical half guided wavelength patch antenna (20 cm on FR4 substrate). A size reduction of the overall antenna of about 90% is achieved. Any arbitrary real input impedance from 0 up to few  $k\Omega$  can be chosen by finding appropriate position of the feeding point along the structure. Simulations and measurements match well whereas radiation pattern is quite omnidirectional in one plane. This antenna has also been designed on a flex substrate to be in terms embedded as a conformal antenna in different applications like ingestible medical wireless capsule. An example of this



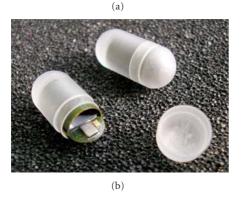


FIGURE 11: Structure of the system.

antenna has been achieved showing the interest of such an approach. A good quality link from pill embedding conformal antenna to a receiver shows the feasibility of this kind of antenna.

#### Acknowledgment

The authors would like to thank NXP Semiconductors for their financial support and for their efforts in manufacturing and test.

#### References

- [1] Q. Wang, K. Wolf, and D. Plettermeier, "An UWB capsule endoscope antenna design for biomedical communications," in *Proceedings of the 3rd International Symposium on Applied Sciences in Biomedical and Communication Technologies (ISA-BEL '10)*, pp. 1–6, Rome, Italy, November 2010.
- [2] D. Zhao, X. Hou, X. Wang, and C. Peng, "Miniaturization design of the antenna for wireless capsule endoscope," in Proceedings of the4th International Conference on Bioinformatics and Biomedical Engineering (ICBBE '10), Chengdu, china, June 2010
- [3] P. M. Izdebski, H. Rajagopalan, and Y. Rahmat-Samii, "Conformal ingestible capsule antenna: a novel chandelier meandered design," *IEEE Transactions on Antennas and Propagation*, vol. 57, no. 4, pp. 900–909, 2009.
- [4] S. H. Lee and Y. J. Yoon, "A dual spiral antenna for ultra-wide-band capsule endoscope system," in *Proceedings of the IEEE International Workshop on Antenna Technology: Small Antennas and Novel Metamaterials (IWAT '08)*, pp. 227–230, Chiba, Jaban, March 2008.

- [5] S. H. Lee, J. Lee, Y. J. Yoon, S. Park, C. Cheon, and S. Nam, "A wideband spiral antenna for ingestible capsule endoscope systems: experimental results in a human phantom and a pig," *IEEE Transactions on Biomedical Engineering*, vol. 58, no. 6, pp. 1734–1741, 2011.
- [6] J. George, M. Deepukumar, C. K. Aanandan, P. Mohanan, and K. G. Nair, "New compact microstrip antenna," *Electronics Letters*, vol. 32, no. 6, pp. 508–509, 1996.
- [7] L. Desclos, Y. Mahe, S. Reed, G. Poilasne, and S. Toutain, "Patch antenna size reduction by combining inductive loading and short-points technique," *Microwave and Optical Technology Letters*, vol. 30, no. 6, pp. 385–386, 2001.
- [8] P. Bhartia, I. Bahl, R. Garg, and A. Ittipiboon, *Microstrip Antenna Design Handbook*, Artech House Antennas and Propagation Library, Norwood, Mass, USA, 2001.
- [9] J. H. Lu and K. L. Wong, "Slot-loaded, meandered rectangular microstrip antenna with compact dual-frequency operation," *Electronics Letters*, vol. 34, no. 11, pp. 1048–1050, 1998.
- [10] Y. Mahe, L. Desclos, R. Moreau, and S. Toutain, "Miniaturized patch antenna for dual-frequency operation," in *Proceedings of* the 31st European Microwave Conference (EuMC '01), London, UK, September 2001.
- [11] C. S. Lee and K. H. Tseng, "Size reduction of microstrip antennas," *Electronics Letters*, vol. 37, no. 21, pp. 1274–1275, 2001.
- [12] A. H. Chaloupa, N. Klien, M. Peiniger, H. Piel, A. Pischke, and G. Splitt, "Miniaturized hightemperature supraconductor patch antenna," *IEEE Transaction on Microwaves Theory and Technique*, vol. 39, no. 9, pp. 1513–1521, 1991.
- [13] M. Kirschning and R. H. Jansen, "Accurate model for effective dielectric constant of microstrip with validity up to millimeter wave frequencies," *Electronics Letters*, vol. 18, no. 6, pp. 272– 273, 1982.

Hindawi Publishing Corporation International Journal of Antennas and Propagation Volume 2012, Article ID 236505, 10 pages doi:10.1155/2012/236505

### Research Article

## **Investigation of Flexible Textile Antennas and AMC Reflectors**

#### M. Mantash, A.-C. Tarot, S. Collardey, and K. Mahdjoubi

(Institute of Electronics and Telecommunications of Rennes) IETR, University of Rennes 1, Campus de Beaulieu, bat. 11D, 35042 Rennes Cedex, France

Correspondence should be addressed to A.-C. Tarot, anne-claude.tarot@univ-rennes1.fr

Received 15 December 2011; Revised 15 February 2012; Accepted 17 February 2012

Academic Editor: Hendrik Rogier

Copyright © 2012 M. Mantash et al. This is an open access article distributed under the Creative Commons Attribution License, which permits unrestricted use, distribution, and reproduction in any medium, provided the original work is properly cited.

In this paper, two different methods for fabric characterization are presented: a single frequency method and a broadband method. Felt and denim fabrics are characterized, and patch antennas are designed using these substrates to test both methods. Prototypes of the antennas on felt and denim are manufactured using conductive textile (called electrotextile) aiming to obtain fully flexible antennas. The prototypes are characterized in anechoic chamber to be compared and obtain conclusions related to the characterization methods. A new dual-band hexagonal AMC reflector combinable with antennas is also proposed to improve their performance and reduce the backward radiation to the human body. A novel broadband CPW-fed monopole antenna is designed to be combined with the AMC. The resulted prototype is characterized and compared with the performance of the CPW-fed antenna alone.

#### 1. Introduction

In recent years, flexible and textile antennas have taken a lot of attention due to their application in wearable systems. A review of wearable textile antennas is presented in [1], whereas, in [2], a GPS textile antenna is tested in realwork conditions. A Bluetooth textile antenna under bending conditions is presented in [3] and has also been combined with artificial magnetic conductors (AMCs [4–7]) aiming to improve their radiation properties [8], reduce the backward scattered radiation to the body [9, 10], or cover dual-band applications [9].

Nowadays, research efforts focus on both the design of new antennas and the development of novel textiles to be used as antenna substrates. Wearable antennas need to be integrated within everyday clothing, be low profile, and be hidden as much as possible. There are also other challenging works to maintain the critical antenna parameters at an acceptable level in all "normal" operation condition and environment. For example, stress (bending) can affect the axial ratio, operating frequency, and efficiency; humidity can affect the conductive textiles, by rusting them and changing their conductivity, as well as the dielectric textiles by changing their relative dielectric permittivity [11].

Bearing in mind all these facts, the selection of a proper conductive textile and a substrate for the antenna design are key points. The electrical parameters of garments are generally not available in literature. Therefore, the first step to accomplish is the characterization of the fabric in terms of dielectric permittivity and loss tangent.

In this paper, two methods for fabric characterization are presented. Two well-known fabrics, felt and denim, are characterized to test the methods, and prototypes of patch antennas on these fabrics are manufactured using electrotextiles as conductive parts. Then, these manufactured prototypes are characterized through return loss and radiation pattern measurements in order to obtain some conclusions regarding the characterization methods. In addition, the design of a novel hexagonal dual-band textile AMC to be combined with antennas in order to improve their performance and protect the human body from radiation is presented. A broadband CPW-fed broadband antenna on felt is proposed to be combined with the dual-band AMC. Finally, a prototype of CPW-fed monopole antenna over AMC using felt is manufactured and characterized. It shows the enhancement of the antenna performance when combined with AMC.

#### 2. Methods of Fabric Characterization

In order to perform the electrical characterization (dielectric constant  $\varepsilon_r$  and loss tangent  $\tan \delta$ ) of the fabrics, two

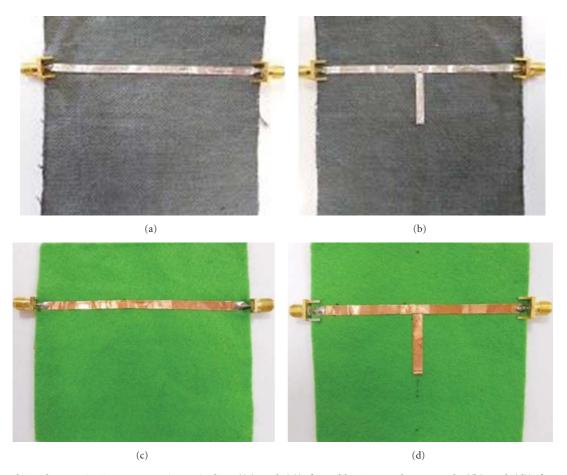


FIGURE 1: Fabric characterization setup: microstrip line ((a) and (c)) for calibration and open stub ((b) and (d)) for permittivity measurement using denim (up) and felt (down).

different methods were used: the method of stub resonator [12] which is valid for a single frequency and a broadband method based on a stripline cell [13]. Both methods are applied to denim and felt fabrics, and their results will be compared.

2.1. Single Frequency Method. The procedure used in the method of stub resonator [12] to perform the electrical characterization (dielectric constant  $\varepsilon_r$  and loss tangent tan  $\delta$ ) of the fabric is as follows: first, the set-up calibration is carried out by measuring the  $S_{21}$  parameter for a microstrip line (see Figures 1(a) and 1(c)) on the fabric. Then, the  $S_{21}$  parameter for  $\lambda/4$  stub (see Figures 1(b) and 1(d)) is measured. After this step, simulation of the  $S_{21}$  parameter for the  $\lambda/4$  stub is carried out using HFSS software [14]. The dielectric constant  $\varepsilon_r$  is then adjusted in simulations in order to match the simulated curve of the  $S_{21}$  parameter to the measured one.

This method of characterization is applied to two commonly used fabrics: denim and felt. Cupper tape is used for the metallic parts (ground plane and lines). The line width and stub length are, respectively, 3.6 mm and 25 mm for denim, and 4 mm and 26.5 mm for felt. For denim, the best match for the resonant frequency is obtained using  $\varepsilon_r$  =

1.6 (Figure 2). Concerning the loss tangent  $(\tan \delta)$ , we obtained 0.05. The estimated values for felt are, respectively,  $\varepsilon_r = 1.22$ , and  $\tan \delta = 0.016$ . These estimated values will be used for antennas simulations.

Compared to other characterization methods [13], the advantages of this one are simplicity, rapidity, no need for specific equipment, and, finally, applicability to all types of fabrics.

This method is well suited to textile whose characteristics are not highly variable with frequency (i.e., the textile that is not dispersive). If the textiles are dispersive, that is permittivity varies versus frequency, a broadband method is preferable [13]. However, it needs some specific setup and software.

2.2. Broadband Method. Suitable for measuring the complex permittivity and permeability of isotropic solid materials, this method is based on a stripline topology (see Figure 3). The samples come in the form of rectangular plates or thin films deposited on a dielectric support.

The electromagnetic analysis of the cell is based on a quasistatic approach. This approach represents the crosssection of the stripline containing the tested sample by an equivalent cross-section consisting of a homogeneous

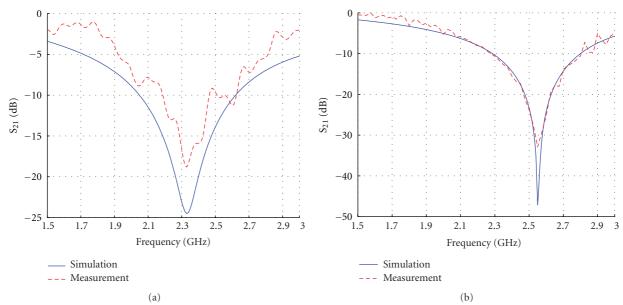


FIGURE 2: Simulation and measurement of  $S_{21}$  parameter for the open stub on denim (a) and on felt (b).

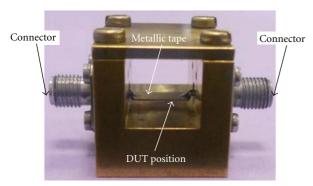


FIGURE 3: Stripline used for measurements.

medium of effective permittivity and permeability  $\varepsilon_{\rm eff}$  and  $\mu_{\rm eff}$ . The measurement parameters  $S_{ij}$  are traced back to the actual parameters of the material. The frequency range is typically 300 kHz–8 GHz. The accuracy of the results is high, with a relative error less than 5% [15]. This method has been used to characterize denim and felt samples to compare the obtained results with those of the single frequency method.

According to this method applied between 1 GHz and 6 GHz, the measured values for relative dielectric constant  $\varepsilon_r$  vary from 1.215 to 1.225 for felt (Figure 4) and from 1.6 to 1.65 for denim (Figure 5). Regarding the loss tangent tan  $\delta$ , the values are 0.016 for felt and 0.05 for denim and relative magnetic permeability  $\mu_r = 1$  for both felt and denim fabrics.

Comparing the obtained results using the two methods, it can be observed that both of them estimate the same values for felt, but there are slight differences for denim.

#### 3. Electrotextiles

The manufacturing of antennas integrable into clothing has become possible through the use of electrotextile, which

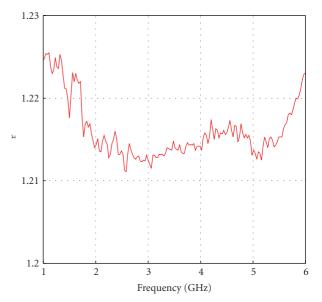


FIGURE 4: Measured permittivity versus frequency for felt.

are conductive fabrics [16] obtained by interleaving normal fabrics with conductive metal/polymer threads. The selection of an appropriate electrotextile is an important step in the design of a textile antenna. In order to ensure the optimum characteristics for a definite application, the electrotextile for textile antennas should exhibit the following properties: low electrical resistance to minimize losses, flexible to be able to be deformed when worn, inelastic and tear resistant to preserve its electrical properties, and light weight to be comfortable.

Bearing in mind all these facts, two different electrotextiles have been selected in this paper: "Pure Copper Taffeta Fabric" and "Shieldit Super." Properties of such

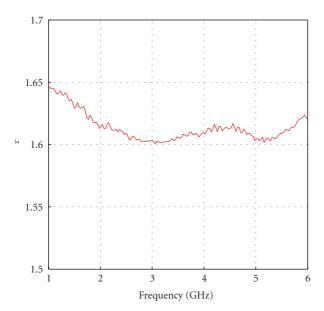


FIGURE 5: Measured permittivity versus frequency for denim.

electrotextiles, provided by supplier are given in Table 1. Photographs taken through a microscope are presented in Figure 6. Moreover, the resistivity of both electrotextiles has been measured in our laboratory IETR, using the "4-probe setup."

"Pure Copper Taffeta Fabric" is made using pure copper and has the advantages of being smooth, flexible, light weight, easy to be cut and sewn.

An additional adhesive layer is unfortunately needed to fix the electrotextile to the fabric, thus increasing the losses.

"Shieldit Super" is made of polyester substrate conductive nickel and copper plated then backed with nonconductive hot melt adhesive. It has the advantages of excellent shielding and low corrosion, it is also easy to be cut and sewn, and, additionally, its adhesiveness is activated at 130°C = 266°F. It can be ironed on to cotton or another fabric. The use of polyester substrate instead of nylon (as in another electrotextile) makes it better for moisture management as it is more hydrophobic and (more difficult it to become wet) which allow to better conserve its electromagnetic properties. For these reasons, Shieldit Super will be used in next section. As a drawback, it can cause skin irritation because of containing nickel, but this is not a major concern in the design presented here as an additional fabric layer can be used to isolate the electrotextile from the body.

#### 4. Antennas on Textile

Two patch antennas at 2.45 GHz using denim and felt fabrics as substrate are designed and characterized. Both use Shieldit Super as electrotextile.

Figure 7 shows the manufactured prototypes. The patch dimensions as well as the return loss and realized gain are given in Figure 8 and Figure 9 for felt and denim fabrics.

Figure 10 shows the setup for measuring the radiation pattern of the prototypes using Satimo stargate SG 32.

There is a good agreement between the measurement and the simulation results both for felt and denim substrates. A slight frequency shift between the simulation and experimental results is observed both for  $S_{11}$  and gain parameters. It can be attributed to the manufacturing tolerances.

Regarding the radiation patterns (see Figure 11), one observes a good agreement between the measured and simulated curves for the principal polarization and a satisfactory one for the cross polarization.

# 5. Artificial Magnetic Conductor (AMC) on Textile

The textile antennas usable in wearable applications can be combined with artificial magnetic conductors (AMCs) with the aim of improving the antenna's radiation properties and reducing their backward radiation to the human body [4–7]. These performances are achieved due to the AMC in-phase reflection property. Here, a dual-band AMC, resonating at 2.4 GHz and 5.5 GHz, is designed to be combined with the dual-band CPW-fed antenna on felt.

The resonance frequency and the bandwidth of an AMC reflectors are determined by the unit-cell geometry, the dielectric permittivity, and the substrate thickness. Thus, for a given dielectric substrate, the unit-cell design plays an important role to obtain dual-band behavior and to ensure sufficient bandwidth at each subband.

Figure 12 shows the geometry of the proposed AMC for dual-band operation. The unit-cell consists of an inner hexagonal patch surrounded by a concentric hexagonal loop. The hexagonal shape offers a rotational symmetry for the wave propagation and the best filling factor which allows the maximum metallic size and consequently the best bandwidth results. Dual-band behavior is due to the fact that the central patch and the surrounding ring have two different resonance frequencies.

Shieldit electrotextile is used for the metallic elements (hexagon unit-cells and the ground plane under the dielectric substrate) and felt fabric with h = 4 mm (thickness),  $\varepsilon_r = 1.22$ , and loss tangent tan  $\delta \cong 0.016$ .

To find the frequency band in which the periodic structure exhibits AMC behavior, we have studied by simulation its reflection coefficient for a uniform plane wave, using commercial software HFSS V.13 of Ansoft [14].

A single cell of the structure has been investigated with periodic boundary conditions (PBCs) on its sides, modeling an infinite structure. Normal incidence plane waves are launched to illuminate the periodic structure using a waveport placed a half-wavelength above it. Following [4], the reflection coefficient phase on the AMC is obtained. The phase reference plane is taken on the periodic surface.

Simulation has shown that the inner hexagon mainly determines the higher resonant frequency. Increasing the elements size, Hex\_out and Hex\_in, lowers the resonant frequency, while increasing the gap 2 dL between unit cells raises the lower frequency. Hex\_cut can be used to control the

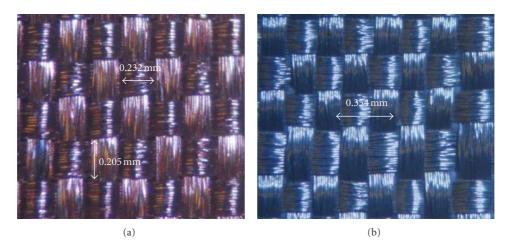


Figure 6: Microphotographs of (a) Pure Cooper Taffeta Fabric. (b) Schieldit Super.

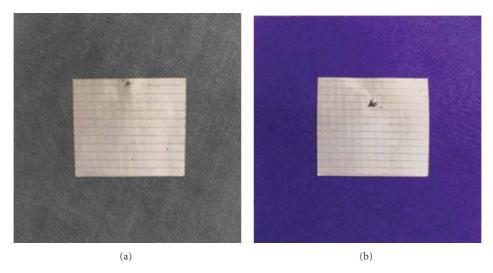


FIGURE 7: Patch antenna on denim (a) and felt (b) using Shieldit Super electrotextile.

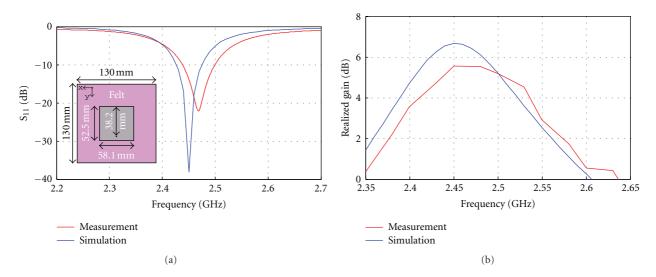


FIGURE 8: Prototype geometry description and characterization results for patch antenna on felt: return loss (a) and realized gain (b).

Table 1: Properties of electrotextiles.

Electrotextile	Pure Copper Taffeta Fabric	Shieldit Super	
Measured resistance (IETR)	0.031 Ohm/sq	0.025 Ohm/sq	
Surface resistance	0.05 Ohm/sq	<0.1 Ohm/sq	
Conductivity	$2.5 \times 10^5  \text{S/m}$	$6.67 \times 10^5  \text{S/m}$	
Thread pitch	0.232 mm	0.146 mm	
Conductive element	Cu	Ni and Cu	
Adhesive backing	No	Yes	
Thickness	0.08 mm	0.17 mm	
Weight	$80  \mathrm{g/m^2}$	$230  g/m^2$	

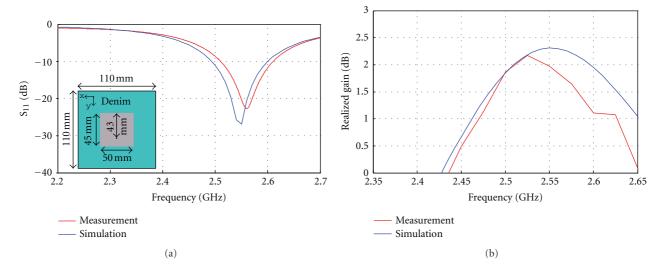


FIGURE 9: Prototype geometry description and characterization results for patch antenna on denim: return loss (a) and realized gain (b).

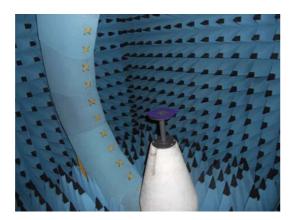


FIGURE 10: Antenna's measurement setup in Satimo stargate SG 32 anechoic chamber.

lower frequency and the upper band bandwidth. To achieve dual-band operation at the intended frequencies, the unit-cell dimensions are optimized. The optimized values are given in Table 2.

According to simulation results shown in Figure 13 and detailed on Table 3, the AMC behavior of the structure

Table 2: Unit-cell dimensions for dual hexagonal AMC.

Dimensions (mm)						
Hex_out	Hex_cut	Hex_in	dL	h		
15.7	12	11.5	0.8	4.0		

Table 3: Frequency bands and bandwidths for dual-band hexagonal AMC.

	Frequencies (GHz)			Bandwidth		
	$f_{\text{Low}}$	$f_r$	$f_{\mathrm{Up}}$	Total (MHz)	%	
Lower band	2.40	2.55	2.70	300	11.76	
Upper band	5.04	5.50	6.04	1000	18.18	

takes place from 2.4 GHz to 2.7 GHz and from 5.04 GHz to 6.04 GHz covering all the WiFi bands.

#### 6. Design of a Novel Broadband Textile Antenna

To show the capabilities of the AMC reflector announced in the previous section in terms of dual-band operation and backward radiation reduction, a novel CPW-fed broadband antenna is designed to be placed over it.

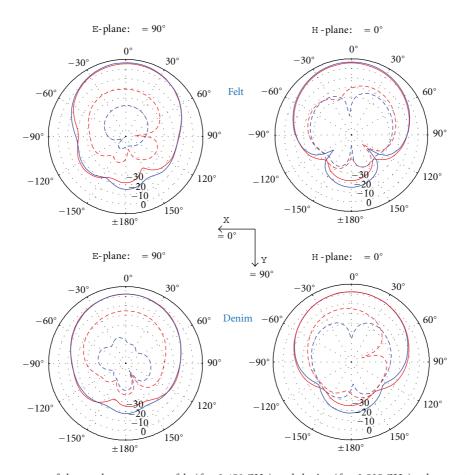


FIGURE 11: Radiation pattern of the patch antennas on felt ( $f = 2.450 \,\text{GHz}$ ) and denim ( $f = 2.525 \,\text{GHz}$ ) substrates. Solid curves present the principal polarization (PP) and the dotted ones the cross polarization (XP). Blue curves correspond to the simulation patterns and red curves to the measured ones.

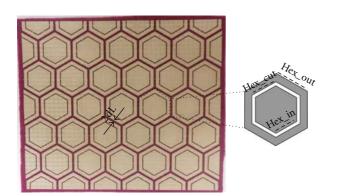


FIGURE 12: Dual-band textile hexagonal AMC-manufactured prototype: top view and unit-cell detail.

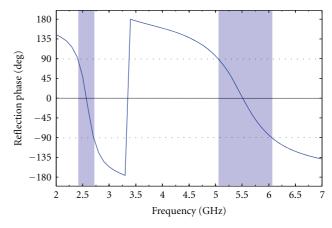


FIGURE 13: Simulated reflection phase of the AMC surface.

The geometry of the proposed CPW-fed broadband antenna is shown in Figure 15. The antenna consists of a rectangular radiating element with two slots and fed by a CPW line. Shieldit Super electrotextile is used to implement these conductive parts which are adhered onto the same side of a 2 mm thick felt substrate.

The antenna geometry has been optimized to cover the  $S_{11}$  bandwidth from 2 GHz to 6 GHz. The resulting optimized dimensions are given in Figure 14.

In Figure 15 is presented the measured and simulated return loss of the manufactured CPW-fed broadband antenna. The measurement results yielding a bandwidth

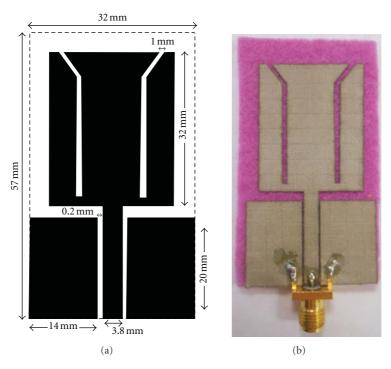


FIGURE 14: CPW-fed broadband antenna geometry and prototype.

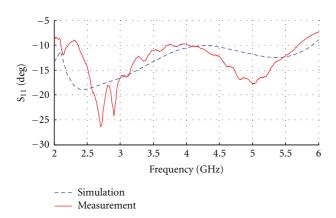


FIGURE 15: Simulated and measured return loss for the CPW-fed broadband monopole antenna on felt.

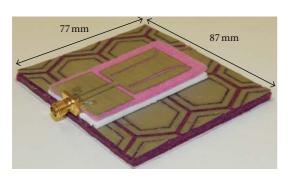


FIGURE 16: CPW-fed antenna on AMC prototype using felt and electrotextile.

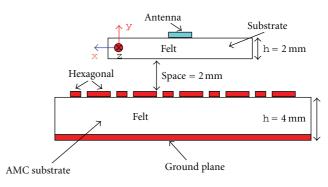


FIGURE 17: Side view of CPW-fed antenna on AMC prototype.

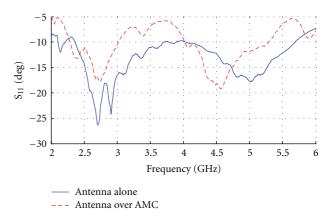


FIGURE 18: Return loss measurement results for the CPW-fed antenna alone and for the CPW-fed antenna on AMC.

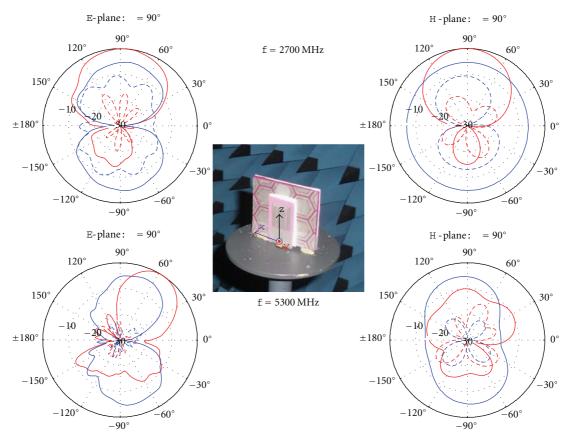


FIGURE 19: Measured radiation patterns (PP in solid line and XP in dashed line) at f = 2.700 GHz and f = 5.300 GHz, CP, for the CPW-fed monopole antenna without (blue) and with (red) AMC reflector, manufactured on felt substrate.

from 2.1 GHz to 5.7 GHz agree quite well with simulation ones exhibiting proper matching from 2 GHz to 5.9 GHz. A slight shift in frequency mainly due to manufacturing tolerances can be observed.

*E*-plane and *H*-plane normalized radiation pattern are depicted in Figure 19 at 2.7 GHz and 5.3 GHz. As it is expected for a monopole antenna alone (in free space), the *H*-plane pattern is almost omnidirectional. The realized gain versus frequency is shown in Figure 20.

#### 7. Antenna over AMC on Textile

Figure 16 shows the manufactured prototype of CPW-fed antenna on AMC using felt and electrotextile. Between the antenna and the AMC, there is a 2 mm foam layer (see Figure 17). The prototype dimensions are  $87 \text{ mm} \times 77 \text{ mm}$ .

In Figure 18, the measured return loss for the CPW-fed antenna on AMC and for CPW-fed antenna alone is presented for comparison. It can be observed that a dual-band performance is obtained for the combined structure due to the AMC dual-band behavior. A slight frequency shift to lower frequencies also appears due to capacitive effects when placing the antenna over the AMC. Finally, the radiation patterns for both prototypes are shown in Figure 19, whereas the gain has been depicted in Figure 20. As it could be expected, the backward radiation of the

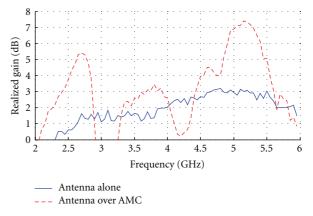


FIGURE 20: Measured realized gain for the CPW-fed monopole antenna alone and for the CPW-fed monopole antenna over AMC.

antenna is reduced by the AMC reflector and the gain is considerably improved.

#### 8. Conclusions

Two methods for fabric characterization are presented in this paper: one working at a single frequency and the other on a broadband range. They allowed to retrieve the permittivity of felt and denim materials. Based on these data, two patch antennas are realized on these materials. We obtained a very good agreement between the simulation and experimental results for return loss, as well as for the gain parameters, confirming the reliability of the retrieved data.

One of the major contributions of this paper is the design of a textile AMC of original shape. This reflector has been designed to be combined with the textile antennas in order to protect the human body from radiation in one hand and to improve the antenna performance in the other hand. AMC structure has a dual-band behavior and is intended to cover both of the Wifi bands.

To examine the validity of the AMC properties, we introduced a novel CPW-fed broadband antenna (working on the whole frequency range from low Wifi band to high Wifi band), realized it on felt substrate, and placed it over the AMC. A remarkable enhancement is obtained for the backward radiation and the gain of the combined structure compared to those of the CPW-fed antenna alone, concluding to the necessity of AMC reflectors for the onbody applications.

#### Acknowledgments

This work has been supported by "Agence Nationale de la Recherche" (ANR), France, under Grants ANR-09-VERS-003 for the METAmateriaux pour VESTements intelligents (METAVEST) project and also by the "Images et Réseaux" cluster.

#### References

- [1] B. Gupta, S. Sankaralingam, and S. Dhar, "Development of wearable and implantable antennas in the last decade: a review," in *Proceedings of the 10th Mediterranean Microwave Symposium*, (MMS '10), pp. 251–252, August 2010.
- [2] L. Vallozzi, W. Vandendriessche, H. Rogier, C. Hertleer, and M. L. Scarpello, "Wearable textile GPS antenna for integration in protective garments," in *Proceedings of the 4th European Conference on Antennas and Propagation*, (EuCAP '10), April 2010.
- [3] I. Locher, M. Klemm, T. Kirstein, and G. Tröster, "Design and characterization of purely textile patch antennas," *IEEE Transactions on Advanced Packaging*, vol. 29, no. 4, pp. 777–788, 2006.
- [4] D. Sievenpiper, L. Zhang, R. F. Jimenez Broas, N. G. Alexöpolous, and E. Yablonovitch, "High-impedance electromagnetic surfaces with a forbidden frequency band," *IEEE Transactions on Microwave Theory and Techniques*, vol. 47, no. 11, pp. 2059–2074, 1999.
- [5] F. R. Yang, K. P. Ma, M. Yongxi Qian, and T. Itoh, "A uniplanar compact photonic-bandgap (UC-PBG) structure and its applications for microwave circuits," *IEEE Transactions* on Microwave Theory and Techniques, vol. 47, no. 8, pp. 1509– 1514, 1999.
- [6] M. E. De Cos, Y. Álvarez, R. C. Hadarig, and F. Las-Heras, "Flexible uniplanar artificial magnetic conductor," in *Proceedings of the Electromagnetic Research (PIER '10)*, vol. 106, pp. 349–362, July 2010.
- [7] M. E. De Cos, Y. Álvarez, and F. Las-Heras, "Planar artificial magnetic conductor: design and characterization setup in

- the RFID SHF band," Journal of Electromagnetic Waves and Applications, vol. 23, no. 11-12, pp. 1467–1478, 2009.
- [8] J. Liang and H. Y. D. Yang, "Radiation characteristics of a microstrip patch over an electromagnetic bandgap surface," *IEEE Transactions on Antennas and Propagation*, vol. 55, no. 6, pp. 1691–1697, 2007.
- [9] S. Zhu and R. Langley, "Dual-band wearable textile antenna on an EBG substrate," *IEEE Transactions on Antennas and Propagation*, vol. 57, no. 4, pp. 926–935, 2009.
- [10] M. Mantash, A-C Tarot, S. Collardey, and K. Mahdjoubi, "Dual-band CPW-fed G-antenna using an EBG structure," in Proceedings of the Antennas and Propagation Conference (LAPC '10), pp. 453–456, Loughborough, UK, 2010.
- [11] C. Hertleer, A. van Laere, H. Rogier, and L. van Langenhove, "Influence of relative humidity on textile antenna performance," *Textile Research Journal*, vol. 80, no. 2, pp. 177–183, 2010.
- [12] D. Liu, U. Pfeiffer, J. Grzyb, and B. Gaucher, Advanced Millimeter-Wave Technologies: Antennas, Packaging and Circuits, chapter 5, Wiley, 2009.
- [13] E. Salahun, P. Quéffélec, M. Le Floc'h, and P. Gelin, "A broadband permeameter for "in situ" measurements of rectangular samples," *IEEE Transactions on Magnetics*, vol. 37, no. 4 I, pp. 2743–2745, 2001.
- [14] Ansoft HFSS, Four Station Square Suite 200, Pittsburgh, Pa, USA.
- [15] http://www.univ-brest.fr/lest/caracterisation/pages/pages\_ francais/.
- [16] A. Tronquo, H. Rogier, C. Hertleer, and L. van Langenhove, "Applying textile materials for the design of antennas for wireless body area networks," in *Proceedings of the European Conference on Antennas and Propagation (EuCAP '06)*, no. ESA SP-626, pp. 1–5, Nice, France, November 2006.

Hindawi Publishing Corporation International Journal of Antennas and Propagation Volume 2012, Article ID 170420, 11 pages doi:10.1155/2012/170420

### Research Article

# Cylindrical Bending of Deformable Textile Rectangular Patch Antennas

#### Freek Boeykens, Luigi Vallozzi, and Hendrik Rogier

Department of Information Technology, Ghent University, St. Pietersnieuwstraat 41, 9000 Ghent, Belgium

Correspondence should be addressed to Freek Boeykens, freek.boeykens@intec.ugent.be

Received 22 November 2011; Accepted 24 January 2012

Academic Editor: Ana Collado

Copyright © 2012 Freek Boeykens et al. This is an open access article distributed under the Creative Commons Attribution License, which permits unrestricted use, distribution, and reproduction in any medium, provided the original work is properly cited.

Textile patch antennas are well known as basic components for wearable systems that allow communication between a human body and the external world. Due to their flexibility, textile antennas are subjected to bending when worn, causing a variation in resonance frequency and radiation pattern with respect to the flat state in which their nominal design is performed. Hence, it is important for textile antenna engineers to be able to predict these performance parameters as a function of the bending radius. Therefore, we propose a comprehensive analytical model that extends the cylindrical cavity model for conformal rigid patch antennas by incorporating the effects of patch stretching and substrate compression. It allows to predict the resonance frequency and the radiation pattern as a function of the bending radius. Its validity has been verified experimentally. Unlike previous contributions, which concerned only qualitative studies by means of measurements and numerical full-wave simulations, the proposed model offers advantages in terms of physical insight, accuracy, speed, and cost.

#### 1. Introduction

Textile antennas emerged during the last decade as a new promising class of antennas that are particularly suitable for use in wearable applications [1–5]. These antennas can be fully integrated into intelligent garments, known as *wearable electronic systems* [6], enabling the transmission of data collected by wearable sensors or the reception of signals sent to wearable actuators integrated into clothing. The applications of wearable systems and textile antennas are numerous, ranging from rescue workers interventions' coordination to monitoring of dependent patients in hospital and sports applications.

In order to allow an optimal integration into garments without hindering the wearer's movements and comfort, the most suitable topology for a textile antenna is the planar patch. This flexible patch may be subjected to bending when the garment is worn, conforming its shape to the surface on which it is placed. As a result, stretching of the patch (resulting in an elongation of the resonant length) and substrate compression (leading to a variation of the dielectric permittivity as a function of the bending radius) can occur.

Since the beginning of textile antenna design, these effects have been taken into account, however, they were not well known and were compensated for by increasing the antenna bandwidth and validating the design afterwards by experiments [4]. Hence, it is essential to model the behaviour of the antenna under bent conditions and to predict the influence of bending on the resonance frequency and the radiation pattern. Full-wave simulation approaches are a potential solution, but most available commercial software tools do not offer the possibility of building a conformal mesh for bent structures, which results in inaccuracies in the obtained results. Moreover, these simulations do not offer physical insight into the bending mechanisms and may require high computational effort and time. Therefore, we propose analytical formulas that help the designer to assess a priori the effects of bending, stretching, and compression. The work described in this paper focuses on cylindrical bending in particular, since, for wearable applications, textile antennas are usually deployed on cylindrical surfaces such as a human arm, a leg, or a torso.

This study starts from past research efforts on rigid conformal antennas attached to cylindrical surfaces, of which

several contributions can be found in literature. Krowne started by extending the popular cavity model for the rectangular patch antenna (introduced by Lo et al. in 1979 [7]) to the cylindrical case [8]. Resonance frequencies for the  $\mathrm{TE}_z$  and  $\mathrm{TM}_z$  modes were theoretically derived, though radiation patterns were not calculated in this model. A more comprehensive study was performed by Dahele et al. [9] and Luk et al. [10]. Their cavity model is only valid for patch antennas with a very thin substrate, but resonance frequencies, far fields, input impedances, and Q-factors were derived analytically. Other analytical approaches were also introduced, which allow to calculate radiation patterns of antennas with patches of arbitrary shape [11–13]. However, they are based on an electric surface current model and assume the surface current distribution to be known on the patch.

Cylindrical bending of *deformable* textile antennas has been an important subject in recent papers, but exclusively from an experimental point of view [4, 5, 14–16]. The general conclusions drawn from these contributions are that bending causes an upward shift of the resonance frequency, a broadening of the radiation pattern, a decrease in gain along broadside, and an alteration of the polarisation (in case of a circularly polarised antenna). Yet, these studies are rather qualitative and do not provide physical insight into the complex mechanisms occurring due to antenna bending.

The present work tries to overcome all drawbacks of the previous analysis methods by proposing a comprehensive study on cylindrical bending of rectangular textile patch antennas. An analytical model based on the cylindrical cavity model for conformal antennas, which allows to calculate both the resonance frequency and the radiation pattern, is constructed. This offers the advantage of requiring only small computational effort for calculating the main antenna performance parameters.

In order to model deformable textile patch antennas, some novel extensions to rigid conformal antenna models are proposed:

- (1) Wearable textile antennas are usually realised with electrotextiles as conductive patch materials, which are subjected to stretching when the antenna is bent. This causes an elongation of the patch along one direction and shifts the resonance frequency [17]. This behaviour is integrated into the model by introducing a factor that determines the location of the original patch width.
- (2) Textile antennas are subjected to compression when bent, which causes a variation of its dielectric permittivity. This can be tackled by proposing an expression for the compressed permittivity  $\epsilon_{r,\text{comp}}$  as a function of the bending radius.

The model is validated by means of

- (1) theoretical validation for large curvature radii using Debye's expansion for large-order Bessel functions;
- (2) experimental validation by measuring five prototypes based on different substrates with different thicknesses, patch materials, and operation frequencies.

The organisation of the paper is as follows. First, the cavity model for cylindrical-rectangular antennas is described in Section 2. The expressions for the resonant fields inside the cavity are calculated, from which the resonance frequencies and radiation patterns are derived. In Section 3, the cavity model is verified for large curvature radii by comparing the obtained dispersion relations with the expression for resonance frequencies in rectangular cavities. Section 4 presents the experimental results. The proposed model is verified by means of five textile antenna prototypes with different geometries and material characteristics. Both resonance frequencies and radiation patterns are compared. Finally, the general conclusions are summarised in Section 5.

#### 2. Theory

The geometry of the cylindrical cavity representing the textile antenna is shown in Figure 1. The length and width of the wearable antenna are denoted by L and W, and the flexible dielectric substrate has a height h and relative permittivity  $\epsilon_r$ . The curvature radius is a, and the angle formed by the edges of the patch is  $\beta$ .

In order to obtain a relationship between W, a, and  $\beta$ , one has to take into account whether the antenna patch is stretchable or not. According to [17], the following relations exist for stretchable patches:

$$\frac{\Delta W}{W} = \frac{h}{2a+h},\tag{1a}$$

$$\beta(a+h) = W + \Delta W, \tag{1b}$$

with  $W + \Delta W$  the width of the bent patch. This is shown in Figure 2. Combining (1a) and (1b) leads to

$$\beta\left(a + \frac{h}{2}\right) = W. \tag{2}$$

This means that the original patch width is located at  $\rho = a+h/2$  due to patch elongation. If the patch is nonstretchable, the patch length does not vary when bending the antenna and groundplane crumpling occurs. The original width W is then still located at  $\rho = a + h$ .

Because textile antennas can be constructed using both stretchable and nonstretchable patches, we introduce a factor d (Figure 2) that determines the location of the original width:

$$W = \beta(a + hd). \tag{3}$$

This factor d can take values between 0.5 and 1. For perfectly stretchable patches we find that d = 0.5 and for perfectly nonstretchable patches d = 1.

2.1. The Cavity Model. We now proceed with the derivation of the cylindrical cavity model [8]. The cavity is bounded by electric walls at  $\rho = a$  and  $\rho = a + h$  and magnetic walls at  $\phi = \pm \beta/2$  and  $z = \pm L/2$ .

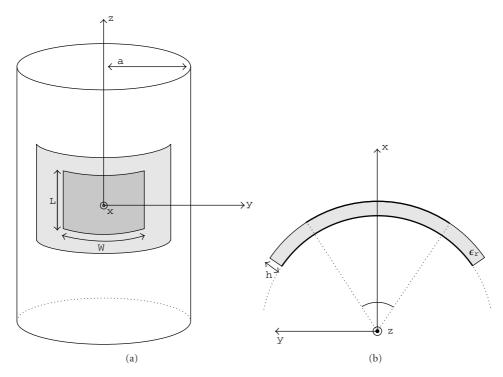


FIGURE 1: Geometry of the cavity: top view (a) and side view (b).

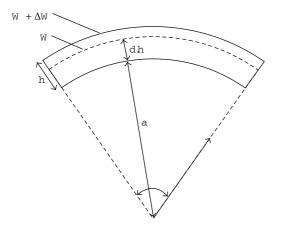


FIGURE 2: Patch elongation.

The electric and magnetic fields inside the cavity are given by

$$\mathbf{E} = -\nabla \times \mathbf{F} - j\omega\mu\mathbf{A} + \frac{1}{j\omega\epsilon}\nabla(\nabla \cdot \mathbf{A}), \tag{4a}$$

$$\mathbf{H} = \nabla \times \mathbf{A} - j\omega \epsilon \mathbf{F} + \frac{1}{j\omega \mu} \nabla (\nabla \cdot \mathbf{F}), \tag{4b}$$

where, given the translation invariance of the structure, the vector potentials are defined by

$$\mathbf{A} = A_z \mathbf{u}_z,$$

$$\mathbf{F} = F_z \mathbf{u}_z.$$
(5)

The scalar wave functions  $A_z$  and  $F_z$  obey the scalar Helmholtz equation

$$\nabla^2 \psi + k^2 \psi = 0, \tag{6}$$

with  $k^2 = \epsilon_r k_0^2$ .

After separation of variables in cylindrical coordinates, the  $TE_z$  solution is found by choosing  $\mathbf{A}=0$ . Applying the boundary conditions leads to

$$\psi = R_{k_{\phi}}(k_{\rho}\rho)\sin\left(\frac{m\pi}{\beta}\phi + \frac{m\pi}{2}\right)\cos\left(\frac{n\pi}{z}z + \frac{n\pi}{2}\right),\tag{7}$$

where

$$R_{k_{\phi}}(k_{\rho}\rho) = c_{\text{TE}}(Y'_{k_{\phi}}(k_{\rho}a)J_{k_{\phi}}(k_{\rho}\rho) - J'_{k_{\phi}}(k_{\rho}a)Y_{k_{\phi}}(k_{\rho}\rho)),$$

$$k_{\phi} = \frac{m\pi}{\beta},$$

$$k_{z} = \frac{n\pi}{L},$$

$$k_{\rho} = \sqrt{k^{2} - k_{z}^{2}}.$$
(8)

The  $TM_z$  solution can be found by choosing  $\mathbf{F} = 0$ . Applying the boundary conditions leads to

$$\psi = R_{k_{\phi}}(k_{\rho}\rho)\cos\left(\frac{m\pi}{\beta}\phi + \frac{m\pi}{2}\right)\sin\left(\frac{n\pi}{z}z + \frac{n\pi}{2}\right), \quad (9)$$

where

$$R_{k_{\phi}}(k_{\rho}\rho) = c_{\text{TM}}(Y_{k_{\phi}}(k_{\rho}a)J_{k_{\phi}}(k_{\rho}\rho) - J_{k_{\phi}}(k_{\rho}a)Y_{k_{\phi}}(k_{\rho}\rho)). \tag{10}$$

The constants  $c_{\text{TE}}$  and  $c_{\text{TM}}$  are proportionality coefficients for the  $\text{TE}_z$  and the  $\text{TM}_z$  modes, respectively. Further in this paper, the  $\text{TE}_z$  and  $\text{TM}_z$  modes will also be referred to as the  $\text{TE}_{mn}$  and the  $\text{TM}_{mn}$  modes.

2.2. Resonance Frequency. The dispersion relations are found by imposing all boundary conditions. For the  $TE_z$  modes, the dispersion relation becomes

$$J'_{k_{\phi}}(k_{\rho}a)Y'_{k_{\phi}}(k_{\rho}(a+h)) = J'_{k_{\phi}}(k_{\rho}(a+h))Y'_{k_{\phi}}(k_{\rho}a).$$
(11)

For the  $TM_z$  modes, one finds

$$J_{k_{\phi}}(k_{\rho}a)Y_{k_{\phi}}(k_{\rho}(a+h)) = J_{k_{\phi}}(k_{\rho}(a+h))Y_{k_{\phi}}(k_{\rho}a).$$
 (12)

The resonance frequencies are found as zeros of these equations.

*2.3. Radiation Pattern.* The radiation pattern can be calculated from the equivalent magnetic currents  $\mathbf{M} = E_{\rho} \mathbf{u}_{\rho} \times \mathbf{u}_{n}$  along the edges of the curved patch [10, 18].

In general,  $E_{\rho}$  can be written as

$$E_{\rho} = \lambda(\rho) \cos\left(\frac{m\pi}{\beta}\phi + \frac{m\pi}{2}\right) \cos\left(\frac{n\pi}{L}z + \frac{n\pi}{2}\right),$$
 (13)

where  $\lambda(\rho)$  is a mode-dependent factor. For the TE<sub>z</sub> modes,  $\lambda(\rho)$  is defined as

$$\lambda_{\text{TE}}(\rho) = -\frac{1}{\rho} \frac{m\pi}{\beta} R_{m\pi/\beta} \left( \sqrt{k^2 - \left(\frac{n\pi}{L}\right)^2} \rho \right). \tag{14}$$

For the  $TM_z$  modes,  $\lambda(\rho)$  becomes

$$\lambda_{\text{TM}}(\rho) = -\frac{j\omega}{\epsilon} \frac{n\pi}{L} \sqrt{k^2 - \left(\frac{n\pi}{L}\right)^2} R'_{m\pi/\beta} \left(\sqrt{k^2 - \left(\frac{n\pi}{L}\right)^2} \rho\right). \tag{15}$$

After some calculations, the following far-field components are found:

$$E_{\theta} = \frac{\lambda(a+h)}{2\pi^{2}\sin\theta} \frac{e^{-jk_{0}r}}{r} \sigma(n, -Lk_{0}\cos\theta)$$

$$\cdot \sum_{p=-\infty}^{+\infty} \frac{e^{jp\phi}j^{p+1}I(m, p, \beta)}{H_{p}^{(2)}((a+h)k_{0}\sin\theta)},$$

$$E_{\phi} = j\frac{\lambda(a+h)}{2\pi^{2}} \frac{e^{-jk_{0}r}}{r}$$

$$\cdot \sum_{p=-\infty}^{+\infty} \frac{e^{jp\phi}j^{p+1}}{H_{p}^{(2)'}((a+h)k_{0}\sin\theta)}$$

$$\times \left(\sigma(m, p\beta)I(n, -k_{0}\cos\theta, L)\right)$$

$$-\frac{p\cos\theta}{(a+h)k_{0}\sin^{2}\theta}$$
(16b)

with

$$\sigma(q,a) = (-1)^{q} e^{-ja/2} - e^{ja/2},$$

$$I(q,a,b) = \int_{-b/2}^{b/2} \cos\left(\frac{q\pi}{b}x + \frac{q\pi}{2}\right) e^{-jax} dx,$$

$$= j \frac{ab^{2} \sigma(q,ab)}{a^{2}b^{2} - a^{2}\pi^{2}}.$$
(17)

# 3. Validation of the Model for Large Curvature Radii

Now, the analytical model will be verified for the limit case where the curvature radius a tends to  $\infty$ . A rectangular cavity is then obtained, and the following relation should be found:

$$k^2 = \left(\frac{m\pi}{W}\right)^2 + \left(\frac{n\pi}{L}\right)^2 + \left(\frac{l\pi}{h}\right)^2. \tag{18}$$

By rewriting (11) and (12) using the substitutions

$$v = \frac{m\pi}{\beta},\tag{19a}$$

$$\sec \alpha = \sqrt{k^2 - \left(\frac{n\pi}{L}\right)^2} \frac{W - \beta hd}{m\pi},$$
 (19b)

$$\sec \gamma = \sqrt{k^2 - \left(\frac{n\pi}{L}\right)^2 \frac{W - \beta h(d-1)}{m\pi}},$$
 (19c)

we obtain

$$J_{\nu}(\nu \sec \alpha) Y_{\nu}(\nu \sec \gamma) = J_{\nu}(\nu \sec \gamma) Y_{\nu}(\nu \sec \alpha), \qquad (20a)$$

$$J'_{\nu}(\nu \sec \alpha) Y'_{\nu}(\nu \sec \gamma) = J'_{\nu}(\nu \sec \gamma) Y'_{\nu}(\nu \sec \alpha). \tag{20b}$$

When taking the limit for a to  $\infty$ ,  $\nu$  also goes to  $\infty$ , while  $\alpha$  and  $\gamma$  remain constant. Debye's asymptotic expansion for large-order Bessel functions can then be utilised for  $\nu \to \infty$  [19]:

$$J_{\nu}(\nu \sec \chi) \sim \sqrt{\frac{2}{\pi \nu \tan \chi}} \left( \cos \xi \sum_{k=0}^{\infty} \frac{U_{2k}(j \cot \chi)}{\nu^{2k}} - j \sin \xi \sum_{k=0}^{\infty} \frac{U_{2k+1}(j \cot \chi)}{\nu^{2k+1}} \right), \tag{21a}$$

$$Y_{\nu}(\nu \sec \chi) \sim \sqrt{\frac{2}{\pi \nu \tan \chi}} \left( \sin \xi \sum_{k=0}^{\infty} \frac{U_{2k}(j \cot \chi)}{\nu^{2k}} + j \cos \xi \sum_{k=0}^{\infty} \frac{U_{2k+1}(j \cot \chi)}{\nu^{2k+1}} \right), \tag{21b}$$

$$J_{\nu}'(\nu \sec \chi) \sim \sqrt{\frac{\sin 2\chi}{\pi \nu}} \left( -\sin \xi \sum_{k=0}^{\infty} \frac{V_{2k}(j\cot \chi)}{\nu^{2k}} - j\cos \xi \sum_{k=0}^{\infty} \frac{V_{2k+1}(j\cot \chi)}{\nu^{2k+1}} \right), \tag{21c}$$

$$Y_{\nu}'(\nu \sec \chi) \sim \sqrt{\frac{\sin 2\chi}{\pi \nu}} \left(\cos \xi \sum_{k=0}^{\infty} \frac{V_{2k}(j\cot \chi)}{\nu^{2k}} - j\sin \xi \sum_{k=0}^{\infty} \frac{V_{2k+1}(j\cot \chi)}{\nu^{2k+1}}\right),$$
(21d)

with

$$\xi = \nu \left( \tan \chi - \chi \right) - \frac{\pi}{4},\tag{22}$$

and  $U_k(p)$  and  $V_k(p)$  polynomials in p of degree 3k, given by  $U_0(p) = V_0(p) = 1$ , and

$$U_{k+1}(p) = \frac{1}{2}p^{2}(1-p^{2})U'_{k}(p) + \frac{1}{8}\int_{0}^{p}(1-5t^{2})U_{k}(t) dt,$$

$$V_{k+1}(p) = U_{k+1}(p) - \frac{1}{2}p(1-p^{2})U_{k}(p)$$

$$- p^{2}(1-p^{2})U'_{k}(p).$$
(23)

Using the lowest-order Debye's expression, one finds for both the dispersion relations:

$$\sin \xi \cos \xi' = \sin \xi' \cos \xi \tag{24}$$

with

$$\xi = \nu(\tan \alpha - \alpha) - \frac{\pi}{4},$$
  

$$\xi' = \nu(\tan \gamma - \gamma) - \frac{\pi}{4}.$$
(25)

This leads to

$$\tan \gamma - \gamma = \tan \alpha - \alpha + \frac{l}{n}\beta. \tag{26}$$

Assuming that  $h \ll \lambda$ , a first-order Taylor expansion can be performed on  $\tan \gamma(h) - \gamma(h)$  and  $\tan \alpha(h) - \alpha(h)$  for  $h \to 0$ . Expression (26) then becomes

$$\sin \alpha(0) = \frac{l\pi}{h} \frac{1}{\sqrt{k^2 - (n\pi/L)^2}}.$$
 (27)

Combining (19b) and (27) results in

$$\sqrt{1 - \frac{1}{\left(k^2 - (n\pi/L)^2\right)(W/(m\pi))^2}} = \frac{l\pi}{h} \frac{1}{\sqrt{k^2 - (n\pi/L)^2}},$$
(28)

which finally leads to (18) and verifies the transition to a rectangular cavity.

# 4. Comparison of Experimental and Theoretical Results

Using this model, the resonance frequencies and radiation patterns of flexible textile antennas can be calculated analytically. However, when comparing the measured resonance frequencies of a fabricated textile antenna with the frequencies obtained from our model for different bending radii, a discrepancy is noticed. This is due to the fact that textile antennas are subjected to compression when bent. Consequently, the substrate permittivity will change as a function of the bending radius. This effect needs to be incorporated in our model in order to provide a good prediction of the resonance frequency. In other words, an expression for the permittivity  $\epsilon_{r,\text{comp}}$  of a substrate subjected to compression needs to be found.

4.1. Experimental Setup. By measuring five prototypes with different specifications and constructed on different flexible materials, the effect of several parameters on  $\epsilon_{r,\text{comp}}$  is investigated. Their geometry is displayed in Figure 3. All prototypes are fed by a probe feed structure, with the probe located on the perpendicular bisector of the  $L_p$  edge.

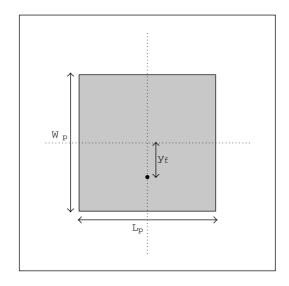
Prototypes 1 and 2 are both fabricated on aramid substrates and are designed for the 1.57 GHz GPS band. The patch material of prototype 1 is the stretchable electro-textile Flectron, whereas nonstretchable copper foil is used for prototype 2. Prototypes 3, 4, and 5 are fabricated on cotton substrates and have copper foil as patch material. Prototypes 3 and 5 are designed for the 1.57 GHz GPS band, whereas prototype 4 operates in the 2.45 GHz ISM band. The difference between prototype 3 and 5 is the thickness of the substrate. The parameters of the prototypes are shown in Table 1, where the substrate height h is determined based on the ISO 5084 standard [20].

For these prototypes, the resonance frequencies in flat and bent state are measured by means of a PNA-X vector network analyser. The bent states are realised by attaching the antennas to plastic cylinders with different radii ranging from 31.5 mm to 90 mm. These radii resemble typical curvatures of human body parts.

When the antennas are bent in the  $W_p$  direction, the model is used by setting  $L = L_p$  and  $W = W_p$ . According to the model, the  $\mathrm{TE}_{10}$  mode is then excited and (11) needs to be solved in order to determine the resonance frequency. Similarly, when bending the antennas in the  $L_p$  direction, one has to set  $L = W_p$  and  $W = L_p$ . According to the model, the  $\mathrm{TM}_{01}$  mode is then excited, and the resonance frequency follows from (12).

TABLE 1:	Parameters	of the	prototypes.
----------	------------	--------	-------------

Prototype	1	2	3	4	5
$L_p$ [mm]	81.2	81.2	78.5	52.5	78.5
$W_p$ [mm]	69.25	69.25	69.3	43.7	68.3
<i>h</i> [mm]	2	2	2.7	2.7	4.05
$y_f$ [mm]	16	16	17	11	16.8
$\epsilon_r$	1.75	1.75	1.715	1.715	1.715
d	0.5	1	1	1	1



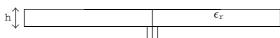


FIGURE 3: Geometry of a prototype.

- 4.2. Compression Effects on the Permittivity. After comparing the measured resonance frequencies of the prototypes for the different bending radii, the following observations are made:
  - (1) The  $\epsilon_{r,\text{comp}}$  is inversely proportional to the bending radius a, since compression becomes stronger as the curvature radius decreases.
  - (2) The part of the substrate that undergoes the largest compression has a height h(d 0.5), and  $\epsilon_{r,\text{comp}}$  is directly proportional to this.
  - (3) The compression is not frequency dependent.

Based on these observations, an empirical formula for  $\epsilon_{r,\text{comp}}$  can be found:

$$\epsilon_{r,\text{comp}} = \epsilon_{r,\text{flat}} \left( 1 + \eta \frac{h(d - 0.5)}{a} \right).$$
(29)

The permittivity  $\epsilon_{r,\text{flat}}$  is obtained by evaluating (18) after measuring the antenna in flat state under well-defined environmental conditions. It therefore captures effects such as humidity, temperature, and fringing effects, while the second term in (29) isolates the effect of bending. The parameter h is the height of the flexible substrate in flat state, measured

Table 2: Proportionality factors  $\eta$  for the compression correction term.

Prototype	2	3	4	5
TE <sub>10</sub> mode	1 589	1 497	1 472	1 485
TM <sub>01</sub> mode	380	214	592	654

Table 3: Relative mean error between the modeled and measured resonance frequencies of the bent prototypes for the  $TE_{10}$  mode.

Prototype	1	2	3	4	5
τ(0) [%]	0.09	1.56	1.97	1.94	2.91
$\tau(\eta)$ [%]	0.09	0.03	0.09	0.07	0.12

Table 4: Relative mean error between the modeled and measured resonance frequencies of the bent prototypes for the TM<sub>01</sub> mode.

Prototype	1	2	3	4	5
τ(0) [%]	0.04	0.37	0.23	0.76	1.28
$\tau(\eta)$ [%]	0.04	0.03	0.07	0.10	0.07

according to the ISO 5084 standard. This simplifies the work of the designer, since he does not need to measure the height of the substrates for each bending radius.

Expression (29) also takes into account the following remarks:

- (1) When *a* tends to  $\infty$ , the antenna becomes planar and  $\epsilon_{r,\text{flat}}$  is found.
- (2) For perfectly stretchable antennas,  $\epsilon_{r,\text{comp}} = \epsilon_{r,\text{flat}}$ . Hence, the resonance frequency will not change when the antenna is bent.

The proportionality factor  $\eta$  can be found for each prototype with a nonstretchable patch by minimising an error function  $\tau(\eta)$ , defined by

$$\tau(\eta) = \frac{1}{N} \sum_{i=1}^{N} \frac{\left| f_{\text{mod },i}(\eta) - f_{\text{meas},i} \right|}{f_{\text{meas},i}}.$$
 (30)

This function represents the relative mean error between the modeled and measured resonance frequencies of a bent prototype, with *N* being the number of cylinders.

The calculation of  $\eta$  is carried out iteratively by combining MATLAB's minimisation function *fminsearch* with our analytical model in Maple. The obtained values for both the TE<sub>10</sub> and the TM<sub>01</sub> modes are shown in Table 2. The  $\eta$ -values for the TE<sub>10</sub> modes are quite similar, whereas the values for the TM<sub>01</sub> mode exhibit larger differences. Also, there is a significant difference between the values for the TE<sub>10</sub> mode and the TM<sub>01</sub> mode. This is due to the geometry and feeding structure of the prototypes. The solid feed points are not located in the center of the patches and thus produce different compression effects, depending on whether the prototypes are bent in the  $W_p$  direction or the  $L_p$  direction.

Tables 3 and 4 display the error values when using  $\epsilon_r = \epsilon_{r,\text{flat}}$  (shown as  $\tau(0)$ ) and  $\epsilon_r = \epsilon_{r,\text{comp}}$  (shown as  $\tau(\eta)$ ) for the TE<sub>10</sub> mode and the TM<sub>01</sub> mode, respectively. A constant

small error of ca. 0.1% can be found for all prototypes when using the ideal proportionality factor  $\eta$ , validating the use of (29).

4.3. Resonance Frequency. Figure 4 shows the modeled and measured resonance frequencies of prototypes 1 and 3 as a function of the bending radius when the antennas are bent in the  $W_p$  direction. Prototype 1 has a stretchable patch, so patch elongation occurs and the substrate will not be compressed ( $\epsilon_{r,\text{comp}} = \epsilon_{r,\text{flat}}$ ). Consequently, the resonance frequency almost does not change when the antenna is bent. Prototype 3 has a nonstretchable patch, therefore the resonance frequency will change with varying curvature radii. The resonance frequencies obtained from the model with and without compression correction are displayed, where the model without compression correction can be seen as if the antenna would be conformally attached to the cylinders. Since the prototypes are flexible deformable antennas, the measured curve follows the curve obtained from the model with compression correction. One also notices that the increase in resonance frequency for smaller bending radii is not as distinct as compared to the conformal case. This behaviour is also observed for the other prototypes.

In Figure 5, the modeled and measured resonance frequencies of prototypes 1 and 3 are displayed as a function of the bending radius when the antennas are bent in the  $L_p$  direction. According to the model, the resonance frequency of prototype 1 does not vary since no compression occurs and the resonant length is not bent in  $TM_z$  mode. For prototype 3, a decrease in resonance frequency now occurs for smaller bending radii. This effect is purely due to compression of the substrate, which can also be noticed by comparison with the curve obtained from the model without compression correction, where the resonance frequency does not change. Again, this result is also observed for the other prototypes.

As a footnote, we like to point out the difference in resonance frequency for the flat state between Figures 4 and 5. The measurements for the  $TM_z$  case were performed later in time than those for the  $TE_z$  case. As a result, the resonance frequencies of the prototypes have changed due to humidity effects. This effect is larger for prototype 3 than for prototype 1, since the cotton substrate suffers more from this effect than the aramid substrate [21]. However, the model still remains accurate, since it only takes into account bending effects. In other words, using this formulation, the effect of bending on the behaviour of deformable antennas can be isolated.

4.4. Radiation Pattern. Figure 6 shows the modeled and measured radiation patterns in the XY plane (as defined in Figure 1) of the stretchable prototype 1 for curvature radii of 90 mm and 31.5 mm at a frequency of 1.567 GHz (the resonance frequency of the planar antenna) when the antenna is bent in the  $W_p$  direction. The radiation pattern calculated by the model is normalised with respect to the measured gain in broadside direction, since only its shape can be predicted. For a curvature radius of 90 mm, the measured 3 dB beamwidth is 75°, and the modeled 3 dB beamwidth is 80°. For a bending

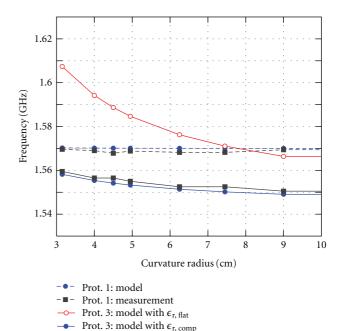


Figure 4: Resonance frequencies of prototypes 1 and 3 as a function of the bending radius when the antennas are bent along the  $W_p$  direction.

Prot. 3: measurement

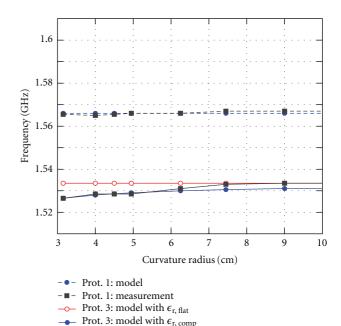


Figure 5: Resonance frequencies of prototypes 1 and 3 as a function of the bending radius when the antennas are bent along the  $L_p$  direction.

Prot. 3: measurement

radius of 31.5 mm, the measured 3 dB beamwidth is  $86^{\circ}$ , and the modeled 3 dB beamwidth is  $84^{\circ}$ .

On Figure 7, the modeled and measured radiation patterns in the XY plane of the nonstretchable prototype 2 are displayed for curvature radii of 90 mm and 31.5 mm at a frequency of 1.573 GHz (the resonance frequency of

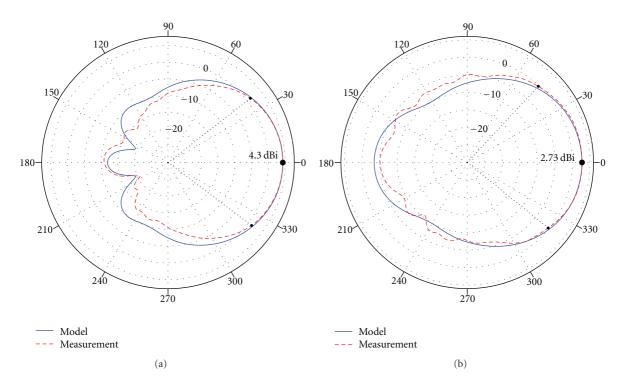


FIGURE 6: Radiation pattern in XY plane of prototype 1 for 1.567 GHz when bent in the  $W_p$  direction. The bending radii are 90 mm (a) and 31.5 mm (b).

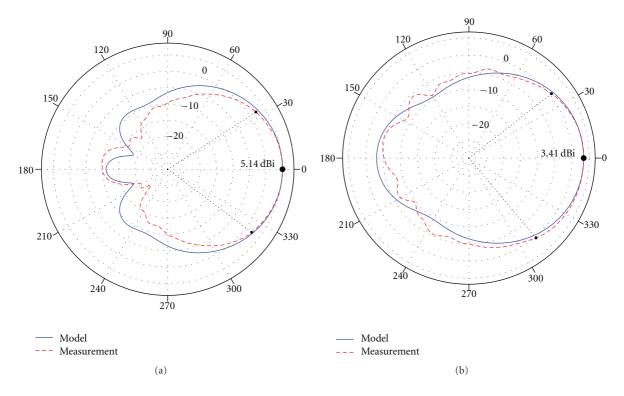


FIGURE 7: Radiation pattern in XY plane of prototype 2 for 1.573 GHz when bent in the  $W_p$  direction. The bending radii are 90 mm (a) and 31.5 mm (b).

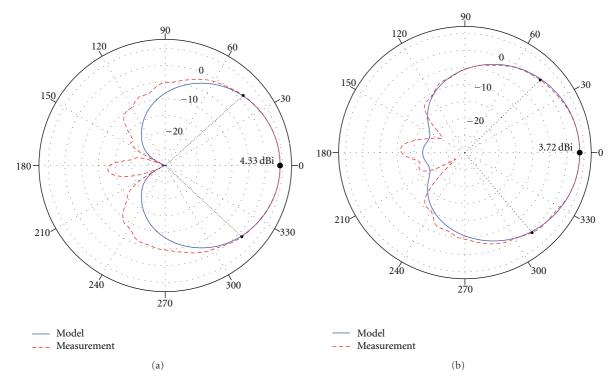


FIGURE 8: Radiation pattern in XY plane of prototype 2 for 1.573 GHz when bent in the  $L_p$  direction. The bending radii are 90 mm (a) and 40 mm (b).

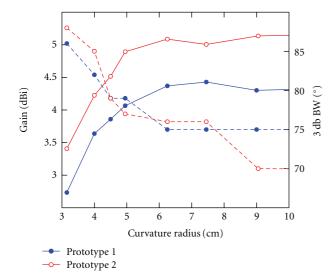


FIGURE 9: Measured gain and 3 dB beamwidth of prototypes 1 and 2 when the antennas are bent in the  $W_p$  direction. The solid lines indicate the gain along broadside, and the dashed lines show the 3 dB beamwidths.

the planar antenna) when the antenna is bent in the  $W_p$  direction. For a curvature radius of 90 mm, the measured 3 dB beamwidth is 70°, and the modeled 3 dB beamwidth is 80°. For a bending radius of 31.5 mm, the measured 3 dB beamwidth is 88°, and the modeled 3 dB beamwidth is 86°.

There is no distinct difference between the shape of the radiation patterns of prototype 1 and 2. Hence, stretching has almost no influence on the radiation pattern of bent flexible antennas. Also, from the model we conclude that the use of the corrected permittivity due to compression has almost no influence on the radiation pattern.

Figure 8 shows the modeled and measured radiation patterns in the XY plane of prototype 2 for curvature radii of 90 mm and 40 mm at a frequency of 1.573 GHz when the antenna is bent in the  $L_p$  direction. For a curvature radius of 90 mm, the measured 3 dB beamwidth is 85°, and the modeled 3 dB beamwidth is 82°. For a bending radius of 40 mm, the measured 3 dB beamwidth is 94°, and the modeled 3 dB beamwidth is 94°.

The influence of bending on the gain along broadside direction and the 3 dB beamwidth is shown in Figure 9. The measured gain and 3 dB beamwidth of prototype 1 and 2 when the antennas are bent in the  $W_p$  direction are displayed. For smaller bending radii, a decrease of the maximum gain and an increase of the 3 dB beamwidth are noticed. This effect is stronger for antennas with nonstretchable patches. The same results can be found when bending the antennas along the  $L_p$  direction.

#### 5. Conclusion

In this paper, a novel analytical model for cylindrically bent textile patch antennas was proposed. The starting point was the existing analytical model for conformal cylindrical-rectangular patch antennas, in which additional effects due to stretching and compression were incorporated. The model allows to calculate textile antenna performance parameters, such as resonance frequency and radiation pattern, as a function of the bending radius. Moreover, it answers the need for a fast and accurate prediction tool for bent textile patch antennas, in contrast to previously proposed measurementor simulation-based analysis methods, which are time consuming, expensive, and do not provide physical insight into the mechanisms of bending. The resonance frequencies as a function of the bending radius can be obtained by numerically solving the cavity's dispersion relations, while the farfield patterns are given in closed-form expressions. Two main novelties were introduced in the proposed model, dedicated to the particular case of textile antennas:

- (1) The patch elongation due to stretching has been derived by geometrical considerations and has been taken into account in the model.
- (2) An expression for the substrate permittivity as a function of the bending radius has been proposed, which isolates the effect of bending from all other external effects.

The validity of the proposed model has been successfully verified in two ways. First, it was analytically demonstrated that for large curvature radii (i.e., for  $a \to \infty$ ) the dispersion relations converge to the one valid for the flat state. Secondly, an experimental verification of the model was performed by means of a measurement campaign in which the resonance frequencies and the radiation patterns of five different textile patch antenna prototypes were measured for different bending radii. In particular, the new model now captures the following two effects:

- (1) Concerning the resonance frequency, the measurements showed a significant variation for antennas with a nonstretchable patch and a nearly constant resonance frequency for antennas with a perfectly stretchable patch.
- (2) Regarding the radiation patterns, the experiments demonstrated that stretching has almost no influence on the radiation pattern of bent flexible antennas.

In summary, an excellent agreement is now obtained between measured results and the new model.

Based on the obtained results, it can be concluded that the proposed model represents a valuable tool for textile antenna design engineers, allowing performance prediction and analysis of bent textile antennas. The model shows clear advantages with respect to previously employed methods, such as measurements and simulations, in terms of accuracy and computational cost. Moreover, it provides physical insight into bending mechanisms of textile patch antennas.

#### Acknowledgments

The work of F. Boeykens was supported by a doctoral grant from the Agency for Innovation by Science and Technology in Flanders (IWT). L. Vallozzi is a postdoctoral fellow of the FWO.

#### References

- [1] P. Salonen, L. Sydanheimo, M. Keskilammi, and M. Kivikoski, "Small planar inverted-F antenna for wearable applications," in *Proceedings of the 3rd International Symposium on Wearable Computers*, pp. 95–100, San Francisco, Calif, USA, October 1999
- [2] M. Klemm, I. Locher, and G. Tröster, "A novel circularly polarized textile antenna for wearable applications," in *Proceedings of the 7th European Conference on Wireless Technology (ECWT '04)*, pp. 285–288, Amsterdam, The Netherlands, October 2004
- [3] P. J. Massey, "Mobile phone fabric antennas integrated within clothing," in *Proceedings of the 11th International Conference on Antennas and Propagation*, pp. 344–347, Manchester, UK, April 2001.
- [4] A. Tronquo, H. Rogier, C. Hertleer, and L. Van Langenhove, "Robust planar textile antenna for wireless body LANs operating in 2.45 GHz ISM band," *Electronics Letters*, vol. 42, no. 3, pp. 142–143, 2006.
- [5] C. Hertleer, H. Rogier, L. Vallozzi, and L. Van Langenhove, "A textile antenna for off-body communication integrated into protective clothing for firefighters," *IEEE Transactions on Antennas and Propagation*, vol. 57, no. 4, pp. 919–925, 2009.
- [6] A. Bonfiglio and D. De Rossi, *Wearable Monitoring Systems*, Springer, New York, NY, USA, 2011.
- [7] Y. T. Lo, D. Solomon, and W. F. Richards, "Theory and experiment on microstrip antennas," *IEEE Transactions on Antennas and Propagation*, vol. 27, no. 2, pp. 137–145, 1979.
- [8] C. M. Krowne, "Cylindrical-rectangular microstrip antenna," IEEE Transactions on Antennas and Propagation, vol. 31, no. 1, pp. 194–198, 1983.
- [9] J. S. Dahele, R. J. Mitchell, K. M. Luk, and K. F. Lee, "Effect of curvature on characteristics of rectangular patch antenna," *Electronics Letters*, vol. 23, no. 14, pp. 748–749, 1987.
- [10] K. M. Luk, K. F. Lee, and J. S. Dahele, "Analysis of the cylindrical-rectangular patch antenna," *IEEE Transactions on Antennas and Propagation*, vol. 37, no. 2, pp. 143–147, 1989.
- [11] J. Ashkenazy, S. Shtrikman, and D. Treves, "Electric surface current model for the analysis of microstrip antennas on cylindrical bodies," *IEEE Transactions on Antennas and Propagation*, vol. 33, no. 3, pp. 295–300, 1985.
- [12] T. M. Habashy, S. M. Ali, and J. A. Kong, "Input impedance and radiation pattern of cylindrical-rectangular and wraparound microstrip antennas," *IEEE Transactions on Antennas and Propagation*, vol. 38, no. 5, pp. 722–731, 1990.
- [13] D. H. Werner, R. J. Allard, R. A. Martin, and R. Mittra, "A reciprocity approach for calculating radiation patterns of arbitrarily shaped microstrip antennas mounted on circularly cylindrical platforms," *IEEE Transactions on Antennas and Propagation*, vol. 51, no. 4, pp. 730–738, 2003.
- [14] T. Kellomäki, J. Heikkinen, and M. Kivikoski, "Effects of bending GPS antennas," in *Proceedings of the Asia-Pacific Microwave Conference (APMC '06)*, pp. 1597–1600, Yokohama, Japan, December 2006.
- [15] L. Vallozzi, H. Rogier et al., "Radiation characteristics of a textile antenna designed for apparel application," in *Proceed*ings of the IEEE Galveston Bay Section Symposium for Space Applications of Wireless and RFID (SWIRF '07), Houston, Tex, USA, May 2007.
- [16] S. Sankaralingam and B. Gupta, "Development of textile antennas for body wearable applications and investigations on their performance under bent conditions," *Progress In Electromagnetics Research B*, no. 22, pp. 53–71, 2010.

- [17] I. Locher, M. Klemm, T. Kirstein, and G. Tröster, "Design and characterization of purely textile patch antennas," *IEEE Transactions on Advanced Packaging*, vol. 29, no. 4, pp. 777–788, 2006.
- [18] R. F. Harrington, *Time-Harmonic Electromagnetic Fields*, McGraw–Hill, New York, NY, USA, 1961.
- [19] F. W. J. Olver, D. W. Lozier, R. F. Boisvert, and C. W. Clark, "Bessel functions," in NIST Handbook of Mathetmatical Functions, pp. 231–232, Cambridge University Press, New York, NY, USA, 2010.
- [20] Determination of thickness of textiles and textile products, ISO Standard 5084, 1996.
- [21] C. Hertleer, A. van Laere, H. Rogier, and L. van Langenhove, "Influence of relative humidity on textile antenna performance," *Textile Research Journal*, vol. 80, no. 2, pp. 177–183, 2010.

Hindawi Publishing Corporation International Journal of Antennas and Propagation Volume 2012, Article ID 687256, 9 pages doi:10.1155/2012/687256

### Research Article

# Flexible Hilbert-Curve Loop Antenna Having a Triple-Band and Omnidirectional Pattern for WLAN/WiMAX Applications

#### Dang-Oh Kim, Che-Young Kim, and Dae-Geun Yang

School of Electronics Engineering, Kyungpook National University, Sankyuk-dong Puk-gu, Daegu 702-701, Republic of Korea

Correspondence should be addressed to Che-Young Kim, cykim@ee.knu.ac.kr

Received 14 December 2011; Revised 20 January 2012; Accepted 25 January 2012

Academic Editor: Ana Collado

Copyright © 2012 Dang-Oh Kim et al. This is an open access article distributed under the Creative Commons Attribution License, which permits unrestricted use, distribution, and reproduction in any medium, provided the original work is properly cited.

A triple-band flexible loop antenna is proposed for WLAN/WiMAX applications in this paper. The proposed antenna is formed by the third-order Hilbert-curve and bending type structure which provides flexible characteristics. Even though the radius of the curvature for bending antennas is changed, a triple-band feature still remains in the proposed antenna. Moreover, the antenna exhibits the characteristics of omnidirectional radiation pattern and circular polarization. To verify the receiving performance of antenna, a simulation on the antenna factor was conducted by an EM simulator. Based on these results, the suggested antenna makes a noteworthy performance over typical loop antennas.

#### 1. Introduction

Recently, the proliferation of radio devices in diverse shapes and rapid progress in flexible technology require the antennas mounted on wireless devices to be manufactured in various shapes. Furthermore, vibrant studies of wearable systems, RFID tags, and flexible displays have spurred on much attention to the flexible antenna technology. Especially, there are increasing requirements of flexible antennas with lowprofile, compact size, and multiband including the wireless local area network (WLAN) band 2.4/5.2/5.8 GHz and the world interoperability for microwave access (WiMAX) band 3.5 GHz due to the explosive growth of demand for wireless data communication. The antennas operating for wearable systems and RFID tags are prone to the proximity effect by the material itself so that they usually suffer from degrading performance due to the resonating currents on the ground plane and their compact size. Particularly, these weaknesses mainly occur in the antennas used for data communications. Once encountered, to mitigate the performance degradation, a loop antenna has been an alternative since the current induced on the ground surface becomes small in magnitude [1-3]. Consequently, the loop antenna is regarded as a reference antenna in this paper.

This paper presents a flexible Hilbert curve loop antenna endorsing the Hilbert curve over the typical rectangular

loop, which is aimed for WLAN/WiMAX applications. The suggested antenna possesses the flexible bending structure and shows triple-band characteristics at 2.4/3.5/5.5 GHz operating bands. In addition, the antenna exhibits the omnidirectional pattern without null in comparison to a traditional loop antenna. In order to check the receiving performance of antenna, the antenna factor K is examined with an EM simulator. The structure of our proposed antenna is different from conventional flexible antennas such as spiral curve-shaped monopole antenna [4], conventional patchshaped antenna [5], meander line antenna [6, 7], combshaped monopole antenna [8], inverted-F-shaped antenna [9], ultra-wideband (UWB) antenna [10], the zeroth-order resonant (ZOR) antenna [11-13], coplanar waveguide-(CPW-) fed monopole antenna [14], and folded slot dipole antenna [15]. Moreover, this is the first time the Hilbert-curve geometry to a loop antenna has been applied to such an application.

#### 2. Description of the Antenna

In this study, the Hilbert curve, first proposed by Hilbert in 1891, was used as the space-filling curve structure. The Hilbert-curve geometry in antenna design has been explored to reduce the antenna size and to make it operate at multiple

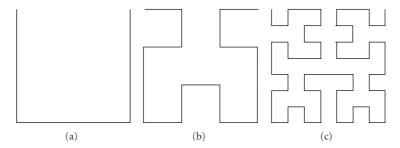


FIGURE 1: The Hilbert curves with increasing iteration order number n. (a) First order, (b) Second order, and (c) Third order.

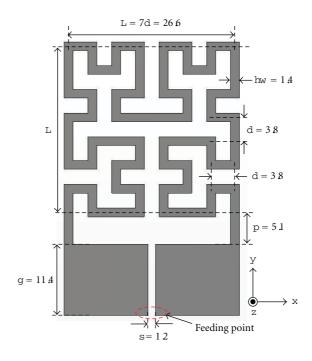


Figure 2: Geometry and dimensions of the proposed Hilbert-curve loop antenna.

frequencies [16-22]. In addition, recent research has shown the use of this curve in the designs of the circular polarized antennas, metamaterial resonators, and high impedance frequency-selective structures (FSSs) [23-26]. The issue on the Hilbert-curve geometry is to find the most effective way to fill the lines in the fixed space. The Hilbert antenna has shown to be an effective structure to obtain small antennas [27]. The performance of the meander line is similar to the Hilbert curve. But unlike the meander line, the Hilbertcurve takes the advantage of tagging the iteration order number associated with geometries and providing other performances such as circular polarization. Figure 1 shows the first few iterations order of Hilbert curve geometry. It is self-evident that as the iteration order increases, the total length of the line segment is increased thereafter. The sum of line segment *S* is given by [18, 24]

$$S = (2^{2n} - 1)d = (2^{n} + 1)L,$$

$$d = \frac{L}{2^{n} - 1},$$
(1)

where L is the side dimension of the Hilbert curve, d is the length of each line segment, and n indicates the order of iteration. Namely, as the iteration order is increased, the total length of the line segment is increased while its footprint size is kept fixed. From the electrical resonance length point of view, this property is what allows the Hilbert curve to possess a relatively low resonant frequency, which could lead to the miniaturization of structure. In this paper, the Hilbert curve with the third-order (n = 3) iteration was fit into a loop antenna forming a closed-loop configuration. Figure 2 shows the configuration and dimensions of the flat Hilbert curve loop antenna in a flat shape without bending. The proposed antenna consists of only a copper film without the dielectric substrate. The top part of the antenna is the third-order Hilbert curve where the bottom part of antenna reaches to the feeding point as shown in Figure 1(c). The matching plane to tune the input impedance of the antenna is embedded in the feeding part. With adjustment of the length g and s sizing the matching plane, the impedance matching is accomplished. Also, the aggregated structure



FIGURE 3: Geometry of the flexible Hilbert-curve loop antenna and radius of its curvature.

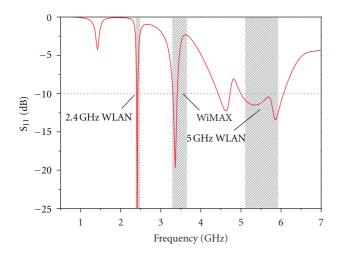


Figure 4:  $S_{11}$  results of the flexible Hilbert-curve loop antenna.

maintains its symmetry about the center line. All of the geometrical parameters of the antenna were optimized by Microwave Studio of CST. Figure 3 shows the radius of curvature of the bending structure and the geometry bent to the flexible Hilbert-curve loop antenna as shown in Figure 2. The antenna of the bending structure with the fixed width W has the radius of curvature r with a corresponding bending level. The degree of bending is measured by the radius of curvature by

$$r = \frac{180 \cdot W}{\pi \theta}.\tag{2}$$

#### 3. Results and Discussion

Figure 4 shows the simulated  $S_{11}$  plots of the finalized flexible Hilbert-curve loop antenna with 55 mm radius of

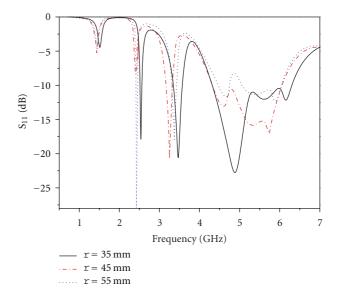


FIGURE 5:  $S_{11}$  results of the proposed antenna in terms of the radius of curvature.

curvature. As depicted by the simulation result, this loop antenna operates at a frequency of WLAN band 2.45 GHz, WiMAX band 3.35 GHz. Moreover, the antenna covers the entire 5 GHz WLAN bands. In here, the side dimension L of the Hilbert curve can be put to about  $0.2\lambda$  (at  $2.45\,\text{GHz}$ ),  $0.3 \lambda$  (at 3.45 GHz), and  $0.5 \lambda$  (at 5.5 GHz). The simulated  $S_{11}$ plots of the antennas bent with different radii of curvature are shown in Figure 5. This figure reveals that the return loss result of the antenna is changed by the adjustment of the bending level of the proposed antenna. Although the resonant frequencies were marginally shifted to adjacent frequency owing to antenna bending, the operating frequencies of the antenna were still maintained in the targeted band within the limit of the partial radius of curvature. From this result, the proposed antenna can be adaptable to bending structures and finds its way to flexible applications.

Figure 6 shows the simulated omnidirectional radiation pattern of the proposed flexible Hilbert-curve loop antenna. The radiation pattern in Figure 6 is suitable for the conventional WLAN/WiMAX communication system requiring the omnidirectional pattern. In addition, its most notable distinction of radiation pattern is a uniform pattern without nulling. The maximum gains and radiation efficiencies of antenna are 3.96 dBi (0.88) at 2.45 GHz, 2.88 dBi (0.96) at 3.35 GHz, and 3.84 dBi (0.92) at 5.5 GHz (parenthesis designates the radiation efficiency). Figure 7 shows the simulated surface current distributions at each resonance frequency. The applied power to each antenna is 1 Watt. The large current distribution is indicated in dark color, and the small one is in light color. It is seen that the resonant surface currents concentrated on the Hilbert curve at 2.4 GHz and 3.5 GHz are higher than the case of 5.5 GHz. This means that many segments of the Hilbert curve at 5.5 GHz could not contribute effectively to the working role of the individual antenna segment.

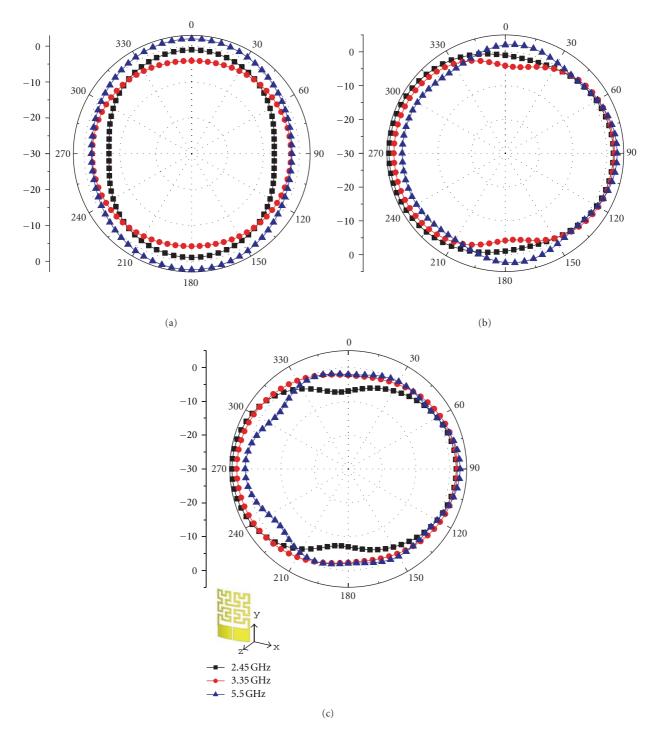


FIGURE 6: Simulated radiation patterns of the proposed antenna at 2.45/3.35/5.5 GHz. (a) xz-plane, (b) yz-plane, and (c) xy-plane.

To demonstrate the superiority of the radiation pattern and receiving performance of the proposed antenna, the conventional rectangular loop antennas operating at each triple band were introduced as a reference antenna in this study. This was rooted in the idea that the operation mechanism and characteristics of the rectangular loop antenna are similar to that of classical circular loop antenna; thus, this rectangular antenna could be a representative of the whole

loop antenna group. Further, the rectangular loop antenna can be analogized with the primitive structure of the proposed Hilbert-curve loop antenna. The geometry and dimensions of the imposed rectangular loop antennas are shown in Figure 8 and tabulated in Table 1. The feeding structure of this antenna is the same as one of the Hilbert-curve loop antennas. For fair comparison between the flexible Hilbert-curve loop antenna and the rectangular loop antenna, three

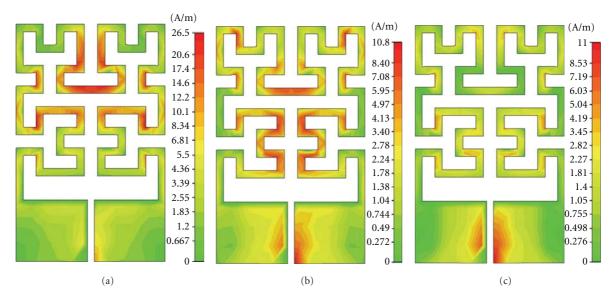


FIGURE 7: Surface current distribution of the proposed antenna at resonance frequencies. (a) 2.45 GHz, (b) 3.35 GHz, and (c) 5.5 GHz.

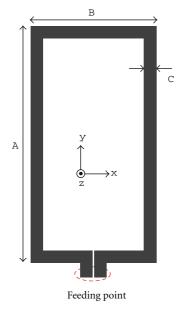


FIGURE 8: Geometry of the reference rectangular loop antenna.

Table 1: Dimensions of the reference rectangular loop antenna.

Dimension	A	В	С
Size (mm) for 2.45 GHz	48.8	26	2.5
Size (mm) for 3.35 GHz	37	19.1	2.5
Size (mm) for 5.5 GHz	22	11.8	1.5

rectangular loop antennas corresponding to each operating band 2.45/3.35/5.5 GHz were designed since the rectangular loop antenna has generally a single operating frequency. The simulated return loss results of the designed rectangular loop antennas are plotted in Figure 9. Note that the size of the Hilbert-curve loop is only 26.6 mm \*26.6 mm compared to

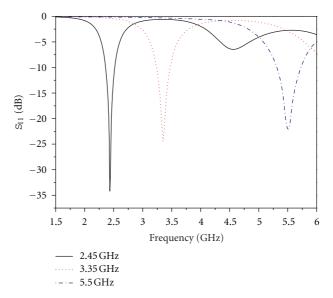


Figure 9:  $S_{11}$  results of the rectangular loop antennas with each operating band.

 $48.8 \,\mathrm{mm} \star 26 \,\mathrm{mm}$  of the rectangular loop, that is, a reduction of two times the area. Figure 10 shows the radiation pattern of the rectangular loop antenna at 2.45 GHz. This pattern is the general radiation pattern of a loop antenna, so other bands such as  $3.35 \,\mathrm{GHz}$  and  $5.5 \,\mathrm{GHz}$  are similar to the pattern of Figure 10. In comparing Figures 6 and 10, in this regard, it is observed that the proposed flexible Hilbert-curve loop antenna achieved an even radiation pattern without null, which indicates that the pattern of the proposed antenna is superior to the pattern of the conventional loop antenna.

To confirm the omnidirectional receiving performance of the proposed antenna, the antenna factor *K* was used in this

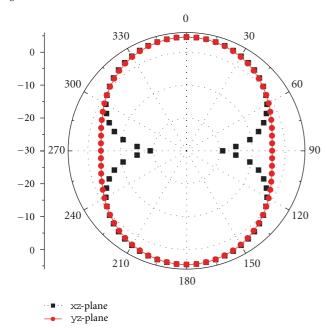


FIGURE 10: Simulated radiation patterns of the reference rectangular loop antenna at 2.45 GHz.

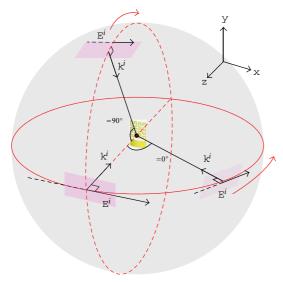
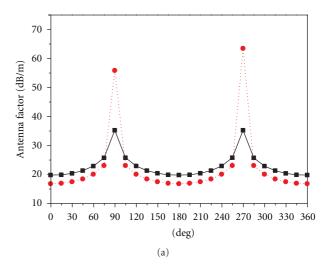


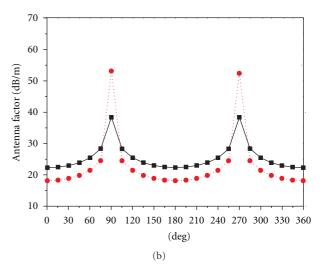
FIGURE 11: Simulation setup of the incident plane wave to obtain the antenna factor K.

paper. The antenna factor is an important antenna parameter to determine the receiving sensitivity of a radio communication system, which becomes one of the significant parameters directly affecting the performance of the WLAN/WiMAX communication system. To calculate the antenna factor, a load resistor of 50  $\Omega$  was connected to the feeding point of the proposed Hilbert loop antenna and rectangular loop antenna. Then, the induced voltage across a load resistor was developed for the incident plane wave. With the obtained voltage, the antenna factor K was calculated through the following equation [28]:

$$K = \frac{E^i}{V_A} [\mathbf{m}^{-1}], \tag{3}$$

where  $V_A$  is the voltage induced on the loaded loop antenna and  $E^i$  is the amplitude of the electric field of the incident





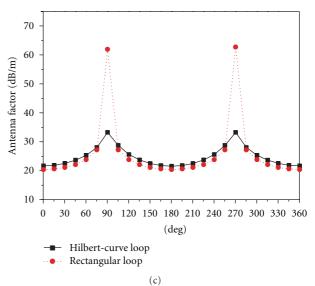
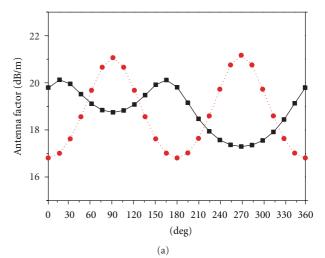


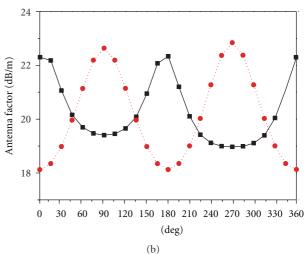
FIGURE 12: Variation of the antenna factor K at  $\phi = 0^\circ$  (xz-plane) for the proposed flexible Hilbert-curve loop antenna and rectangular loop antenna. (a) 2.45 GHz, (b) 3.35 GHz, and (c) 5.5 GHz.

plane wave. Based on the aforementioned simulation, the resultant antenna factor for the various directions of the incident plane wave could be obtained for the proposed antenna and rectangular loop antenna. Figure 11 depicts the simulation configuration of the antenna factor. The amplitude of the incident electric field is the stationary 1 [V/m], and an incident plane wave is propagating toward the center of the antenna. The incident angle of plane wave has two cases: one with  $\phi = 0^{\circ}$  (xz-plane) and the other with  $\phi = 90^{\circ}$  (yz-plane) for all of the rotated angle  $\theta$  in this simulation. The polarization of the incident wave kept its direction as shown in Figure 11. The simulation in Figure 11 was performed for the proposed flexible Hilbert-curve loop antenna at each operating band and for the three rectangular loop antennas. The outcomes are indicated in Figures 12 and 13.

The relative variation of the antenna factor is given in Figures 12 and 13 because the proposed and the reference antenna do have their own physical length for respective resonances. As seen in Figure 12, the deviations of the antenna factor of the proposed flexible Hilbert-curve antenna for  $\phi = 0^{\circ}$  (xz-plane) and all operating bands are within  $10 \sim 20$ [dB/m], whereas the rectangular loop antennas are in range of 40~50 [dB/m]. It was observed that the shape of the curve in Figure 12 was also in good agreement with the radiation pattern of the antenna in Figures 6 and 10. In other words, the peaking angles of the antenna factor observed at  $\theta = 90^{\circ}$  and  $\theta = 270^{\circ}$  correspond to that of the null angle appeared in the radiation pattern. Moreover, the antenna factor at  $\phi = 90^{\circ}$  (yz-plane) of the proposed antenna was 2.8~3.3 [dB/m], while the rectangular loop antennas were 4.4~4.7 [dB/m] as shown in Figure 13. As seen in Figures 12 and 13, a big difference in the antenna factor between the two antennas was observed at  $\phi = 0^{\circ}$  whereas a small difference was observed at  $\phi = 90^{\circ}$ . To sum up, the proposed antenna reveals more omnidirectional characteristics than the conventional loop antenna. This feature values the proposed antenna for wireless communication applications. We have addressed the usefulness of the antenna factor together with the radiation pattern to evaluate the receiving performance. However, most papers treating similar topics only adhere to the radiation pattern rarely mentioning the antenna factor.

Figure 14 represents a degree of circular polarization in terms of axial ratio (AR) with respect to the angle  $\theta$  at  $\phi = 0^{\circ}$ for the proposed and the reference antenna. In general, the conventional loop antennas have a linear polarization with a very high value of axial ratio. However, the proposed flexible Hilbert-curve loop antenna reveals a circular polarization performance (AR < 4 dB) as shown in Figure 14. This circular polarization property was observed at 2.45 GHz and 3.35 GHz bands since all the segments of the Hilbert cur ve were cooperative in their phases and magnitudes in these bands. This phenomenon agrees with the result in Figure 7. In recent years, there has been some research on generating the circular polarization from the Hilbert-curve antennas [23, 29]. Though not appeared toward a boresight, the observed circular polarization may find its usefulness in some applications.





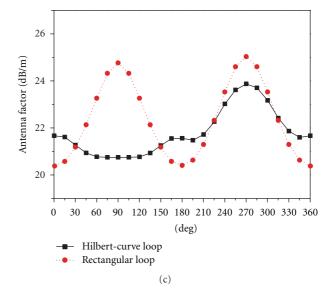


FIGURE 13: Variation of the antenna factor K at  $\phi = 90^{\circ} (yz$ -plane) for the proposed flexible Hilbert-curve loop antenna and rectangular loop antenna. (a) 2.45 GHz, (b) 3.35 GHz, and (c) 5.5 GHz.

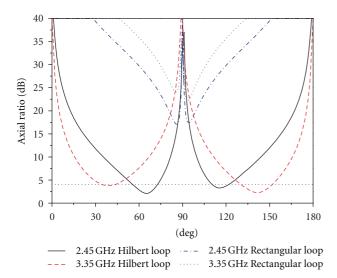


FIGURE 14: Axial ratio of the proposed flexible Hilbert-curve loop antenna and rectangular loop antenna at  $\phi = 0^{\circ}$ .

#### 4. Conclusion

In this paper, the Hilbert-curve loop antenna with an omnidirectional radiation pattern was proposed, and the simulation results are discussed focusing on the flexibility. The finalized antenna possesses the triple-band performance for the WLAN/WiMAX communication system. To compare with the proposed antenna performance, the rectangular loop antenna was used as a reference antenna. On the basis of the far-field characteristics and the result of antenna factor, it was seen that the proposed antenna achieved good omnidirectional radiation pattern and circular polarization performance. The presented results in this paper will be helpful for designing and constructing a flexible Hilbert-curve loop antenna. Furthermore, the proposed antenna could be suitable for the application in WLAN/WiMAX communication systems.

### References

- [1] Y. W. Chi and K. L. Wong, "Internal compact dual-band printed loop antenna for mobile phone application," *IEEE Transactions on Antennas and Propagation*, vol. 55, no. 5, pp. 1457–1462, 2007.
- [2] Z. Xing, L. Wang, C. Wu, J. Li, and M. Zhang, "Characteristics and application of a novel loop antenna to UHF RFID receivers," *International Journal of Antennas and Propagation*, vol. 2011, Article ID 480717, 7 pages, 2011.
- [3] C. W. Chiu, C. H. Chang, and Y. J. Chi, "Multiband folded loop antenna for smart phones," *Progress in Electromagnetics Research*, vol. 102, pp. 213–226, 2010.
- [4] G. Y. Chen and J. S. Sun, "Design of flexible printed antenna," *Electronics Letters*, vol. 40, no. 17, pp. 1034–1035, 2004.
- [5] A. Tronquo, H. Rofier, C. Hertleer, and L. Van Langenhove, "Robust planar textile antenna for wireless body LANs operating in 2.45 GHz ISM band," *Electronics Letters*, vol. 42, no. 3, pp. 142–143, 2004.

- [6] G. Y. Chen, J. S. Sun, S. Y. Huang et al., "The Pliant Monopole Antenna (PMA) design for handset phone operation," in *Proceedings of the 7th International Symposium on Antennas, Propagation and EM Theory (ISAPE '06)*, pp. 46–49, Guilin, China, October 2006.
- [7] J. Jung, H. Lee, and Y. Lim, "Broadband flexible meander line antenna with vertical lines," *Microwave and Optical Technology Letters*, vol. 49, no. 8, pp. 1984–1987, 2007.
- [8] J. Jung, H. Lee, and Y. Lim, "Broadband flexible comb-shaped monopole antenna," *IET Microwaves, Antennas and Propagation*, vol. 3, no. 2, pp. 325–332, 2009.
- [9] D. E. Anagnostou, A. A. Gheethan, A. K. Amert, and K. W. Whites, "A direct-write printed antenna on paper-based organic substrate for flexible displays and WLAN applications," *IEEE/OSA Journal of Display Technology*, vol. 6, no. 11, pp. 558–564, 2010.
- [10] H. K. Yoon, Y. J. Yoon, H. Kim, and C. H. Lee, "Flexible ultrawideband polarisation diversity antenna with band-notch function," *IET Microwaves, Antennas and Propagation*, vol. 5, no. 12, pp. 1463–1470, 2011.
- [11] T. J. Jung, J. H. Kwon, and S. Lim, "Flexible zeroth-order resonant antenna independent of substrate deformation," *Electronics Letters*, vol. 46, no. 11, pp. 740–742, 2010.
- [12] S. H. Choi, H. J. Lee, and K. B. Lee, "Flexible antenna based on composite right/left-handed transmission line," *Electronics Letters*, vol. 46, no. 17, pp. 1181–1182, 2010.
- [13] J. Lee, S. I. Kwak, and S. Lim, "Wrist-wearable zeroth-order resonant antenna for wireless body area network applications," *Electronics Letters*, vol. 47, no. 7, pp. 431–433, 2011.
- [14] W. C. Liu and C. F. Hsu, "Flexible CPW-fed double meandered monopole antenna for dual-band WLAN operation," *Mi*crowave and Optical Technology Letters, vol. 48, no. 8, pp. 1529–1532, 2006.
- [15] M. L. Scarpello, D. Kurup, H. Rogier et al., "Design of an implantable slot dipole conformal flexible antenna for biomedical applications," *IEEE Transactions on Antennas and Propagation*, vol. 59, no. 10, pp. 3556–3564, 2011.
- [16] S. R. Best, "A comparison of the performance properties of the Hilbert curve fractal and meander line monopole antennas," *Microwave and Optical Technology Letters*, vol. 35, no. 4, pp. 258–261, 2002.
- [17] M. Z. Azad and M. Ali, "A miniaturized hilbert PIFA for dualband mobile wireless applications," *IEEE Antennas and Wireless Propagation Letters*, vol. 4, no. 1, pp. 59–62, 2005.
- [18] J. Zhu, A. Hoorfar, and N. Engheta, "Bandwidth, cross-polarization, and feed-point characteristics of matched Hubert antennas," *IEEE Antennas and Wireless Propagation Letters*, vol. 2, pp. 2–5, 2003.
- [19] J. Anguera, C. Puente, E. Martínez, and E. Rozan, "The fractal Hilbert monopole: a two-dimensional wire," *Microwave and Optical Technology Letters*, vol. 36, no. 2, pp. 102–104, 2003.
- [20] D. Gala, J. Soler, C. Puente, C. Borja, and J. Anguera, "Miniature microstrip patch antenna loaded with a space-filling transmission line based on the fractal Hilbert curve," *Microwave and Optical Technology Letters*, vol. 38, no. 4, pp. 311–312, 2003.
- [21] J. Anguera, C. Puente, C. Borja, and J. Soler, "Fractal-shaped antennas: a review," *Encyclopedia of RF and Microwave Engineering*, vol. 2, pp. 1620–1635, 2005.
- [22] J. Anguera, Fractal and broad-band techniques on miniature, multifrequency, and high-directivity microstrip patch antennas,

- Ph.D. thesis, Universitat Politècnica de Catalunya, Barcelona, Spain, 2003.
- [23] S. S. Bor, T. C. Lu, J. C. Liu, and B. H. Zeng, "Fractal monopole-like antenna with series Hilbert-curves for WLAN dual-band and circular polarization applications," *Microwave and Optical Technology Letters*, vol. 51, no. 4, pp. 876–880, 2009.
- [24] D. O. Kim, C. Y. Kim, J. K. Park, and N. I. Jo, "Compact band notched ultra-wideband antenna using the Hilbert-curve slot," *Microwave and Optical Technology Letters*, vol. 53, no. 11, pp. 2642–2648, 2011.
- [25] J. McVay, N. Engheta, and A. Hoorfar, "Numerical study and parameter estimation for double-negative metamaterials with Hilbert-curve inclusions," in *Proceedings of the IEEE Antennas and Propagation Society International Symposium*, vol. 3, pp. 328–331, July 2005.
- [26] J. McVay, N. Engheta, and A. Hoorfar, "High impedance metamaterial surfaces using hilbert-curve inclusions," *IEEE Microwave and Wireless Components Letters*, vol. 14, no. 3, pp. 130–132, 2004.
- [27] K. J. Vinoy, K. A. Jose, V. K. Varadan, and V. V. Varadan, "Resonant frequency of Hilbert curve fractal antennas," in *Proceedings of the IEEE Antennas and Propagation Society International Symposium*, pp. 648–651, July 2001.
- [28] W. L. Stutzman and G. A. Thiele, *Antennas Theory and Design*, John Wiley & Sons, New York, NY, USA, 2nd edition, 2003.
- [29] J. C. Liu, B. H. Zeng, H. L. Chen, S. S. Bor, and D. C. Chang, "Compact fractal antenna with self-complementary hilbertcurves for WLAN dual-band and circular polarization applications," *Microwave and Optical Technology Letters*, vol. 52, no. 11, pp. 2535–2539, 2011.

Hindawi Publishing Corporation International Journal of Antennas and Propagation Volume 2012, Article ID 486565, 6 pages doi:10.1155/2012/486565

### Research Article

# **Inkjet Printed Planar Coil Antenna Analysis for NFC Technology Applications**

### I. Ortego, N. Sanchez, J. Garcia, F. Casado, D. Valderas, and J. I. Sancho

- <sup>1</sup> Electronics and Communications Department, CEIT and Tecnun University of Navarra, Manuel de Lardizábal 15, 20018 San Sebastián, Spain
- <sup>2</sup> Communications Area, IKERLAN-IK4, P J.M. Arizmendiarrieta, 20500 Arrasate-Mondragon, Spain

Correspondence should be addressed to I. Ortego, iortego@ceit.es

Received 15 December 2011; Accepted 9 January 2012

Academic Editor: Ana Collado

Copyright © 2012 I. Ortego et al. This is an open access article distributed under the Creative Commons Attribution License, which permits unrestricted use, distribution, and reproduction in any medium, provided the original work is properly cited.

The aim of this paper is to examine the potential of inkjet printing technology for the fabrication of Near Field Communication (NFC) coil antennas. As inkjet printing technology enables deposition of a different number of layers, an accurate adjustment of the printed conductive tracks thickness is possible. As a consequence, input resistance and *Q* factor can be finely tuned as long as skin depth is not surpassed while keeping the same inductance levels. This allows the removal of the typical damping resistance present in current NFC inductors. A general methodology including design, simulation, fabrication, and measurement is presented for rectangular, planar-spiral inductors working at 13.56 MHz. Analytical formulas, computed numerical models, and measured results for antenna input impedance are compared. Reflection coefficient is designated as a figure of merit to analyze the correlation among them, which is found to be below  $-10 \, \mathrm{dB}$ . The obtained results demonstrate the suitability of this technology in the fabrication of low cost, environmentally friendly NFC coils on flexible substrates.

### 1. Introduction

Near Field Communication (NFC) is a recent wireless technology working on HF band that enables the exchange of data in a short range. It is an ideal solution where reliable exchange of data is paramount to quality user operations such as mobile payments. It is estimated that this system will be used in more than 1.2 billion smartphones by 2015 [1]. Therefore, it is necessary to reduce the cost of the manufacturing process keeping at the same time an environmentally friendly approach to pave the way for this promising technology.

In this context, there are a number of approaches to implement an NFC antenna layout onto a selected substrate. The earliest and most cumbersome method of antenna fabrication has been subtractive etching on a metalplated laminate (e.g., FR4). Subtractive etching has matured to the point where it has become a low-tech process requiring inexpensive off-the-shelf materials and equipment. However, for larger production runs, etching creates signif-

icant amounts of metal salt and chemical waste products, incurring increased costs due to regulatory fees.

Contrary to the traditional etching technique, inkjet printing technology is a direct-write technology by which the designed pattern is transferred directly to the substrate [2]. This technology has become a major topic in scientific research, especially drop-on-demand (DOD) inkjet printing systems [3]. With these systems, the production costs of electronic devices are dramatically reduced, as material can be deposited on demand.

It has been estimated that there are about 1500 world-wide research units working on various aspects of flexible electronics [4]. The fabrication of thin conductive tracks by methods of inkjet printing has been recently investigated extensively [5, 6].

Up to date, inks made of silver conductive nanoparticles have been used to produce printed electronic circuits on flexible surfaces. Metallic nanoparticle inks typically consist of silver or gold nanoparticles with diameters ranging from just 2 nm to over 50 nm, encapsulated by a protective shell

and dispersed in a liquid solvent [7, 8]. Once printed, a continuous conducting structure can be obtained by sintering, that is, by increasing the temperature of the structure so that the separate nanoparticles melt together.

In the fabrication process, several parameters are involved, such as, size of ink nanoparticles, substrate, surface tension of the particle and of the substrate, time and temperature of the ink sintering, among others [9], which provide a wide range of degree of freedom for circuit designs, and particularly for antennas, on flexible substrates. Future terminals, such as smartphones, are envisaged to be completely flexible in the near future [10–12]. The antenna has a considerable size in the system; therefore, its flexibility is crucial if a flexible terminal is desired.

The usage of inkjet technology for NFC implementation on flexible terminals stills finds another motivation for the antennas involved. The *Q* factor required for the antenna is directly related to the read range to be achieved by the technology. For example, in a typical RFID system, for a distance of 38 cm, *Q* factors close to 40 are required [13, 14]. As NFC allows for shorter distances motivated for a whole sort of reasons, as, for example, security and privacy of users, restrictions on tag *Q* factors are relaxed to get the same voltage to energize the RFID tag integrated circuit.

As long as a decreasing of Q factor can be tolerated by performing antennas with tracks thinner than their skin depth, the input resistance can be increased to make up a possible removal of the damping resistance. With copperetched antennas, Q-factors of more than 100 could be realized [13, 15]. In this technology, the conductive track thickness is fixed and longer than the skin depth of the copper (18  $\mu$ m at 13.56 MHz). However, inkjet printing technology allows to vary the thickness of the printed layers with approximately 1  $\mu$ m resolution all the way from 0  $\mu$ m to the skin depth. Thus, typical coil antenna manufactured by inkjet printing technology exhibits small Q factors of around 4–10 [5].

Therefore, an exploration of the potentials and limitations of inkjet printing technology for NFC flexible terminals should be addressed in this context since it provides a low cost, environmentally friendly manufacturing process on flexible materials with no damping resistance involved.

This paper provides a rigorous approach, involving analytical and computational models, for rectangular planar spiral coils at 13,56 MHz with subsequent experimental verification on flexible substrates. It is divided into four parts. The second section deals with the methodology, where a general method for the design, fabrication, simulation, and measurement of inkjet printed loop antennas for NFC systems on a flexible substrate is explained. The third part includes the implementation and obtained results. Lastly, the fourth part states the conclusions.

### 2. Methodology

2.1. Analytical Approach. In this section, all the necessary equations to analytically calculate the total inductance, Q factor, and resistance of a rectangular planar spiral inductor (Figure 1) will be shown.

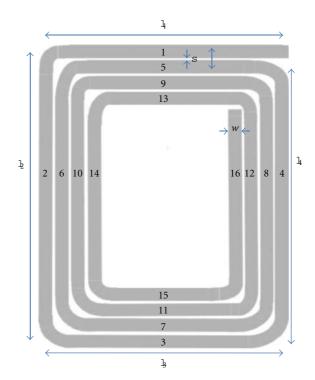


FIGURE 1: Rectangular planar spiral inductor.

2.1.1. Inductance Calculation. The total inductance of an N-turn planar spiral inductor coil (Figure 1) can be calculated as follows:

$$L_T = L_0 + M_+ - M_- [\mu m], \tag{1}$$

where  $L_T$  is the total inductance,  $L_0$  is the sum of self inductances of all straight segments,  $M_+$  is the sum of positive mutual inductances, and  $M_-$  is the sum of negative ones.

The self inductances of a rectangular cross-section conductor can be obtained using the following equation [14]:

$$L = 0,002l \left\{ \ln \left( \frac{2l}{w+t} \right) + 0.50049 + \frac{w+t}{3l} \right\} [\mu \text{m}], \quad (2)$$

where w, t, and l are the segment's width, thickness, and length in cm, respectively.

The mutual inductance is the inductance that results from the magnetic fields produced by adjacent conductors. The mutual inductance is positive when the directions of the current along the conductors are in the same direction, and negative when the directions of currents are in opposite directions. The mutual inductance between two parallel conductors of equal length is a function of the length of the conductors and of the geometric mean distance d between them. It is calculated by [16]

$$M = 2lF[nH], (3)$$

where *F* can be calculated as

$$F = \ln\left\{ \left(\frac{l}{d}\right) + \left[1 + \left(\frac{l}{d}\right)^2\right]^{1/2} \right\} - \left[1 + \left(\frac{d}{l}\right)^2\right]^{1/2} + \left(\frac{d}{l}\right). \tag{4}$$

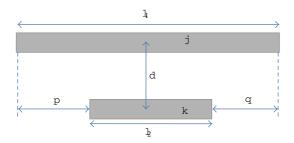


FIGURE 2: Two conductor segments for mutual inductance calculation

The geometric mean distance d is approximately equal to the distance between the track centres of the conductors involved. When the two segments are not equal in length, (5) should be applied according to Figure 2:

$$M_{k,p} = \frac{1}{2} \left\{ \left( M_{k+p} + M_{k+q} \right) - \left( M_p + M_q \right) \right\}, \tag{5}$$

where

$$M_{k+p} = 2l_{k+p}F_{k+p},$$

$$F_{k+p} = \ln\left\{ \left( \frac{l_{k+p}}{d_{j,k}} \right) + \left[ 1 + \left( \frac{l_{k+p}}{d_{j,k}} \right)^{2} \right]^{1/2} \right\}$$

$$- \left[ 1 + \left( \frac{d_{j,k}}{l_{k+p}} \right)^{2} \right]^{1/2} + \left( \frac{d_{j,k}}{l_{k+p}} \right).$$
(6)

2.1.2. Resistance and Quality Factor Calculation. The thickness of the conductive track deposited by inkjet printing technology can be adjusted by the number of layers micron by micron. Provided that skin effect at 13,56 MHz is approximately  $47\,\mu\mathrm{m}$  for the silver conductive ink, the input resistance varies inversely with the thickness t according to the following expression:

$$R = \frac{1}{\sigma} \cdot \frac{L}{S} = \frac{1}{\sigma} \cdot \frac{L}{t \cdot w},\tag{7}$$

where R is the electrical resistance,  $\sigma$  is the ink's conductivity, L is the longitude, S is the track cross section, t is the thickness, and w is the width of the track.

The spiral inductor Q factor is then calculated as:

$$Q = \frac{L\omega}{R}. (8)$$

- 2.2. Numerical Computation. Frequency domain solver implemented by CST MICROWAVE STUDIO simulation software has been selected to make the numerical computation of the design. Adaptative hexahedral mesh is used and local mesh refinement strategy is adopted within the coil conductive track.
- 2.3. Implementation. The material used as substrate is Dupont Kapton polyimide film 127  $\mu$ m thick. It can remain stable in a wide range of temperatures, from -269 to  $+400^{\circ}$ C.



FIGURE 3: Cartridge and Printer Dimatix 2831 [17].

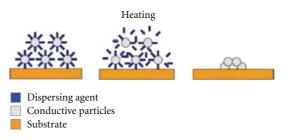


FIGURE 4: Sintering process [9].

SunTronic Jettable Silver U5714 ink by Sunjet has been used as conductive ink. It is a solvent-based silver nanoparticle inkjet ink and 20% of its weight is due to silver particles.

The printer that has been used is the Dimatix Materials Printer DMP-2831 (Figure 3). The platen temperature can be varied from 28°C to 60°C. In the fabricated prototypes, 60°C is chosen as it prevents the ink from spreading out.

DMC-11610 cartridge which has 16 nozzles,  $254 \,\mu m$  spaced with a nominal opening of  $21 \,\mu m$ , and a 10 pL drop volume capacity has been employed. Only two nozzles with 16-17 v applied voltage,  $40^{\circ} C$  of temperature and a meniscus vacuum of 4,5 inches  $H_2O$  have been used at a height of 0,5 mm with a drop spacing of  $20 \,\mu m$ .

Once the prototypes have been printed, a sintering process is required to improve the conductivity of the ink. The manufacturer recommends a range of temperature and time to sinter the silver ink and this depends on the amount of solid material present in the ink. In general, the lower the sintering time or temperature, the higher the electric resistance since a larger gap between the nanoparticles occurs. This process (Figure 4) determines the final performance of the ink. A sintering process of 30 min@200°C has been selected for all the prototypes.

#### 2.4. Measurements

2.4.1. Thickness of Printed Traces. Once the methodology to print is defined, some traces are printed into a substrate to study the corresponding thickness depending on the number of layers.

A KLA-Tencor P-16+ Profiler has been used to measure the overall thickness of the printed traces and estimate the one of each layer by average. In Figure 5, the obtained profile of the printed traces is shown for different number of layers.

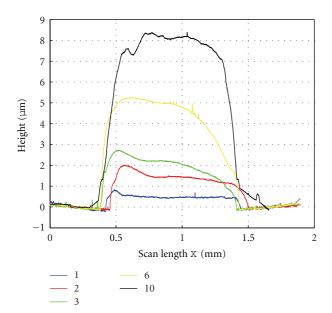


Figure 5: Obtained profiles for different number of printed layers.

TABLE 1: Obtained conductivity values with 30 min@200°C sintering process.

Material: silver	Conductivity $(\Omega m)^{-1}$	Conductivity with respect to pure silver (%)
Pure	$63.01 \cdot 10^6$	100
One layer	$8\cdot 10^6$	12.6
Two layers	$9\cdot 10^6$	14.3
Three layers	$7.9 \cdot 10^{6}$	12.5
Six layers	$8.5 \cdot 10^{6}$	13.5

A thickness of  $0.8\,\mu\mathrm{m}$  for each layer can be assumed when considering the obtained profiles and the measured thickness.

2.4.2. Characterization of the Conductivity of the Ink. Once the thickness of the printed layers is found, conductivity is characterized.

Although conductivity is independent of the number of printed layers, the conductivity study has been done in samples with different number of layers, which correspond to different electrical resistance and thickness pairs for comparison purposes. The electrical resistance of the structure has been measured using a Keithley 6517B Electrometer/High Resistance Meter.

The conductivity can be calculated using (7). Table 1 shows averaged results collected from various samples.

The obtained results by this method are in accordance with the ones found in bibliography [9, 18]. As an indicative value, a 10% or 20% of the conductivity of the pure silver can be considered. In this work, a conductivity of  $8 \cdot 10^6 \; (\Omega m)^{-1}$  has been considered as representative of ink performance.

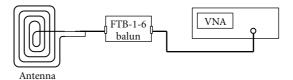


FIGURE 6: Measurement set up.

2.4.3. Input Impedance and Q Factor. Once the antenna has been printed, its impedance can be measured by a standard VNA according to the setup shown in Figure 6 and the corresponding Q factor can be calculated. A FTB-1-6 balun by Mini-Circuits is employed between the feeding cable and the fabricated prototype. The flexibility of the substrate and the ink do not allow the use of typical soldering methods. Therefore, pad connections are implemented by conductive adhesive tape.

2.5. Methodology Validation. The reflection coefficient will be used as figure of merit to estimate the correlation between the results obtained by analytical formulas, computed numerical models, and measurements.

The amplitude of the reflection coefficient between two different complex impedances can be calculated as [19]

$$|\Gamma| = 20 \log \left( \left| \frac{Z_1 - Z_2^*}{Z_1 + Z_2} \right| \right),$$
 (9)

where  $Z_1$  and  $Z_2$  are the complex impedances. The methodology is based on this equation by substituting  $Z_1$  and  $Z_2$  for pairs chosen among analytically calculated, simulated, and measured results referred to the same coil layout. The only consideration to apply this equation is that for the correct calculation one of the impedances must be conjugated (e.g.,  $Z_2 = Z_{\rm ant2}^*$ ). In that way, if  $|\Gamma| \leq -10$  dB, a good correlation is achieved.

### 3. Implementation and Results

An analytical study of the effect of the thickness for a 5 turn rectangular ( $80 \text{ mm} \times 50 \text{ mm}$ ) planar spiral inductor with w = s = 1 mm has been realized. These dimensions have been selected to fulfil the ISO7810 standard [20]. This standard defines the physical characteristics of identification cards (Table 2).

The analytically obtained inductance for the presented antenna is  $2.82 \,\mu\text{H}$  according to expressions (1)–(7), and it remains unchanged with thickness t. However, this parameter has a strong impact on the input impedance (as the damping resistance is changed) and therefore on the coil quality factor. The obtained results are shown in Figure 7 where expressions (7) and (8) are used.

A Q value up to 90 can be theoretically achieved by this technology as long as the thickness is kept below the skin depth (47 microns). For thicknesses deeper than skin depth, input resistance and Q factor is no longer adjustable by this degree of freedom.

Table 2: Nominal dimensions of ID-1 card type.

Width (mm)	Height (mm)	Thickness (mm)
85.6	53.98	0.76

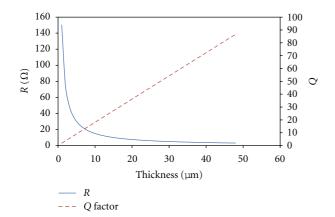


FIGURE 7: Calculation of *R* and *Q* for different thickness.

TABLE 3: Obtained results of the two prototypes: analytical (A), simulation (S), and measured (M).

		A	S	M
4 layers	$R [\Omega]$	46,58	51,13	50,25
	$L [\mu H]$	2,82	2,79	2,9
	Q	5,16	4,64	4,91
6 layers	$R [\Omega]$	31	35,118	32,35
	$L [\mu H]$	2,82	2,79	2,947
	Q	7,75	6,77	7,76

In practice, it is not feasible to fabricate coil antennas with such a high thicknesses due to the ink spilling over the track when too many layers are mounted on it. Two different prototypes have been implemented; one with 4 layers and another one with 6 layers (Figure 8) to validate the proposed methodology. The obtained results are shown in Table 3.

The correlation between the three outcomes (analytical, simulated, and measured) is studied as explained in the methodology validation section. The obtained values are summarized in Table 4.

All the correlations are below -10 dB; therefore, it can be concluded that the obtained results are reliable. In order to explore inkjet printing technology limits once the procedure is validated, a prototype with 10 layers has been fabricated. This represents a reasonable trade off between delivered performance in terms of Q values and complexity of the manufacturing process due to the number of layers. A measured inductance value of  $2.9\,\mu\text{H}$ , a resistance of  $23.5\,\Omega$  and a Q factor of 10.5 are obtained in perfect accordance with the aforementioned results.

### 4. Conclusions

The potential of using inkjet printing technology to fabricate NFC antennas has been investigated. A general methodology

TABLE 4: Results validation.

	Comparison		Γ  [dB]
	A	S	-25.16
4 layers	A	M	-21.94
	S	M	-20.35
6 layers	A	S	-22.78
	A	M	-15.39
	S	M	-14.08



FIGURE 8: Printed prototype (6 layers).

for the design, simulation, fabrication, and measurement process has been explained.

The ink conductivity is shown to be around  $8 \cdot 10^6 \ (\Omega \text{m})^{-1}$  and the approximate thickness of each deposited layer  $0.8 \ \mu \text{m}$ . The resistance can be controlled by the capability of this technology of varying the track thickness, which prevents from extra damping resistor implementations. With the aforementioned resolution, Q values ranging from 4 to 10 can be obtained while keeping the same inductance value.

Inkjet printing technology is therefore a promising technique for the fabrication of NFC coil antennas. Moreover, due to its low cost manufacturing process and substrate flexibility, it is a perfect candidate for the implementation of environmentally friendly NFC terminals into flexible substrates.

### Acknowledgment

Iñaki Ortego's scholarship has been granted by the Department of Education of the Basque Government. Joseba García's contract is partially supported by the Spanish Ministry of Education within the framework of the Torres Quevedo Program, and cofinanced by the European Social Fund. The authors would like to thank the collaboration agreement between Tecnun and CST that has made possible the achievements of this piece of research.

### References

[1] "Wireless Design Online," http://www.wirelessdesignonline .com/article.mvc/NFC-Chip-Shipments-To-Surpass-12-Billio-

- n-By-0001? section Code=News& template Code=Sponsor Header& user=1742815& source=nl: 32237.
- [2] A. Rida, R. Vyas, L. Yang, C. Kruesi, and M. M. Tentzeris, "Low cost inkjet-printing paper-based modules for RFID sensing and wireless applications," in *Proceedings of the 38th European Microwave Conference (EuMC '08)*, pp. 1715–1718, Amsterdam, The Netherlands, October 2008.
- [3] T. H. J. van Osch, J. Perelaer, A. W. M. de Laat, and U. S. Schubert, "Inkjet printing of narrow conductive tracks on untreated polymeric substrates," *Advanced Materials*, vol. 20, no. 2, pp. 343–345, 2008.
- [4] J. Hu, "Overview of flexible electronics from ITRI's view-point," in *Proceedings of the 28th IEEE VLSI Test Symposium* (VTS '10), p. 84, Santa Cruz, Calif, USA, April 2010.
- [5] M. L. Allen, K. Jaakkola, K. Nummila, and H. Seppa, "Applicability of metallic nanoparticle inks in RFID applications," *IEEE Transactions on Components and Packaging Technologies*, vol. 32, no. 2, pp. 325–332, 2009.
- [6] S. H. Yoon, J. H. Lee, P. C. Lee et al., "Sintering and consolidation of silver nanoparticles printed on polyimide substrate films," *Macromolecular Research*, vol. 17, no. 8, pp. 568–574, 2009.
- [7] J. B. Szczech, C. M. Megaridis, D. R. Gamota, and J. Zhang, "Fine-line conductor manufacturing using drop-on-demand PZT printing technology," *IEEE Transactions on Electronics Packaging Manufacturing*, vol. 25, no. 1, pp. 26–33, 2002.
- [8] D. Kim and J. Moon, "Highly conductive ink jet printed films of nanosilver particles for printable electronics," *Electrochemical and Solid-State Letters*, vol. 8, no. 11, pp. J30–J33, 2005.
- [9] R. D. Mancosu, J. A. Q. Quintero, and R. E. S. Azevedo, "Sintering, in different temperatures, of traces of silver printed in flexible surfaces," in *Proceedings of the 11th International Conference on Thermal, Mechanical and Multi-Physics Simulation, and Experiments in Microelectronics and Microsystems* (EuroSimE '10), pp. 1–5, Bordeaux, France, April 2010.
- [10] "Samsung And Nokia Are Moving Towards With Flexible Screens Smartphone," http://www.mobiussite.com/samsung-nokia-moving-flexible/1830.html.
- [11] "Samsung flexible display phones & tablets in 2012," http:// www.slashgear.com/samsung-flexible-display-phones-tabletsin-2012-28191673/.
- [12] Y. Min, "Mobile Terminal Using Flexible Display And Method Of Controlling The Mobile Terminal," U.S. Patent US 2010/ 0117975 A1, 2010.
- [13] A. L. Scholtz and R. Weigel, "Antenna design for future multistandard and multi-frequency RFID systems," 2009.
- [14] Youbok Lee, "Antenna circuit design for RFID applications," Microchip, pp. 1–50, 2003.
- [15] M. Gebhart and R. Szoncso, "Optimizing design of smaller antennas for proximity transponders," in *Proceedings of the 2nd International Workshop on Near Field Communication (NFC '10)*, pp. 77–82, Monaco, April 2010.
- [16] C. R. Paul, *Inductance—Loop and Partial*, John Wiley & Sons, New York, NY, USA, 2010.
- [17] "Dimatix. Fujifilm," http://www.dimatix.com/.
- [18] A. Rida, L. Yang, R. Vyas, and M. M. Tentzeris, "Conductive inkjet-printed antennas on flexible low-cost paper-based substrates for RFID and WSN applications," *IEEE Antennas and Propagation Magazine*, vol. 51, no. 3, pp. 13–23, 2009.
- [19] U. Karthaus and M. Fischer, "Fully integrated passive UHF RFID transponder IC with 16.7-µW minimum RF input power," *IEEE Journal of Solid-State Circuits*, vol. 38, no. 10, pp. 1602–1608, 2003.

[20] Identification cards—Physical Characteristics, *International Standard ISO 7810*.

Hindawi Publishing Corporation International Journal of Antennas and Propagation Volume 2012, Article ID 407973, 8 pages doi:10.1155/2012/407973

### **Application Article**

### Low-Interference Dual Resonant Antenna Configurations for Multistandard Multifunction Handsets and Portable Computers

### Mohamed Sanad<sup>1</sup> and Noha Hassan<sup>2</sup>

<sup>1</sup>R & D Department, Amant-Antennas, Giza 12451, Egypt

Correspondence should be addressed to Mohamed Sanad, msanad@hotmail.com

Received 13 August 2011; Accepted 19 December 2011

Academic Editor: Ana Collado

Copyright © 2012 M. Sanad and N. Hassan. This is an open access article distributed under the Creative Commons Attribution License, which permits unrestricted use, distribution, and reproduction in any medium, provided the original work is properly cited.

Low-interference dual resonant antenna configurations are developed for multistandard multifunction mobile handsets and portable computers. Only two wideband resonant antennas can cover most of the important wireless applications in portable communication equipment. The frequency bands of the dual antenna configuration can be adjusted according to the wireless applications that are required to be covered. The bandwidth that can be covered by each antenna is about 80% without using matching or tuning circuits. Three sample dual antenna configurations with different frequency bands are presented. The interference between the low-band and high-band antennas of these three configurations is investigated, and the ways of reducing this interference are studied. The most effective factor on the interference between the low-band and high-band antennas is their relative orientations. When the low-band and high-band antennas of each configuration are perpendicular to each other, the isolation between them significantly increases. This eliminates the need for any special tools or techniques to suppress the mutual coupling between them. The new antennas have very small cross-sectional areas, and they are made of a flexible material. They do not require any additional components or ground planes. They can be used as internal, external, or partially internal and partially external antennas.

### 1. Introduction

The number of mobile wireless applications is continuously increasing. Furthermore, most wireless applications have different standards with different frequency allocations worldwide. Hence, it is desirable to have multistandard multifunction handsets and portable computers. In order to cover the frequency bands of all applications, several antennas have to be used. The problem is that the frequency bands of some applications are very close to each other or even overlapping as in GSM (824-894 MHz) and UHF mobile TV "DVB-H" (470-862 MHz) [1]. As a result, there will be a severe interference between their antennas. In this research, low-interference dual resonant antenna configurations are developed for multistandard multifunction mobile handsets and portable computers. Only two wideband antennas can cover most of the important wireless applications in portable communication equipment. The frequency bands of the dual antenna configuration can be adjusted according to the

wireless applications that are required to be covered. The maximum bandwidth that can be covered by each antenna is about 80% without using matching or tuning circuits.

Three sample dual antenna configurations will be presented. The first configuration covers a frequency band from 470 MHz to 2.7 GHz, which is divided into two subbands; 470–960 MHz and 1.2–2.7 GHz. Each subband is covered by a wideband resonant antenna. Since the low-band antenna resonates from 470 to 960 MHz, it can cover the bands of UHF mobile digital TV "DVB-H" (470–862 MHz), 700 MHz WiMax, CDMA/TDMA/GSM800 (824–894 MHz) and E-GSM900 (880–960 MHz) [2]. The high-band antenna resonates from 1.2 to 2.7 GHz, and it can cover the bands of low L band GPS (1.2 GHz), L-band DVB-H (1452–1492 MHz), GPS (1575 MHz), GSM1800 (1710–1880 MHz), PCS1900 (1859–1990 MHz), UMTS (1900–2170 MHz), Bluetooth/WiFi (2.4 GHz), WiMax (2.3–2.5 GHz), and IMT-2000 WiMax (2.5–2.69 GHz). The bandwidths of these two

<sup>&</sup>lt;sup>2</sup> Department of Biomedical Engineering, Cairo University, Giza 12613, Egypt

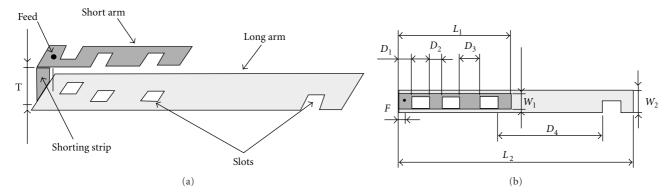


FIGURE 1: Geometry of the new wideband resonant antenna.



FIGURE 2: The antennas of the first dual antenna configuration.

antennas are 69% and 77%, respectively. There is a frequency gap between the two subbands which is not utilized by any important application. This frequency gap helps in increasing the isolation between the low-band and high-band antennas, which means reducing the mutual coupling and the interference between them. It should be noted that linearly polarized antennas can be used with all the above applications including GPS, which is circularly polarized. This is because the advantages of using circularly polarized GPS antennas disappear in heavy multipath environments as it was experimentally verified in [3].

In another dual antenna configuration, the high-band antenna is modified to resonate from 1.575 to 3.6 GHz (with 78% bandwidth) instead of resonating from 1.2 to 2.7 GHz in order to cover the 3.5 GHz WiMax band. This also increases the frequency gap between the low and high subbands which further reduces the mutual coupling between their antennas. A third dual antenna configuration covers the frequency bands; 750 MHz–1.65 GHz and 1.71–3.9 GHz. The antennas of this configuration are much shorter than the antennas of the other two configurations. The interference between the low-band and high-band antennas of the above three configurations are investigated, and the ways of reducing this interference will be presented.

### 2. Results

Figure 1 shows the geometry of the new wideband resonant antennas [2]. They consist of two narrow printed metallic arms connected together by a shorting metallic strip. The two arms may be parallel to each other or may have any angle between them. The length of the short arm is  $L_1$  and its width is  $W_1$ , while the length of the long arm is  $L_2$  and

its width is  $W_2$  and the antenna is fed with a coaxial feed line at a distance F from the shorted edge. The two arms of the antenna can have equal or unequal widths  $W_1$  and  $W_2$ . Furthermore, the two arms can be shaped in different ways in order to optimize the antenna performance. As shown, each arm has a set of slots having different configurations. These slots can be circular, rectangular, square, triangular, or other shapes. The arm lengths of the new antenna, especially the length of the short arm, are the main parameters that determine the operating frequency of the antenna. The feed location is adjusted in each configuration in order to improve the return loss as much as possible. The bandwidth, the peak gain, and the efficiency of the antenna are mainly determined by the widths of the two arms, the angle between them, the thickness of the antenna, and the configurations of the slots, which are all optimized together in order to enhance the antenna performance, especially the bandwidth. The antennas are completely self-contained and do not need extended ground planes or any additional components. Thus, the new antenna can be mounted anywhere, inside or outside any handset, because the antenna does not use a part of the handset as an extended ground plane, which usually happens with most available internal antennas. Furthermore, the antenna is made of a flexible printed material and can be bent and/or folded in different forms in order to fit any available space inside or outside the handset. Actually, it can be used as an internal, external, or partially internal and partially external antenna. Moreover, the overall size of the antenna is small and its manufacturing costs are low.

Different prototypes of the new antennas have been designed, manufactured, and tested. Figure 2 shows the low-band and the high-band antennas of the first configuration that covers a frequency band from 470 MHz to 2.7 GHz,

TABLE 1: The distance between the successive slots in the arms of the high-band antenna.

$\overline{D_1}$	$D_2$	$D_3$	$D_4$
5 mm	5 mm	10 mm	45 mm

which is divided into two subbands; 470-960 MHz and 1.2-2.7 GHz. The antennas are made of a flexible printed material "PET" with a dielectric constant  $\varepsilon_r = 3.5$  and a tangent loss  $\delta = 0.015$ . The dimensions and the results of this lowband antenna were presented in [2]. The dimensions of the high-band antenna are  $L_1 = 4$  cm,  $L_2 = 9$  cm,  $W_1 = 2.6$  mm,  $W_2 = 3.5$  mm, and T = 2 mm. Hence, the overall size of the high-band antenna is  $9 \times 0.35 \times 0.2 = 0.63$  cm<sup>3</sup>. It should be noted that this is the overall volume of the antenna because it does not require additional ground planes, matching circuits, or any other additional components. All slots in both arms of the antenna are selected to be rectangular in shape. The length of each slot is 5 mm, and its width is 2 mm. The distance between the shorted edge and the first slot and the distances between the successive slots are shown in Table 1. The locations of the slots in the short arm are exactly repeated in the long arm. However, since the long arm is wider than the short arm, the slots are positioned close to the middle of the long arm forming rings while they are located at the edge of the short arm as shown in Figure 1.

The return loss and the radiation patterns of the new antennas are numerically calculated by a software package that uses the moment method. They were also measured at IMST antenna labs in Germany [4]. Figure 3 shows the calculated and the measured return loss of the high-band antenna. The agreement between the numerical and the measured results is within the acceptable limits. The return loss is less than  $-5 \, dB$  over most of the band, which has more than 77% bandwidth. The calculated and the measured radiation patterns of the high-band antenna at a sample frequency of 2.4 GHz are shown in Figures 4(a) and 4(b), respectively. The agreement between them is very good. The coaxial feed connection was included in the simulation model. Figure 5 shows the calculated and the measured efficiency of the high-band antenna from 1200 MHz to 2700 MHz. The average efficiency is about 50%. The antenna efficiency was measured using the radiation pattern method.

# 3. Adjusting the Frequency Bands of Dual Antenna Configurations

The frequency band of the above dual antenna configuration can be adjusted according to the wireless applications that are needed to be covered by a mobile handset or a portable computer. However, the maximum bandwidth that can be covered by each antenna is about 80%. For example, if L2-GPS (1227.6 MHz) and L-band DVB-H (1452–1492 MHz) are not required to be added to a mobile handset or a portable computer while the 3.5 GHz WiMax is needed, the high-band antenna can be modified to resonate from 1575 to 3.6 GHz (with 78% bandwidth) instead of resonating from 1.2 to 2.7 GHz. This also increases the frequency gap between

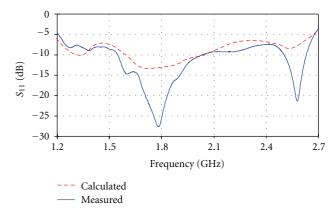


FIGURE 3: Calculated and measured return loss of the high-band antenna of the first dual antenna configuration.

the low-band and the high-band antennas from 240 MHz (960 MHz –1.2 GHz) to 600 MHz (960 MHz–1.56 GHz), which results in increasing the isolation between them. The length of the modified high-band antenna is reduced from 9 cm to 6.5 cm. The modified high-band antenna and the original low-band antenna form a second sample of dual antenna configurations, which ranges from 470 MHz to 3.6 GHz. The measured return loss of the modified high-band antenna is shown in Figure 6. The return loss is better than –7 dB over most of the band.

On the other hand, if the L-band mobile TV "DVB-H" is used instead of the UHF DVB-H, the length of the low-band antenna can be significantly reduced [5]. In a third sample dual antenna configuration, the low-band antenna is designed to resonate from 750 MHz to 1.65 GHz while the high-band antenna resonates from 1.71 to 3.9 GHz. The length of the low-band antenna is reduced from 25 cm in the first configuration to 14 cm in the third configuration, while the length of the high-band antenna is reduced to 6 cm. The calculated and measured return loss of the low-band and high-band antennas of the third configuration are shown in Figures 7 and 8, respectively. The third configuration covers an overall bandwidth ranges from 750 MHz to 3.9 GHz. Thus, although it still covers the 750 MHz WiMax, it can also cover more WiMax standards (3.7–3.9 GHz).

# 4. The Isolation between the Low-Band and High-Band Antennas

It is important to increase the isolation between the low-band and high-band antennas in dual antenna configurations as much as possible in order to reduce the mutual coupling and the interference between them. Usually, special techniques have to be used in order to suppress or reduce the mutual coupling between adjacent antennas in multiantenna configurations [6–11]. The isolation between the two antennas of the above three dual antenna configurations is investigated. The isolation between the low-band and high-band antennas depends on the distance and the frequency gap between them as well as their relative orientations. The isolation is

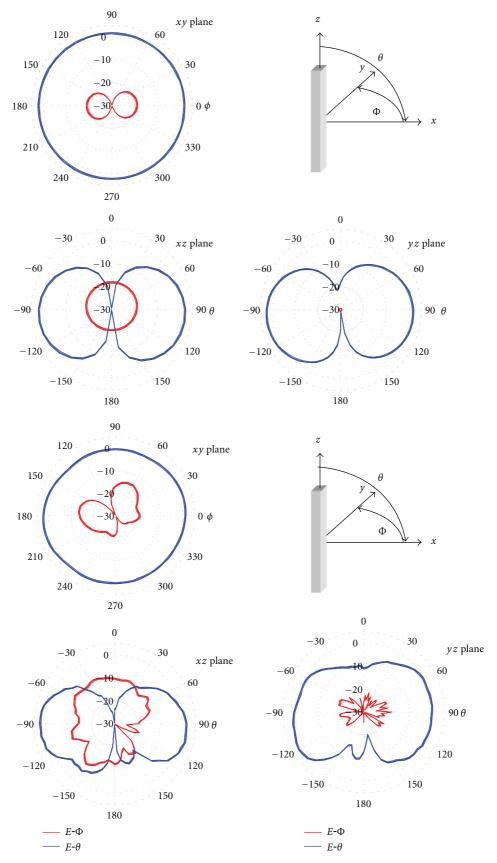


FIGURE 4: (a) Calculated radiation patterns of the high-band antenna at 2.4 GHz. (b) Measured radiation patterns of the high-band antenna at 2.4 GHz.

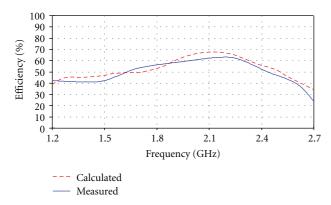


FIGURE 5: Calculated and measured efficiency of the high-band antenna of the first dual antenna configuration.

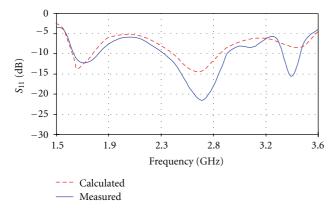


FIGURE 6: Calculated and measured return loss of the high-band antenna of the second dual configuration.

also significantly affected by the harmonics of the low-band antenna [12]. For example, the low-band and high-band antennas are oriented parallel to each other and separated by 5 cm. In this case, the measured maximum isolation in the three configurations is  $-21 \, \mathrm{dB}$ ,  $-25 \, \mathrm{dB}$ , and  $-16 \, \mathrm{dB}$ , respectively. Thus, for a fixed distance between the low-band and high-band antennas, the second configuration has the highest isolation because it has the widest frequency gap between the low and high bands while the third configuration has the lowest isolation because it has the narrowest frequency gap.

On the other hand, the calculated and the measured mutual coupling  $S_{12}$  between the low-band and high-band antennas of the above three configurations while the two antennas are perpendicular to each other is shown in Figures 9, 10, and 11, respectively. In the measurement setup, a piece of foam was used to fix the distance between the antennas under test. In the first configuration, the maximum isolation is increased from  $-21 \, \mathrm{dB}$  when the two antennas were parallel to each other to  $-32 \, \mathrm{dB}$  when they were perpendicular to each other. In the second configuration, the maximum isolation is increased from  $-25 \, \mathrm{dB}$  to  $-38 \, \mathrm{dB}$  while for the third configuration it is increased from  $-16 \, \mathrm{dB}$  to  $-36 \, \mathrm{dB}$ . It should be noted that, although the third

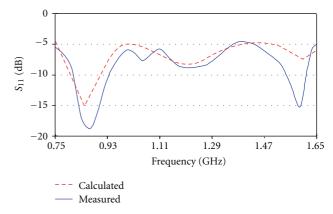


FIGURE 7: Calculated and measured return loss of the low-band antenna of the third dual antenna configuration.

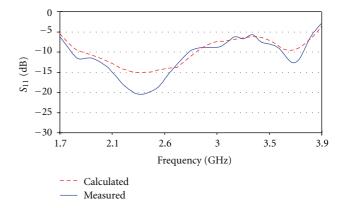


FIGURE 8: Calculated and measured return loss of the high-band antenna of the third configuration.

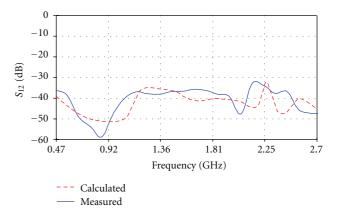


FIGURE 9: Mutual coupling  $(S_{12})$  between the antennas of the first configuration while the antennas are perpendicular to each other.

dual antenna configuration has the smallest frequency gap between the low-band and the high-band, it has a higher isolation than the first configuration when the low-band and high-band antennas are perpendicular to each other. This is because with such high isolation levels, the effect of the harmonics on the isolation level is more dominant than the effect of the width of the frequency gap.

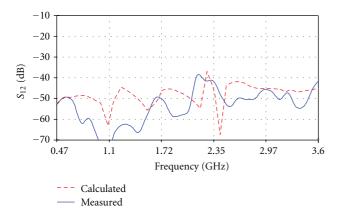


FIGURE 10: Mutual coupling  $(S_{12})$  between the antennas of the second configuration while the antennas are perpendicular to each other.

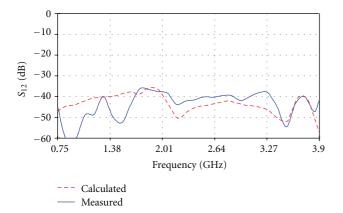


FIGURE 11: Mutual coupling ( $S_{12}$ ) between the antennas of the third configuration while the antennas are perpendicular to each other.

The isolation between the low-band and high-band antennas is also affected by the objects and components located between them, which are usually parts of a handset or a portable computer. Locating the two antennas of the dual antenna configuration on handsets is always more challenging than portable computers because of the small size of handset. The positions and orientations of the two antennas on the handset have to be optimized according to the available space in order to increase the isolation between them as much as possible. Figure 12 shows a sample handset with the two antennas of the third configuration positioned perpendicular to each other. The space on the handset does not allow the two antennas to be located away enough from each other. Furthermore, a small part of the low-band antenna is folded in order to reduce the length of the antenna without causing any significant effect on its performance [2]. Figure 13 shows the calculated and measured mutual coupling between the two antennas with a maximum isolation of about -31 dB. Since portable computers do not suffer from such size limitations, the locations of the low-band and high-band antennas can be easily optimized in order to reduce the isolation between them as shown in Figure 14. The calculated and the measured

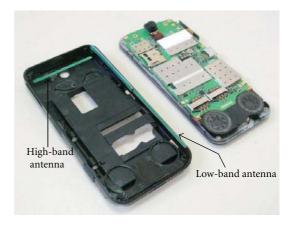


FIGURE 12: The third dual antenna configuration on a handset.

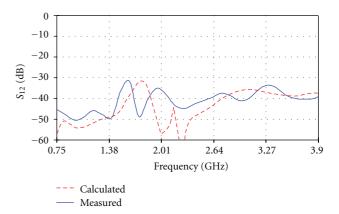


FIGURE 13: Mutual coupling  $(S_{12})$  between the antennas of the third configuration on a handset.

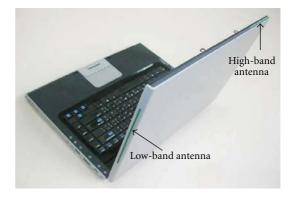


FIGURE 14: The third dual antenna configuration on a laptop computer.

mutual coupling are shown in Figure 15 with about  $-53\,\mathrm{dB}$  isolation. In the numerical EM software, an ABS plastic material was used to simulate the parts of the handset and the portable computer on which the antennas were mounted.

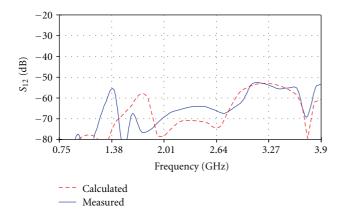


FIGURE 15: Mutual coupling ( $S_{12}$ ) between the antennas of the third configuration on a laptop computer.

### 5. Conclusions

Low-interference dual resonant antenna configurations were developed for multistandard multifunction mobile handsets and portable computers. Only two wideband antennas could cover most of the important wireless applications in portable communication equipment. The frequency bands of the dual antenna configuration could be adjusted according to the wireless applications that were required to be covered. The maximum bandwidth that could be covered by each antenna was about 80% without using matching or tuning circuits. Three sample dual antenna configurations were presented. The first configuration was designed to cover a frequency band from 470 MHz to 2.7 GHz, which was divided into two subbands; 470-960 MHz and 1.2-2.7 GHz. Each subband was covered by a wideband resonant antenna. There was a frequency gap between these two subbands which was not utilized by any important application. This frequency gap helped in reducing the coupling between the low-band and high-band antennas. In another dual antenna configuration, the high-band antenna was modified to resonate from 1.575 to 3.6 GHz instead of resonating from 1.2 to 2.7 GHz in order to cover the 3.5 GHz WiMax band. This also increased the frequency gap between the low and high subbands which further reduced the mutual coupling between their antennas. A third dual antenna configuration was designed to cover the frequency bands; 750 MHz-1.65 GHz and 1.71-3.9 GHz. The antennas of this configuration were much shorter than the antennas of the other two configurations.

The isolation between the two antennas of the above three configurations was investigated. The isolation between the low-band and high-band antennas depended on the distance and the frequency gap between them as well as their relative orientations. The isolation was also significantly affected by the harmonics of the low-band antenna. The mutual coupling  $S_{12}$  between the low-band and the high-band antennas of the above three configurations while the two antennas were parallel to each other and separated by 5 cm was measured. The second configuration had the highest isolation because it had the widest frequency gap between the low and high bands. The third configuration

had the lowest isolation because it had the narrowest frequency gap. On the other hand, when the low-band and high-band antennas of the above three configurations were perpendicular to each other, the isolation between them significantly increased. This eliminated the need for any special tools or techniques to suppress the mutual coupling between them.

### Acknowledgments

The authors would like to thank Mohamed Osama, Mahetab Salama, and Lamiaa Mamdouh for their great effort in preparing this paper.

### References

- [1] M. Sanad and N. Hassan, "A resonant handset antenna that can cover all bands of UHF mobile TV, GSM and CDMA without using matching circuits," in *Proceedings of the International Symposium on Antennas and Propagation and CNC-USNC/URSI Radio Science Meeting—Leading the Wave (AP-S/URSI '10)*, pp. 1–4, July 2010.
- [2] M. Sanad and N. Hassan, "A 470 to 960 MHz resonant antenna: covering uhf mobile TV and CDMA/GSM without tuning circuits," *Microwave Journal*, vol. 53, no. 11, pp. 56–73, 2010.
- [3] V. Pathak, S. Thornwall, M. Krier, S. Rowson, G. Poilasne, and L. Desclos, "Mobile handset system performance comparison of a linearly polarized GPS internal antenna with a circularly polarized antenna," in *Proceedings of the International Antennas and Propagation Symposium and USNC/CNC/URSI North American Radio Science Meeting*, pp. 666–669, June 2003.
- [4] http://www.imst.com/en/home.php.
- [5] M. Sanad and N. Hassan, "Dual antenna configuration for multi-standard multifunction handsets and portable computers," in *Proceedings of the 3rd European Wireless Technology Conference (EuWiT '10)*, pp. 173–176, September 2010.
- [6] Y. J. Song and K. Sarabandi, "Suppression of the mutual coupling between two adjacent miniaturized antennas utilizing printed resonant circuits," in *Proceedings of the IEEE International Symposium on Antennas and Propagation and USNC/URSI National Radio Science Meeting (APSURSI '09)*, pp. 1–4, June 2009.
- [7] K. S. Min, D. J. Kim, and Y. M. Moon, "Improved MIMO antenna by mutual coupling suppression between elements," in *Proceedings of the 8th European Conference on Wireless Technology*, pp. 125–128, October 2005.
- [8] M. M. Nikolić, A. R. Djordjević, and A. Nehorai, "Microstrip antennas with suppressed radiation in horizontal directions and reduced coupling," *IEEE Transactions on Antennas and Propagation*, vol. 53, no. 11, pp. 3469–3476, 2005.
- [9] H. Xin, K. Matsugatani, M. Kim et al., "Mutual coupling reduction of low-profile monopole antennas on highimpedance ground plane," *Electronics Letters*, vol. 38, no. 16, pp. 849–850, 2002.
- [10] J. G. Yook and L. P. B. Katehi, "Micromachined microstrip patch antenna with controlled mutual coupling and surface waves," *IEEE Transactions on Antennas and Propagation*, vol. 49, no. 9, pp. 1282–1289, 2001.
- [11] M. A. Khayat, J. T. Williams, D. R. Jackson, and S. A. Long, "Mutual coupling between reduced surface-wave microstrip

- antennas," *IEEE Transactions on Antennas and Propagation*, vol. 48, no. 10, pp. 1581–1593, 2000.
- [12] L. Huang and P. Russer, "Tunable antenna design procedure and harmonics suppression methods of the tunable DVB-H antenna for mobile applications," in *Proceedings of the 37th European Microwave Conference (EUMC '07)*, pp. 1062–1065, October 2007.